Study of Υ production as a function of charged-particle multiplicity in proton-proton collisions at $\sqrt{s} = 13$ TeV with ALICE at the LHC

Tasnuva Chowdhury

Université Clermont Auvergne

École Doctorale des Sciences Fondamentales

THÈSE

présentée pour obtenir le grade de

DOCTEUR D'UNIVERSITÉ

Spécialité: Particules, Interactions, Univers

présentée par

Tasnuva Chowdhury

Study of Υ production as a function of charged-particle multiplicity in proton-proton collisions at $\sqrt{s} = 13$ TeV with ALICE at the LHC

Thèse soutenue le 5 juillet 2019, devant le jury d'examen:

Président:	P. DUPIEUX	LPC (Clermont-Ferrand, France)
Rapporteurs:	A. ANDRONIC	IKP (Münster, Germany)
	R. ARNALDI	INFN (Turin, Italy)
Examinateurs:	D. CALVET	LPC (Clermont-Ferrand, France)
	H. PEREIRA-DA-COSTA	CEA/DPHN (Saclay, France)
	S. PORTEBOEUF-HOUSSAIS	LPC (Clermont-Ferrand, France)

Directeurs de thèse:

V. RAMILLIEN	LPC (Clermont-Ferrand, France)
S. PORTEBOEUF-HOUSSAIS	LPC (Clermont-Ferrand, France)

Acknowledgment

In the past three years, many people supported me through my Ph.D. to whom I would like to express my gratitude. First of all a warm thanks to the members of the ALICE group at LPC for giving me the opportunity to work with them. I would like to thank my Ph.D. advisers, Valerie Ramillien and Sarah Porteboeuf for their helpful advice. I would also like to thank the director of LPC- Dominique Pallin and the group leader of ALICE-LPC- Philippe Crochet for their help to finish my thesis successfully.

Many people in ALICE collaboration helped me at different stages of my analysis. The comments and suggestions from the conveners of the ALICE-DQ Group, Roberta Arnaldi and Hugo Pereira-Da-Costa have been extremely beneficial.

I want to thank to the members of my jury for accepting to be part of it. Thanks to my rapporteurs, Anton Andronic and Roberta Arnaldi for their patience reading this document, Pascal Dupieux for having accepted to preside the jury and my examinateurs David Calvet and Hugo Pereira-Da-Costa for the discussion before and during the defence.

I would like to thank Jana, Jonathan, Arthur, Deepak, Laura, Alex, Louis-Pierre, Nicoleta and Riyad for all the moral support they gave me along these three years. Many friends, not all of them physicists, have been a constant source of support. From helping me with my code or to go over a presentation or by just simply being there. It is beyond my power to list all of them here and I thank them all very much.

Last but not least, lots of love and thanks to my family- dad, mum and Abir without you it wouldn't be possible- Thank you.

Abstract

The study of quarkonium (J/ψ or Υ) in proton-proton (pp) collisions is interesting as both perturbative and non perturbative aspects of Quantum ChromoDynamics (QCD) are involved in the production mechanism. The quarkonium production as a function of charged-particle multiplicity has been measured in pp collisions with the ALICE detector at the Large Hadron Collider (LHC). They exhibit a non-trivial correlation that can lead to a better understanding of the multi-parton interaction mechanism in the initial state of the collision as well as possible collective effects in small systems. The study of the latest data sample recorded at the LHC in pp collisions at the highest collision energies ever reached in the laboratory ($\sqrt{s}$ = 13 TeV) will allow to investigate high multiplicity events. In ALICE, quarkonia are measured down to zero transverse momentum. Charmonia (J/ψ, $c\bar{c}$) are detected via their decay into di-electrons at mid-rapidity ($|y|< 0.9$) and dimuons at forward rapidity ($2.5 < y < 4$). Bottomonia (Υ, $b\bar{b}$) are detected via their decay into dimuons at forward rapidity. Charged-particle multiplicity is measured using track segments in the silicon pixel detector in $|\eta|< 1$. In this thesis, we will present the first ALICE measurements of relative Υ(1S) and Υ(2S) production as a function of multiplicity in pp collisions at $\sqrt{s}$ =13 TeV. We will discuss the ratio of the relative Υ(2S) over Υ(1S) as a function of charged-particle multiplicity. The comparison between the relative J/ψ and Υ(1S) yields measured at forward rapidity as a function of multiplicity will also be discussed. This will provide insight of possible dependence of the measured correlation with different mass and quark contents as well as the evolution with rapidity range and the collision energy.

Contents

Chapter 1

Introduction

The curiosity of understanding the elementary particles of which each matter is made of led to the formulation of one of the most successful theories of physics called the Standard Model (SM) [1, 2] of particle physics. The SM describes the elementary particles and their interactions. In the SM framework, the main constituents of matter are the quarks and gluons [3]. The quarks are confined by the strong nuclear force into a composite form called hadron (e.g. proton, neutron). The strong nuclear force [4, 5] is described by the theory of Quantum ChromoDynamics (QCD). One of the interesting QCD prediction is that at high enough temperatures or densities, matter undergoes a phase transition to a state where quarks and gluons become deconfined, known as the Quark Gluon Plasma (QGP). The SM predictions can be studied in an experimental facility by colliding high energy hadrons/nuclei. The Large Hadron Collider (LHC) is one of the most powerful facilities where several high energy collisions (proton-proton (pp), proton-nucleus (pA), nucleus-nucleus (AA)) are being investigated. ALICE (A Large Ion Collider Experiment) is the dedicated heavy-ion experiment at the LHC which is designed to study QGP in Pb-Pb collisions.

The hadronic collision is a very complex system where several processes are at play. These processes can be defined as hard or soft process depending on high or low momentum transfer during the collision. The production cross section of any particle includes both hard and soft processes, so it cannot distinguish the correlation between hard and soft processes. To understand this correlation more differential studies are needed such as particle production as a function of charged-particle multiplicity. At high energy pp collisions, this correlation becomes non-trivial due to several hadronic activities such as multiple-parton interactions (MPI). Several measurements were performed to study this correlation for example J/ψ ($c\bar{c}$) as a function of multiplicity in pp collisions at $\sqrt{s} = 13$ TeV. It shows that the relative J/ψ yield is increasing almost quadratically with increasing mean multiplicity. The reason for reaching such high multiplicities in pp collisions similar to the heavy-ion collisions are still not obvious. Another interesting measurement is the upsilon ($\Upsilon(b\bar{b})$) production as a function of multiplicity performed by the CMS (Compact Muon Solenoid) experiment at LHC [6]. The disappearance of the excited states of Υ is reported in different collision systems and center of mass energies where the Υ and multiplicities are measured in the same kinematic region. This correlation between the hard and soft processes can be affected by initial or final state effects of the collision. The study of this correlation in different systems and kinematic regions can contribute to our current understanding of any particle production associated with the underlying event mechanism. The focus of the doctoral research presented in this thesis is the study of upsilon ($b\bar{b}$) production as a function of charged-particle multiplicity in pp collisions at $\sqrt{s} = 13$ TeV. Upsilons are produced in hard scatterings. In this thesis, Υ and multiplicities are studied in different kinematic regions. Studying the observables with a difference between their

kinematic regions can shed some light on the understanding of the measured correlation.

The structure of this thesis is described in the following: the first chapter is dedicated to the theoretical background of the measurements presented here. A generic description of the behavior of matter and of the strong interaction under extreme conditions is given, followed by an introduction of the related measurements in heavy-ion collisions. A short description of the hadronic collision is given. Then the evolution of charged-particle multiplicities with increasing collision energies is discussed. The chapter ends by discussing some new signatures observed in pp and pA collisions. The second chapter introduces the observable used for this thesis. The experimental results which inspired this work, have been summarized in this chapter. In the third chapter, the experimental facility used for this work will be introduced. A part of the future ALICE upgrade will be presented in the fourth chapter which was done as a service task for the ALICE collaboration. The fifth chapter contains the data analysis procedure developed for this study and the results. The measurement of Υ production as a function of charged-particle multiplicity will be interpreted and discussed in the sixth chapter. The conclusions and future prospects are summarized in the last chapter.

Chapter 2

Fundamental overview

In this chapter, we will start by introducing the general context of Standard Model particles and their properties. We will present the state of matter called QGP which is believed to be existed at the early stage of Universe evolution after the Big Bang. We will also discuss the hadronic collisions, different components of a collision and the observables which will later be used for the work presented in this thesis.

2.1 The Standard Model of Particle Physics

The Standard Model (SM) [1, 2] is a theory based on the gauge symmetry group. The theory describes the properties of fermions (spin $\frac{1}{2}$ particles) and their strong and electroweak (EW) interactions. These interactions are mediated by bosons (spin 1 particles). Among the three fundamental forces: the strong force is carried by the massless gluon (g), the weak force is mediated by the massive vector gauge bosons ($W^{\pm}$, Z) and the electromagnetic force is mediated by the photon (γ). The SM theory can not describe the gravitational interaction, so this will not be a part of the following discussion.

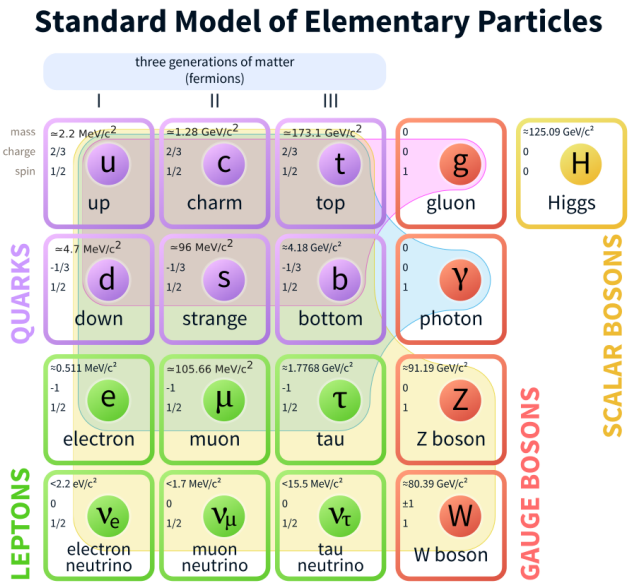

Figure 2.1: Elementary particles of Standard Model [7]

The SM is composed of three families of fermions which are classified in two kinds: quarks and leptons (shown in Fig.2.1). Leptons carry either only electric charge or neutral charge

(neutrinos) and the quarks carry both color charge (red, green or blue) and electric charge. All quarks and leptons carry mass. The elementary fermions are classified into three generations of particles where each particle has a corresponding anti-particle with identical properties but opposite quantum numbers. For both quarks and leptons, the generations follow an increasing mass hierarchy. There are six flavors of quarks (up u, down d, strange s, charm c, bottom b and top t) and anti-quarks ($\bar{u}$, $\bar{d}$, $\bar{s}$, $\bar{c}$, $\bar{b}$, $\bar{t}$). Concerning the leptons, there are three types of negatively charged leptons (e^-, μ^-, τ^-) and three types of neutral left-handed neutrino (ν_e^L, ν_μ^L, ν_τ^L). On the other hand their corresponding positively charged anti-leptons are (e^+, μ^+, τ^+). Each member of a generation has a greater mass than the corresponding particles of lower generations. The ordinary matter consist only of the first generation particles. The higher mass particles are highly unstable and are observed only in very high-energy environments. A summary of the SM particles is shown in Fig.2.1. The interaction between the particles are described in following shortly:

The electromagnetic force governs the interaction among two elementary particles with an electric charge. The force is due to the exchange of a massless photon. The photon is a particle with spin 1 and it does not carry any electric charge. The electromagnetic interaction is effective in an infinite range. The theory describing the electromagnetic interaction is the Quantum Electrodynamics (QED).

The weak force is mediated by massive particles ($W^{\pm}$, Z). The weak interaction has a finite range ($\sim 10^{-18}$ m). The W boson can carry either a positive or a negative electric charge. It has a mass of 80 GeV/c^2. The Z has a mass of 91 GeV/c^2 and is electrically neutral. The massive bosons also have an integer spin. The weak interaction is unified with the electromagnetic interaction in the electroweak (EW) theory [2, 8]. Another piece of SM model is the Higgs Mechanism. The mechanism that breaks electroweak symmetry [9], implies the existence of a scalar particle, the Higgs boson H. The discovery of Higgs boson at CERN was reported in 2012 [10, 11].

The strong interaction [4, 5] acts between particles carrying color charges. The interaction is mediated by gluons which can carry color charge and anti-color charge. A gluon is also a massless particle with spin 1. Gluons can also interact among themselves. The theory describing the strong interaction is QCD. A summary of the SM forces has been listed in Tab. 2.1.

Boson	Spin	Charge	Mass (GeV)	Interaction	Range (m)
γ	1	0	0	Electromagnetic	∞
$W^{\pm}$, z	1	± 1, 0	80.385, 91.188	Weak	10^{-18}
g	1	0	0	Strong	10^{-15}

Table 2.1: Vector bosons in the Standard Model

All the leptons in SM can be observed in nature as free particles, as they do not experience the strong force. On the other hand, quarks and gluons are not seen as individual particles. It is because of the phenomenon in QCD, called **color confinement**. The strong interaction between color charged particles force the quarks and gluons to be confined in hadrons. Hadrons are colorless. In addition to the valence quarks determining the quantum number of the hadrons, they contain a sea of virtual quarks and gluons, which contribute to the total energy and momentum. There are two kinds of hadrons (mesons and baryons). A meson is a quark-antiquark pair in a color-anticolor state. For example, J/ψ and Υ are the bound states of $c\bar{c}$ and $b\bar{b}$. A baryon is composed of quarks where each of them has a

different color such as proton(uud), neutron(udd), etc. Protons and neutrons are bound together to form a nucleus by the nuclear force. The matter observed in nature is made of atoms which are composed of a nucleus and one or more electrons bound to the nucleus.

In the formalism of the parton model [12], the constituents of a hadron are referred as partons. The scale of a strong interaction is the four momentum transferred between the partons participating in the hard scattering, Q^2. An interaction involving a large transfer of momentum is called hard and an interaction involving a small momentum transfer is called soft. At the leading order the strength of the strong coupling is given by the dependence of the strong coupling constant (α_s) with Q^2 [3] and can be written as:

$$\alpha_s(Q^2) = \frac{4\pi}{(11 - \frac{2}{3}n_f)ln\frac{Q^2}{\Lambda^2_{QCD}}} \tag{2.1}$$

where n_f is the number of quark flavors and Λ_{QCD} ($\sim$ 200 MeV) is a constant which corresponds to the limit where, for smaller energy transfers, the perturbative QCD (pQCD[1]) calculations is not applicable anymore.

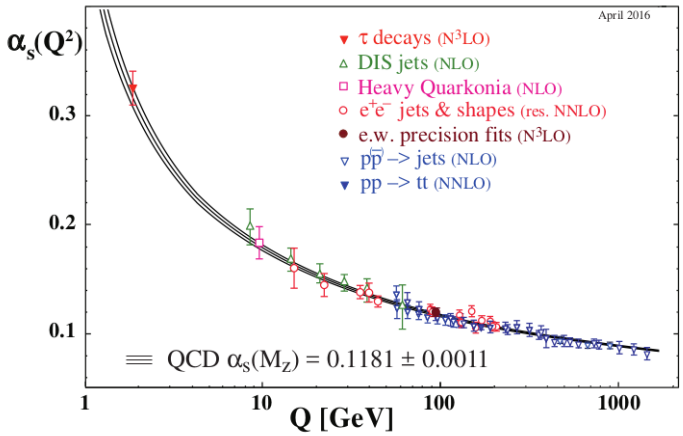

Figure 2.2: Summary of measurements of α_s as a function of the energy scale Q [7].

The strength of the strong force gets asymptotically reduced as the energy scale is increased. Perturbative QCD can then be fully applied to the asymptotic free regime since the strong coupling constant is small. Fig.2.2 shows that at small distances, or high Q^2 , the strength of the coupling constant α_s becomes small and this phenomenon is known as **asymptotic freedom** [13, 14].

The intensity of the strong force increases when the energy scale is reduced or the distance is increased as seen in Fig. 2.2. At low Q^2, the coupling becomes large, such that soft processes cannot be calculated using a perturbative expansion. The large distance behavior of the coupling constant leads to the confinement properties of the strong interaction.

[1]pQCD is a perturbative treatment of QCD which is valid for small values of α_s (at large Q^2).

2.2 The Quark-Gluon Plasma (QGP)

At high energy densities, QCD predicts a phase transition from hadron to a deconfined state of partonic matter called the Quark-Gluon Plasma (QGP) [15, 16].

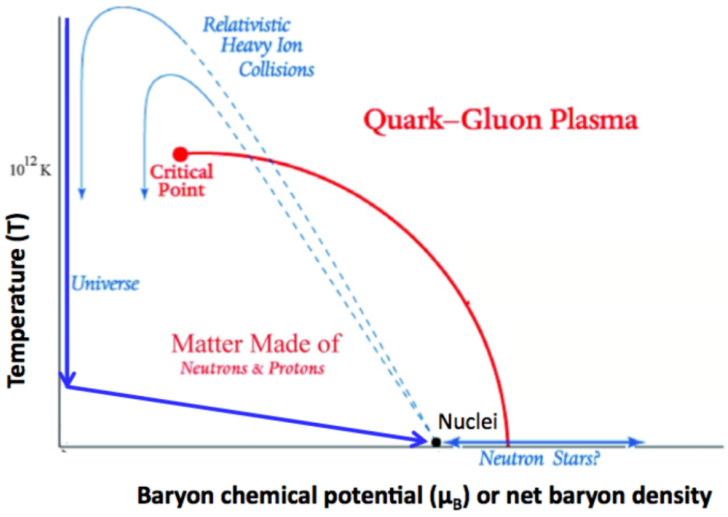

Figure 2.3: The QCD phase diagram. The temperature T as a function of the baryon chemical potential μ_B or the net baryon density [17].

In this regime of asymptotic freedom, quarks and gluons are not confined in color-neutral objects and become the relevant degrees of freedom for the QGP. This phase transition is illustrated in the QCD phase diagram shown in Fig. 2.3. The x-axis is the net baryon density and the y-axis is the temperature of the QCD matter [18]. The baryon chemical potential (μ_B) can be viewed as a measure of the excess of matter over anti-matter and it is proportional to the baryon density. The phase transition can be triggered by either compressing the hadronic matter to large density (large μ_B) or heating it to high temperature. A first-order transition from partonic matter to hadronic matter is expected, at the critical end point [19]. The temperature at the critical point is known as critical temperature (T_c) in the $T - \mu_B$ phase diagram.

This deconfined state of matter is believed to exist in the cosmological era from electroweak decoupling to hadron formation. The calculations of Lattice QCD (lQCD[2]) at μ_B=0 predicts the crossover at a temperature 156.5 $\pm$ 1.5 MeV or a critical energy density 0.42 GeV/fm^3 [20].

2.2.1 Evolution of heavy-ion collision

Since nuclei are objects of finite size and area, the collision can have different geometries depending on how the collision takes place. A Schematic view of a typical collision of two heavy nuclei is shown in Fig. 2.4. The axes of the two nuclei are separated by a distance b, defined as the impact parameter.
The collision is central when the two nuclei collide with zero or very small impact parameter. In this case, the interaction area is large and the number of nucleons participating is high. The number of participating nucleons is denoted as N_{part} (participant) and the rest are called the spectators (shown in Fig. 2.4 right). The collision is called peripheral

[2]lQCD is a discrete formulation of QCD.

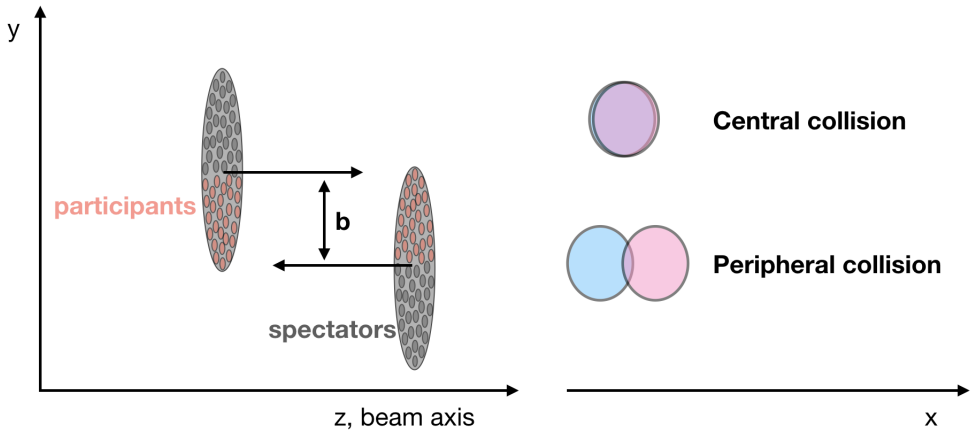

Figure 2.4: Illustration of heavy-ion collision.

if the nuclei are colliding with a large impact parameter or ultra-peripheral when nuclei are just grazing each other. The overlap region of heavy ions is defined by the key parameter called centrality, which depends on the impact parameter. Centrality is expressed in percentiles, where low values indicate more central collisions. The total number of binary nucleon-nucleon interactions is usually denoted as N_{coll}.

The dynamic evolution of a relativistic heavy-ion collision is shown in Fig. 2.5 where different stages of the evolution are identified:

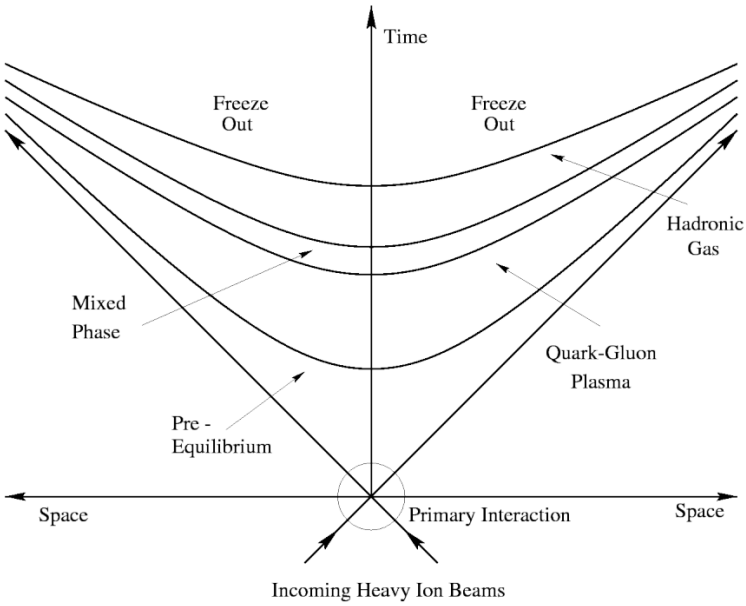

Figure 2.5: The space-time evolution of a heavy-ion collision [21]

(a) Pre-equilibrium: The collision of the nuclei takes place at $\tau = 0$. Pre-equilibrium phase is created in the beginning of the collision by the multiple hard scatterings between the partons of the nuclei.

(b) QGP formation and hydrodynamic expansion: If the energy density of the system is high enough the QGP is formed. Subsequently, the system evolves as a nearly-perfect

fluid. The hot medium further expands and cools down.

(c) Mixed state: The expanding system cools down. When the temperature drops below the critical temperature, the quarks-gluon plasma hadronize.

(d) Hadronic gas phase: Once all the quarks and gluons are confined, the system can be described by an expanding hadronic gas phase.

(e) Freeze-out: The hadron gas experience first a chemical freeze-out when the inelastic collisions between hadrons cease, fixing the composition of the particles. Subsequently, the system reaches a kinetic freeze-out when the elastic scatterings between hadrons ends, fixing the kinematic distributions of the particles. The particles stream freely to the detectors.

The QGP can not be directly measured experimentally since once it is created it only exists for a very short time. It can be studied indirectly by measuring how the properties of particles and the system produced in the collision are modified by the presence of the QGP. The production mechanism of each experimental probe depends on the momentum scale of the process. The hard probes are the signatures that are produced in processes involving large momentum transfer and created in the initial stages of the collisions. Some important hard probes are used to study the nuclear medium includes the electroweak bosons and quarkonia [22, 23, 24]. The majority of the particles produced in heavy-ion collisions are soft and constitutes the bulk of the system. Soft probes are used to study the thermal and hydrodynamical evolution of the medium. In section 2.5, some of the probes will be discussed.

2.3 Hadronic Collisions

A hadron-hadron (i.e p-p) collision can be categorized into elastic and inelastic collisions. The total pp cross section can be described as a sum of the elastic and inelastic components, $\sigma_{Total} = \sigma_{EL} + \sigma_{IN}$. The proton-proton scatter elastically through small angle, exchanging momentum but there are no new particles. In inelastic collision, one or both hadrons have a change in energy and direction and also produce particles. Inelastic collision can be classified into non-diffractive, single-diffractive, double-diffractive, and central-diffractive collisions. An inelastic collision is diffractive when no internal quantum numbers are exchanged between the colliding particles. In diffractive scatterings, the energy transfer between the two interacting protons remains small, but one or both protons dissociate into multi-particle final states with the same quantum numbers of the colliding protons. The interaction is Non-Diffractive if there is an exchange of color charge and subsequently more hadrons are produced. If only one of the protons dissociates then the interaction is Single Diffractive (SD). If both colliding protons dissociate, then is Double Diffractive (DD). The interaction is a Central-Diffractive (CD) when both protons remain intact and are seen in the final state.

2.3.1 Components of a hadronic collision

One interesting tool to study the high energy collisions are Monte Carlo (MC) event generators [25] which simulate collisions that are as similar as possible to real events which are provided by the experimental facility, down to the level of final stable particles. Example of some largely used MC event generators are PYTHIA [26] and EPOS [27].

A schematic picture of hadron-hadron collision is illustrated in Fig. 2.6 where two protons collide and produce several final-state particles. The understanding of a complete pp collision require the knowledge of the hard and soft-components of the collision. In following, different components of a non-diffractive inelastic collision in the context of PYTHIA event generator will be discussed in short:

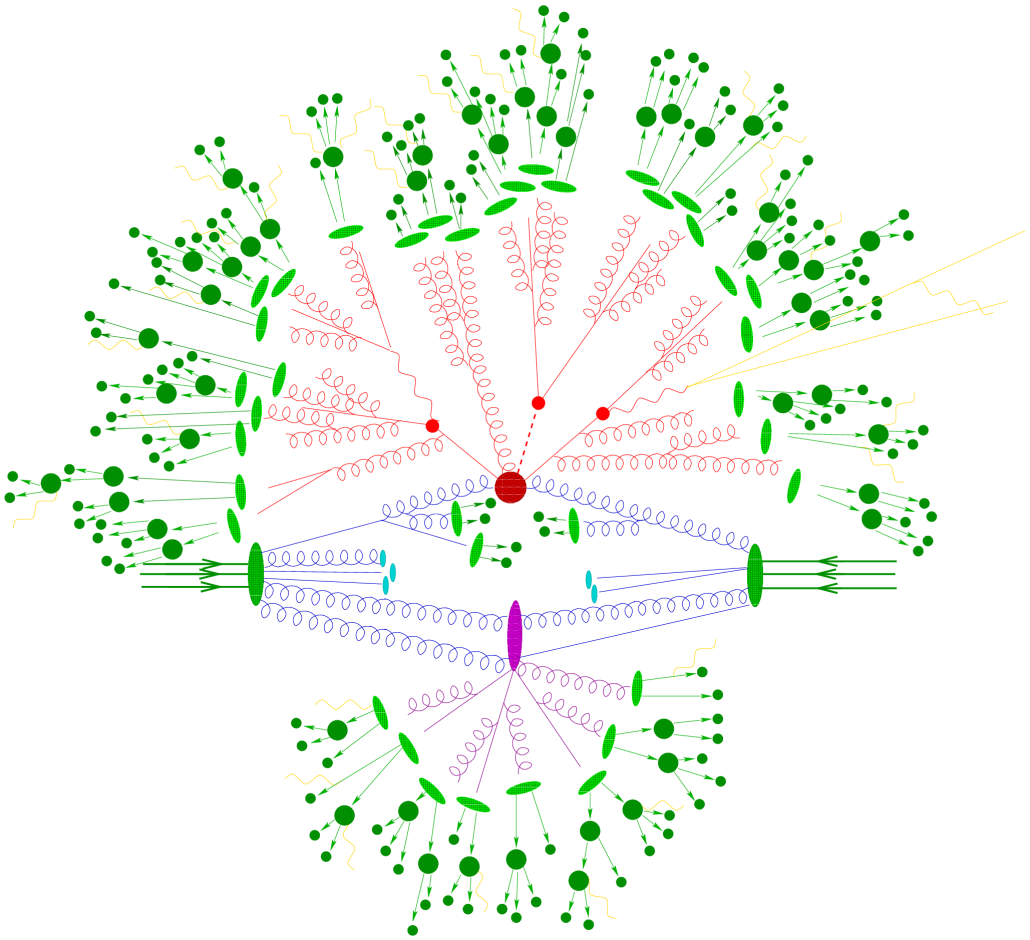

Figure 2.6: A sketch of a hadron-hadron collision in PYTHIA event generation. The red blob in the center represents the hard collision, surrounded by a tree-like structure representing Bremsstrahlung as simulated by parton showers. The purple blob indicates a secondary hard scattering event. Parton-to-hadron transitions are represented by light green blobs, dark green blobs indicate hadron decays, while yellow lines signal soft photon radiation.[28]

(a) The hard process is characterized by the highest momentum transferred (e.g. production of jets or heavy quarks) in a hadron-hadron collision. Each of them consists of many partons (quarks, antiquarks, and gluons) whose distribution can be characterized by Parton Distribution Functions (PDFs). The PDF $f_i(x, Q^2)$ describes

the probability of finding a parton i with the momentum fraction x of the total momentum of the particle probed at a scale Q^2. PDFs are parameterizations of experimental data. Several parameterizations exist[3].

(b) An initial-state shower (or initial state radiation) is the radiation that develops from incoming partons.

(c) A final-state shower (or final state radiation) is the radiation that develops from an outgoing parton of the hard subprocess. This process is especially important for higher energies.

(d) Multiple parton interactions (MPI) describes the possibility to have more than one distinct and simultaneous parton interaction inside the same hadronic collision.

(e) Beam-beam remnants (BBR) are remaining partons which did not take part in the hard scattering and other processes. It is detected only in the detector part close to the beam pipe. Beam-beam remnants mainly contribute to the soft part.

Underlying Event (UE) is a generic term in a hadronic collision, which includes most of the occurring partonic interactions excluding the hard scattering. Many of the effects described in earlier can be associated with the UE: ISR, FSR and BBR.

2.3.2 Kinematic Variables

In high energy physics, the position of a particle in the detector is expressed in terms of azimuthal angle ϕ and the rapidity y or the pseudo-rapidity η. To simplify our further discussion we will give a short description of these variables in following.

The positive z-axis lies along the incident proton beam direction (Fig 2.7). The origin of the coordinate system is fixed where the beams collide. The θ_{cm} is the polar angle in xz plane 2.7b and ϕ is the azimuthal angle around the beam axis in xy plane 2.7c. The momentum of the considered particle is denoted as p and its three components along x, y and z axes are p_x, p_y and p_z respectively. The transverse momentum of the particle is denoted as p_{T} which can be derived as:

$$p_{\mathrm{T}} = \sqrt{(p_x^2 + p_y^2)}$$

The rapidity (y) relative to a beam axis is defined in terms of the particle kinematics. It can be written as:

$$y = \frac{1}{2}\ln\Big(\frac{E + p_z c}{E - p_z c}\Big)$$

Here, E is the energy of the particle being considered and c is the speed of light in a vacuum.

Another commonly used spatial coordinate is the pseudo-rapidity, η , which describes the angle of a particle relative to the beam axis. The pseudo-rapidity is a very useful variable as it does not need measurements of particle's energy and momentum but the polar angle. It is defined as

$$\eta = -\ln[\tan(\frac{\theta_{cm}}{2})]$$

[3]The generated events additionally rely upon the choice of the PDFs, i.e. the default setup for PDFs in PYTHIA is CTEQ5L [29]. This parametrization results from a global fit to high energy lepton-hadron and hadron-hadron collision measurements.

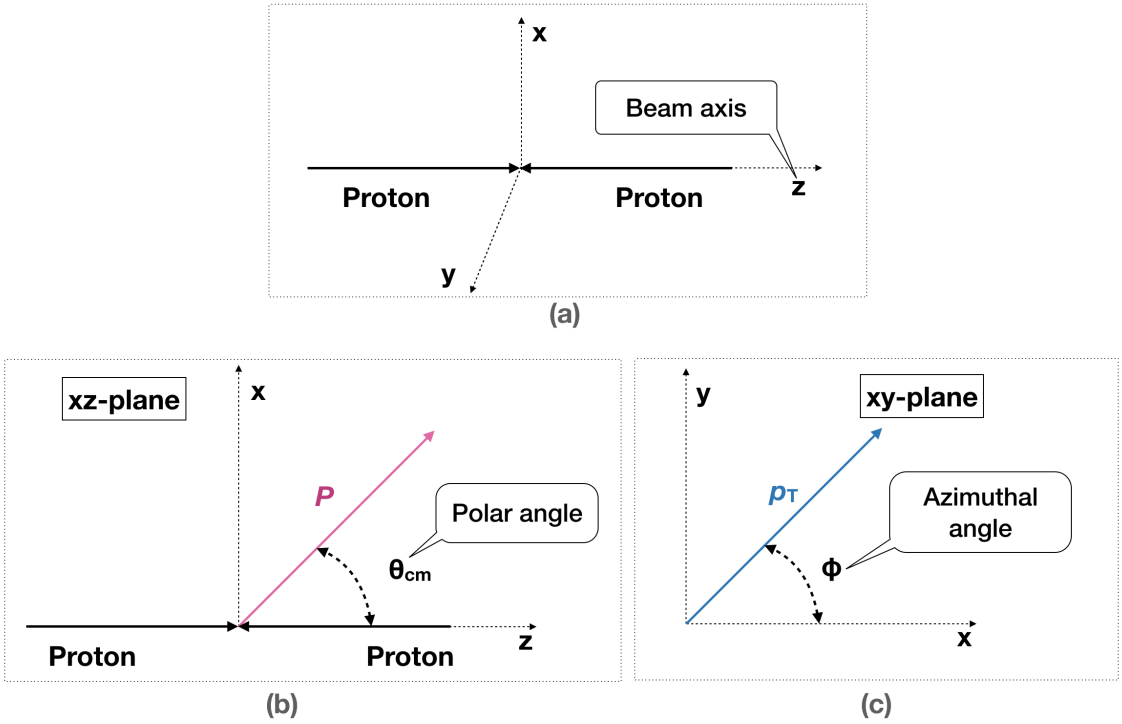

Figure 2.7: Illustration of the coordinate system in a pp collision.

2.4 Charged-particle multiplicity

The charged-particle multiplicity is one of the basic observables in high-energy collisions. It is very useful to study the underlying mechanism in a collision. The total number of charged-particle multiplicity is largely dominated by the soft processes which lies in the non-perturbative QCD regime. It is also important to understand this observable as a function of collision energy. The energy dependence is studied by investigating the behavior of $\mathrm{d}N_{ch}/\mathrm{d}\eta$ at $\eta = 0$ as a function of $\sqrt{s}$ and the average multiplicity in different phase space $\langle N_{ch} \rangle$ vs. $\sqrt{s}$. In following paragraphs, we will give a short overview of the base calculations that can describe the charged-particle multiplicity to some extent:

In 1969 Feynman suggested that the average number of particles produced in collisions rises with the logarithm of $\sqrt(s)$ [30]. According to Feynman, the probability of finding a particle of type i for a given momentum and mass:

$$P_i(p_{\mathrm{T}}, p_z, m) = f_i(p_{\mathrm{T}}, p_z/W)\frac{dp_z d^2p_{\mathrm{T}}}{E} \tag{2.2}$$

where $W = \sqrt{s}/2$ is half the collision energy, equal to the energy of one of the colliding particles if colliding identical beams f_i is the structure function. This assumption is the Feynman scaling and f_i is called scaling function.

In 1972 Koba, Nielsen and Olesen (KNO) showed that Feynman scaling leads to scaling of multiplicity distributions [31]. Specifically, they showed that the distribution of the number of particles n in the final state should be a function only of the variable $z = n/\langle n \rangle$, $\langle n \rangle$ is the average multiplicity at $\sqrt{s}$. It can be written as

$$P_n(s) = \frac{\sigma_n(s)}{\sigma_{tot}(s)} = \frac{1}{\langle n \rangle}\Psi\Big(\frac{n}{\langle n \rangle}\Big) \tag{2.3}$$

where $\sigma_{tot}(s)$ is the total cross section and $\sigma_n(s)$ is the cross section of event with multiplicity n. $\Psi(z = \frac{n}{\langle n \rangle})$ is a universal function which is energy-independent. This means that multiplicity distributions at all energies fall onto one curve when plotted as a function of z. However, $\Psi(z)$ can be different depending on the type of interaction and the type of measured particles. Therefore, the multiplicity distribution in general, and the ratio of the width of the distribution to the mean remain the same. Deviations are observed for inelastic events at center-of-mass energies above about 30 GeV and for non-single diffractive (NSD[4]) events above 200 GeV.

In 1985, the UA5 (Underground Area 5) experiment showed that the multiplicity distribution at $\sqrt{s} = 540$ GeV can be well described by a Negative Binomial Distribution (NBD) [32]. The distribution can be written as:

$$P_{p,k}^{NBD}(n) = \binom{n+k-1}{n} (1-p)^n p^k \tag{2.4}$$

where n is the number of successes, $k-1$ is the number of failures before the k^{th} failure and p is the probability of a successful Bernoulli trial. The binomial coefficient gives the number of ways to arrange n failures from a group of $(n+k-1)$ trials. The number of trials in the coefficient is 1 less than the total number of trials, as the last trial is the k^{th} trial resulting in failure. In the limiting case of $k \longrightarrow \infty$ the NBD becomes the Poisson distribution and it becomes a geometric distribution when k = 1. To describe the multiplicity probability distribution $(P(n)/\langle n \rangle)$ at higher energy, combinations of two or more NBDs are used.

2.4.1 Experimental results for multiplicity measurements

The CERN Intersecting Storage Ring (ISR) was the first hadron collider, producing collisions between protons with center of mass energy $\sqrt{s} \sim 30$, 44, 53 and 62 GeV. The multiplicity distributions observed at these energies for NSD events are shown in Fig. 2.8, and all follow KNO scaling [33].

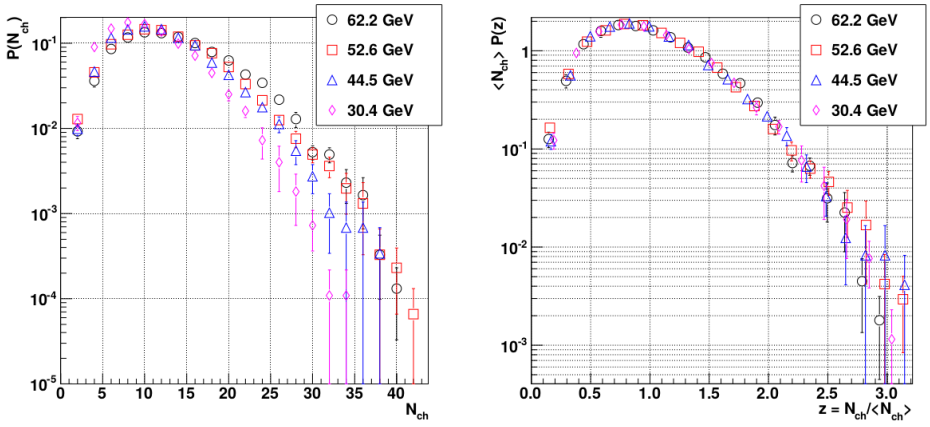

Figure 2.8: The normalized multiplicity distributions in full phase space (left) observed at the ISR with $\sqrt{s}$ between 30.4 and 62.2 GeV, also shown in KNO variables (right) for NSD interactions [33].

[4]Non Single Diffractive (NSD) events are basically the sum of Non-Diffractive (ND) and Double Diffractive (DD) events

The UA5 experiment observed collisions at the SPS collider from $\sqrt{s}$ = 200 to 900 GeV. It measured multiplicity distributions in pseudo-rapidity bins up to $|\eta|<$ 5.0 as well as full phase space for NSD collisions of protons and anti-protons. The observed multiplicity distribution in full phase space at $\sqrt{s}$ = 900 GeV was the first that could not be described by a single NBD fit, also indicating a violation of KNO scaling, as shown in Fig.2.9 (left). A combination of two NBDs was successfully fitted to the UA5 $\sqrt{s}$ = 900 GeV distribution as shown in Fig.2.9 (right), describing contributions to the total multiplicity from soft and semi-hard events. The average multiplicity of soft events was seen to be roughly half that of semi-hard events, and still followed KNO scaling, unlike semi-hard events.

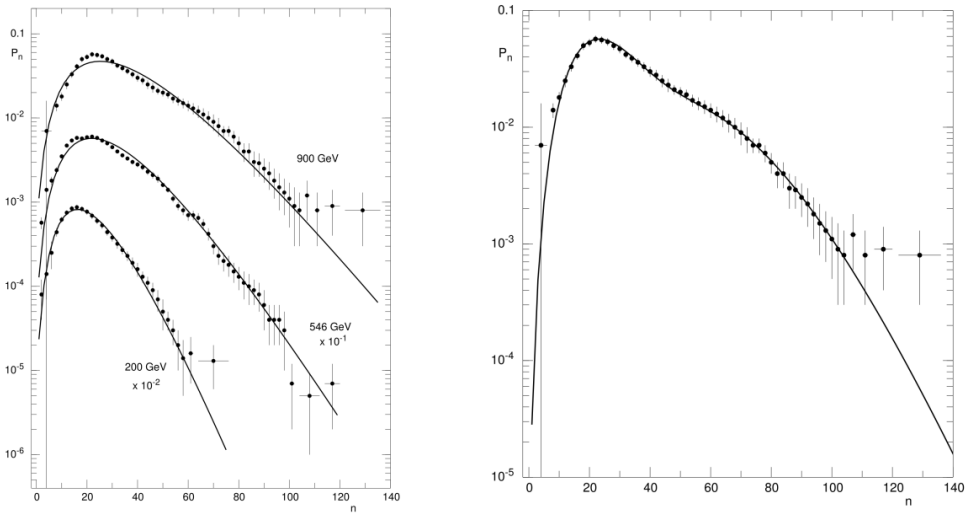

Figure 2.9: Left: UA5 multiplicity distributions in full phase space (from an acceptance of $|\eta|<$ 5.0) for NSD events in proton-anti-proton collisions at $\sqrt{s}$= 200, 546 and 900 GeV, showing the best of a NBD. The $\sqrt{s}$ = 900 GeV data clearly show a shoulder structure above n = 60. Right: Using the sum of 2 NBDs reproduces the structure avobe n =60 [34].

The Tevatron at Fermilab collided protons with anti-protons up to $\sqrt{s}$ = 1800 GeV and the E735 experiment published multiplicity measurements for NSD events in the full phase space, these are shown in comparison to lower collision energy distributions in KNO variables from UA5 and ISR in Fig. 2.10. The onset of KNO scaling violation is visible as the collision energy increases.

For NSD events KNO scaling has been observed at the ISR from $\sqrt{s}$ = 30.4 $\sim$ 62.2 GeV and starts to fail starting at about 200 GeV [33, 36]. For NSD events, the multiplicity distribution can be described by an NBD up to $\sqrt{s}$ = 540 GeV in full phase space (ISR, UA5) [37, 38] and up to 1.8 TeV in $|\eta|<$ 0.5 (UA5, CDF). For inelastic events, KNO scaling has been observed in $|\eta|<$ 1.5 for 23.6- 62.8 GeV (ISR). For full phase space it has not been found from $\sqrt{s}$ = 30.4 GeV. In very central pseudo-rapidity window $|\eta|<$ 0.5 the KNO-scaling is still maintained at $\sqrt{s}$ = 2.36 TeV [39]. With rising $\sqrt{s}$, the high multiplicities are enhanced.
The underlying production process can be described by uncorrelated emission, i.e. the production of an additional particle is independent from the already produced particles, the multiplicity distribution is expected to be of Poissonian form. Any difference to this, indicates correlations between the produced particles. Understanding the multiplicity

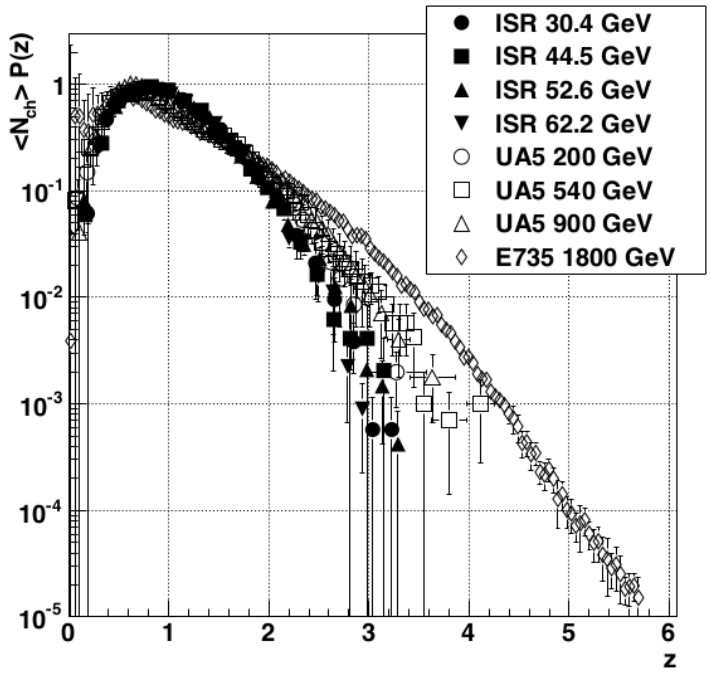

Figure 2.10: The violation of KNO scaling with increasing collision energy [35].

distribution is still a challenge as with increasing collision energy, it is largely influenced by multiple-parton interactions. In chapter 3, we will discuss the correlation between hard and soft processes where charged-particle multiplicity is one of the key observables.

2.5 Hints of collectivity in small system

The proton-proton collision system is showing non-trivial collective behavior with increasing collision energy and multiplicity. In following, we will discuss few examples:

A measurement of the two-particle angular correlation in pp collisions producing high number of particles (referred as high-multiplicity collisions) has been performed by the CMS collaboration. Fig. 2.11 presents the two-particle $\Delta\eta - \Delta\phi$ correlation function measured by the CMS collaboration in pp collisions at $\sqrt{s} = 7$ TeV [40], where $\Delta\phi$ is the azimuthal angle difference between the two particles and $\Delta\eta$ is the difference in their pseudo-rapidity. The results show a long-range structure ($2.0 < \Delta\eta < 4.8$) of near-side ($\Delta\phi \sim 0$) two-particle correlations, often called "ridge". The structure is seen for particles with 1 GeV/c < p_{T} < 3 GeV/c , produced in high-multiplicity ($N > 110$) pp collisions.

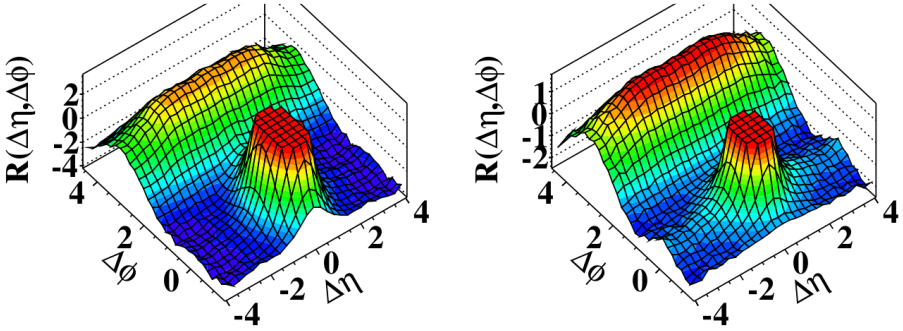

Figure 2.11: 2-D two-particle correlation functions for 7 TeV pp high multiplicity (left) N_{trk} ≥110 events with $p_{\mathrm{T}} > 0.1$GeV/c and (right) high multiplicity $N_{trk} \geq 110$ events with $1 < p_{\mathrm{T}} < 3$ GeV/c

A similar ridge-like structure had already been observed at RHIC in heavy-ion collisions [41], which was understood as a result of the hydrodynamic expansion of the QGP, but the phenomenon found in high multiplicity p-p collisions was completely unexpected at the time and it is still not fully understood.

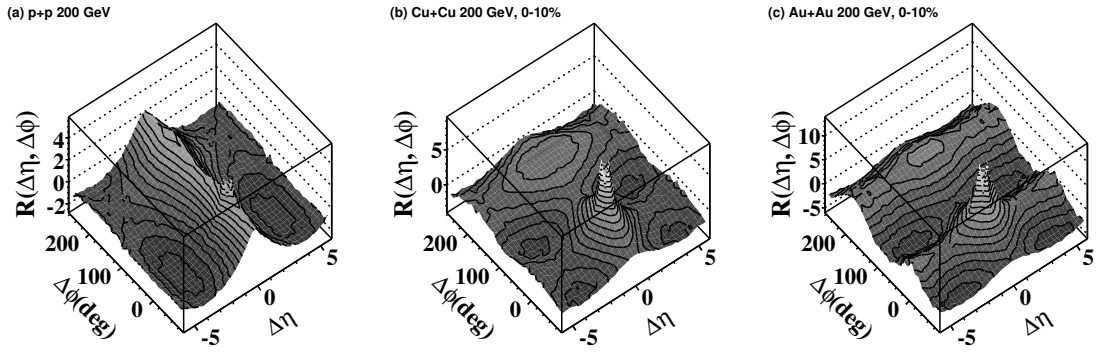

Figure 2.12: Two-particle correlation functions in $\Delta\eta$ and $\Delta\phi$ for (a) p+p, the most central 10% (b) Cu+Cu and (c) Au+Au collisions at $\sqrt{s}$ or s_{NN} = 200 GeV [41].

In hadronic collisions, strange quark-antiquark pairs (ss) are produced in parton-parton interactions via gluon fusion ($gg \rightarrow ss$) or quark annihilation ($qq \rightarrow ss$), and through gluon splitting ($g \rightarrow ss$) during the evolution of the system. The production of strange hadrons in proton-proton collisions is suppressed relative to hadrons made of light quarks

(i.e. pions), due to the higher mass of the strange quark.

In heavy-ion collisions, where the QGP is formed, it was proposed by Johann Rafelski and Rolf Hagedorn [42] in 1980, that the enhancement of strangeness[5] could be a probe of the QGP. Due to the large gluon density and energy present in the hot medium, the gluon fusion becomes the dominant production mode of strange-quark pairs in the QGP. When the temperature of the QGP decreases and the partons hadronize, the production of hadrons containing strange (anti-)quarks is enhanced relative to the production of pions. Moreover, at high collision energies, the strange quarks can also bind to charm and bottom quarks during hadronization, producing many exotic hadrons (e.g. strange D_s or B_s mesons) that would otherwise be rarely seen without the presence of the QGP. In summary, one expects an overall increase of strange-quark pair production, leading to an enhancement of the production of strange hadrons in central heavy-ion collisions compared to proton-proton collisions [43].

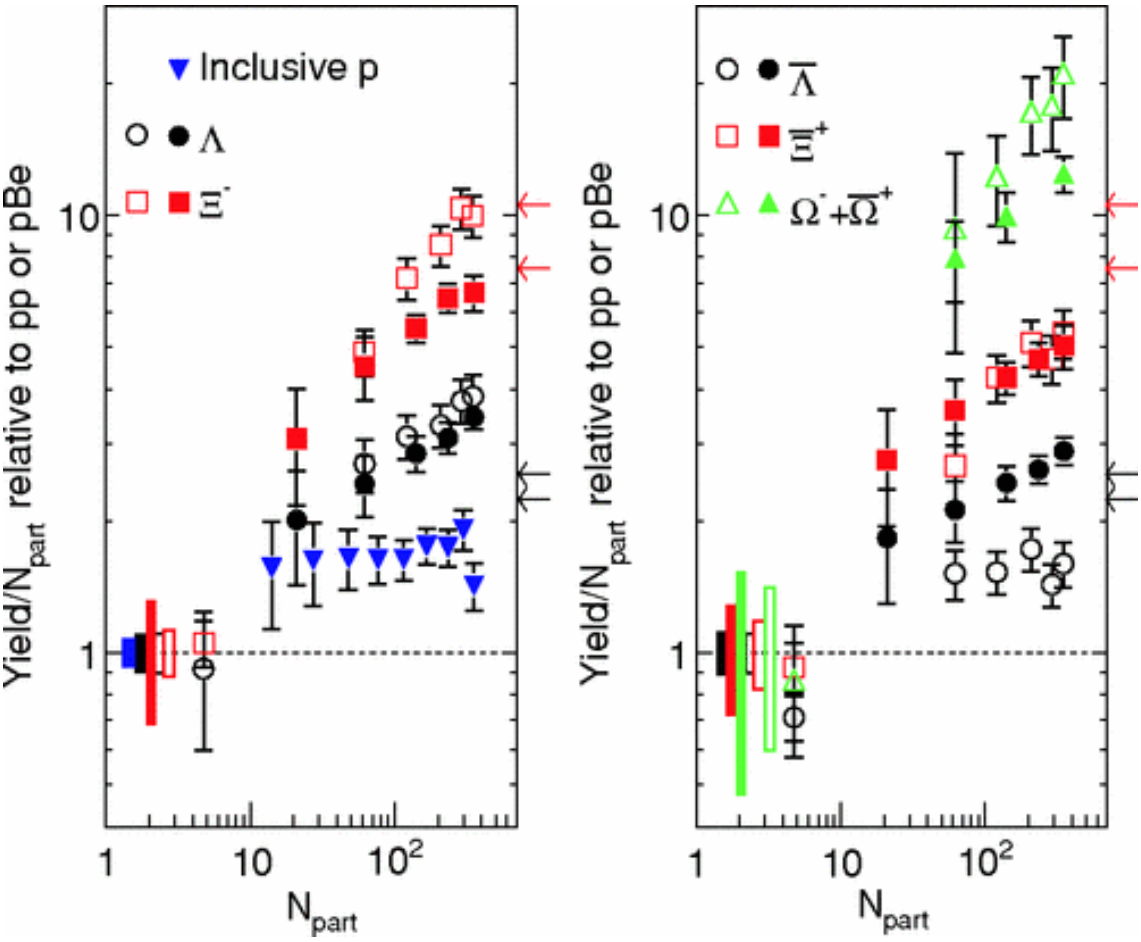

Figure 2.13: Distribution of the yield of inclusive protons and strange baryons, measured by the STAR collaboration in Au-Au collisions at $\sqrt{s_{NN}} = 200$ GeV (solid symbols) and by the NA57 collaboration in Pb-Pb collisions at = 17.3 GeV (empty symbols), relative to the corresponding yield in p-p (at RHIC) or p-Be (at SPS) collisions scaled by N_{part} [43].

[5]Strange (s) quarks belong to the second generation of quarks and are roughly 20-40 times more massive than u and d quarks. The number of strange quarks can be quantified through the quantum number called strangeness, which can take values of + 1, - 1 and 0, for strange quarks

The enhancement of strange hadrons has been observed at SPS [44, 45] and RHIC [46]. The production yields in heavy-ion collisions of strange hadrons measured at RHIC and SPS are shown in Fig.2.13. The results show a clear enhancement of the production of strange baryons in heavy-ion collisions relative to p-p (at RHIC) or p-Be (at SPS) collisions, increasing for higher N_{part} (more central collisions) and strangeness content.

The ALICE collaboration published in [47] the observation of an enhanced production of strange hadrons in high-multiplicity proton-proton collisions at $\sqrt{s} = 7$ TeV, as presented in the right plot of Fig.2.14. The results at LHC show a continuous increase of the enhancement of the strangeness production as a function of charged-particle multiplicity from high-multiplicity p-p to p-Pb to Pb-Pb collisions.

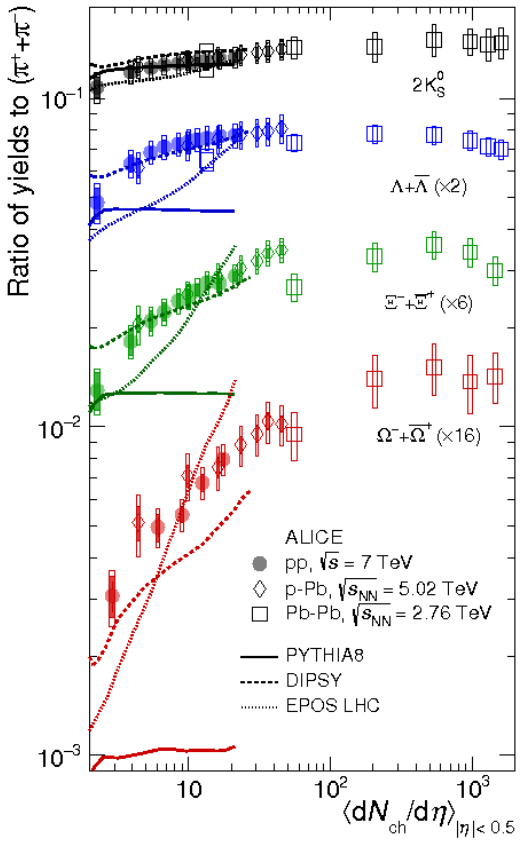

Figure 2.14: Distribution of the p_{T} integrated yield ratios of strange hadrons to pions as a function of the average charged-particle multiplicity measured in $|\eta|<0.5$ by the ALICE collaboration in p-p, p-Pb and Pb-Pb collisions at $\sqrt{s} = 7$ TeV, $\sqrt{s_{NN}} = 5.02$ TeV and $\sqrt{s_{NN}} = 2.76$ TeV, respectively.

These observations in high multiplicity pp collisions raise questions to our current understanding of the pp collisions modeling. Therefore, it is necessary to have a better understanding of the initial state of the collision, especially in high multiplicity pp collisions. Thus it is essential to understand how the produced charged particles are correlated or not, to the production of the hard probes.

Summary

The first part of this chapter introduces the Standard model being a very successful theory in describing the elementary particles and their interactions. The quarks and gluons which take part into the strong interaction of the SM model are not found free in nature due to their confinement properties. At high energies, quarks become asymptotically free where hadronic matter transit through a de-confined partons state known as QGP. It can be investigated in the heavy-ion collisions. The second part of this chapters describes hadronic collision and it's different components. The observable "charged-particle multiplicity" is discussed which in general is used to study the soft particle production. Finally, the collective like effect in pp collision has also been presented. In the next chapter we will introduce the quarkonia as a hard probe and the possible dependence of their production mechanism as a function of charged-particle multiplicity.

Chapter 3

Quarkonium production as a function of charged-particle multiplicity

In this chapter we will present a short description of Quarkonia and their production mechanism. We will discuss about the quarkonium production as a function of multiplicity from experimental and phenomenological point of view which is the main focus of this thesis.

3.1 Quarkonia

Quarkonia are bound states of a heavy quark-antiquark pair. Bound states of $(c\bar{c})$ are called charmonia, while $(b\bar{b})$ are known as bottomonia. Their production mechanisms include both soft and hard scales of QCD. They are also important in QGP studies as due to their heavy mass, the heavy quarks are produced in the initial hard scattering processes in hadronic collisions. In consequence, they are able to experience the full evolution of the p-Pb or Pb-Pb collisions. Moreover, the presence of nuclear matter can affect their hadronisation. Heavy flavor hadrons are hence an important tool to study QGP in pPb and PbPb collisions.

3.1.1 Charmonium

The J/ψ meson has a mass of 3.1 GeV/c^2. It was discovered in 1974 by two different laboratories almost at the same time. S. Ting observed a sharp peak in the electron-positron invariant mass spectrum studying 30 GeV protons accelerated by the Alternating Gradient Synchrotron (AGS) at Brookhaven National Laboratory (BNL) colliding on a fixed target (showed in Fig. 3.1) [48]. B. Richter found the same structure in e^+e^- annihilation at the electron-positron storage ring SPEAR at the Stanford Linear Accelerator Center (SLAC) [49]. The first excited state of J/ψ the ψ(2S) or ψ' was discovered by the same group at SLAC. Fig. 3.2 shows the different charmonium states with their masses and quantum numbers, hadronic transitions among them, and the different open charm thresholds.

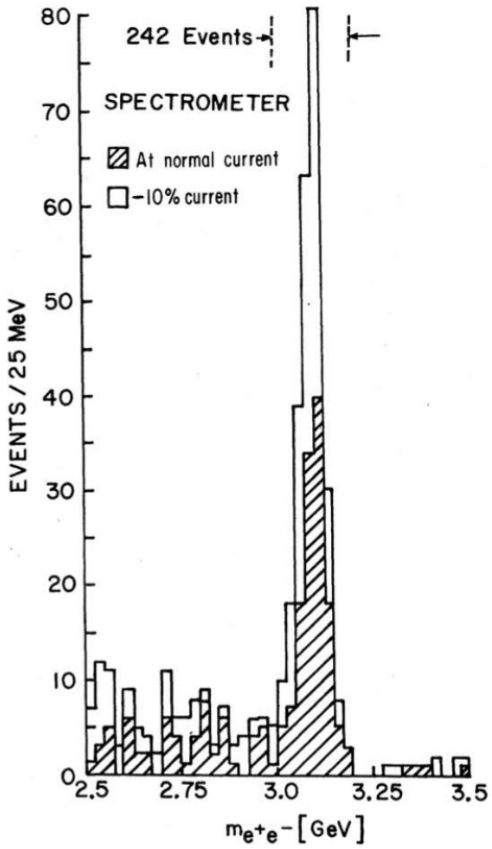

Figure 3.1: Mass spectrum of e^+e^- pairs produced in the reaction p+Be from proton beams accelerated at the alternating gradient synchrotron of the BNL [48].

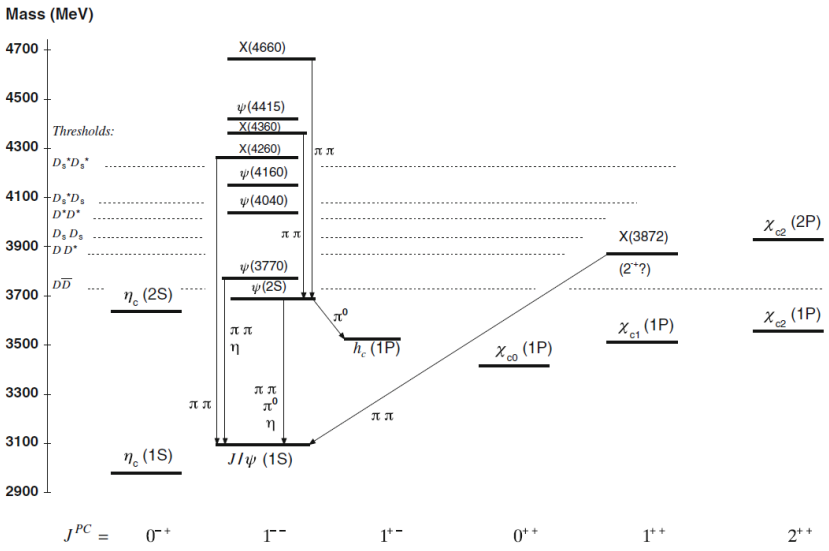

Figure 3.2: Charmonium decay modes with spectroscopy notation [7].

3.1.2 Bottomonium

In 1977, a new resonance called Υ which is similar to the J/ψ appeared in the dimuon mass spectrum (Fig. 3.3) at around 9.5 GeV/c^2 in 400 GeV proton-nucleus collisions at FNAL. This particle was interpreted as the lightest $b\bar{b}$ vector meson [50]. The Υ(2S) and Υ(3S) were claimed to be observed in 1977 [51] and 1979 [52] respectively.

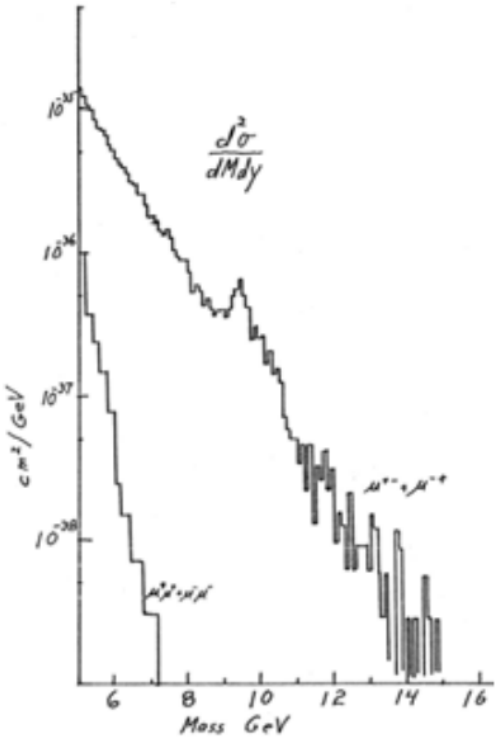

Figure 3.3: Measured dimuon production cross sections as a function of the dimuon invariant mass. The peak of the Υ resonances is well visible at around 9.5 GeV/c^2 [50].

Tab. 3.1 contains the latest and most accurate measurements of mass (m), full width (Γ), relevant quantum numbers and symmetries and the most important decay modes of the three Υ states [7]. It is important to note the large the Υ(1S) component is from heavier states feed down. In fact, the Υ(2S) has a quite high probability to decay into the fundamental state plus two pions ($\sim$ 17.85%) and the χ_b ($1P$) produced with a photon in the radiative decays can themselves decay into Υ(1S) plus another photon. The Υ(3S) has the same behavior: it can decay into (2S) plus $\pi\pi$ or $\gamma\gamma$ or into Υ(1S)$\pi\pi$. The various $\chi_b(2P)$ usually decay as well into Υ(2S) or, more rarely, into Υ(1S) plus a photon [7]. From CDF measurements in $p\bar{p}$ collisions at 1.8 GeV, 27% of all the Υ(1S) with $p_{\mathrm{T}} >$ 8 GeV/c are originated from χ_b ($1P$), almost 11% come from χ_b ($2P$) and only 51% are directly produced [53]. The Υ decays are also summarized in Fig. 3.4.

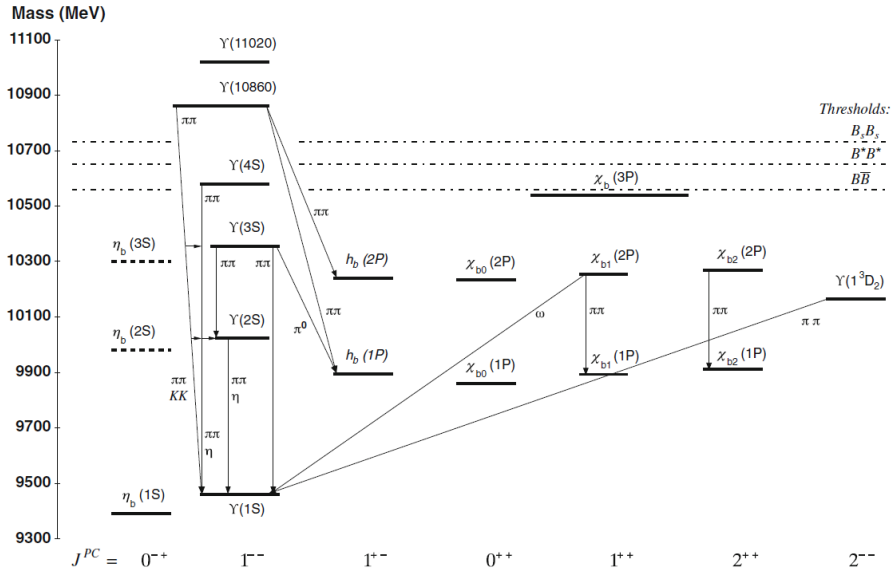

Figure 3.4: Bottomonium decay modes with spectroscopy notation [7].

State	Υ(1S)	Υ(2S)	Υ(3S)
m (MeV/c^2)	9460.30±0.26	10023.26±0.31	10355.2±0.5
Γ (keV/c^2)	54.02±1.25	31.98±2.63	20.32±1.85
Principal hadronic decays	ggg (81.7%) γgg (2.2%) $\eta' X$ (2.9%) $D^{*\pm}X$ (2.5%)	ggg (58.8%) γgg (8.8%) Υ(1S)$\pi^+\pi^-$ (17.9%) Υ(1S)$\pi^0\pi^0$ (8.6%)	ggg (35.7%) Υ(2S)$\pi^+\pi^-$ (2.8%) Υ(2S)$\pi^0\pi^0$ (1.9%) Υ(2S)$\gamma\gamma$ (5.0%) Υ(1S)$\pi^+\pi^-$ (4.4%) Υ(1S)$\pi^0\pi^0$ (2.2%)
Principal leptonic decays	e^+e^- (2.4%) $\mu^+\mu^-$ (2.5%) $\tau^+\tau^-$ (2.6%)	e^+e^- (1.9%) $\mu^+\mu^-$ (1.9%) $\tau^+\tau^-$ (2.0%)	$\mu^+\mu^-$ (2.2%) $\tau^+\tau^-$ (2.3%)

Table 3.1: Summary of the most important characteristics of the three Υ states. The percentages near the decay modes are the branching ratios

3.2 Quarkonium production mechanism

The theoretical study of quarkonium production mechanism involves both perturbative and non-perturbative aspects of QCD. First, the creation of a $Q\bar{Q}$ pair occurs at short distance scale and can be calculated in perturbative approach. The $Q\bar{Q}$ pair creation involves a momentum transfer of the order of m_Q (heavy quark mass), higher than the QCD scale parameter Λ_{QCD}. Then the evolution of the $Q\bar{Q}$ pair into the physical quarkonium state is non-perturbative. The typical momentum scales in such case is the momentum of the heavy-quarks, $m_Q v$, in the bound-state rest frame where m_Q is the heavy quark mass, v is the velocity of the heavy quark or antiquark in the quarkonium rest frame. For example: the v^2 is around ∼0.3 for $c\bar{c}$ pair and ∼0.1 for $b\bar{b}$ [54].

An overview of models describing production of quarkonia can be found in [55]. We will discuss the common theoretical approaches which try to describe the quarkonium production mechanism with different treatment of the non-perturbative part.

3.2.1 Color Evaporation Model (CEM)

The CEM model is a phenomenological approach which was initially introduced in 1977 [56]. This model is based on the principle of quark-hadron duality [57]. The production cross section of quarkonia (σ_Q) is expected to be directly connected to a $Q\bar{Q}$ pair production in an invariant mass region where it can hadronize into a quarkonium. The $Q\bar{Q}$ cross-section is then multiplied by a phenomenological factor F_Q which is related to the probability that the pair hadronizes into this state. An assumption was proposed based on the spin J_Q of the quarkonium Q, $F_Q = 1/9 \times (2J_Q+1)/\sum_i(2J_i+1)$, where the sum over i runs over all the charmonium states below the open heavy-flavor threshold [58].

$$\sigma_Q = F_Q \int_{2m_Q}^{2m_H} \frac{d\sigma_{Q\bar{Q}}}{dm_{Q\bar{Q}}} dm_{Q\bar{Q}} \tag{3.1}$$

In Eq. 3.1 the kinematical threshold to produce a quark pair is $2m_Q$, and that to create the lightest open-heavy-flavor hadron pair is $2m_H$. This model has no constraints on the color or spin of the final state. The $Q\bar{Q}$ pair is supposed to neutralize its color by interaction with the collision-induced color field by color evaporation randomizing the spin of the pair. This assumption leads to the prediction that the quarkonium production rate is independent of the quarkonium spin of the quarkonium states. The fractions are determined by data and assumed to be universal.

3.2.2 Color Singlet Model (CSM)

The CSM model was proposed shortly after the J/ψ discovery. According to this approach the production of quarkonium is correlated to the $Q\bar{Q}$ production. The heavy quark pair has to be produced in a color-singlet state with the same quantum numbers as the quarkonium. The production cross section of a given quarkonium state can be expressed as the product of the cross section for the production of a $Q\bar{Q}$ pair with zero relative velocity and the square of the color-singlet $Q\bar{Q}$ wave function evaluated at zero $Q\bar{Q}$ separation:

$$d\sigma_{A+B\to Q+X} = \sum_{i,j} \int dx_i dx_j f_i^A(x_i,\mu_F) f_j^B(x_j,\mu_F) d\hat{\sigma}_{i+j\to Q\bar{Q}+X}(\mu_F,\mu_R) |\Psi(0)|^2 \tag{3.2}$$

where i and j represent partons with a relative momentum x_i and x_j of hadrons A and B, respectively. The corresponding parton distribution function's are $f_i(x_i,\mu_F\ )$ and $f_j(x_j,\mu_F)$. μ_F is the factorization scale, while $\hat{\sigma}$ is the partonic cross section to produce a $Q\bar{Q}$ pair at energy μ_F which depends on the strong coupling constant α_s evaluated at the renormalization scale μ_R. The probability $|\Psi(0)|^2$ can be extracted from subsequent decays of the formed quarkonium state. Fig. 3.5 shows that the CSM describes the J/ψ and Υ(1S) total cross sections as a function of the collision center-of-mass energy within the large theoretical uncertainties, except for very low energy [59].

3.2.3 Non-Relativistic QCD (NRQCD)

The NRQCD is based on the QCD effective theory [60]. This model describes the probability for a heavy quark pair to form a quarkonium via long-distance matrix elements (LDMEs) with a usual power expansion of the coupling constant α_s. The NRQCD framework introduces an expansion in v where the $Q\bar{Q}$ pair is considered as an octet state with

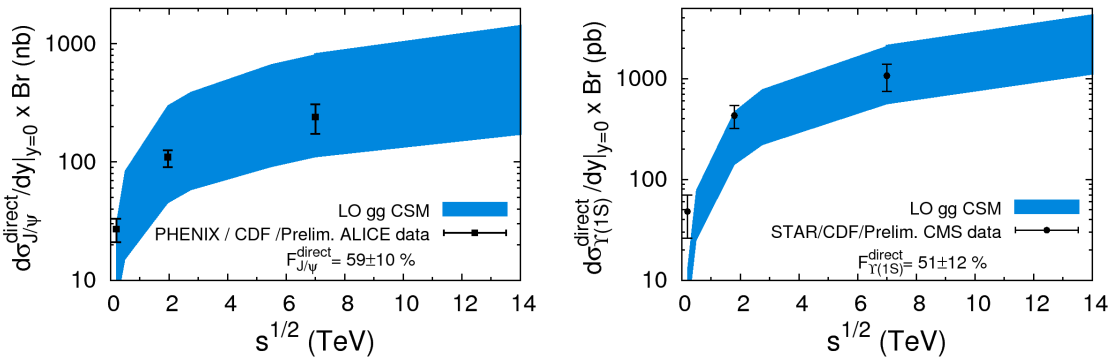

Figure 3.5: $d\sigma^{direct}_{J/\psi}/dy|_{y=0}$ × Br (left) and $d\sigma^{direct}_{\Upsilon(1S)}/dy|_{y=0}$ × Br (right) computed with CSM model for gg fusion at LO in pp collisions for $\sqrt{s}$ from 200 GeV up to 14 TeV compared to the PHENIX, CDF, ALICE and CMS data [59].

different angular momentum and spin states.

$$d\sigma_{A+B\to Q+X} = \sum_{i,j,n} \int dx_i dx_j f_i^A(x_i,\mu_F) f_j^B(x_j,\mu_F) d\hat{\sigma}_{i+j\to(Q\bar{Q})_n+X}(\mu_R,\mu_F,\mu_\Lambda)\langle\mathcal{O}_Q^n\rangle \tag{3.3}$$

In Eq.3.3, the individual n terms of this sum are called partial cross sections σ_n. The LDMEs, $\langle\mathcal{O}_Q^n\rangle$ are assumed to be constant and universal in the NRQCD factorization formula. Such as, they do not depend on the kinematics of the $Q\bar{Q}$ pair and are supposed to be the same for any collision system. The LDMEs scale with powers of the relative velocity v of the heavy quark or antiquark, depending on the quantum state of the intermediate $Q\bar{Q}$ pair. The LDMEs are determined through a fitting procedure of measured cross sections by three different groups (Hamburg [61], IHEP [62] and PKU [63]).

The understanding of quarkonium production mechanism is complex and most likely to be model dependent. Each of the current models has different way of treating the non-perturbative calculation and has its own short-coming. These models describe the inclusive production of quarkonia but not the associated multiplicity. The focus of this thesis is to study the Υ yields in term of the charged-particle multiplicity, in the next section we will focus on available studies on the correlation between the hard and soft particle production and the models trying to describe the correlation.

3.3 Correlation of hard and soft particle production

The study of particle production as a function of multiplicity is a very interesting way of investigating the interplay of the hard and soft processes in different collision systems. The underlying event comprises production of all the final state particles associated with the hard scattering (i.e the MPI, soft hadronic processes (hadronization, decays), or fragmentation of beam remnants). The heavy quark production could be affected by the underlying event. The approach to study the correlation between hard and soft processes with self-normalized quantities was first proposed in 2010 [64]. Fig. 3.6 represents a very simple correlation between the self-normalized quarkonium yield and self-normalized multiplicity. A self-normalized quarkonium yield ($\frac{dN_Q/dy}{\langle dN_Q/dy\rangle}$) can be described as the quarkonium yields normalized by the average quarkonium yield and the self-normalized multiplicity ($\frac{dN_{ch}/d\eta}{\langle dN_{ch}/d\eta\rangle}$) is a representation of KNO variables.

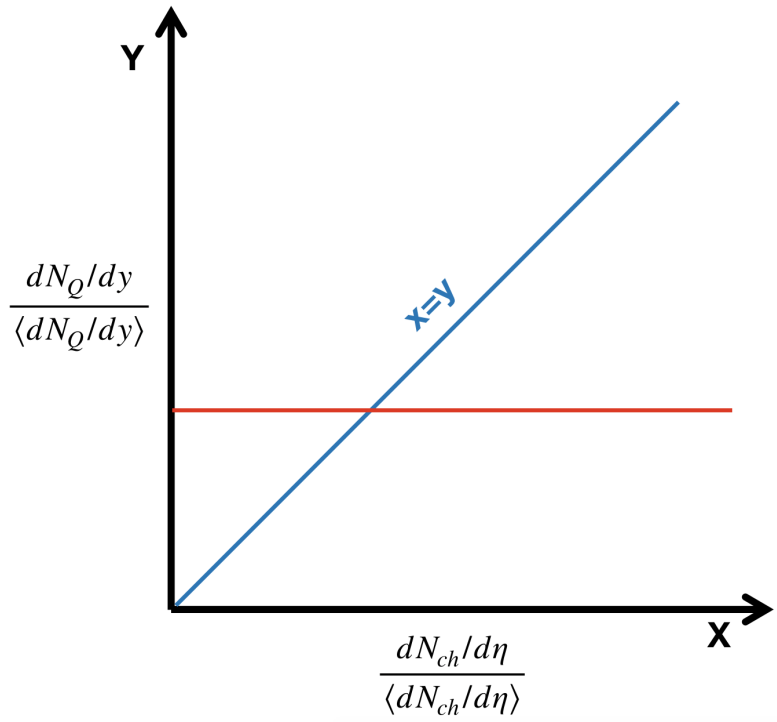

Figure 3.6: Axes construction for the correlation between self-normalized quarkonium and self-normalized charged-particle multiplicity

One could expect an independent correlation (red line) if the multiplicity production is uncorrelated with the quarkonium production. From a very simple expectation of a MPI scenario, the number of MPI occurring in a collision is proportional to the number of hard interaction which is proportional to the number of charged particles produced in the same collision. In this case, the self-normalized quarkonium yield should increase linearly with respect to the increasing multiplicity (blue line). The correlation between them can be affected by other mechanisms at play in the initial or final state which can lead to a deviation from the linearity. This correlation can be investigated in different systems, energies and rapidity regions for different hard probes.

Several experimental studies can be found on the dependencies of this correlation. Table. 3.2 shows the existing twenty-one measurements on this correlation for quarkonia and open heavy flavor and one recent measurement which will be covered by this thesis. The

first three columns represent the probe, system and energy of the measurements respectively. And the following columns represent the kinematic regions of the measurements, observations and references. The observations are noted as:

- *linear*: linear increase
- *weaker*: weaker than linear increase
- *stronger*: stronger than linear increase

In the following, we will present the measurements performed at different energies from 500 GeV to 13 TeV by different experiments at LHC (ALICE, CMS) and RHIC (STAR). The discussions will be grouped by potential dependencies on the correlation between hard probe and multiplicity:

- **Rapidity dependence:** The study based on rapidity gives the opportunity to study the hard probe and multiplicity in various rapidity region and their possible correlations (see section 3.3.1).
- **Collision energy dependence:** The collision energy dependent studies are needed to understand the evolution of this correlation from low energy to higher energies (see section 3.3.2).
- **Collision system dependence:** The behavior of this correlation can be studied in small (pp, pPb) or dense (PbPb) systems. This can help to understand the correlation in dense medium (see section 3.3.3).
- **Hardness of the probe:** The correlation can be studied on different hard probes. This will help to understand how this correlation can be affected by different resonances (see section 3.3.4).

In section 3.3.5, the theoretical prediction for these studies will be discussed.

Probe	**System**	**Energy**	**Rapidity (y-) gap between probe & multiplicity**	**Observation**	**Experiment, reference**
J/ψ	pp	500 GeV	*No*, J/ψ (mid-y), multiplicity (mid-y)	stronger/linear	STAR, [65]
		7 TeV		stronger	ALICE, [66]
		13 TeV			ALICE, [67]
	pp	7 TeV	*No*, Non-prompt J/ψ (mid-y), multiplicity (mid-y)		ALICE, [68].
		5.02 TeV	*Yes*, J/ψ (forward-y), multiplicity (mid-y)	linear	ALICE, [69]
		7 TeV			ALICE, [66]
		13 TeV			ALICE, [69]
	p-Pb	5.02 TeV			ALICE, [70]
		8.16 TeV			ALICE, [71]
		5.02 TeV	*No*, J/ψ (mid-y), multiplicity (mid-y)	stronger	ALICE, [70]
	Pb-p	5.02 TeV	*Yes*, J/ψ (backward-y), multiplicity (mid-y)	weaker	ALICE, [70]
		8.16 TeV			ALICE, [71]
D meson	pp	7 TeV	*No*,D (mid-y), multiplicity (mid-y)	stronger	ALICE, [72]
	pPb	5.02 TeV			ALICE, [72]
	pp	7 TeV	*Yes*,D (mid-y), multiplicity (forward-y)	stronger	ALICE, [72]
	pPb	5.02 TeV		linear	ALICE, [72]
Υ	pp	500 GeV	*No*, Υ (mid-y), multiplicity (mid-y)	stronger/linear	STAR, [73]
		2.76 TeV		stronger	CMS, [6]
		7 TeV			CMS, [74]
		13 TeV	*Yes*, Υ (forward-y), multiplicity (mid-y)	this thesis	ALICE
	p-Pb	5.02 TeV	*No*, D (mid-y), multiplicity (mid-y)	stronger/linear	CMS, [6]
	Pb-Pb	2.76TeV		linear	CMS, [6]

Table 3.2: Summary of multiplicity differential quarkonia and open heavy flavor studies

3.3.1 Rapidity dependence

The correlation between quarkonium or open heavy flavor can be studied in two different rapidity configurations. In the following, we will discuss the experimental results for these two configurations. One configuration is to measure the hard probe and multiplicity in different rapidity regions (will be denoted as **rapidity (y-) gap** in further discussion) and the other one is to measure both in the same rapidity region (without rapidity gap).

The first measurement of J/ψ yield as a function of multiplicity was reported by ALICE in 2012 in pp collision at $\sqrt{s}$ =7 TeV [66]. In this article two measurements were shown where charged-particle multiplicity was always measured at mid-rapidity but J/ψ yields were extracted in two different rapidity regions (forward and mid-rapidity). The forward rapidity J/ψ was studied in di-muon ($\mu^+\mu^-$) channel. This measurement with rapidity gap shows a linear correlation between the J/ψ yield and multiplicity. On the other hand, the measurement without rapidity gap were performed with both J/ψ decaying into di-electron (e^+e^-) and multiplicity measured at mid rapidity. The two measurements shown in Fig. 3.7, are in agreement within the current uncertainties except for the last measured points with some tension. These *linear* and *stronger* than linear correlations are quoted in the 5^{th} column of table 3.2.

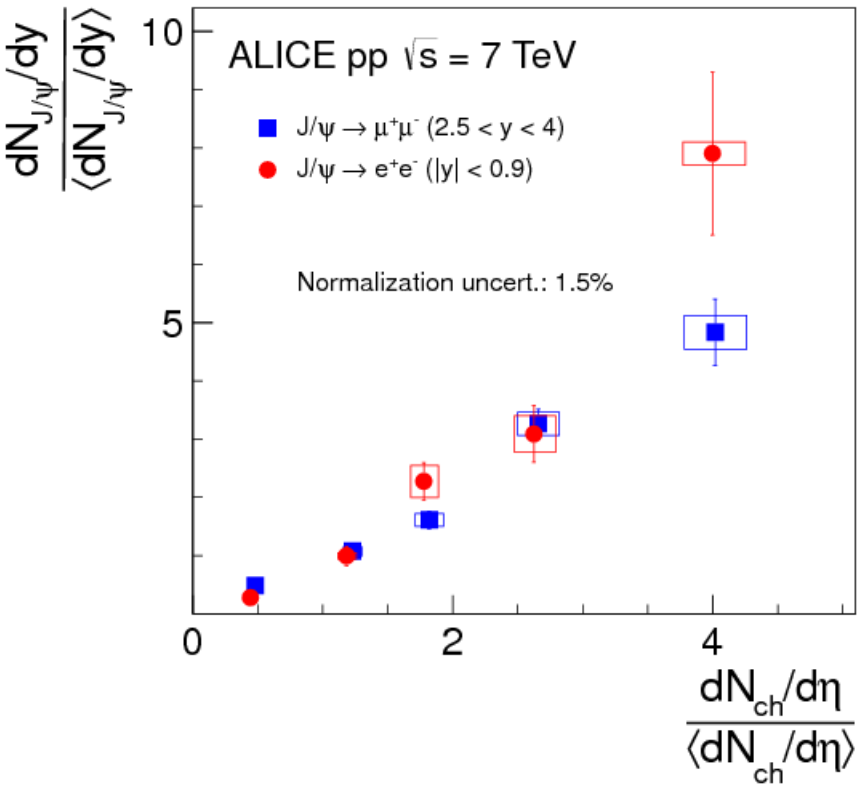

Figure 3.7: Self-normalized J/ψ yields measured at mid and forward rapidity as a function multiplicity at mid-rapidity in pp collision at $\sqrt{s}$ =7 TeV [66].

The studies are available for some other hard probes: D-meson and Υ. The relative D-mesons as a function of multiplicity was studied in different $p_{\rm T}$ intervals without any rapidity gap in pp collisions at $\sqrt{s}$ = 7 TeV [68]. Fig. 3.8 shows the average relative D-meson yields in $|y_{lab}|<$ 0.5 as a function of the relative charged-particle multiplicity at mid-rapidity $|\eta|<$ 1 within a transverse momentum $1 < p_{\rm T} < 2$ GeV/c. It shows a stronger increase with increasing multiplicity. In this article, the *stronger* increase has been seen

for all the p_{T} intervals, more precisely the *stronger* increase become more clearly observed in higher p_{T} intervals [68]. The observation is similar for D-mesons and J/ψ as a function of multiplicity when both the probe and multiplicity were measured at mid-rapidity.

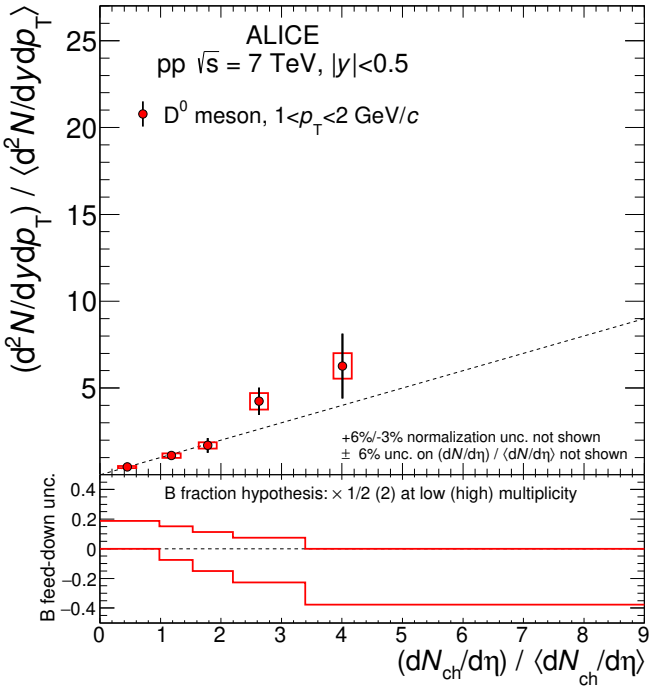

Figure 3.8: Average D-meson as a function of charged-particle multiplicity [68].

An article on the Υ production as a function of multiplicity in pp collisions at $\sqrt{s} = 2.76$ TeV was published by CMS collaboration in 2014 [6]. Here, the Υ and multiplicity were both measured at mid-rapidity. A stronger than linear increase has been observed for the three states of Υ (1S, 2S, 3S) as a function of multiplicity which are in agreement with the J/ψ and D-meson results in mid-rapidity [66, 68].

3.3.2 Collision energy ($\sqrt{s}$) dependence

In 2016, the measurements of J/ψ yields as a function of multiplicity with and without rapidity gap are reproduced, using a larger data sample in pp collisions at $\sqrt{s}$=13 TeV. Fig. 3.9 shows the two measurements whereas the stronger than linear increase is now clearly visible for J/ψ measured at mid-rapidity. On the other hand, J/ψ measured at forward rapidity shows almost a linear increase which indicates a different correlation while measuring the J/ψ and multiplicity using a rapidity gap than the measurement without rapidity gap (J/ψ at mid-rapidity). Till now there is no clear sign of collision energy dependence for the correlation between J/ψ yield and multiplicity for 7 and 13 TeV.

The measurement of self-normalized J/ψ as a function of multiplicity with a rapidity gap in pp collisions at $\sqrt{s} = 5.02$ TeV is shown in Fig. 3.10. It shows a similar *linear* increase as the one measured in pp collisions at $\sqrt{s} = 7$ and $\sqrt{s} = 13$ TeV with the same rapidity.

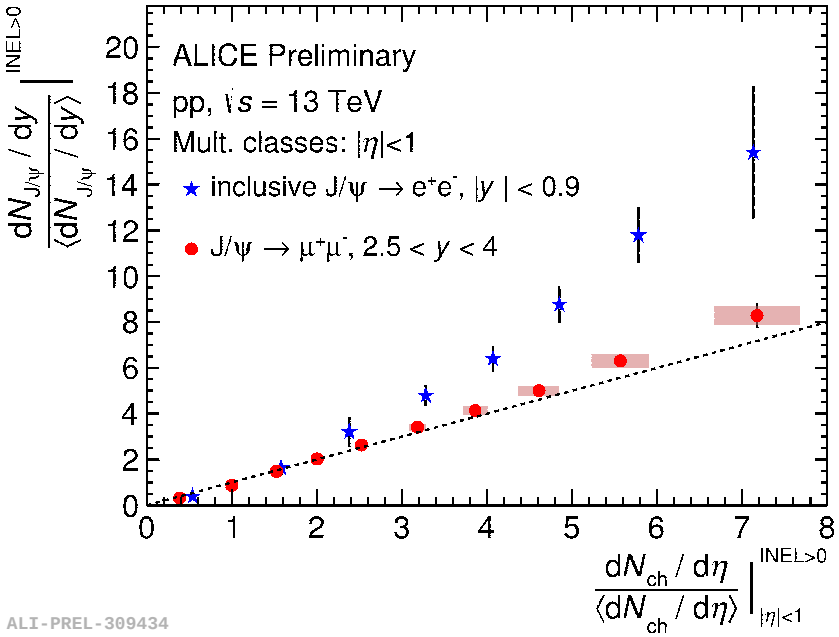

Figure 3.9: Self-normalized J/ψ yields measured at mid [67] and forward [69] rapidity as a function multiplicity at mid-rapidity in pp collision at $\sqrt{s}$ =13 TeV

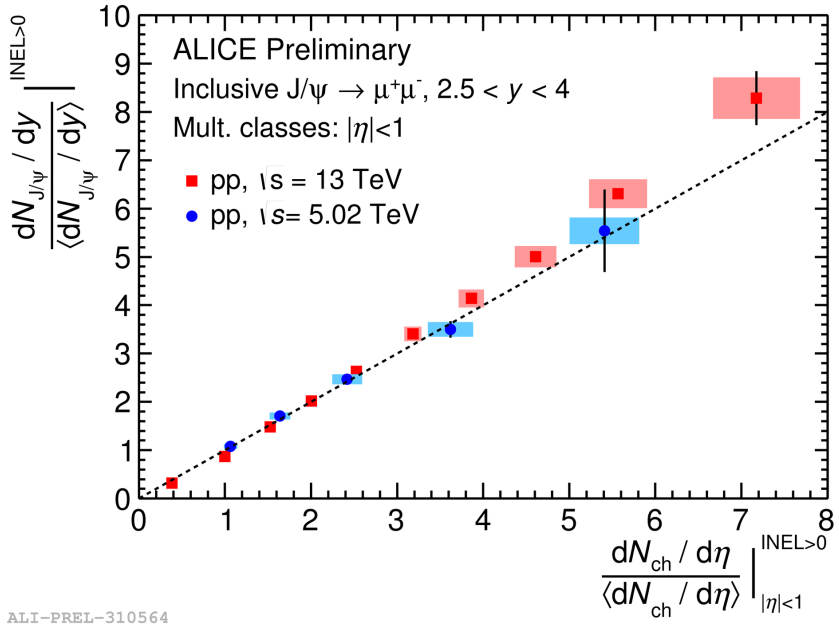

Figure 3.10: Self-normalized J/ψ yields measured at forward rapidity as a function multiplicity at mid-rapidity in pp collision at $\sqrt{s}$ =5.02 and 13 TeV.

A similar measurement is released as preliminary by the STAR collaboration in pp collision at $\sqrt{s} = 500$ GeV [75]. The J/ψ (in di-muon and in di-electron) and multiplicity are measured at mid-rapidity as shown in Fig. 3.11. The result show a *stronger* than linear increase for the measurement in di-electron channel which is also in agreement with the J/ψ measurement at mid-rapidity by ALICE. In case of di-muon channel only ~ 2.5 times mean multiplicity is reached.

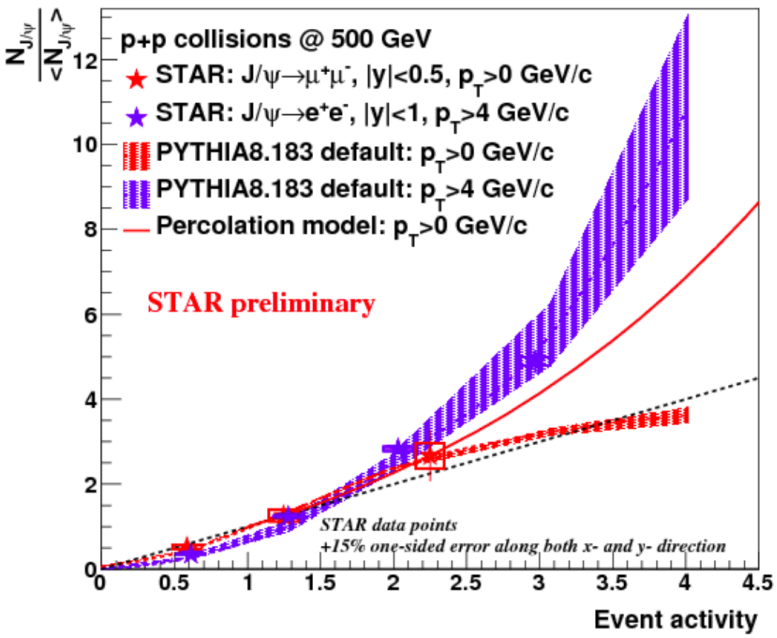

Figure 3.11: Relative J/ψ yield vs event activity compared to the default PYTHIA 8 tune and to the percolation model [75].

The energy dependence for Υ can be seen at 500 GeV, 2.76 TeV [6] and 7 TeV. In these measurements both Υ and multiplicity were studied at mid-rapidity in pp collisions. A stronger than linear increase has been observed in each measurements.

3.3.3 Collision system dependence

The correlation between J/ψ and multiplicity has been studied in p-Pb collisions at $\sqrt{s}$ = 5.02 TeV [70]. Fig. 3.12 shows the self-normalized inclusive J/ψ yields measured at forward (blue), backward (red) and mid-rapidity (black) while multiplicity is measured at mid-rapidity. The black points refers to the inclusive J/ψ mesons measured at forward rapidity which shows almost linear dependence as it is seen for forward J/ψ in pp collisions at $\sqrt{s}$ = 5.02 TeV (Fig.3.10). A direct comparison between pp and p-Pb collision systems is not possible as in p-Pb system so called 'Cold Nuclear Matter' (CNM[1]) effects can have an impact on quarkonium production. Even though a direct comparison is not possible for the mid-rapidity J/ψ at p-Pb 5.02 TeV and pp 13 TeV [67], we observe a stronger than linear increase.
The measurements of relative D-meson yields as a function of multiplicity in pp and p-Pb collisions are shown in Fig. 3.13. A stronger than linear increase is found for the measurements without the rapidity gap in pp 7 TeV and p-Pb 5.02 TeV. On the contrary, the measurements with the rapidity gap show a *linear* increase. In both cases, the trends we observe for D-meson are similar to the trends found for J/ψ.

The measurement of the multiplicity dependence of Υ reported by the CMS collaboration [6] shows the correlation in three different collisions systems (pp, p-Pb and Pb-Pb). The Υ production at $|y_{cms}|<$ 1.93 was studied as a function of the transverse energy at large

[1]The CNM effects are related to the nuclear environment of the collision, for example: multiple scatterings of the incoming partons before the hard scattering, gluon radiation and absorption in the nuclear medium [76]

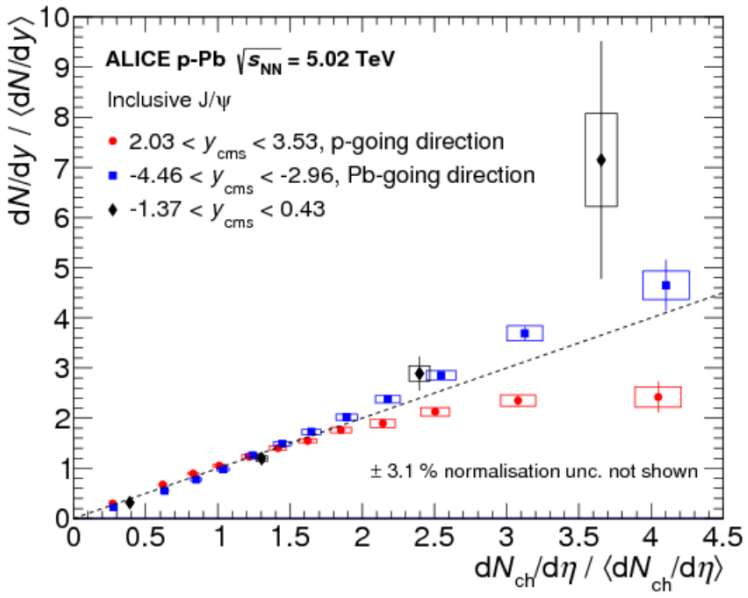

Figure 3.12: Relative yield of inclusive J/ψ mesons, measured in three rapidity regions, as a function of relative charged-particle multiplicity, measured at mid-rapidity. The error bars show the statistical uncertainties, and the boxes represent the systematic uncertainties. [70].

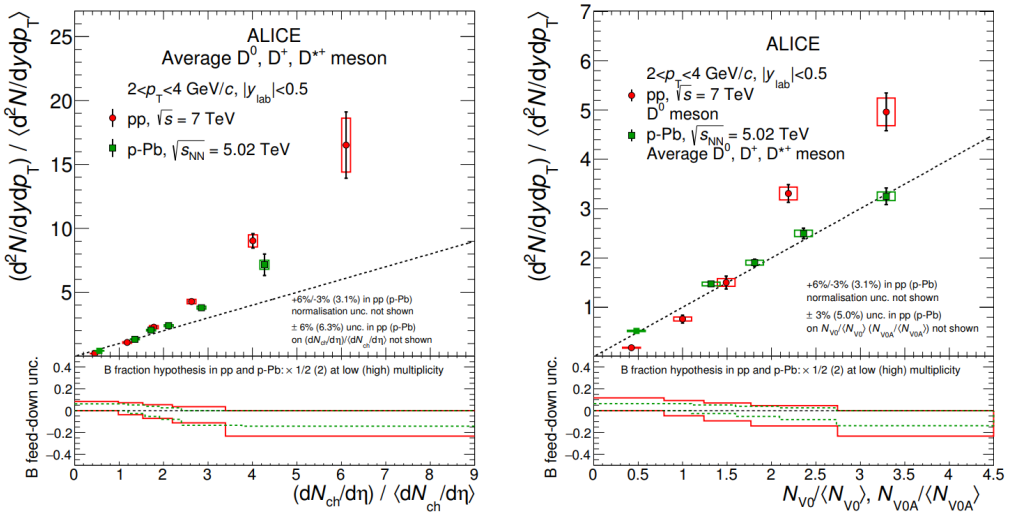

(a) Multiplicity at central rapidity

(b) Multiplicity at backward rapidity

Figure 3.13: Average relative D-meson yields in $|y_{lab}|< 0.5$ as a function of (a) the relative charged-particle multiplicity at mid-rapidity $|\eta|< 1$, and (b) at backward-rapidity $2.8 < \eta < 5.1$ (including also $3.7 < \eta < 1.7$ in pp data) for $2 < p_{\mathrm{T}} < 4$ GeV/c. The relative yields are presented in the top panels with their statistical (vertical bars) and systematic (boxes) uncertainties, apart from the uncertainty on the B feed-down fraction, which is drawn separately in the bottom panels. The dashed lines are drawn to the diagonal [72].

rapidity $4 < |\eta_{lab}|< 5.2$ and as a function of the charged particle tracks at mid-rapidity $|\eta_{lab}|< 2.4$

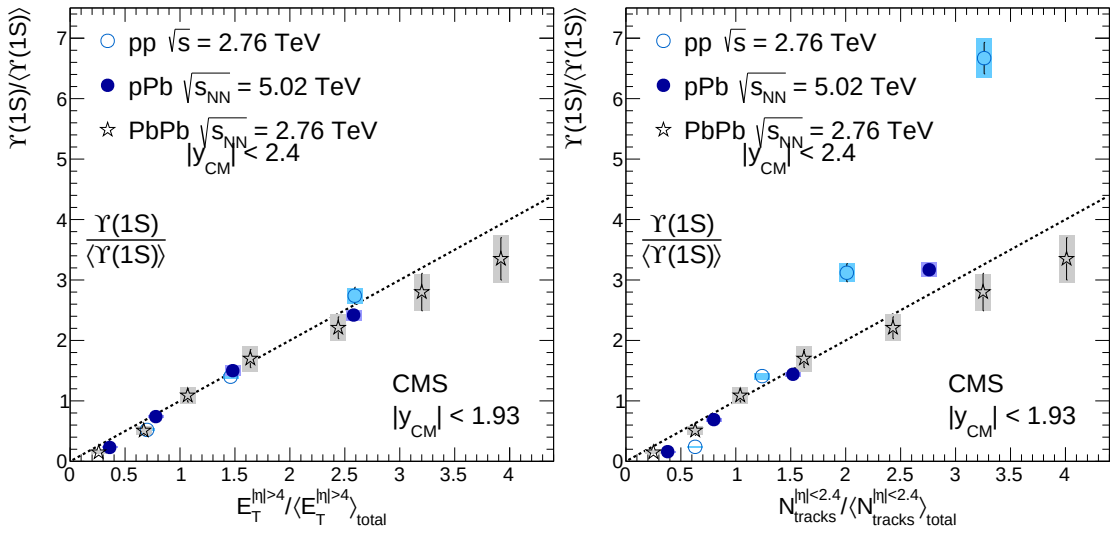

Figure 3.14: The left panel shows the Υ(1S) cross section versus transverse energy measured at $4 < |\eta| < 5.2$ in pp collisions at $\sqrt{s} = 2.76$ TeV and p-Pb collisions at $\sqrt{s_{\rm NN}} = 5.02$ TeV. The right panel shows the Υ(nS) cross section versus charged-track multiplicity measured in $|\eta| < 2.4$, measured in $|y_{CM}| < 1.93$ collisions at $\sqrt{s} = 2.76$ TeV and pPb collisions at $\sqrt{s_{\rm NN}} = 5.02$ TeV [6].

Fig. 3.14 (left) shows the dependence on self-normalized transverse energy (therefore with y-gap between the multiplicity estimator and the Υ yields) and Fig. 3.14 (right) shows the dependence on charged-track multiplicity without a rapidity gap. A *linear* increase has been observed within the uncertainties for the measurements with rapidity gap. On the other hand, the measurements without the rapidity gap show approximately a linear increase in p-Pb and Pb-Pb collisions but *stronger* increase in pp collisions within the current uncertainties. Almost 7 times mean $\langle\Upsilon(1S)\rangle$ was reached at around 3.5 times mean multiplicity in pp collisions while in Pb-Pb collisions it is around 3.5 times mean $\langle\Upsilon(1S)\rangle$ at 4 times the mean multiplicity. Note that the figures have slightly different observables in the x-axes which is why a direct comparison with ALICE measurements are not possible. The observed trends for Υ(2S) and Υ(3S) are similar to the Υ(1S). The available results in p-Pb and Pb-Pb are not sufficient to draw any conclusion yet. The trends for Υ as function of multiplicity in pp collisions are similar to the trends those we observe for J/ψ measurements in pp collisions. In p-Pb and Pb-Pb collisions, the correlation between Υ and multiplicity shows a *linear* increase in CMS results with or without the rapidity gap whereas the ALICE measurements for J/ψ in p-Pb still shows a similar trend as in pp collisions. To investigate the origin of these observations more precise measurements are needed in the same energy for all collisions systems with and without the rapidity gap.

3.3.4 Hardness of the probe

In addition to the above dependencies, this multiplicity dependent correlation was studied for different hard probes (J/ψ, Υ, D-meson) to understand the impact of the mass, quark content and their production mechanisms. In section 3.3.1, we presented that the currently published results show stronger than linear multiplicity dependence for J/ψ, Υ and D-meson when multiplicity and hard probes are measured at mid rapidity. The multiplicity differential D production at mid-rapidity $|y| < 0.5$ was studied in ALICE with respect to event activity determined both at mid-rapidity $|\eta| < 1$ and at forward rapidity from combined charge collected in two scintillator arrays at $-3.7 < \eta < -1.7$ and $2.8 < \eta < 5.1$

[68]. The latter measurement introduces an y-gap between the yield and the multiplicity. The average D-meson yields in Fig. 3.13, measured at $|y|< 0.5$ in pp at $\sqrt{s} = 7$ TeV, display a qualitatively identical increase regardless of whether the rapidity gap is introduced or not in the multiplicity estimation. Fig.3.15 (left) reveals that for mid-rapidity yields, the behavior is consistent for D-mesons and inclusive J/ψ. The inclusive J/ψ yields are dominated by the prompt production. The non-prompt contribution is set side by side with open charm yields in Fig. 3.15 (right). These three hadrons differ in their hadronization process.

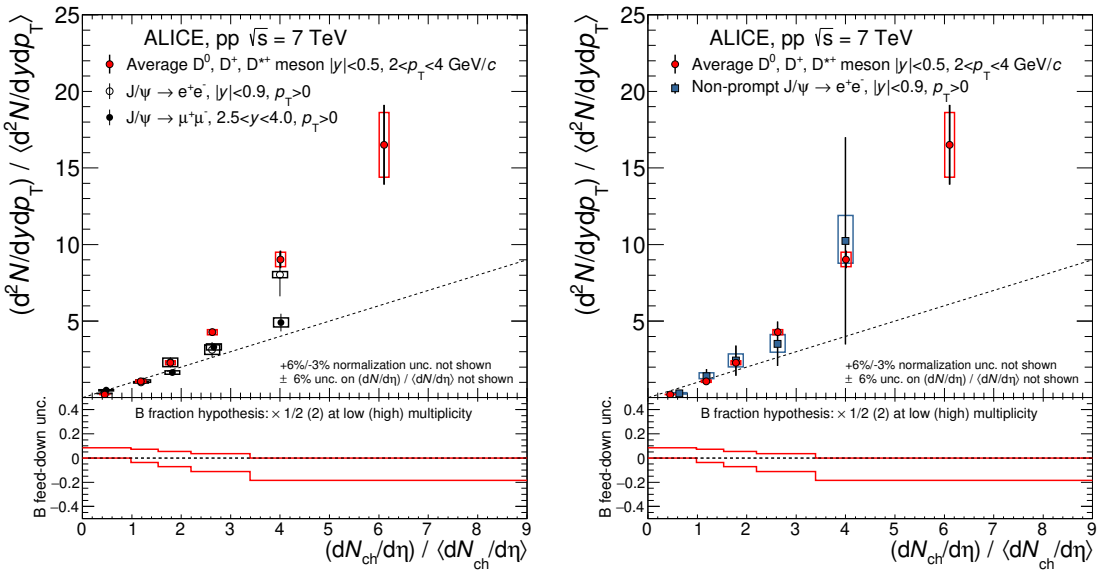

Figure 3.15: Relative yields of charmed hadrons as a function of $\mathrm{d}N_{\mathrm{ch}}/\mathrm{d}\eta$ in pp collisions at $\sqrt{s} = 7$ TeV. Left figure shows inclusive J/ψ at mid- and forward rapidity versus prompt D. Right figure shows non-prompt J/ψ at mid-rapidity versus prompt D [68].

The multiplicity dependence of Υ reported by the CMS collaboration shows stronger than linear correlation for three Υ states ($\Upsilon(1S)$, $\Upsilon(2S)$ and $\Upsilon(3S)$). These measurements show that the correlation is identical for J/ψ, Υ and D-meson when multiplicity estimator and hard probes are measured at mid-rapidity. [6]. Moreover, the article presents an excited to ground state disappearance in pp, p-Pb and Pb-Pb collisions which gives a hint of resonance dependence when the measurements are performed without rapidity gap (Fig 3.16 (left)).

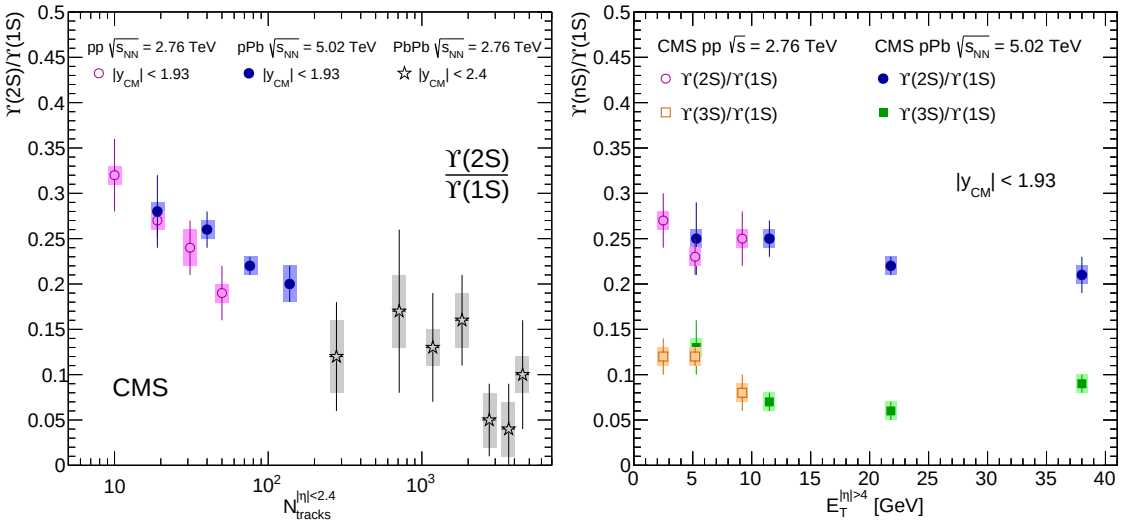

Figure 3.16: Single cross section ratios Υ(2S) over Υ(1S) for $|y_{CM}|< 1.93$ as a function of charged track (on left) and transverse energy (on right) [6].

Fig 3.16 (right) shows the dependence of this correlation between Υ and charged particles is less when the measurement is performed with a y-gap. Note that the figure on the left has different observable in x-axis than the one in the right. In the paper, two possible explanations were reported concerning the difference among the Υ states as a function of multiplicity. In the first hypothesis, the Υ(1S) are systematically produced with more particles than the excited states. This would affect the underlying distribution of charged particles and create an artificial dependence when sliced in small multiplicity bins. In the second hypothesis, the Υ are interacting with the surrounding environment, the Υ(1S) is expected, as the most tightly bound state and the one of smallest size, to be less affected than Υ(2S) and Υ(3S), leading to a decrease of the Υ(nS)/Υ(1S) ratios with increasing multiplicity. In either case, the ratios will continuously decrease from the pp to pPb to PbPb systems, as a function of event multiplicity. The origin of the decrease in the excited to ground state ratios is still not understood. To understand this effect, more precise measurements with rapidity gap are needed.

3.3.5 Theoretical models and event generators

In the following paragraphs, we will explain the event generators physics and theoretical models which are compared to experimental results.

3.3.5.1 PYTHIA 8 event generator

The basic PYTHIA physics processes have already been discussed in section 2.3.1. PYTHIA8 [77] includes improved MPI and color reconnection[2] (CR) which were not present in PYTHIA6 [26]. PYTHIA allows to study these processes individually to understand their contribution. The latest version of PYTHIA includes the heavy-flavor production via following mechanisms:

[2]In CR scenery, strings can be rearranged between partons. Partons from different interactions can connect to each other which leads to a reduction of total string lengths resulting in reduced number of charged particles.

1. The first hard process (which involves the highest momentum transfer), where the initial c/b quarks originate from the first 2$\longrightarrow$2 hard process, mostly by gluon fusion ($gg \longrightarrow c\bar{c}$) or involving a c/b sea-quark

2. The subsequent hard processes in MPI, produced via the same mechanisms as the first hard process but in consecutive interactions, that we refer to as hard process in MPI

3. Each produced gluon has a probability to split into a $c\bar{c}$ or $b\bar{b}$ pair When the initial gluon originates from a hard process, either the first one or a subsequent process (in MPI)

4. Initial- or final-state radiation (ISR/FSR)

The multiplicity dependent D-meson production [68] is shown in Fig.3.17 with the contribution of different processes. The top-left panel presents results for D mesons, revealing an increasing trend of the relative yields as a function of the relative charged-particle multiplicity for MPI, the gluon splitting process contribution instead shows a weaker dependence on the multiplicity: a slight increase is at low multiplicities followed by a saturation. The average B mesons, on the top-right panel, presents similar features as that of D mesons. The trend for the first hard process contribution shows an increase at low multiplicities and then saturates. The other contributions to particle production increase faster with multiplicity for B than for D mesons. These differences can be understood as being due to the larger B-meson mass, allowing a larger event activity in MPI and ISR/FSR processes.

Fig.3.17 (bottom panels) presents the D-meson relative yields as a function of the relative charged-particle multiplicity in PYTHIA 8 for different p_{T} intervals. The bottom-left panel shows the linear trend for the sum of all contributions. The slope increases with increasing p_{T}. The bottom-right panel shows the p_{T} evolution for the first hard processes only. The relative D-meson yield decreases with multiplicity. This feature is caused in PYTHIA 8 by the fact that MPI are ordered by their hardness. Thus production of charm and beauty at low p_{T} is associated mostly with low multiplicity events, whereas heavy-flavor hadron production in high p_{T} intervals is associated to higher multiplicity events.

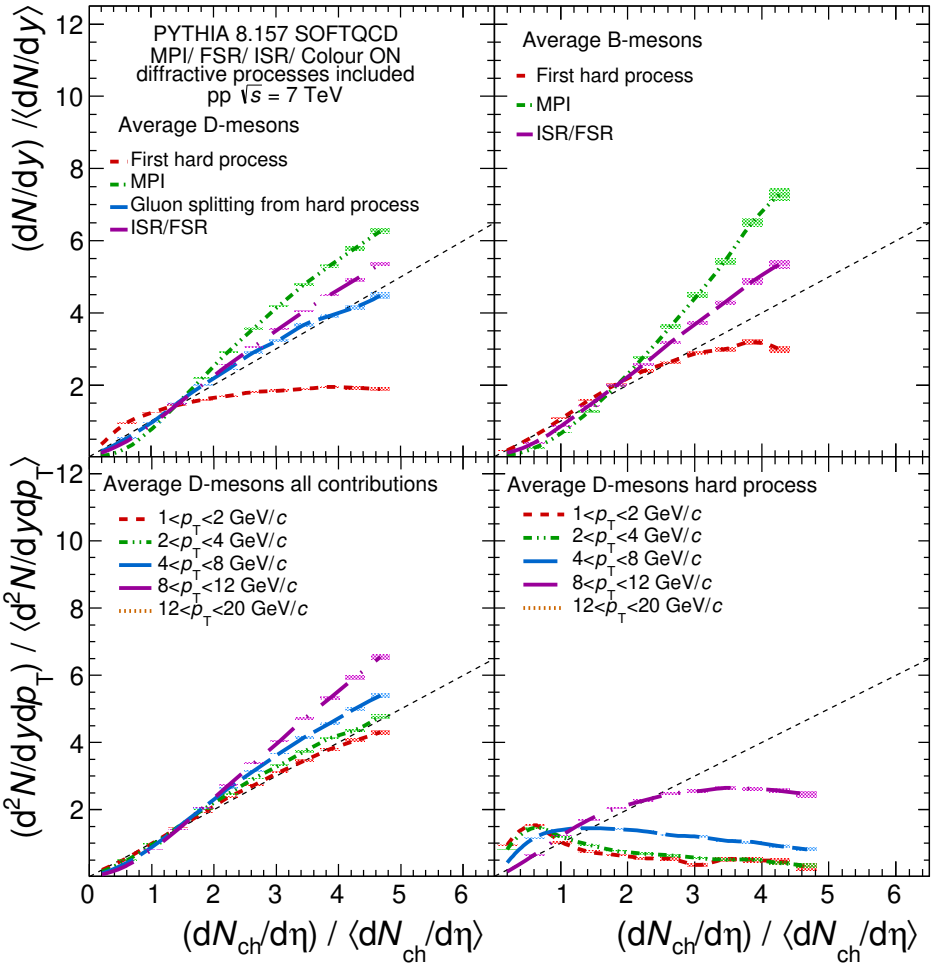

Figure 3.17: D- and B-meson relative yield as a function of the relative charged-particle multiplicity at central rapidity calculated with the PYTHIA 8.157 event generator [77]. The different c and b quark production processes are separated on the top panels: first hard process, hard process in multiple interactions (MPI), gluon splitting from hard processes and initial/final state radiation (ISR/FSR). The bottom panels present the multiplicity dependence in several p_{T} intervals for prompt D-meson production, on the left for all contributions and on the right for first hard process only. The colored lines represent the calculation distributions, whereas the shaded bands represent their statistical uncertainties at given values of $(\mathrm{d}N_{\mathrm{ch}}/\mathrm{d}\eta)/\langle \mathrm{d}N_{\mathrm{ch}}/\mathrm{d}\eta\rangle$. [68].

The study of multiplicity dependent J/ψ based on PYTHIA8 can be found in a more recent article [78]. In this article, inclusive J/ψ production is studied as a function of multiplicity. A stronger than linear increase is found for the correlation when both J/ψ and multiplicities are studied at mid-rapidity.

3.3.5.2 EPOS event generator

EPOS 3 is a universal generator for pp, p-Pb and Pb-Pb collisions [79]. In EPOS, the MPIs are treated via the Gribov-Regge multiple scattering framework combined with pQCD [27]. The scattering is expressed through parton ladders associated to the so-called Pomerons. The number of such Pomeron exchanges characterizes the geometry of the collision. Each parton ladder is identical to a flux tube. This will eventually breaks into individual strings and later into hadrons and jets. Parton saturation effects in the nucleus are summarized

by a saturation scale Q_s for each Pomeron individually. The scale Q_s depends on the mass number A and can be expressed in function of the momentum fraction x or as dependent on the number of participants N_{part} (and therefore centrality). This approach gives a different scaling at low and high transverse momenta, corresponding to a soft component scaling with N_{part} and a hard component scaling with the number of binary collisions N_{coll}. In heavy ion collisions and in high multiplicity pp and pA events, the high density of strings will result in a creation of a thermalised, collectively expanding bulk matter. Such bulk is referred to as 'core'. The string close to the surface of the bulk and/or with high p_{T} will escape the bulk and produce hadrons and jets. These segments are referred to as 'corona'. The 'core-corona' separation is a dynamical process, which provides the initial conditions for the subsequent viscous hydrodynamical evolution.EPOS predicts a stronger than linear increase for multiplicity differential D-meson.

3.3.5.3 Percolation model

The Percolation model [80] by Ferreiro and Pajares has a different approach than Pythia. It considers colored "strings" as a fundamental variable which is produced during parton-parton scattering. The number of strings N_s is proportional to the number of parton-parton interactions when considering the hard particle production ($n_{J/\psi}$), but not for soft particle production ($dN/d\eta$).
In the string percolation approach, the multiplicity is defined by

$$dN/d\eta = F(\rho)N_s\mu_1 \tag{3.4}$$

where μ_1 is the multiplicity of a single string in the rapidity range and $F(\rho)$ is a factor induced by the string interaction

$$F(\rho) = \sqrt{(1-e^{-\rho})/\rho} \text{ and string density } (\rho) = N_s\sigma_0/\sigma \tag{3.5}$$

where σ_0 and σ corresponds to the transverse area of a single string and the whole collision, respectively. So at large N_s, ρ increases and consequently $F(\rho)$ becomes smaller. Hence the multiplicity decreases proportionally to the damping factor.

At low multiplicities the number of strings is small which gives a linear increase as:

$$n_{J/\psi}/\langle n_{J/\psi}\rangle = \frac{dN/d\eta}{\langle dN/d\eta\rangle} \tag{3.6}$$

On the other hand, N_s increases with increasing collision at high multiplicities. Thus, a quadratic dependence is seen.

$$n_{J/\psi}/\langle n_{J/\psi}\rangle = \langle\rho\rangle(\frac{dN/d\eta}{\langle dN/d\eta\rangle})^2 \tag{3.7}$$

The percolation model predicts a linear increase of the heavy particle production a low multiplicity and a gradual change into quadratic increase at high multiplicity.

3.3.5.4 Higher Fock States model

The higher fock states model by Kopeliovich et al [81] draws an analogy between high multiplicity proton-proton and proton-nucleus collisions. In a boosted high-energy nucleus there is an overlap of gluons in the longitudinal direction at small-x. Therefore, the gluons can be treated as a single gluon cloud originating from one source with increased density. This is equivalent in high energy pp collisions reaching high multiplicity due to the higher

Fock states containing an increased number of gluons. From this analogy the authors claimed that observations from pA collisions can be used to make predictions for pp collisions. The ratio of the mean hadron multiplicities in pA to pp collisions is denoted as nuclear ratio R_h^{pA} and is defined as:

$$R_h^{pA} = \frac{\langle dN_h^{pA}/dy \rangle}{\langle dN_h^{pp}/dy \rangle} \tag{3.8}$$

The model predicts a *linear* increase of the yields with multiplicity.

Till now the predictions for multiplicity differential studies are only available for D-mesons or J/ψ. The predictions can be seen from Fig 3.18. It shows the currently available model prediction for self-normalized J/ψ yields as a function of multiplicity in pp collisions at $\sqrt{s}$= 13 TeV, measured at mid-rapidity.

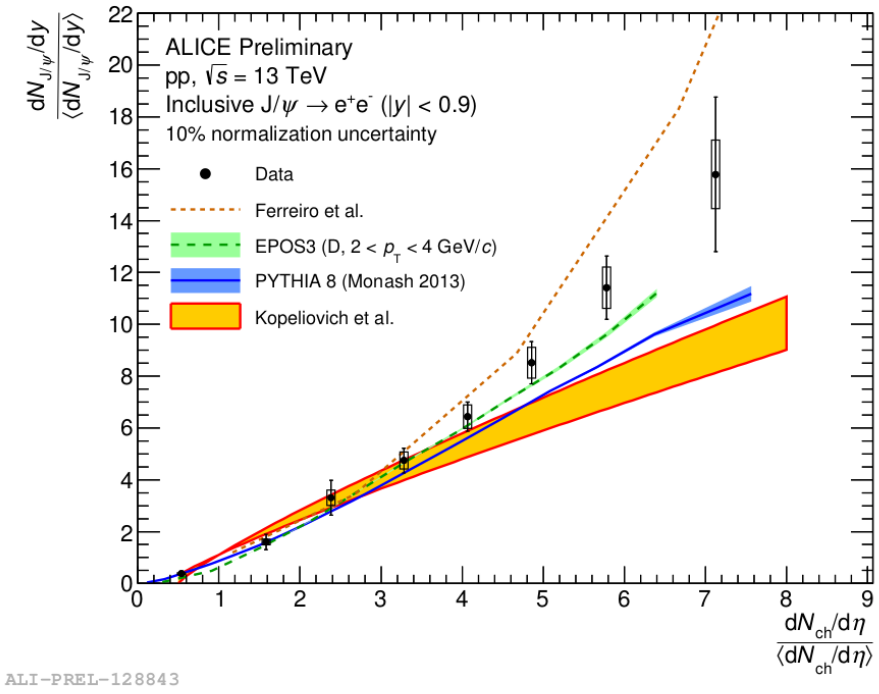

Figure 3.18: Multiplicity-dependent self-normalized inclusive J/ψ yields in pp collisions at $\sqrt{s}$= 13 TeV, measured at midrapidity. The measurement is compared with available calculations: percolation model by Ferreiro [80], EPOS3 [79], PYTHIA [77] and a calculation by Kopeliovich [81]

In Fig.3.18, the orange dashed line represents the prediction from percolation model, the orange band represents the prediction from higher fock states, the blue line represents the prediction from PYTHIA8 and the green dashed line shows the prediction from EPOS3. Qualitatively, all models can reproduce the linear increase of the J/ψ yield with respect to the event multiplicity when the mean multiplicity is low (below $\sim$ 3 times mean multiplicity). PYTHIA and Kopeliovich model slightly underestimate the correlation at high multiplicity where percolation model overestimates it. EPOS 3 provides a prediction for D-meson which also describes the J/ψ data.

Summary

Quarkonium is a very useful QGP probe, which makes the understanding of quarkonium production mechanism in different collision systems very important. The theoretical models based on quarkonia production describe the inclusive production which can not describe multiplicity differential studies. The existing results are quantitatively in agreement within current uncertainties from different experiments and shows a strong dependence with rapidity. While the multiplicity dependence of J/ψ and D-mesons are studied rigorously, the study of Υ mesons needs more attention to have a precise understanding from the experimental point of view. In chapter 4, we will present the experimental facility used in this thesis. In chapter 6, we will present the measurement of Υ production as a function of multiplicity with a y-gap.

Chapter 4

Experimental facility

In this chapter we will present an overview of the Large Hadron Collider (LHC) and A Large Ion Collider Experiment (ALICE). We will also present detail description of different ALICE sub-detectors which are related to the work presented in this thesis.

4.1 The Large Hadron Collider

The Large Hadron Collider (LHC) is the largest and most complex particle accelerator. The facility has a circumference of 26.7 km and is built at European Organization for Nuclear Research (CERN) about 100 meters underground across the French-Swiss border [82]. It consists of a two-ring-superconducting hadron accelerator. Two high-energy particle beams travel in opposite directions in the ultrahigh vacuum beam pipes. These beams collide at four locations around the accelerator ring, where four main experiments are located: ATLAS, CMS, ALICE and LHCb. Fig. 4.1 represents the CERN accelerator complex.

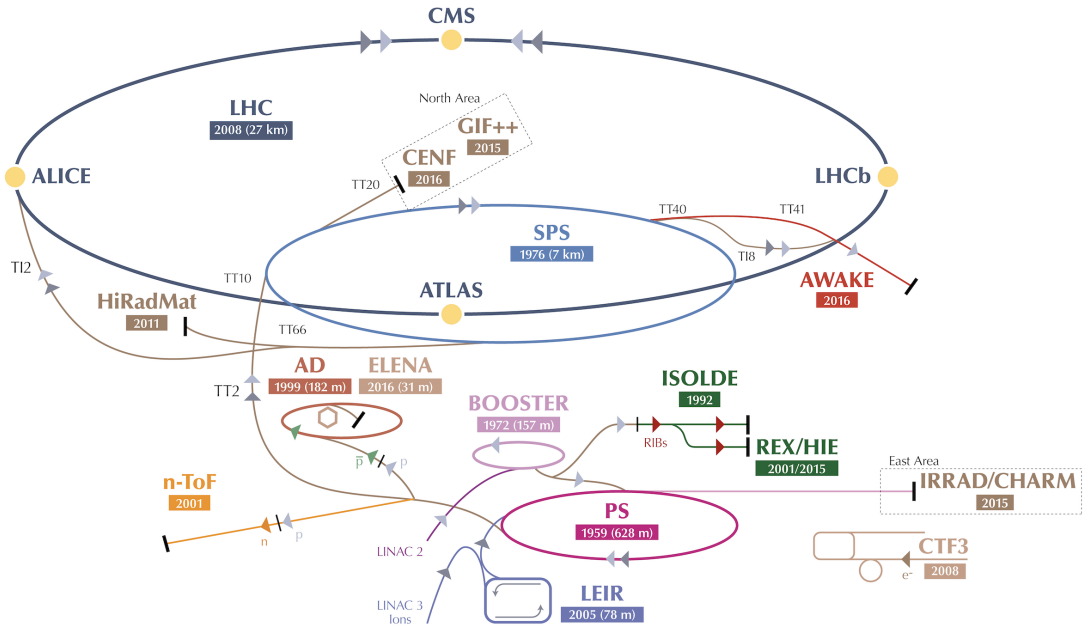

Figure 4.1: Schematic view of the CERN accelerator complex and its four largest experiments [83].

A Toroidal LHC Apparatus (ATLAS) [84] and the Compact Muon Solenoid (CMS) [85]

are general purpose physics experiments, designed to measure established SM processes, detect the Higgs boson and potential physics beyond the SM. These two experiments share the same goal but use different experimental set-ups. In 2012, the Higgs boson was discovered by ATLAS and CMS [10, 11]. Apart from proton-proton collisions, these two experiments study heavy ion collisions as well.

Large Hadron Collider beauty (LHCb) [86] experiment is mainly focused on heavy-flavor physics. It was designed primarily to measure the parameters of CP (charge conjugation parity) violation in the interactions of b-hadrons. LHCb can also be operated in a fixed-target mode and investigate cosmic ray physics.

A Large Ion Collider Experiment (ALICE) [87] was designed to study the hot and dense medium created in heavy ion collisions. ALICE uses pp and pPb primarily as a reference for the PbPb measurements but also as a standalone physics program. This thesis is dedicated to the analysis of quarkonium probes using the pp data recorded by ALICE. The detector will be described in section 4.2.

4.2 A Large Ion Collider Experiment

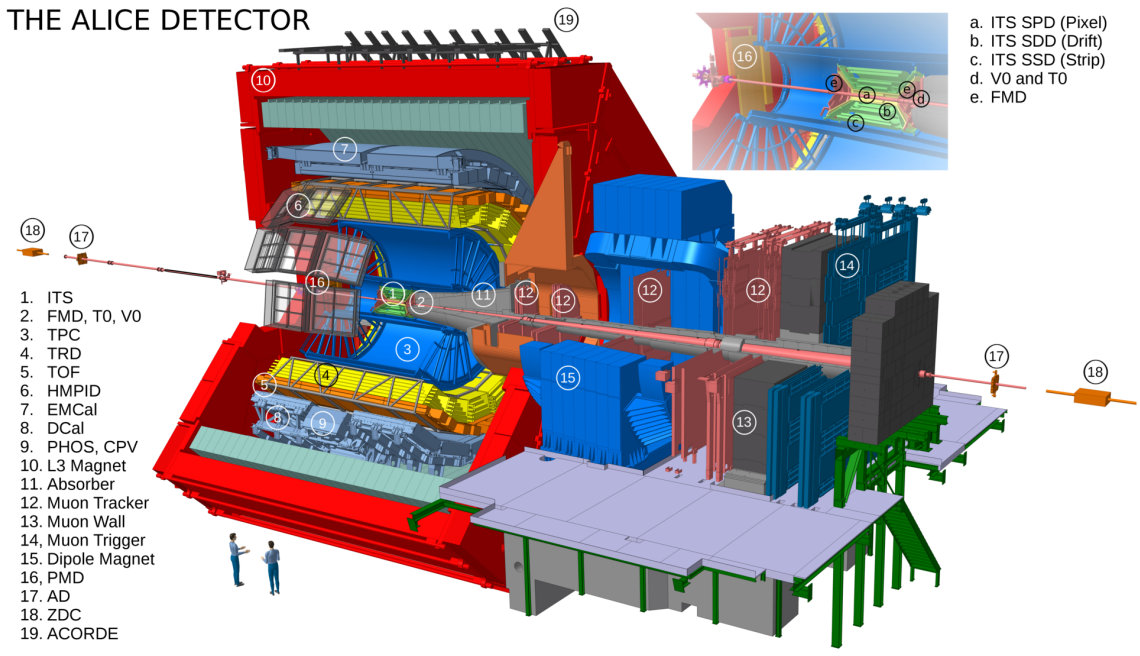

Figure 4.2: 3D ALICE Schematic RUN2 - with Description

ALICE [87] is unique among the LHC experiments because of its excellent particle tracking ability and identification. ALICE can track particles down to low transverse momenta and identify them in a wide kinematic region. Fig. 4.2 shows a schematic layout of the ALICE detector. A short summary of its individual components will be given below. ALICE consists of 19 subsystems that can be grouped as given in following:

- The central barrel detectors.
- The forward or global detectors.

The central barrel detectors at mid-rapidity ($|\eta|$<0.9), are surrounding the interaction point (IP) and are encapsulated by the L3 magnet. This provides a 0.5 T solenoid magnetic field. The following detectors can be enlisted in this group: the Inner Tracking System (ITS) [88], the Time Projection Chamber (TPC) [89], the Time Of Flight (TOF) [90, 91], the Transition Radiation Detector (TRD) [92], the High Momentum Particle Identification detector (HMPID) [93], the Electromagnetic Calorimeter (EMCal) [94], the Di-jet Calorimeter (DCal) [95], the Photon Spectrometer (PHOS) [96] and the Photon Multiplicity Detector (PMD) [97].

The forward or global detectors which include V0 [98, 99], T0 [98], the Zero Degree Calorimeters (ZDC) [100], the ALICE Diffractive (AD) [101] and the Muon Spectrometer. FMD [102], PMD, V0, T0 and ZDC are used for triggering, event characterization (centrality, event plane, etc) and beam luminosity measurements. The Muon Spectrometer ($-4.0 < \eta < -2.5$), has its proper dipolar magnetic field of 3 T.m and is dedicated to muon tracking and triggering. The system is completed by the ALICE Cosmic Ray Detector (ACORDE) [103], an array of scintillators on top of the L3 magnet to trigger on cosmic rays (ACORDE). In the following section, we will briefly describe different ALICE sub-detectors which are relevant to study Quarkonia production as a function of multiplicity.

4.3 The Inner Tracking System

The Inner Tracking System (ITS) [88] is the innermost detector. Fig. 4.3 shows the ITS layout. The ITS is surrounding the beam-pipe (beryllium cylinder with a diameter of 6 cm and wall thickness of 800 μm), covering the pseudo-rapidity range of $|\eta|<$ 0.9. It consists of 6 layers of silicon detectors in three subsystems: the first two layers are Silicon Pixel Detectors (SPD), the second two layers are Silicon Drift Detectors (SDD) and the two following layers are Silicon Strip Detectors(SSD).

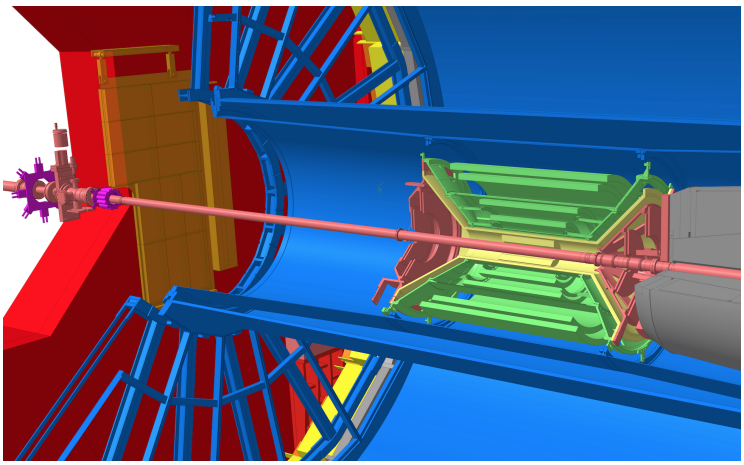

Figure 4.3: Layout of the ITS detector in Run II [88].

The number and position of the layers are optimized for efficient track finding and vertex resolution. The outer radius is chosen to optimize the track matching with the TPC. The inner one is chosen to have the minimum compatibility with the beam pipe. The silicon detectors feature a high granularity and excellent spatial precision required due to the

high particle density. The system covers the central rapidity region $|\eta|< 0.9$. for vertices located within $\pm$ 10.6 cm of interaction point along the beam direction. The dimensions used for each detector layer are summarized in Tab. 4.3.

Layer	Type	r_{in} (cm)	r_{out} (cm)	$\|\eta\|$
1,2	Pixel	3.9	7.6	2.0,1.4
3,4	Drift	15.0	23.9	0.9
5,6	Strip	38.0	43.0	1.0

Table 4.1: Dimensions of individual layers of ITS [104].

The ITS is used to reconstruct primary vertices, secondary vertices from decays of strange and heavy flavor hadrons. It is also used for the primary tracks reconstruction in the Central Barrel and the Muon Spectrometer. The SPD layers are fundamental in the determination of the primary vertex position and multiplicity estimation. The SSD measures the specific energy loss per unit path length dE/dx and enables the identification of low momentum particles with p_{T} <200 MeV/c or passing through dead regions of the TPC. In the following we will describe the SPD detector more precisely as it is one of the important detector used for this analysis.

4.3.1 Silicon Pixel Detector

The SPD consists of two layers of silicon pixel detector modules located around the beampipe. It is at an average distances between 3.9 cm and 7.6 cm from the beam axis. Apart from the determination of primary vertex position, it also can perform the measurement of secondary tracks originating from the weak decays of strange, charm and beauty particles. The SPD layers positioned at 3.9 cm and 7.6 cm have a pseudo-rapidity coverage range of $|\eta|<2$ and $|\eta|< 1.4$, respectively. The SPD was built to provide, a continuous charged particle multiplicity coverage, together with the FMD. It also serves as a trigger detector and is used to identify in-bunch pile-up events, for example: events in which more than one pp collisions from the same bunch crossing took place. The information from the SPD is used in analyses of centrality or charged-particle multiplicity dependent particle production.

4.3.2 SPD vertex and tracking

The tracks reconstruction in ALICE starts by the SPD vertex determination. The SPD vertex is reconstructed from the SPD clusters[1] mainly using two algorithms. The first one is the 3D-vertexer. This algorithm reconstructs x, y, and z positions of the interaction vertex. The reconstruction efficiency and resolution is largely dependent of the charged-particle multiplicity. The resolution improves with increasing multiplicity. The second algorithm is 1D-vertexer and is used when the first one fails to find a vertex, specially in low multiplicity events. The 1D-vertexer uses precise z position, the x and y coordinates are taken from the run average. The segment of tracks (called tracklets from now on) contribution to the vertex measurement is called contributors. In case of several vertexes found, the primary vertex is chosen as the one with the highest number of SPD tracklets. The SPD is able to determine the primary vertices of the interactions with resolution better than 100 μm.
The tracklets are reconstructed using the SPD vertex information. The algorithm considers one straight line from the vertex to a cluster in each (inner and outer) layer respectively.

[1] A cluster is made up of one or more hit adjacent pixels

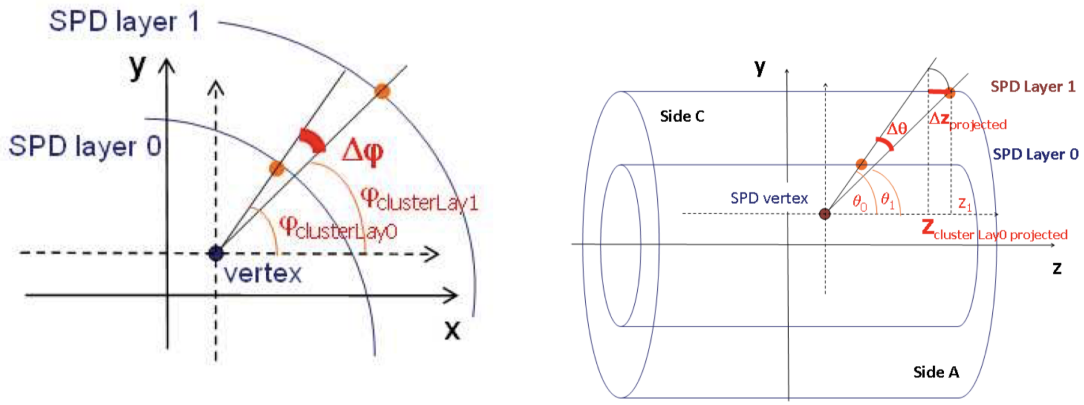

Figure 4.4: Schematic drawing of the tracklet reconstruction algorithm principle. In the left panel, the transverse plane view of the detector illustrates how the $\Delta\phi$ is calculated and the z-y plane view in right panel illustrates how the $\Delta z_{projected}$ is calculated [105].

Two differences ($\Delta\phi$ and $\Delta z_{projected}$) are computed using the vertex as origin for each cluster in the inner layer. $\Delta\phi$ is the difference in azimuthal angles between this cluster and each cluster in the outer layer. $\Delta z_{projected}$ is the difference between the longitudinal coordinate of the prediction from the straight line in the outer layer and the longitudinal coordinate of each cluster in the outer layer. The differences are schematically shown in Fig. 4.4. The $\Delta\phi$ and $\Delta z_{projected}$ are used for rejecting combinatorial background tracklets.

4.4 Time Projection Chamber

The TPC [89] is one of the main detector for the tracking of charged particles. Fig. 4.5 shows the TPC layout. It has an aximuthal coverage of 2π and a pseudo-rapidity coverage of $|\eta|<0.9$. It has a cylindrical shape. The inner and outer radius of the cylinder is about 85 cm and 250 cm respectively. The length of the TPC is 5 m along the beam direction. The active volume of TPC is splitted into half by the central high voltage cathode with voltage up to 100 kV. It allows to have an uniform drift fields of up to 400 V/cm along the beam direction. A gas mixture of $Ar - CO_2$ is filled in the active volume which is ionized while particle passing through the chamber. The free electrons produced by this ionization drift along the electric field to the read-out caps. The read-out caps have 18 sectors where each sector is radially segmented into two chambers (inner and outer read-out chamber). The chambers are optimized for the radially dependent track density consisting in several pads with varying size. The track coordinates (x, y) are reconstructed from the pad signal of drifting electrons hitting the cap. The z coordinate is the product of drift time Δt of the electron cluster and the average electron drift velocity υ_e.

TPC also provides the particle identification (PID) via specific ionization energy loss (dE/dx). For a given material the energy loss depends on the charge, the velocity β and the Lorentz factor γ, can be described by the Bethe-Bloch curve [107]

$$\langle \mathrm{d}E/\mathrm{d}x \rangle = f(\beta, \gamma, C_i) \tag{4.1}$$

where, β is the velocity of the particle, $\gamma=\frac{1}{\sqrt{1-\beta^2}}$ and C_i are detector specific constants. Fig. 4.6 represents dE/dx values as a function of the particle momentum, together with the expected energy loss for the various particle species from the parametrized Bethe-

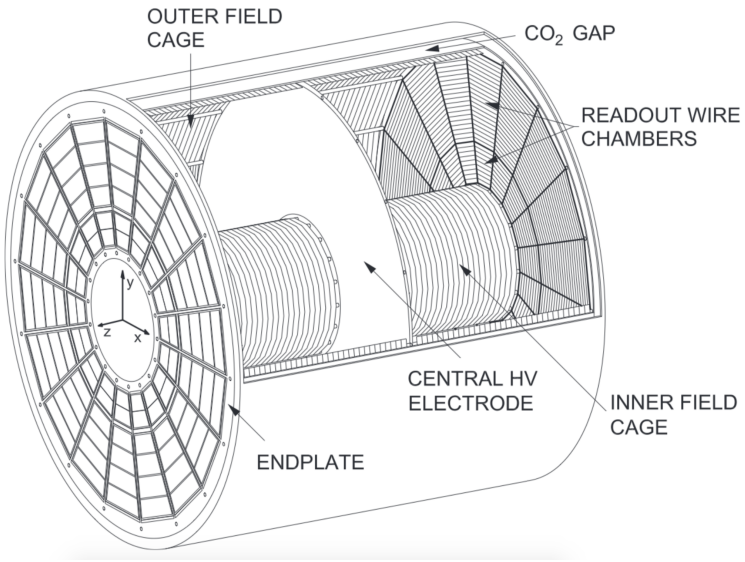

Figure 4.5: The TPC layout [106]

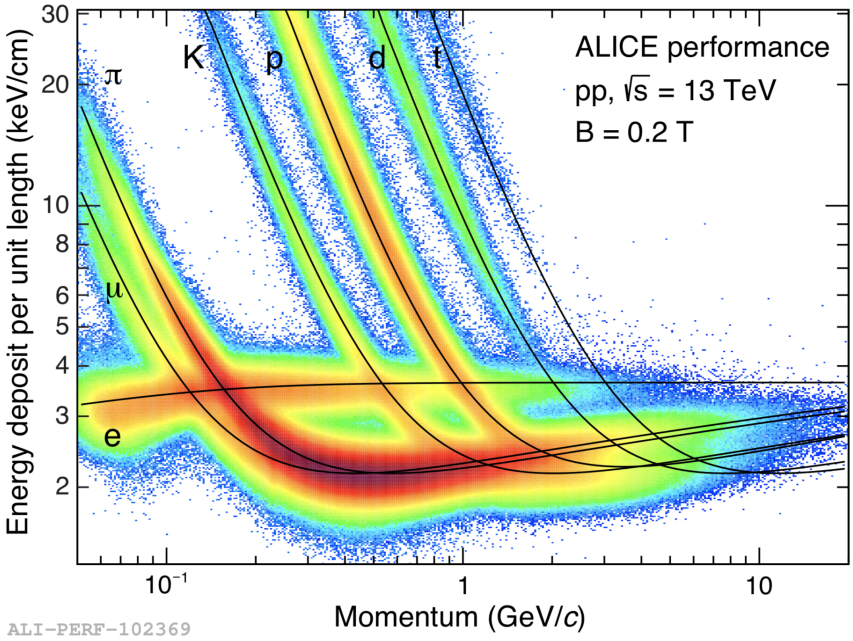

Figure 4.6: Specific energy loss ($\mathrm{d}E/\mathrm{d}x$) in the TPC versus particle momentum in pp collisions at $\sqrt{s}$ = 13 TeV. The lines show the parametrizations of the expected mean energy loss for different particle species.

Bloch curve.

4.5 V0 Detector

The V0 [98, 99] is a small angle detector. It consists of two sets of scintillator arrays (V0A and V0C). These scintillator arrays located asymmetrically on either side of the nominal interaction point (IP). The V0A covers a pseudo-rapidity range 2.8< η <5.1 and located at $z = +330$ cm. On the other hand VOC covers -3.7< η <-1.7 installed on $z = -90$ cm.

The position of the two V0 arrays within the general layout of the ALICE experiment is shown in Fig. 4.7.

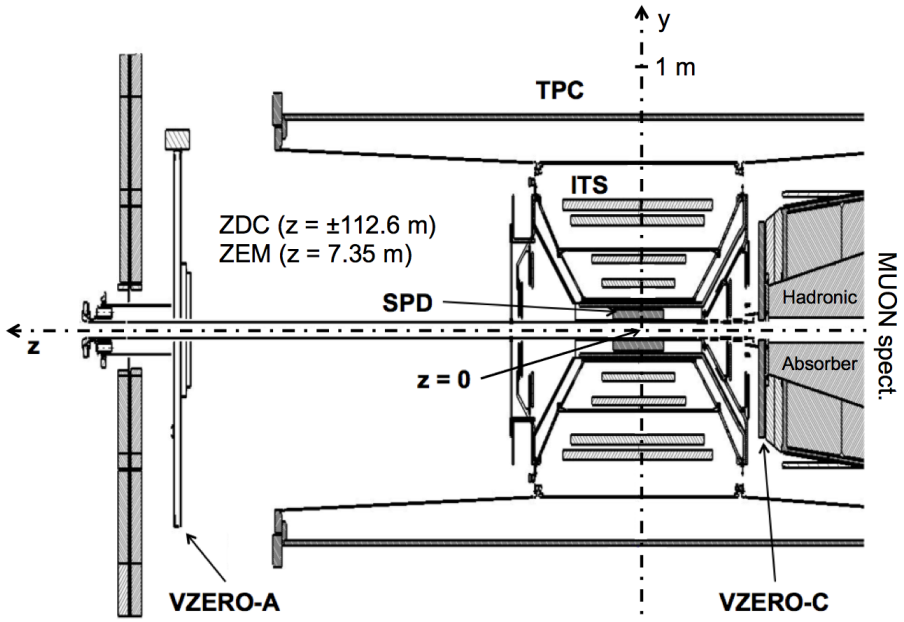

Figure 4.7: Placement of the V0A and V0C arrays within the ALICE detector [99].

The V0 detectors are segmented into 64 elementary counters in 8 rings. The measurement of the time difference between the two subsystems allows to identify and reject the beam-gas events. This provides a minimum bias (MB) trigger (in pp, pA and AA) for the central barrel detectors and a validation signal for the Muon Trigger [98]. In pp collisions, V0 provides two types of MB triggers (MB_{OR} and B_{AND}).

• MB_{OR} was primarily used in 2009 and 2010 pp collisions and is defined as coincidence of a signal from SPD and a signal from either V0A or V0C.

$$\text{SPD \&\& (V0A || V0C)}$$

• MB_{AND} is used from 2011 further on after the increase of the LHC luminosity. This is defined as a coincidence of signals from both VOA and VOC and LHC_{bunchX} (LHC bunch crossing signal):

$$\text{(V0A \&\& V0C) \&\& } LHC_{bunchX}$$

MB_{AND} rare signals can be combined with a signal from detector triggering on specific rare event topology, such as the Muon Spectrometer:

$$\text{(V0A \&\& V0C) \&\& } LHC_{bunchX} \text{ \&\& MUON}$$

The V0 can measure charged-particle multiplicity distributions which serves as an indicator of the centrality of the AA collisions. The V0 is also used for the determination of the integrated luminosity $\mathcal{L}_{int}$. $\mathcal{L}_{int}$ is calculated as a ratio of the number MB triggered events N_{V0AND} and the total cross section σ_{V0AND} from the Van Der Meer (VDM) scan [108].

$$\mathcal{L}_{int} = \frac{N_{V0AND}}{\sigma_{V0AND}} \tag{4.2}$$

4.6 The Muon Spectrometer

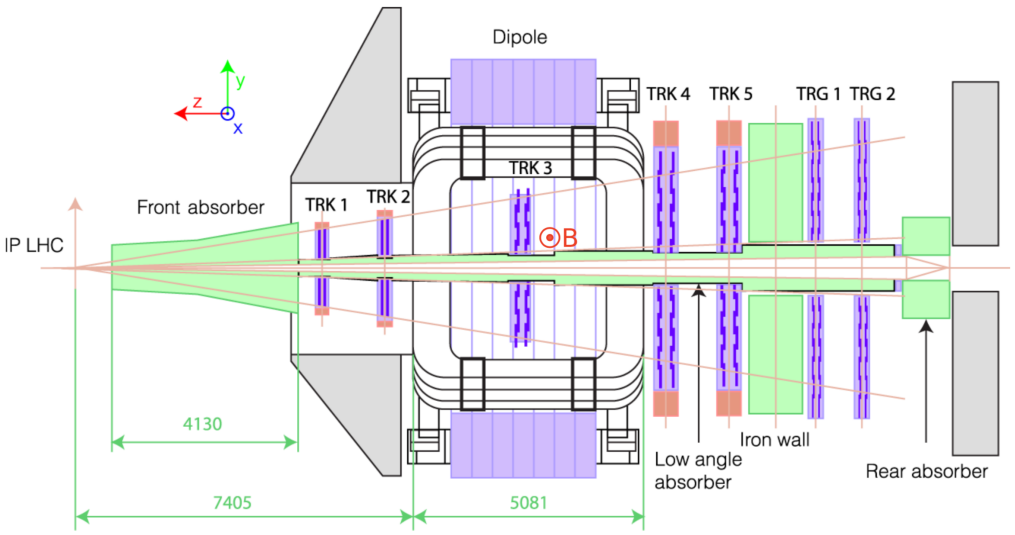

Figure 4.8: Layout of ALICE Muon Spectrometer

The muon spectrometer [109] allows to study low-mass vector mesons, quarkonia (charmonia and bottomonia), vector gauge bosons ($W^{\pm}$ & Z^0) in the di-muon decay channel. Open heavy flavor (D- and B-mesons) can also be studied in their semi-leptonic decay channel by the spectrometer. It has a pseudo-rapidity coverage of -4.0< η <-2.5. The spectrometer is able to reconstruct heavy flavor hadrons over a wide p_T range. Fig. 4.8 shows the layout of the muon spectrometer.
The muon spectrometer has a total length of about 17 m. Starting from the interaction point (from the left side of Fig. 4.8), it consists of the following components: an absorber to filter the background, a set of tracking chambers before, inside and after the magnet and a set of trigger chambers. The different components of the Muon Spectrometer (Fig. 4.8) are discussed in more details in the following sections.

4.6.1 Absorbers and shielding

The system of absorbers has four separated parts: front absorber, beam shield, iron wall and rear absorber.

Front absorber: It is located at a distance of 90 cm from the IP, inside the central barrel solenoid magnet. The front absorber is 4.13 m long. It is designed to reduce the flux of hadrons and photons produced in the interaction vertex. It also reduces the background of the secondary muons from pion and kaon decays. It limits the multiple scattering and energy loss by muons which is important to obtain a reasonable resolution to separate the bottomonium states.
The internal structure of the front absorber is shown in Fig. 4.9. The body of the absorber which is close to the IP is made of low Z material (carbon and concrete). It limits the multiple small-angle scatterings and energy loss of muons. On the other hand, the rear end is composed of concrete, several layers of lead and boronated polyethylene to absorb the secondary particles produced in the absorber and low energy protons and neutrons. Finally, an external coating made of lead and boronated polyethylene is applied to the absorber to avoid the recoil particles to reach the TPC .

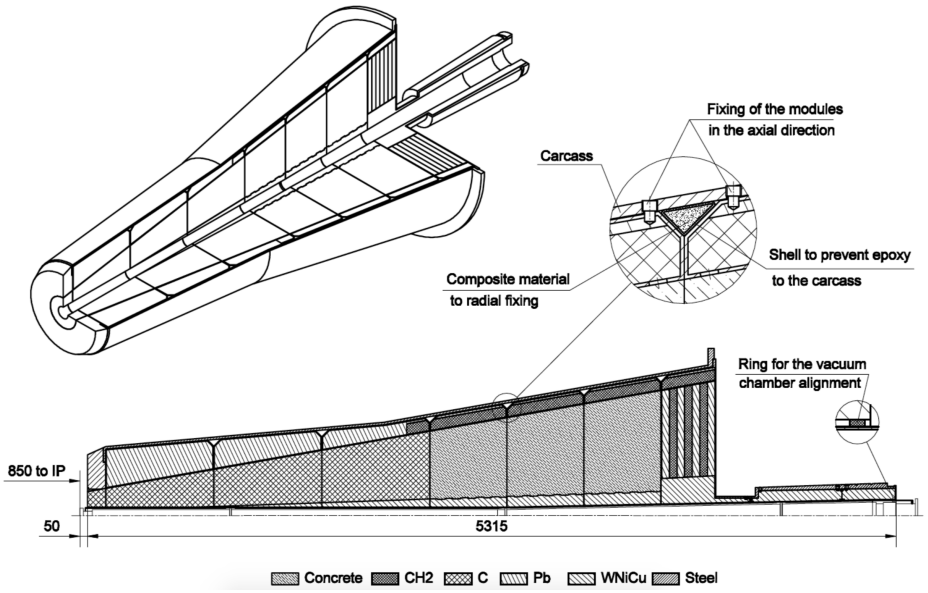

Figure 4.9: Layout of the front absorber of the Muon Spectrometer [109].

Beam shield: The beam pipe is shielded all along the Muon Spectrometer. The shield is made of tungsten, lead and stainless steel. It reduces the background coming from the interaction of low angle particles with the beam pipe or beam-gas interactions.

Iron wall: To provide further shielding to the muon trigger chamber (MTR), an iron wall of 1.2 m thickness is placed between the last muon tracking chamber and the first trigger chamber. This iron wall is called as muon filter. Together with the front absorber and the muon filter, the shielding prevent the muon with momentum (p) below 4 GeV/c to reach the MTR.

Rear absorver: The rear absorber provides additional shielding to the rear side of the MTR. This reduces the background originating by the beam-gas interactions in the beam pipe. This is highly useful when LHC provides low luminosity beams during pp data taking [110].

4.6.2 Dipole magnet

A warm dipole magnet is used to bend the tracks. It is located at $\sim$ 7 m from the interaction vertex. It can create a maximum central field of 0.7 T and an integral field of 3 T.m. The direction of the field is perpendicular to the beam pipe in the horizontal plane. Thus the zy plane is defined as the bending plane where muons are deviated and the xz plane is defined as the non-bending plane.

4.6.3 Muon tracking system

The Muon Tracking system is designed to have a working capability in high multiplicity environment. A spatial resolution better than 100 μm in the bending plane is needed to achive the expected mass resolution for the Υ. In contrast, a resolution better than 2 mm is enough for the non-bending plane to find a good track.

The tracking system consists of five stations including two Cathode Pad Chambers in each. The chambers are Multi-Wire Proportional Chambers (MWPC) with Cathode pad read-out. A sketch of the MWPC working principle is shown in Fig. 4.10 where each chamber equipped with two cathode planes with a plane of anode wires in between. A mixture of Ar and CO_2 is filled in the space between the cathode planes. When traversing the detector, a charged particle ionize the gas along its trajectory. Then the electrons drift towards the nearest anode. They generate an avalanche of secondary electrons due to the presence of intense electric field. Thus a charge distribution on the cathode pads close to the avalanche position is induced by the resulting ion clouds. These charge distributions in bending and non-bending planes allows to obtain the bi-dimensional position where the charged particle traverse the chamber.

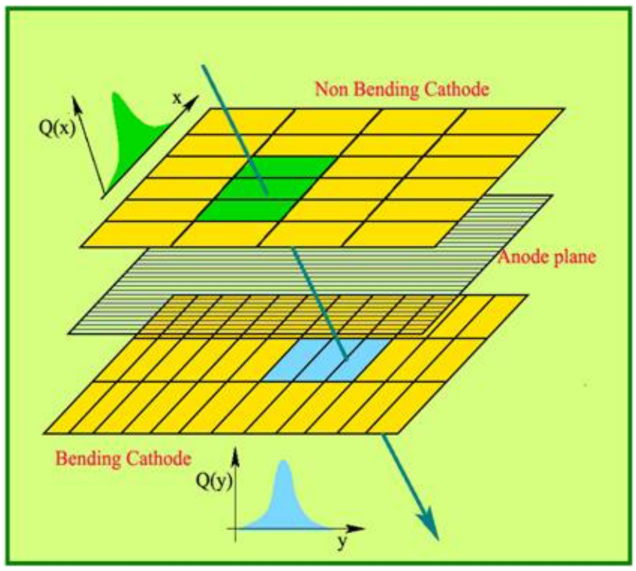

Figure 4.10: Sketch of the working principle of a Multi-Wire Proportional Chamber.

The design of the chambers is adapted to fit particular geometrical requirements. A geometrical projection of the angular coverage of the spectrometer determines the size of the chambers in first two stations. They have a quadrant structure (Fig. 4.11 left). The chambers in the other three stations have slat (horizontal module) design with higher dimensions to cope with the deviations of muons in the magnetic field (Fig. 4.11 right). A certain overlap of quadrants and slats allows to avoid dead zones.

4.6.4 Muon Trigger Chambers

The ALICE Muon Trigger Chamber (MTR) serves to select the muon candidate during the collisions, more precisely the high p_{T} muons which were produced in heavy quarkonia, open charm, open bottom decays. It rejects all the low p_{T} muons which mainly come from pion and kaon decays. This system allows to put a p_{T} cut at trigger level on each individual muons. The data sample for 2016 was collected after rejecting tracks of $p_{\mathrm{T}} < 1$ GeV/c^2.

The MTR consists of four planes of Resistive Plate Chambers (RPC). These RPCs are grouped into two stations (MT1 and MT2) spaced 1 m apart. The two stations in muon trigger have in total four planes (MT11, MT12, MT21, MT22) of single gap Resistive Plane Chamber detectors. The MTR stations are located behind the muon filter at a

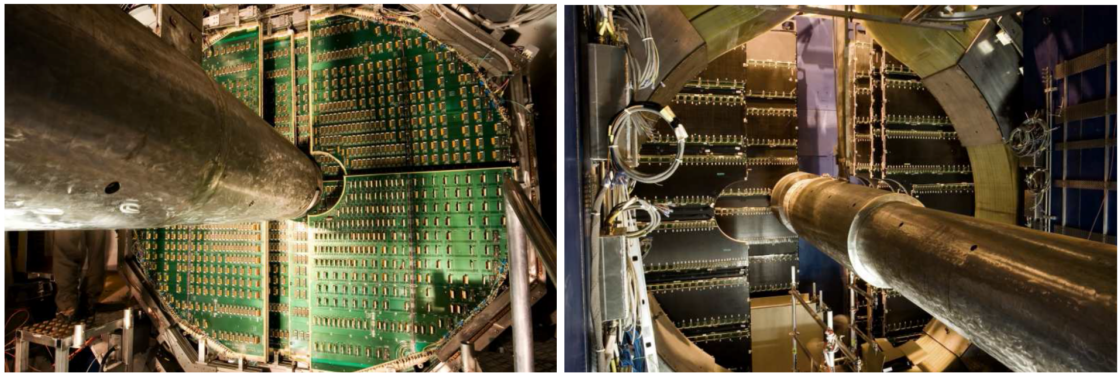

Figure 4.11: Left: Picture of a quadrant design chamber. Right: Picture of a slat design chamber. [111]

distance of $\sim$ 16 m from the IP. The planes in the same station are 17 cm apart with a detection area $\sim$150 m^2.

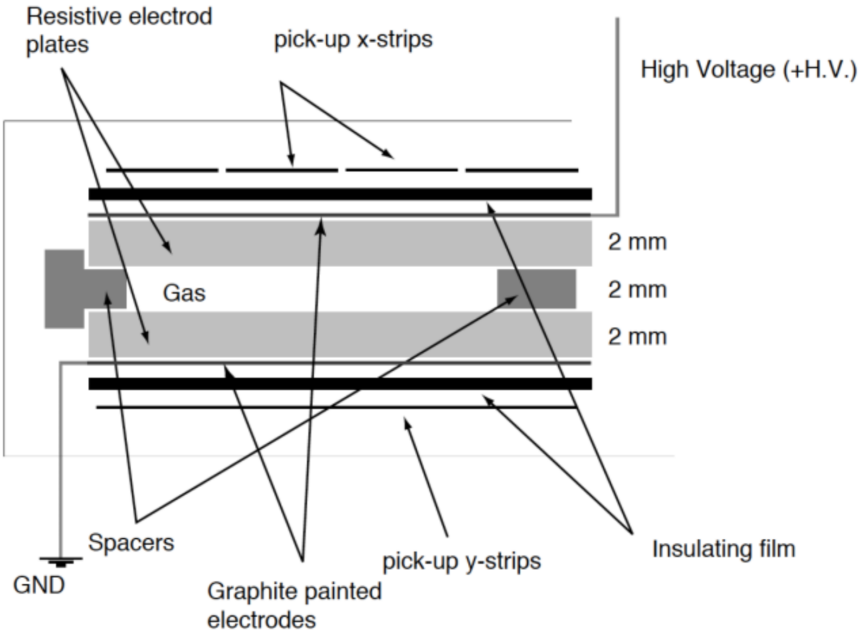

Figure 4.12: The RPC structure in Muon Trigger system [109].

In Fig. 4.12, there is a 2 mm volume gap between the resistive plates filled by gas. The outer faces of the plates are painted with graphite and one is connected to high voltage and the other is grounded. The graphite electrodes are covered by some insulating film. Aluminum strips are placed outside of the chamber. In one side, the strips are aligned with the x-axis of the ALICE reference system. They measure the deviation in the bending plane. On the other side, the strips are aligned with the y-axis and measure the non-bending direction. The pitch and length of the strips increases with their distance from the beam axis. The RPCs pulses are collected in each plane by a total 20992 strips. These strips are located on both sides of the RPCs. Each strip is connected to one FEE channel. The RPCs read-out planes collect opposite sign electrical signals: positive signal

for x-strips and negative signals for y-strips. FE electronics are propagated through cables to the 234 local boards, acting as readout interfaces and in charge of the first stage of the muon trigger decision. In section 5.1 we will describe the study on FEE upgrade as a part of the ALICE service work.

The chambers have a spatial resolution which is below 1 cm. This is necessary to cut low p_{T} muons from the pions and kaons decays. The time resolution of the chambers to identify the bunch crossing to which a given muon belongs is ∼2 ns. The system has two p_{T} cuts (low and high). In general, the low and high p_{T} cuts are ∼ 0.5 GeV/c and ∼ 4 GeV/c respectively. These cuts help to reduce the combinatorial background in quarkonia analyses. The following trigger inputs are usually defined for muon data taking:

0MSL, at least one reconstructed muon satisfying the low p_{T} cut
0MSH, at least one reconstructed muon satisfying the high p_{T} cut
0MUL, at least one reconstructed unlike signed di-muon pair satisfying the low p_{T} cut
0MLL, at least one reconstructed like signed di-muon pair satisfying the low p_{T} cut

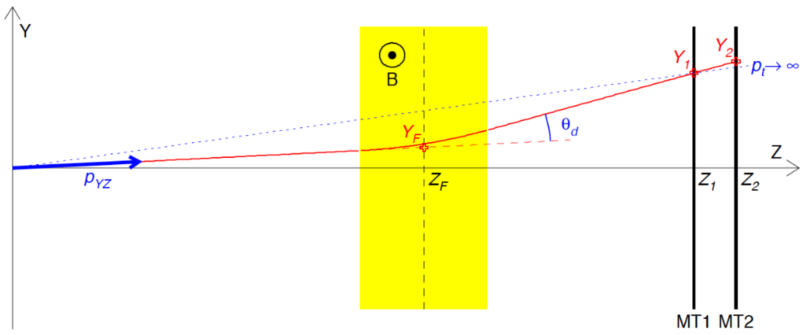

Figure 4.13: The Muon Spectrometer trigger principle.

In Fig. 4.13, a muon trajectory (in red line) is deviating due to the presence of the magnetic field B. Later it intersects in MT1 in y_1 and MT2 in y_2. The transverse momentum of muons crossing the trigger chambers can be estimated by measuring the deviation of measured tracks caused by the dipole magnet. The muon track momentum in the bending plane can be expressed as:

$$p_{\mathrm{yz}} = |\frac{\mathrm{qLB}}{\theta_d}| \tag{4.3}$$

where θ_d is the deviation angle, L is the length of dipole magnet, q is the charge of particle and B is magnetic field. Then, the θ_d can be calculated by

$$\theta_d = \frac{z_1 y_2 - z_2 y_1}{z_f(z_2 - z_1)} \tag{4.4}$$

where z_f is the position of the dipole magnet along the z axis, (y_1, z_1) and (y_2, z_2) to the muon tracks crossing positions at MT1 and MT2. The component is then:

$$p_{\mathrm{T}} = p_{yz}\frac{\sqrt{x_f^2 + y_f^2}}{x_f} \tag{4.5}$$

where (x_f, y_f) is the position where the muon track crosses the center plane of the dipole magnet, and can be estimated by extrapolating the positions of the track (x_1, y_1, z_1) and

(x_2, y_2, z_2) corresponding to MT1 and MT2, respectively:

$$x_f = x_1.\frac{z_f}{z_1} \text{ and } y_f = y_2 - \frac{y_2 - y_1}{z_2 - z_1}.(z_2 - z_f) \tag{4.6}$$

The trigger condition is estimated by measuring the deviation of track position from MT1 to MT2. The process starts with measuring the track position from MT1 and then building a straight line to the IP (muon with infinite p). In the next step it calculates the deviation of the measured track positions from MT1 and MT2 with respect to the straight line. This measured deviation should be smaller than the given p_{T} cut to satisfy the trigger condition.

4.6.5 Upgrade of the ALICE muon trigger electronics

A major upgrade of the ALICE detector is foreseen during the next LHC long shutdown (2019-2020) [112] in order to achieve higher readout rates in PbPb collisions. The upgrade project includes a replacement of the current MTR system with Muon IDentifier (MID) which will read out all events interaction trigger before online selections. The goal is to read out at the minimum bias rate of 100 kHz in PbPb collisions (including a safety factor of 2), two orders of magnitude above the present design. For the most exposed RPCs, the total integrated charge will be as high as 100 mC/cm^2 with rates up to 100 Hz/cm^2, which is above the present limit for safe operation. The foreseen luminosity for RUN 3 and 4 is up to 6 $10^{27}\mathrm{cm}^{-2}\mathrm{s}^{-1}$. A replacement of the RPC front-end electronics (FEE) is foreseen, more details will be given in section 5.1.

4.7 ALICE Trigger System and Data Acquisition

The ALICE Trigger system processes very different environments like pp, p-Pb, Pb-Pb collisions at the CERN LHC. This system consists of the Central Trigger Processor (CTP in Fig. 4.14) and 24 Local Trigger Units (LTU) working as an uniform interface to sub-detector front-end electronics. The CTP [113] is designed to collect the information from all the triggering detectors in ALICE, and to send the correct sequences of trigger signals to all detectors in order to make them read out correctly. The CTP has three levels of hierarchical hardware triggers (L0, L1 and L2) [114].

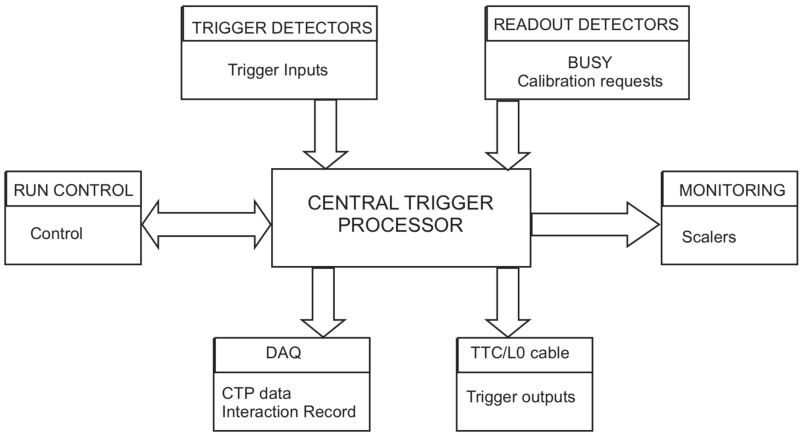

Figure 4.14: Context diagram for CTP

• The L0 (level 0) trigger inputs are the first to arrive to the CTP. The L0 inputs are generally sent by the detectors such as SPD, V0, T0, EMCAL, PHOS and MTR. The

latency of L0 trigger, the time between the interaction to the arrival of the trigger signal to the read-out detectors, is $\sim 1.2\ \mu s$.

• The L1 (level 1) trigger inputs are supplied to the CTP from TRD and ZDC in the events accepted by L0. The L1 has a latency of $\sim 6.5\ \mu s$. This latency is mainly caused by the computation time in TRD and EMCAL and the propagation time to ZDC.

• The L2 is taken after $\sim 100\ \mu s$. The time of the TPC is the reason for this delay.

The information on counts for all trigger classes at each of these levels before (L0b) and after (L0a) the CTP decision, is stored in the so called scalers. The CTP vetoes (when the CTP do not generate any L0 signal) might happen for some reasons such as busy cluster in at least one detector, mismatch between the L0 input and bunch crossing, the past-future protection (the rejected events in a collision within the TPC drift time in order to avoid pile-up), or the downscaling of a certain trigger classes to allow more DAQ bandwidth for rare events. If there is no CTP vetoes, sub-detectors are readout after the successful L2 trigger. Then the event is sent to High Level Trigger (HLT) for further implementation of more sophisticated trigger criteria [115]. After processing the readout data from the detectors, HLT accepts or rejects events.

The accepted events then undergoes several processes through ALICE Data Acquisition (DAQ) system. Then data are stored into CERN computing center by ALICE DAQ, a first pass is processed. During the first pass reconstruction, the detector alignment and calibration data are stored in Offline Condition Data Base (OCDB). The information filed and stored in the OCDB is later accessed in all reconstruction, analysis, and simulation of the data. An Event summary Data (ESD) file is created to store the results of each reconstruction pass. These ESD files include information from the different detectors that is later used for analysis, calibration, and detector performance studies. Then these ESD files pass through several re-filtering based on the specifications of different analysis to create the Analysis Object Data (AOD) files. These AOD files contain reduced and specific information depending on the type of analysis. The AOD file takes small storage compared to the ESD files and much faster to analyze. The work presented in this thesis is performed using AOD files.

4.7.1 Data Sample for the analysis

For this thesis work, the analysed data sample used is collected in 2016 in pp collisions at $\sqrt{s} = 13$ TeV. We used specific AOD filtered for MUON from general purpose reonstructed data. The events used in this analysis have fired the CMUL7-B-NOPF-MUFAST, CINT7-B-NOPF-MUFAST and CMSL7-B-NOPF-MUFAST (for normalisation only) triggers. The following trigger classes are usually defined in muon data taking:

- CMUL7-B-NOPF-MUFAST is the di-muon trigger. This is defined by a coincidence of signals in V0A and V0C systems with a pair of unlike sign muons satisfying the low p_{T} threshold in the Muon Spectrometer.
- CMSL7-B-NOPF-MUFAST is the low p_{T} single muon trigger. This is defined by a coincidence of signals in V0A and V0C systems with a muon satisfying the low p_{T} threshold in the Muon Spectrometer.
- CMSH7-B-NOPF-MUFAST is the high p_{T} single muon trigger. This is defined by a coincidence of signals in V0A and V0C systems with a muon satisfying the high p_{T}

threshold in the Muon Spectrometer.

- CMLL7-B-NOPF-MUFAST is the like sign di-muon trigger. This is defined by a coincidence of signals in V0A and V0C systems and of a pair of like signed muons satisfying the low p_{T} threshold in the Muon Spectrometer.
- CINT7-B-NOPF-MUFAST is the minimum bias (MB) trigger and is defined by a coincidence of signals in V0A and V0C.
- C0TVX-B-NOPF-CENTNOTRD is another MB trigger which is defined as a coincidence of signals in T0A and T0C requiring a T0 vertex within $|z|<30$ cm from the IP.

The name of each trigger class contains information on the trigger input (e.g. CMUL7 means 0MUL input with V0AND), B indicates bunches from both beams on the bunch crossing mask from LHC, NOPF means there is no vetoes applied for past-future protection and MUFAST is the cluster name which includes SPD, MCH, MTR, T0, V0, AD. During muon data taking a large amount of bandwidth is allocated to the rare triggers (CMUL7, CMLL7, CMSL7 and CMSH7). For this allocation the minimum bias (MB) triggers are down-scaled. The triggers that has been used for this analysis are listed in Tab. 4.2.

Trigger class	trigger description
CINT7-B-NOPF-MUFAST	V0A && V0C
CMUL7-B-NOPF-MUFAST	V0A && V0C && low-p_{T} di-muon (p_{T} cut at 0.5 GeV/c)
CMSL7-B-NOPF-MUFAST	V0A && V0C && low-p_{T} single muon (p_{T} cut at 0.5 GeV/c)

Table 4.2: Trigger definition in Υ vs. multiplicity analysis.

Summary

ALICE is a dedicated heavy-ion experiment which consists of twenty two sub-detectors. These sub-detectors are grouped into two main parts, the central barrel at the mid rapidity and the muon spectrometer in the forward rapidity. A detail explanation of the SPD has been presented which is used for the charged particle measurement of this thesis. Similarly the section of the muon spectrometer contains explanation about the detector configuration, the working principle of the tracking and trigger chambers and the track reconstruction which is used for the Υ measurement in di-μ decay channel. We have also discussed about the muon trigger upgrade project which is the main focus of the next chapter. Finally we have also presented DAQ system in ALICE and the data sample which is used for the work presented in chapter 6.

Chapter 5

Statistical exploitation of the measurements performed with the test bench of the FEERIC cards

One of the ALICE upgrades for LHC RUN 3 and 4, will be the replacement of the front end electronics (FEE) of the Resistive Plate Chambers (RPC) of the Muon Trigger system [116]. A new electronic card has been developed at LPC for the upgrade of FEE. In this chapter we will discuss the measurements performed on the new FEERIC cards as a part of my service task in ALICE.

5.1 Overview

The Muon IDentifier (MID) is the proposed designation of the present Muon Trigger system [87]. The description of the MID project can be found in the Technical Design Report (TDR) of the upgrade of the ALICE Readout and Trigger System [117]. The current operational mode of the RPCs is "maxi-avalanche" [118] with present FEE (ADULT ASIC) [117, 119], which does not include any amplification stage. In the current RPC working conditions, the charge per hit is ∼100 pC while the maximum dose which can be accumulated by RPC should not exceed 50 mC/cm^2 typically. The instantaneous counting rate is limited to 50 Hz/cm^2 [120] for short-term safe operation.

collision type	Pb-Pb
collision rate (kHz)	100
$\sqrt{s_{\mathrm{NN}}}$ (TeV)	5.5
mean-peak hits/s/cm^2	75-125

Table 5.1: Expected counting rates of the RPCs [121]

The expected counting rate (max=125 Hz/cm^2, as seen in Table 5.1) is too high for the maxi-avalanche mode. The RPCs are proposed to be operated in saturated avalanche mode (as in ATLAS [122] and CMS [123] RPCs) for the LHC Run 3 and 4 which will improve the counting rate capability and slow down the detector aging. In this mode the RPCs will be operated with a significant reduction of the charge produced in the gas, hence limiting aging effects. The goal is to operate the new FEE with a threshold corresponding to a fast charge q ∼100 fC at the FEE input. The new FEE called FEERIC (for Front-End Electronics Rapid Integrated Circuit) will perform amplification of the analog input signals. This will allow for RPC operation in a low-gain avalanche mode, with a much smaller charge deposit (factor 3-5) in the detector as compared to the present conditions.

5.1.1 FEERIC cards

The FEERIC cards perform the processing of analog signals from 72 RPC detectors. The total number of electronics channels is 20992. The input signals have a typical rise time of 2 ns. The FEERIC ASIC is the main component of the FEERIC card. Fig. 5.1 shows a schematic of one channel of FEERIC ASIC consisting in a transimpedance amplifier, zero-crossing discriminator and a one-shot. The transimpedance amplifier performs the amplification of the analog RPC signals, the zero-crossing discriminator provides the digital signal and the one-shot system is a shaper which sets the output signal width to 23 ns while preventing the retriggering during 100 ns.

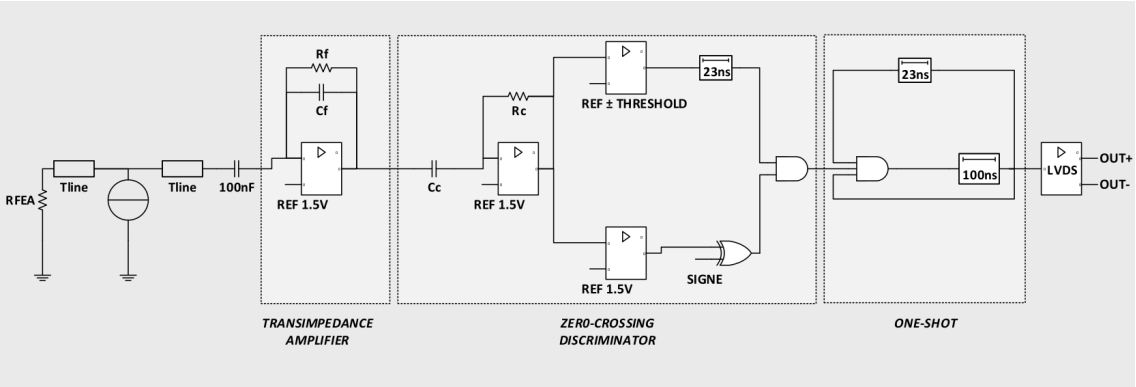

Figure 5.1: Block diagram of one channel of the FEERIC ASIC

At the output of the one-shot, the digital signal is converted in LVDS (Low Voltage Differential Signal) electrical standard. Each FEERIC ASIC has eight channels. The printed circuit board (PCB) includes mostly the FEERIC ASIC, the input/output connectors and an injection circuit to test online functionality. The discrimination threshold is either received as an external analog voltage or digital one via the I2C protocol. A manual selector allows to configure the cards for either positive or negative input signals.

The FEERIC cards can be classified in 6 different formats according to strip width (about 1 cm, 2 cm or 4 cm strip width and detector station 1 or 2). Each format can be configured in positive and negative polarity.

Type	Width	Height	Channels	Number of cards Series			Number of cards Pre-Series		
				POS	NEG	Total	POS	NEG	Total
FEERIC11	167 mm	50 mm	16	140	0	140	10	0	10
FEERIC12	175 mm	50 mm	16	140	0	140	10	0	10
FEERIC21	167 mm	50 mm	8	590	240	830	10	10	20
FEERIC22	167 mm	50 mm	8	590	240	830	10	10	20
FEERIC41	304 mm	50 mm	8	180	160	340	10	10	20
FEERIC42	304 mm	50 mm	8	180	160	340	10	10	20
Grand Total				1820	800	2620	60	40	100

Table 5.2: Number and type of FEERIC cards from production and pre-production.

Table. 5.2 shows the number of cards produced (including spare cards). The dimensions of the PCBs, the number of cards in different polarity (POS or NEG) are also listed in the table.

5.1.2 Production test bench

The purpose of using the test bench is to check 2720 FEERIC cards including 14% spares. The target list for this check includes the measurements of power consumption, noise level, Front End Test (FET) validation, injected charge just above threshold for four threshold values, response time and output LVDS pulse duration, one-shot duration for each FEERIC channel and/or card. The main focus of this work is on the measurement of injected charge just above threshold for 4 threshold values and response time, and will be presented in section 5.2 and section 5.3.

The production test bench used for this work is shown in Fig. 5.2. The production test bench is controlled by a PC. The test processes are managed by Labview software running on this PC. The test bench has different slots to test the different formats of FEERIC cards (1 cm, 2 cm or 3 cm strip width, pitches of MID station 1 and 2). The tests can be done in all slots simultaneously or individually. The slots are called as SLOT 0, 1, 2, 3, 4, 5. The cards of 1 cm and 2 cm can be tested either on (SLOT 0, SLOT 1) or (SLOT 3, SLOT 4) for station 1 and 2 format respectively. The cards of 4 cm can only be tested on SLOT 2 and SLOT 5 for station 1 and 2 format respectively.

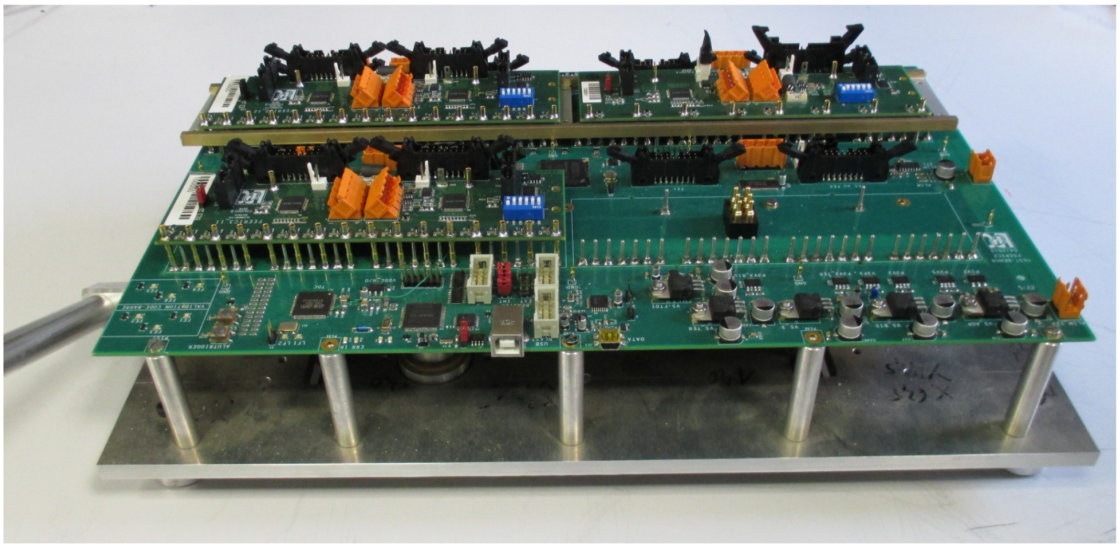

Figure 5.2: Production test bench

There are "piston" connectors on the board (in front of contacts on FE cards). These are dedicated to power up the FE cards and to transmit the FET signal. The FET signal checks the functionality of FE card during the operation. Then there is an interface called I2C shown in Fig. 5.3 which can set the required threshold while passing the signal via the "piston" connectors.
The FEERIC thresholds are generated by mean of a 10 bit DAC (Digital to Analog Converter) with 3 V full range by steps of 3 mV. The test starts by the detection of the number, format and position of cards on the bench. The test of a FE card continues by sending a FET signal to the FE card. Then the test bench checks all channels delivering a LVDS compliant signal on output.

The noise levels are checked for each FE card channel by simply searching for the threshold value, without any input signal injection, up to a point where at least one FE output signal is detected (meaning that LVDS output signal is present because of noise) in a wide time window of 1 μs.

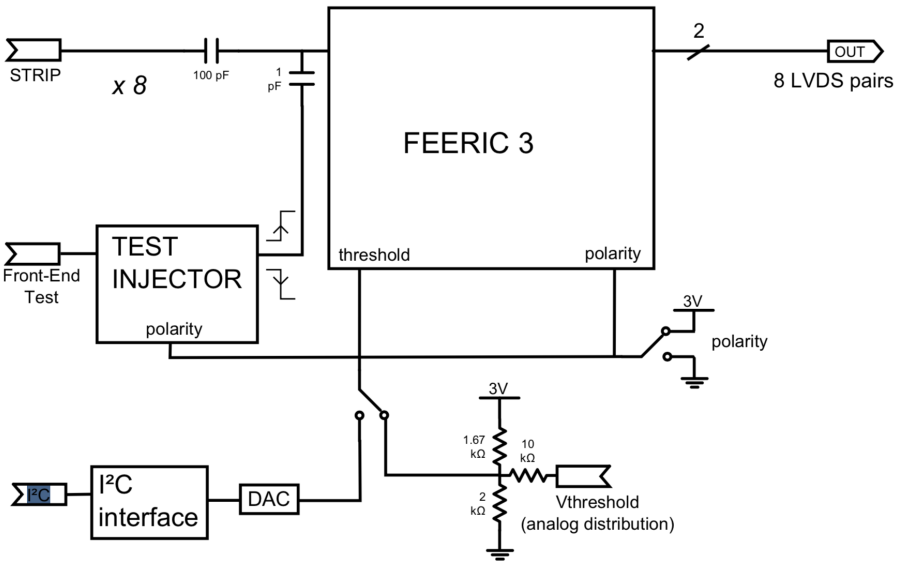

Figure 5.3: FEERIC board block diagram

The one-shot prevents FEERIC re-triggering in a time window of ∼90ns . This is done to hide the case of long discharges in the gas. The duration is measured indirectly by counting the number of FE output signals in a time window of 2 μs.

The threshold value is usually expressed in mV. The region where the relation between the threshold value and the injected charge just above threshold is proportional defines the so called gain. For example: if the threshold is 180 mV and the injected charge is 200 fC, the gain will be 0.9 mV/fC. In the production readiness review (PRR) [124], the gain (in direct injection) was estimated for a fixed threshold (140 mV), searching for the charge just above the threshold. The gain in Fig. 5.4 is in the range of 0.8-1.07 mV/fC for all the channels of FEERIC22 boards and 0.7-1 mV/fC for FEERIC42 boards. The gain uniformity is satisfactory, in spite of some systematic uncertainties. The gain decreases with PCB input track length and tends to be higher for positive signals (for the given test threshold of 140 mV).

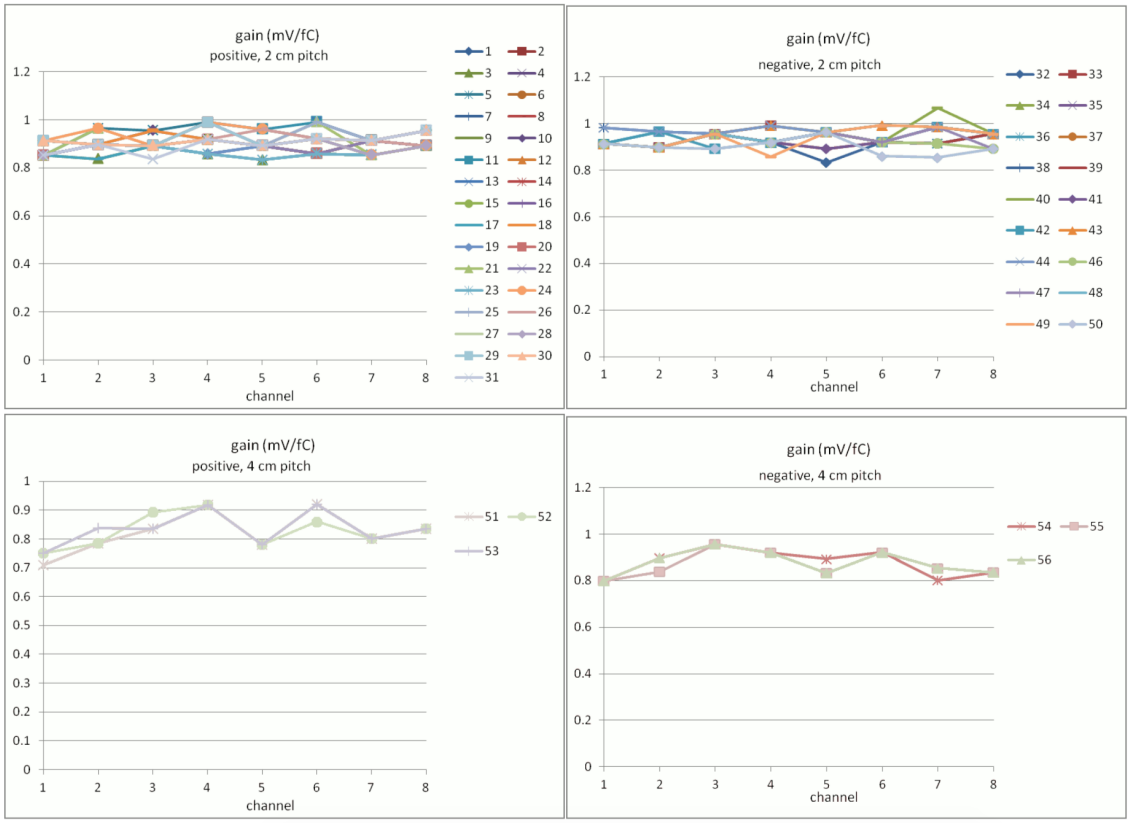

Figure 5.4: Gain uniformity for FEERIC22 (top) and FEERIC42 (bottom) [124]

For the measurement of the charge just above the threshold, four values have been chosen, respectively of 200 fc, 400 fc, 600 fc and 800 fc. The calibrated charges are generated by mean of a 12 bit DAC with 5 V full range delivering a voltage pulse in a 2.7 pF capacitor. In the end, the injected charge at the FE input is ∼1 fC/lsb[1]. In section 5.2 we will present the measurements of charge injection for the four proposed thresholds values.

Time measurements make use of a 8 channels TDC-GPX [125] configured for ∼ 200 ps bin resolution. For safety, the TDC is accurately calibrated by mean of signals from an oscillator (known delays) at the beginning of each test sequence. For this test sequence, the FE threshold is set to 180 mV above (below) reference voltage (corresponding to 1.5 V) for the positive (negative) configuration of the card. The gain of FEERIC in direct injection being ∼0.9 mV/ fC, 180 mV correspond to an equivalent threshold close to 200 fC.

A label with bar-code on each FE card, scanned by a bar-code reader with the interface to PC, is used for its identification. The card polarity is specified in the bar-code and must correspond with the polarity selector on the FE card (the test bench would generate an error if this is not the case). The duration of a test sequence, not including the FE card installation, is close from 0.5 s per channel (∼ 32 s in the most crowded case with 4 FE cards of 16 channels each). In section 5.3 we will describe the measurement of time response performed on the test bench for all the cards from the production.

The LVPS is remotely started and stopped at the start and stop of a test process for the protection of the electronics. A mechanical system helps to eject the FE cards at the end of the test process.

[1]lsb corresponds to the least significant bit

5.2 Measurement of injected charge just above threshold

In this section, we will present the measurements of injected charge just above threshold performed on the test bench. The top panel of Fig. 5.5 is an example plot of the charge injection just above the threshold 200 fC for FEERIC11 cards. And the bottom panel shows the projection of the charge injection for channel 1. The RMS (the arithmetic mean of the squares of each value in a histogram) of the projected histogram represents the dispersion.

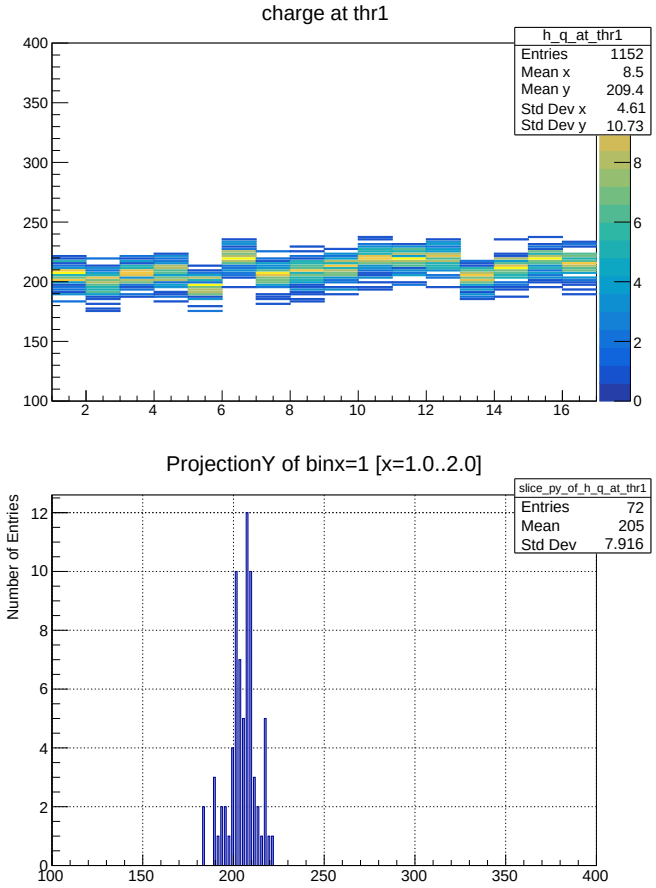

Figure 5.5: Injection charge just above threshold 200 fC for FEERIC11 (top panel) and the projection of the injection charge for FEERIC11 channel 1 (bottom panel).

Fig. 5.6 and 5.7 show some example plots of injected charge just above threshold per channel of different FEERIC card formats tested on different slots and polarity. We have studied the following effects for the injected charge just above threshold:

- Different thresholds for all card formats (200 fC, 400 fC, 600 fC, 800 fC).
- Different card formats (FEERIC11, FEERIC12, FEERIC21, FEERIC22, FEERIC41, FEERIC42).
- Different polarity.

The injected charge per channel just above the four thresholds shows similar trend (increase of the injected charge with increasing threshold) for each format of FEERIC cards. The dispersion is larger for cards tested on higher thresholds.

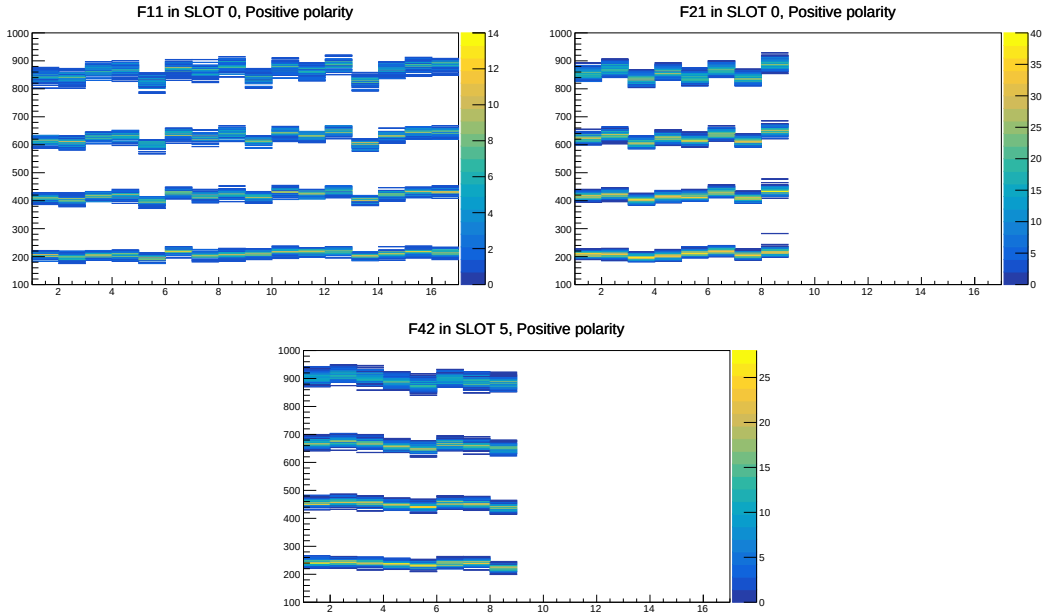

Figure 5.6: Injection charge just above four thresholds for FEERIC11, FEERIC21 and FEERIC42 tested on positive polarity.

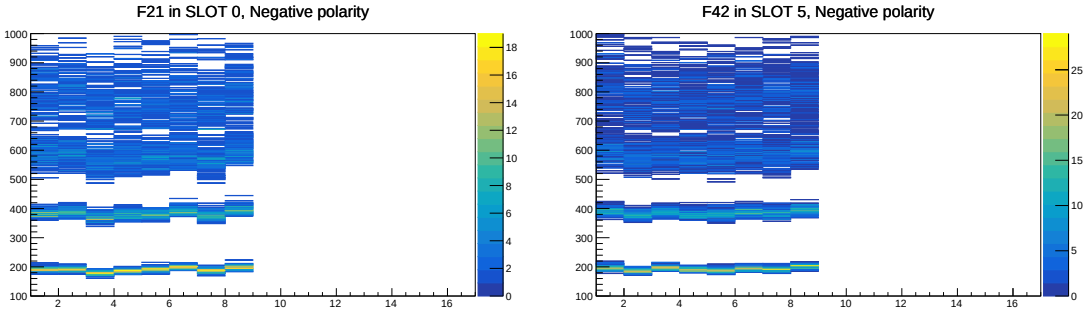

Figure 5.7: Injection charge just above four thresholds for FEERIC21 and FEERIC42 tested on negative polarity.

Most interestingly, we have also studied the dependence of the charge above threshold vs. the card polarity. Cards of 2 cm and 4 cm were tested on positive and negative polarity (Fig.5.6 and 5.7).

In following figures (Fig.5.8 - 5.11) we present average injected charge per channel for different card formats. Here, the central values represent the average charge per channel and the vertical error bars represent the corresponding dispersions.
The tests performed on negative polarity (Fig. 5.11) for FEERIC21, FEERIC22 and FEERIC42 show a similar trend as the test performed on the positive polarity (Fig.5.9 and 5.10). However, we observe the dispersions of the injected charge per channel just above thresholds of 600 fC and 800 fC are larger than the one in positive polarity.
To conclude our measurement of charge injection per channel, we presented the injected charge just above the four thresholds as a function of the FEERIC channels. They show similar trends for different format of cards. The dispersion of the charge increases with increasing threshold.

We observe no significant difference in the values of average charge above the thresholds

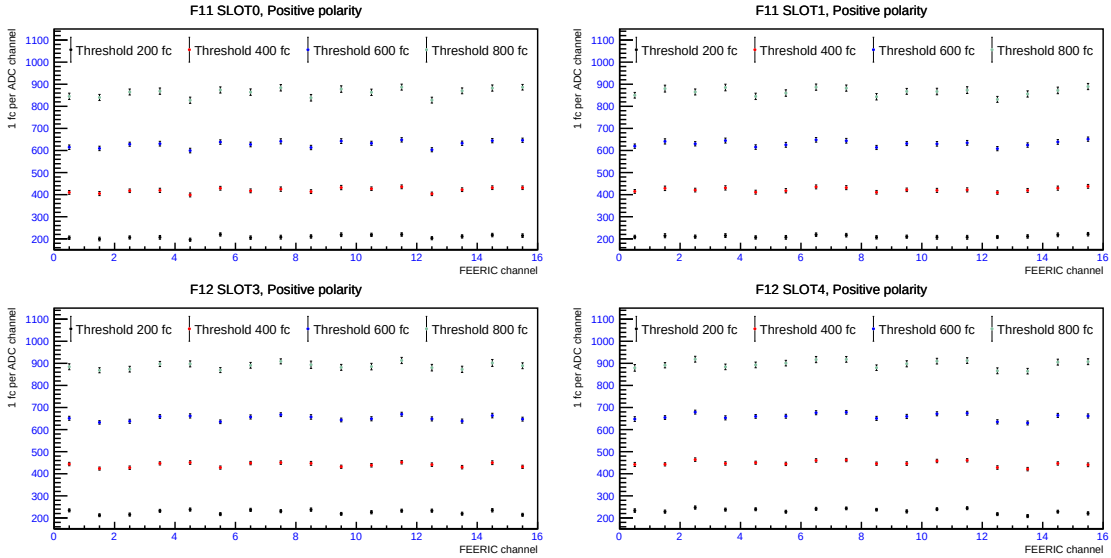

Figure 5.8: Average charge injection at four different thresholds for FEERIC11 cards on positive polarity.

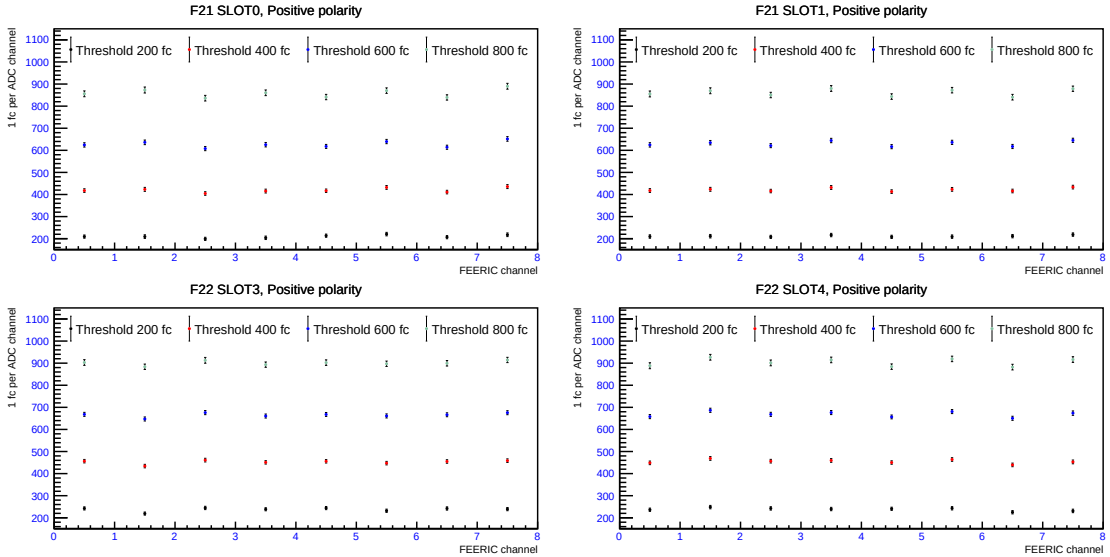

Figure 5.9: Average charge injection at four different thresholds for FEERIC21 cards on positive polarity.

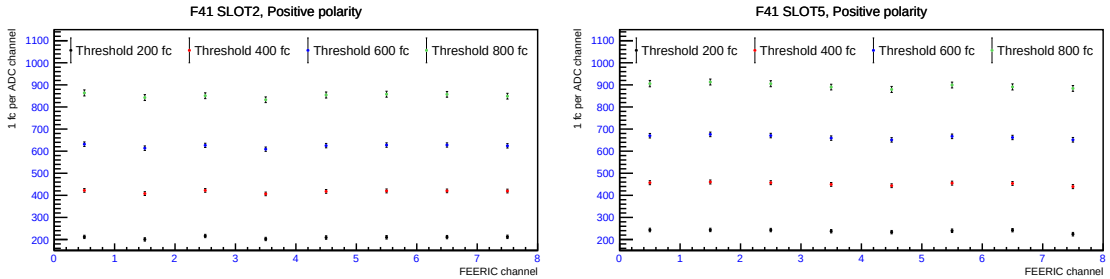

Figure 5.10: Average charge injection at four different thresholds for FEERIC41 cards on positive polarity.

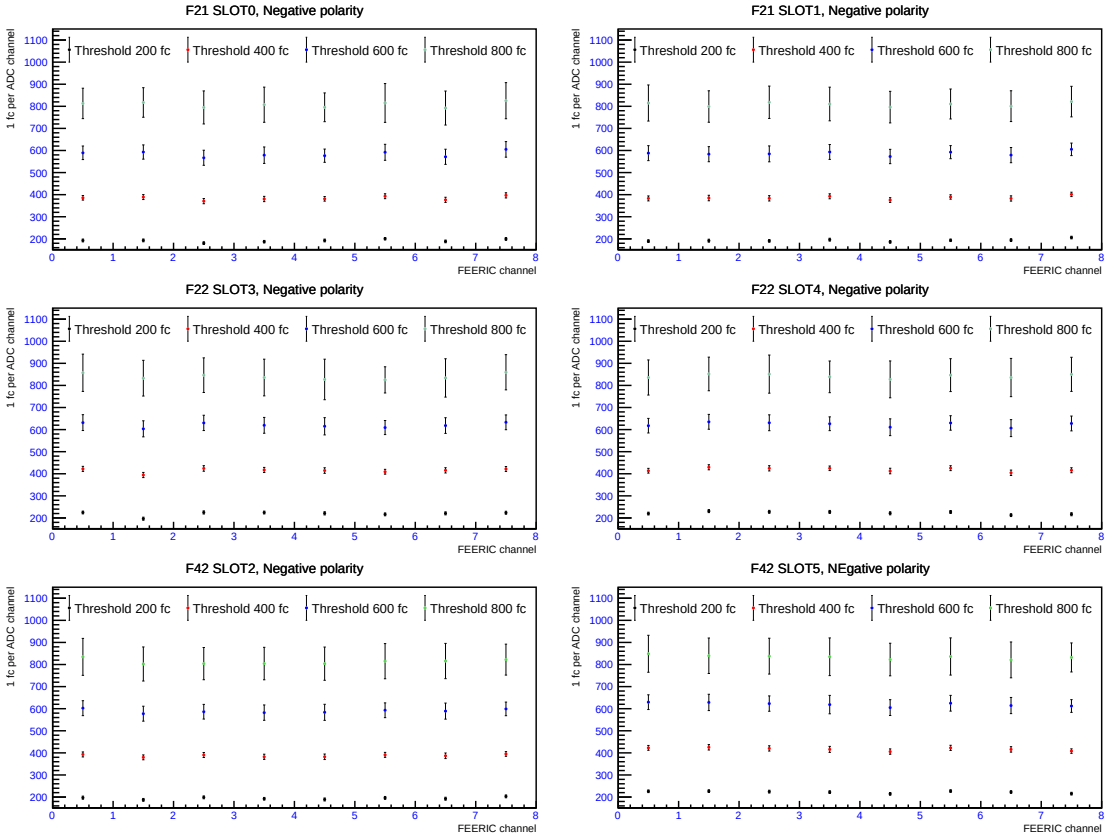

Figure 5.11: Average charge injection at four different thresholds for FEERIC21, FEERIC22 and FEERIC42 cards on negative polarity.

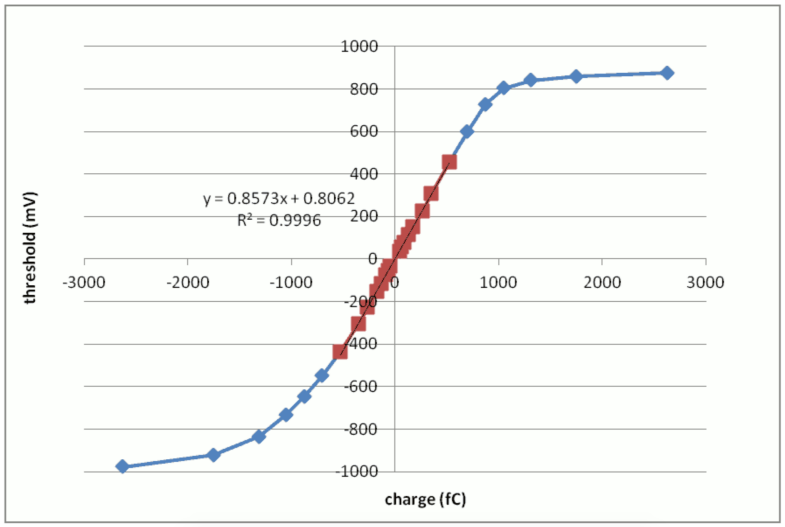

Figure 5.12: Threshold versus charge

for the cards tested in different polarity. The dispersion in the higher thresholds for negative polarity is however much larger than in positive polarity. The larger dispersion on negative polarity can be attributed to the PMOS input transistors of the amplifier and comparators (for more detail see [124])

Fig. 5.12 is taken from [124]. It represents the threshold as a function of charge. We

observe a linear region (from − ∼400 mV to + ∼ 400 mV) with a slope (called the gain) of 0.86 mV/fC and outside this region a non-linear evolution to saturation. In positive configuration, the response is linear for charge below 800 fC and the transition threshold saturates at 880 mV. In negative configuration, the linear zone extends to -1 pC and is followed by a slower transition to saturation to a threshold of -1 V. The saturation of the system is noticed around 1 pC for positive input signals and -1.5 pC for negative input signals. This asymmetric behavior results from the architecture of the comparator. During normal operation, the threshold will always be in the linear region ∼100 fC.

5.3 Measurement of response time

The response time is defined as the delay between the input and the output pulse of FEERIC. In this section we will present the measurement of time response for different card formats of positive polarity. Fig. 5.13 shows the response time (in TDC channels) for each FEERIC channel of FEERIC11 cards. The dispersion is the RMS of the projection of each channel as explained for the injection charge measurement. The response time can be converted into normal time unit (ns) using Eq. 5.1.

$$T_{response} = N_{channel} \times 0.170ns \tag{5.1}$$

where,
$T_{response}$ is the response time in ns and $N_{channel}$ is the number of TDC channels.

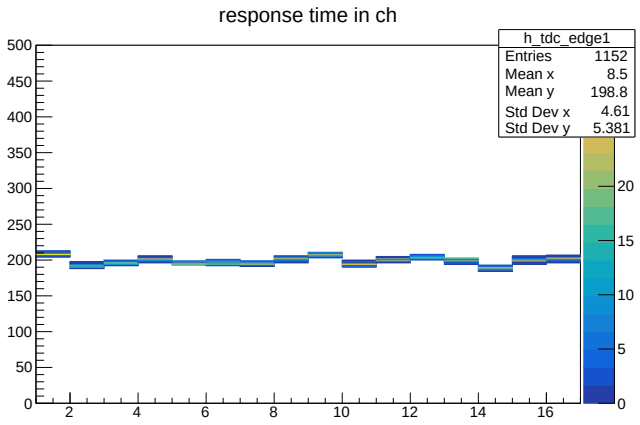

Figure 5.13: Response time per channel of FEERIC11. Here the time response is shown in TDC channels.

After the conversion to normal time unit, we studied the average time response per FEERIC channel for different formats of FEERIC cards. Fig. 5.14 shows the measured average response time (in ns) per FEERIC channel for all 6 formats of cards. We observed that the response time has slot dependence which means different values are observed for same card on different slots. This difference is partly due to the different PCB trace path lengths from the slot to the output of the test bench. In other word, the response time need to be corrected from an offset, for each channel of the test bench.

To encounter this discrepancy we have subtracted an offset which is obtained from the time response measured by mean of an oscilloscope (Table. 5.3) which gives access to an absolute calibration of the time response. We can formulate our absolute time response by

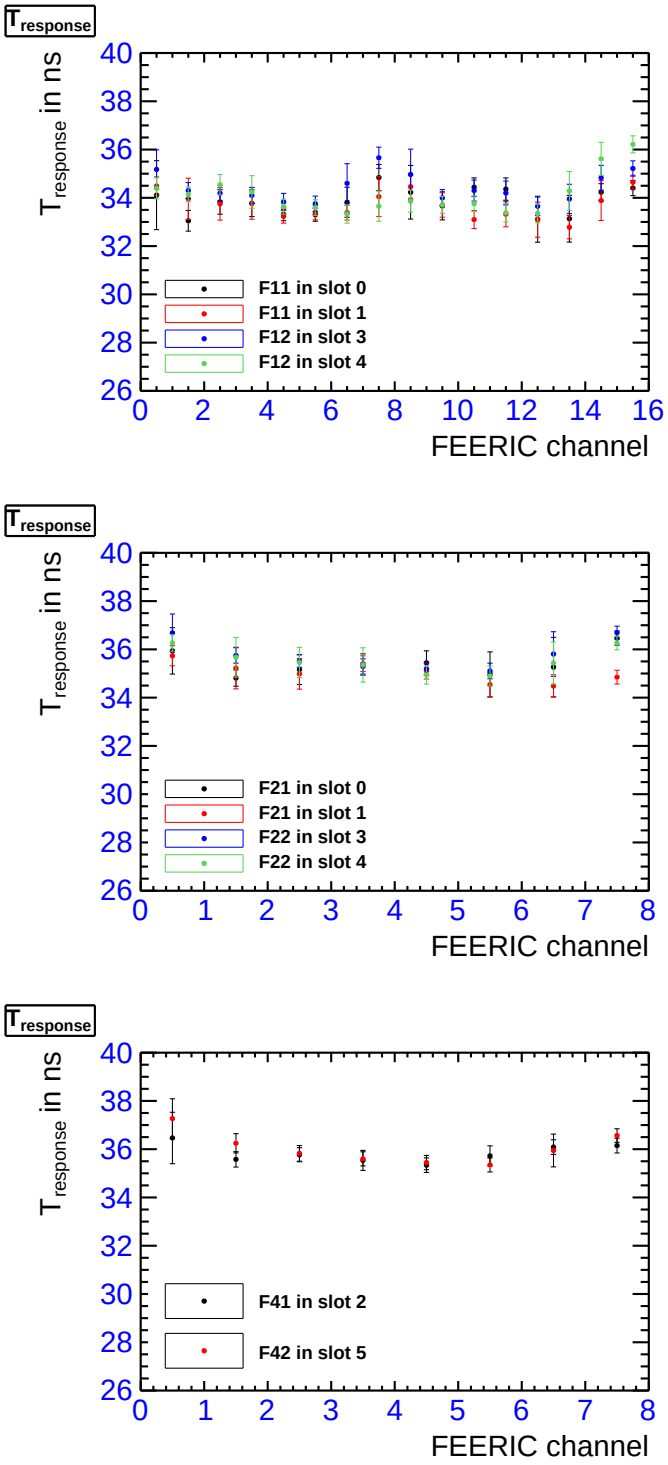

Figure 5.14: The average response time per FEERIC channel for FEERIC11, FEERIC12, FEERIC21, FEERIC22, FEERIC41 and FEERIC42 before applying any offset for calibration.

$$T^{abs}_{response} = T_{response} - Offset \tag{5.2}$$

Channels	F11 POS	F12 POS	F21 POS	F22 POS	F41 POS	F42 POS	F21 NEG	F22 NEG	F41 NEG	F42 NEG
01	18.88	19.01	20.05	20.34	20.88	21.12	20.32	20.4	20.87	21.05
02	18.82	19.03	20	20.32	20.87	20.92	20.26	20.27	20.81	20.95
03	18.76	18.99	19.96	20.34	20.78	20.88	20.22	20.32	20.79	20.88
04	18.78	18.93	19.87	20.21	20.72	20.81	20.09	20.17	20.73	20.74
05	18.70	18.90	19.89	20.15	20.71	20.71	20.21	20.28	20.74	20.81
06	18.78	18.97	19.95	20.39	20.79	20.85	20.18	20.29	20.8	20.87
07	18.78	19.02	19.91	20.28	20.82	20.92	20.2	20.33	20.89	20.96
08	18.88	19.07	19.97	20.34	20.94	21.05	20.14	20.34	20.93	21.04
09	18.86	18.77								
10	18.90	18.77								
11	18.81	18.74								
12	18.80	18.69								
13	18.76	18.66								
14	18.84	18.74								
15	18.81	18.73								
16	18.99	18.80								

Table 5.3: The absolute time response values from the oscilloscope using the FEERIC cards from pre-series. Each value corresponds to the response time averaged values (per channel) over 10 cards.

Fig. 5.15 shows the absolute average time response (in ns) per FEERIC channel after the offset correction (which means that cards of the same format measured on different slots of the test bench can be merged). The trend is similar for the tested cards of the station 1 and 2. The average response time is homogeneous between the channels.

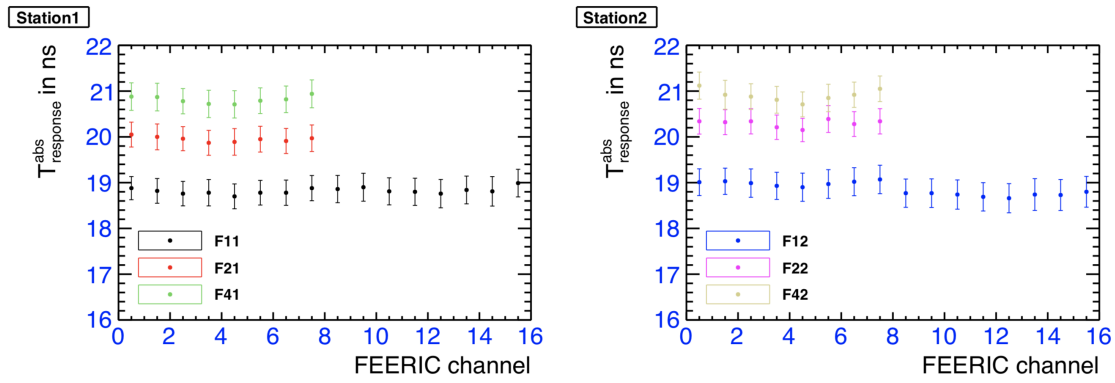

Figure 5.15: The absolute average response time per FEERIC channel for FEERIC11, FEERIC12, FEERIC21, FEERIC22, FEERIC41 and FEERIC42 (offset corrected).

We observe a dependence on strip width corresponding to different card formats. The response time decreases with strip width in station 1 and 2. The difference between card formats is related to the different PCB input trace length, which increases with the pitch. A similar trend was shown during production readiness review (see Fig. 5.16) with few prototype cards. This conclusion is however somehow biased by the the fact that the normalization (offset) is obtain from oscilloscope measurements of a sample of the production (the pre-series, 10 cards of each format) only.

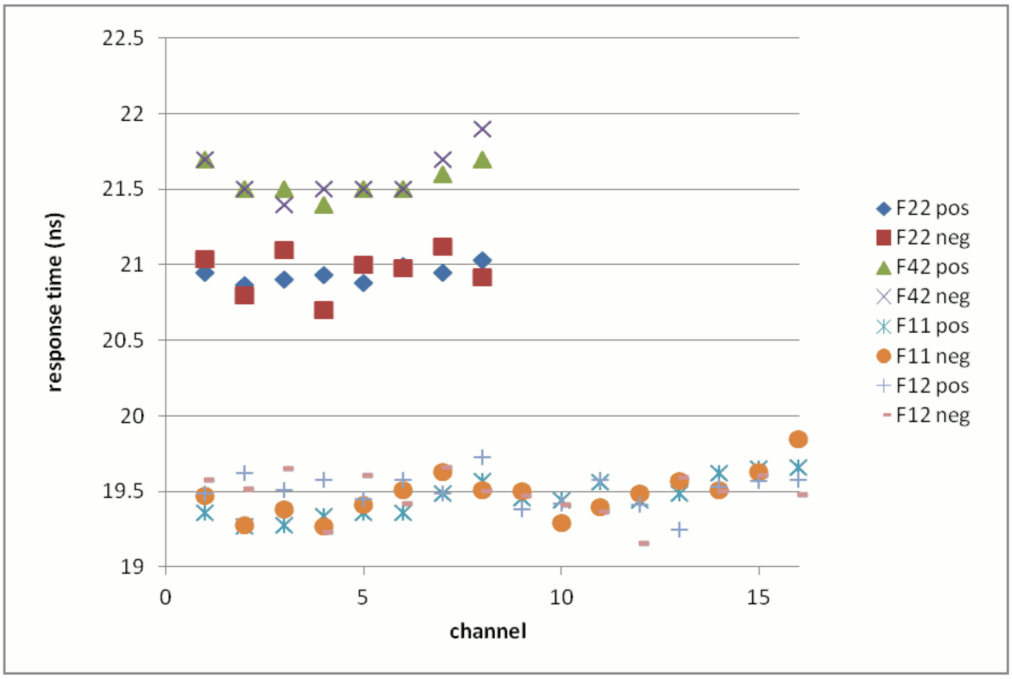

Figure 5.16: Response time for different strip pitches [124].

5.3.1 De-convolution of time response dispersion sources

We have also studied the dispersion sources of response time. While testing on the test bench there are dispersions in the time response introduced by the card itself, test bench and series of cards. We have performed our measurement for two samples:

- All series measurement
- Single card measurement

In all series measurement, cards of all format were tested only once for each card. The total dispersion, σ_{Total} can be defined as (Eq. 5.3).

$$\sigma^2_{Total} = \sigma^2_{Series} + \sigma^2_{TestBench} + \sigma^2_{SingleCard} \tag{5.3}$$

where σ_{Series} is the dispersion caused by series, $\sigma_{TestBench}$ is caused by the test bench itself and $\sigma_{SingleCard}$ is the dispersion from one single card.

The dispersion (σ_{Series}) coming from series measurement can be deduced from (Eq.5.3)

$$\sigma_{Series} = \sqrt{\sigma^2_{Total} - (\sigma^2_{TestBench} + \sigma^2_{SingleCard})} \tag{5.4}$$

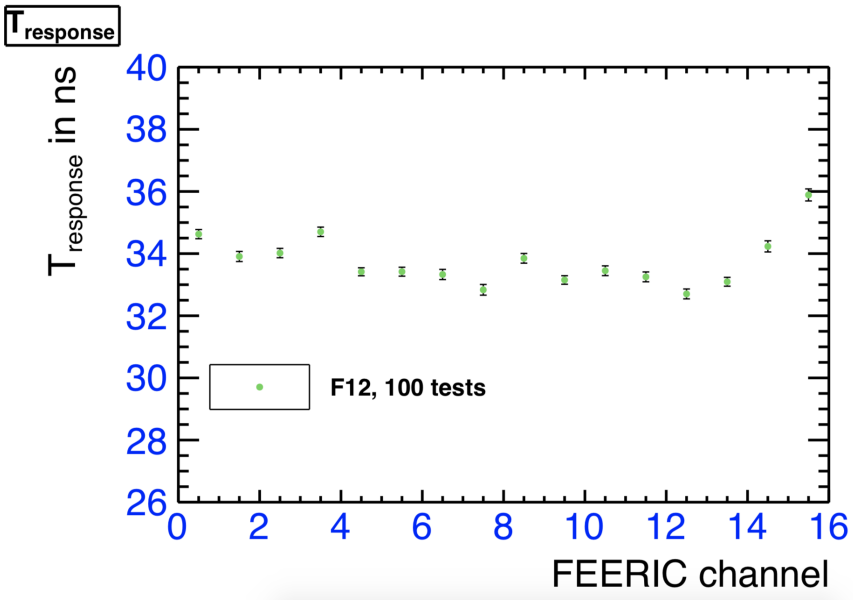

Figure 5.17: Response time for FEERIC12

The time measurement was performed 100 times for a single FEERIC12 card on the same slot. Fig. 5.17 shows the measured response time per FEERIC channel. From this measurement, we get the measured $\sqrt{\sigma^2_{TestBench} + \sigma^2_{SingleCard}}$ values and we already have the measured σ_{Total} values from the series measurement. Then we calculated the σ_{Series} values by using Eq.5.4.

Table. 5.4 shows the measured total dispersion, σ_{Total} in the first column and measured dispersion for a single card plus test bench $\sqrt{\sigma^2_{TestBench} + \sigma^2_{SingleCard}}$ is shown in second

FEERIC channel	σ_{Total}	$\sqrt{\sigma^2_{TestBench} + \sigma^2_{SingleCard}}$	σ_{Series}
01	0.291993	0.147607	0.251937
02	0.28696	0.162916	0.236230
03	0.309857	0.150544	0.270828
04	0.296515	0.151395	0.254952
05	0.30776	0.129066	0.279389
06	0.313836	0.143607	0.279052
07	0.305678	0.163722	0.258136
08	0.31098	0.172322	0.258870
09	0.309111	0.155613	0.267085
10	0.312518	0.137048	0.280865
11	0.319334	0.156953	0.278101
12	0.309839	0.158565	0.266190
13	0.318395	0.158848	0.275940
14	0.347197	0.142344	0.316676
15	0.338325	0.179356	0.286871
15	0.336145	0.193673	0.274744

Table 5.4: Dispersion from series, test bench and single card measurement

column. The third column shows the calculated dispersion, σ_{Series}. We observe that the total dispersion is dominated by the dispersion coming from series which was the aim of the measurement of the time dispersion.

Summary

The FEERIC cards are intended to be fully operational after the Long Shutdown 2 in order to process the analogue signals coming from the Resistive Plate Chamber detectors of the Muon IDentifier (MID). A description of these electronic cards and their components is first given. Then, the test bench for the tests and measurements of the FEERIC card production are presented, with a description of its structure, specifications, and a list of the parameters that this test bench is designed to control. The following sections consist in the description and the data analysis of two important parameters, the injected charge above threshold, for four threshold values and the response time. For both parameters, the values and dispersions are within the requirements for different types of FEERIC cards. For the response time, an additional analysis has been performed to de-convoluate the dispersion sources of response time. All the results obtained from these measurements confirms that the cards from the production series is in good agreement with the required specifications.

Chapter 6

Measurement of forward Υ production as a function of charged-particle multiplicity at mid-rapidity in pp collisions at $\sqrt{s}$ =13 TeV

The motivation behind this analysis is to study the dependence of Υ production on event activity which we discussed earlier in chapter 3. In this chapter, we will present the analysis of forward Υ production rate as a function of charged-particle multiplicity in pp collisions at $\sqrt{s} = 13$ TeV. The Υ are reconstructed with the ALICE Muon Spectrometer within the rapidity $2.5< y <4$. The charged-particle multiplicity are measured with the SPD tracklets within the pseudo-rapidity range $|\eta|<1$. We will start by explaining the methodology and the data sample analyzed for this analysis. Then we will explain the procedures to obtain the multiplicity bins (section 6.3), signal extraction of Υ yields in corresponding multiplicity bins (section 6.4) and the associated systematic uncertainties. Finally we will present the results which will be discussed in the next chapter.

6.1 Methodology

Our goal is to obtain the self-normalized Υ yields as a function of the relative charged-particle multiplicity $\mathrm{d}N_{\mathrm{ch}}/\mathrm{d}\eta/\langle \mathrm{d}N_{\mathrm{ch}}/\mathrm{d}\eta\rangle$. The first part of this measurement is to estimate the charged-particle multiplicity. The charge-particle multiplicity is the number of primary charged particles produced during the collision. The prompt particles produced during the collision, including all their decay products and excluding the strange particles from weak decays are defined as the primary charged-particles. The charged-particle distribution is divided into several multiplicity slices (i). The self-normalized charge-particle multiplicity $(\mathrm{d}N_{\mathrm{ch}}/\mathrm{d}\eta/\langle \mathrm{d}N_{\mathrm{ch}}/\mathrm{d}\eta\rangle)_i$ is calculated in each multiplicity slices.

In the second part of the measurement, we use the defined multiplicity slices to obtain the di-muon invariant mass spectra in each slices. Then we perform the signal extraction (explained in section 6.4.2) on the dimuon invariant mass spectra of raw Υ yields in each slices. Finally we obtain the self-normalized Υ yields, $\frac{dN_\Upsilon/dy}{\langle dN_\Upsilon/dy\rangle}$ for each multiplicity bin using Eq. 6.1.

$$\Upsilon_i^{rel} = \frac{\Upsilon_i}{\Upsilon_{tot}} = \frac{dN_\Upsilon/dy}{\langle dN_\Upsilon/dy\rangle} \tag{6.1}$$

Here, Υ_{tot} is the number of Υ yields in integrated sample, Υ_i is the number of Υ yields in the each multiplicity slice i.

The formulation of Eq. 6.1 will be discussed briefly in section 6.4. For this study we use self-normalized quantities. In proton-proton collisions acceptance times efficiency correc-

tions do not vary in multiplicity bins and thus this correction cancel in ratios for self-normalized quantities. So it is not considered in this thesis. In Pb-Pb collision system, the highest multiplicity reached is much higher than in pp system and acceptance times efficiency corrections are not constant anymore in multiplicity bins and thus would not cancel in ratios.

6.2 Data Sample and Event Selection

6.2.1 Data Sample

This work is based on LHC 16 data for pp collisions in $\sqrt{s} = 13$ TeV. We have already introduced all the applied triggers in Tab. 4.2. The full data sample consists of five periods (h, j, k, o and p), 103 M CMUL7 events and 29 M CINT7 events.

6.2.2 Event selection

6.2.2.1 Pile-up rejection

In high luminosity colliders, there is a non-negligible probability that one single bunch crossing may produce several separate events, so-called pile-up events. In the ALICE experiment, a significant number of pile up events is expected. It is because of the detector read-out time ($\sim$ 100 ns) which is larger than time bin between two pp interactions in a pile up event. In fact, these two pp interactions are expected to be almost simultaneous if they belong to the same bunch crossing. The two pp interactions are separated by a time bin multiple of $\sim$ 25 ns if they belong to different ones[1].

In this work the pile-up events were rejected using ALICE Physics Selection (APS) framework. This framework uses predefined cuts to remove pile-up events. These cuts have been tuned for each period individually and are applied on SPD selection criteria and V0 timing. In following paragraphs we will explain these cuts and their effects[2] individually:

i **Past-Future protection:** This allows to reject an event at the physics selection level if another collision happens in a given time window before and/or after the trigger. This out-of-bunch pileup cut is based on V0 past-future info which includes two correlations. One is the correlation between online trigger charge integrated over 25 ns and offline trigger charge integrated over longer time V0M (Fig. 6.1). It shows the events before (left) and after (right) pile-up removal using the correlation of online-vs-offline V0M.

The other one is the online-vs-offline SPD Fast-OR correlation between online (integrated over 100 ns) and offline (integrated over 300 ns) shown in Fig.6.2. It shows the events before (left) and after (right) pile-up removal using the correlation of online-vs-offline SPD clusters.

ii **Multiple vertices with SPD:** The APS runs an algorithm to reconstruct the in-bunch pile-up in the SPD. The function identifies the main vertex in the SPD in a single event and loops over all secondary vertices in the same event. If a

[1] 25 ns is the time bin between two subsequent bunch crossings

[2] The effect of each cuts shown individually in Fig. 6.1, 6.2, 6.3,6.4 and 6.5 where the full 2016 data sample is used.

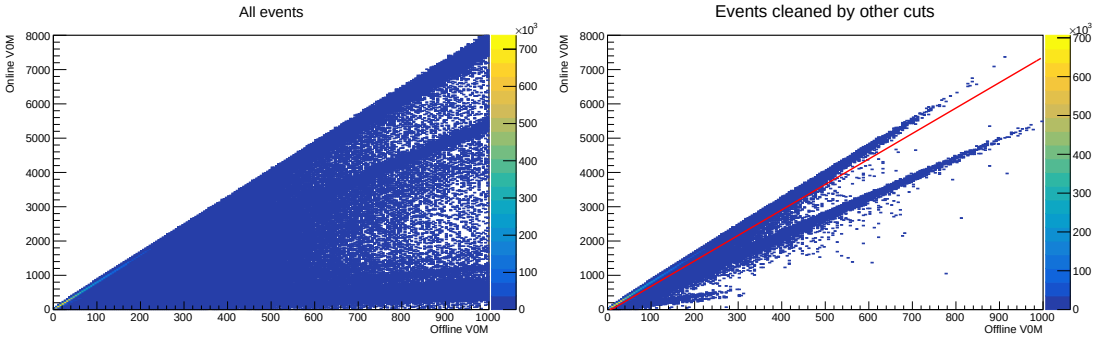

Figure 6.1: Correlation of online and offline information in the V0

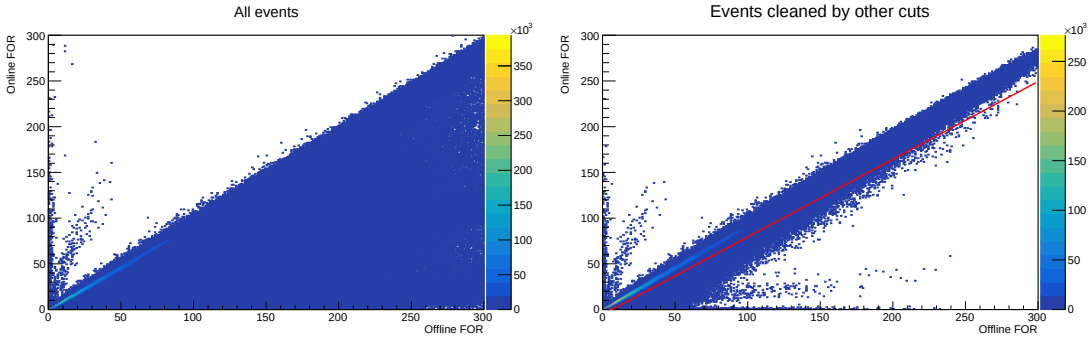

Figure 6.2: Correlation of online and offline information in the SPD

secondary vertex has more than a given number of contributing tracklets $N_{contributor}$ and the distance between the primary and the secondary vertex is longer than a given threshold value d[3], the event is rejected as pile-up. The parameters used for this cut is $N_{contributor} > 5$ and d= 0.8 cm. Fig. 6.3 shows the number of events before and after this cut.

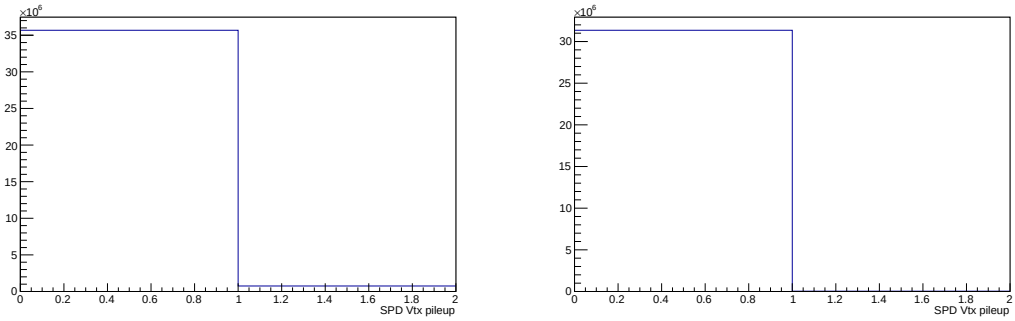

Figure 6.3: Effects due to multiple vertices cut. The left panel shows the events before using any cuts where there are some events with d $>$ 0.8. After using this cut a small fraction of events is removed (right panel)

iii **Correlation between multiplicity estimators and detector clusters:** Events with out-of-bunch pileup can be identified and rejected exploiting the fact that the event multiplicity (or centrality) estimated from the signals measured with detec-

[3]d = Minimum distance (in cm) along z-direction between the main and candidate pileup vertices

tors with different readout times are affected differently by out-of-bunch pileup. Fig. 6.4 and Fig. 6.5 shows the correlation of V0 multiplicity-SPD tracklets and SPD clusters-SPD tracklets respectively.

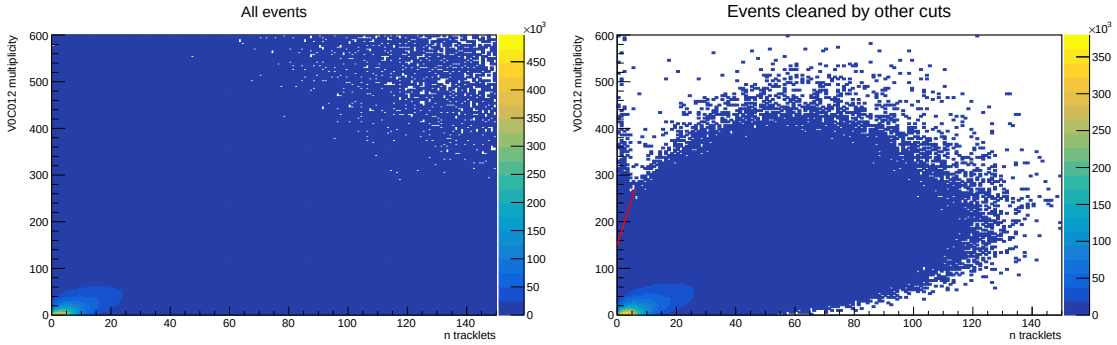

Figure 6.4: Correlation of V0 clusters with SPD tracklets

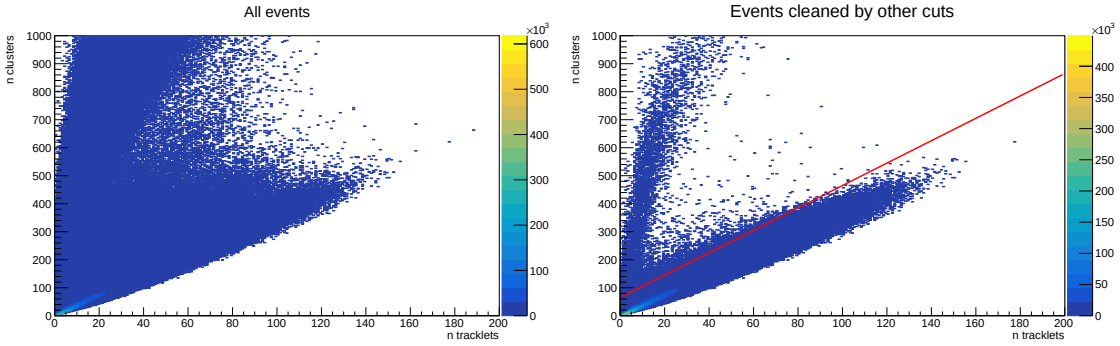

Figure 6.5: Pile-up due to the correlation between SPD clusters and tracklets. On left the figure is before pile-up removal and on right figure is after pile-up removal.

Finally the effect of APS is shown in Fig.6.6. In Fig.6.6, the left column top plot shows the SPD tracklets distribution before pile-up removal where we observe some events having very high number of tracklets. The left column bottom plot shows the SPD tracklets distribution after pile-up removal using APS. Similarly the right column top and bottom plot show the distribution for CINT7 trigger before and after pile-up removal. The disappearance of the long tail at high number of tracklets is observed after pileup rejection for both CMUL7 and CINT7 trigger. Note that the right column shows the effect when all the cuts discussed earlier are applied.

6.2.2.2 SPD vertex selection

The multiplicity determination requires events with good reconstructed vertex from the SPD. The following vertex based criteria were imposed for the event selection. These criteria are called vertex Quality Assurance (vertex QA).

1. $N_{\text{contributors}} > 0$: The selected events are required to have a reconstructed primary vertex with at least one primary vertex contributor. $N_{\text{contributors}} <= 0$ correspond to events where the vertex finding algorithm fails due to absence of SPD clusters

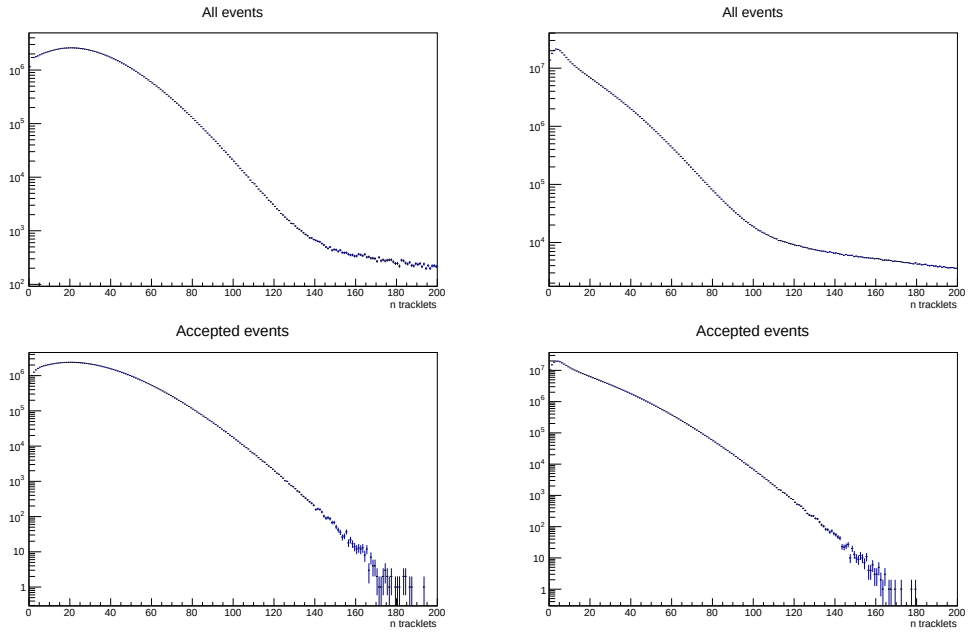

Figure 6.6: SPD tracklet distribution for CMUL7 trigger (left col.) and CINT7 trigger (right col.) before and after pile-up removal using APS.

or unavailability to build suitable tracklets. This cut ensures that only events with good vertexes are accepted.

2. $\sigma(v_z^{\mathrm{SPD}}) < 0.25$ cm: The resolution of the z-coordinate of the SPD vertex must be lower than 0.25 cm. This cut is applied for events with a vertex reconstructed by 1D-vertexer. Since the vertex resolution of 1D-vertexer is worst than that of 3D-vertexer (explained in section 4.3.2), it is necessary to require a resolution better than 0.25 cm.

3. $|v_z|< 10$ cm: The selected events are required to have a SPD vertex reconstructed within $|v_z|< 10$ cm. The vertex must be reconstructed within a distance $|v_z|< 10$ cm from the nominal interaction point (IP) to assure proper reconstruction of tracklets taken into account in this study. Fig. 6.7 represents the z-vertex distribution of SPD.

Table 6.1 shows the number of events passed through each criteria consecutively after the pile-up rejection.

Events selection criteria	Accepted CMUL events (%)	Accepted CINT7 events (%)
All Event	118.98 M	36.43 M
All Event (+ APS)	106.99 M (89.9%)	31.35 M (86.1%)
+ $N_{\mathrm{contributors}} > 0$	105.42 M (88.6%)	30.59 M (83.9%)
+ $\sigma(v_z^{\mathrm{SPD}}) < 0.25$ cm	103.88 M (87.3%)	29.86 M (81.9%)
+ $|v_z|< 10$ cm	103.05 M (86.6%)	29.32 M (80.5%)

Table 6.1: Number of events passing each selection criteria.

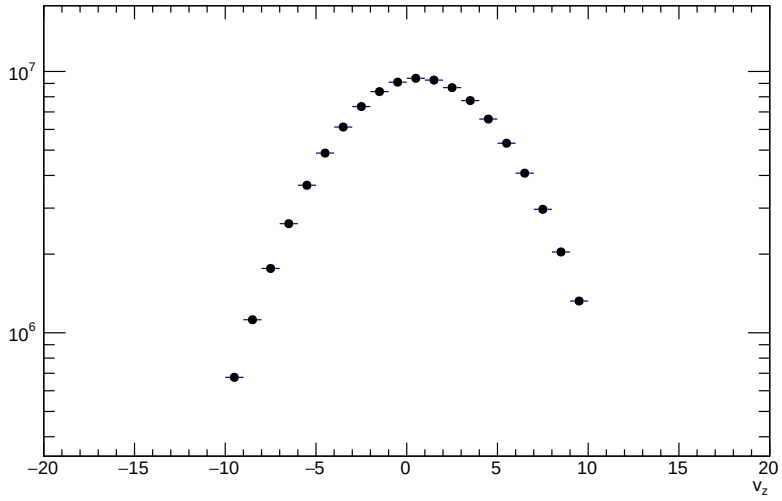

Figure 6.7: SPD z-vertex distribution when selecting the events within $|v_z|<$ 10 cm.

6.3 Charged-particle multiplicity determination

In this section we will focus on the measurement of the pseudo-rapidity density of charged particles $\mathrm{d}N_{\mathrm{ch}}/\mathrm{d}\eta$, the average number of primary charged particles produced in an η range. The primary goal of this analysis is to obtain a multiplicity estimator to classify the events in different multiplicity bins. Different steps to obtain the pseudo-rapidity density of charged particles $\mathrm{d}N_{\mathrm{ch}}/\mathrm{d}\eta$ are:

1. The choice of SPD tracklets (section 4.3.2) as a multiplicity estimator
2. Correction of SPD inefficiency by applying the data-driven correction
3. Charged-particle multiplicity estimation from SPD tracklets
4. Estimation of systematic uncertainties on charged-particle multiplicity

6.3.1 SPD tracklet as a multiplicity estimator

We used the SPD tracklets (N_{trk}) which are counted at mid-rapidity ($|\eta|<1$) as our multiplicity estimator. Fig. 6.8 represents the SPD tracklets as a function of z-vertex and η before any selection is applied. In order to get a reasonable SPD acceptance, we restrict our analysis with $|v_z|<$ 10 cm where tracklet reconstruction is most efficient. We also apply a selection in $|\eta|<1$ for the tracklets individually. The black dashed lines in Fig. 6.8 represents the boundaries concerning the v_z and η. All the figures will be shown in further correspond to the whole 2016 data sample except for the figures quoted with different samples.
During data taking periods the SPD acceptance may vary due to dead or noisy modules which affects the tracklet information. In order to estimate the number of charged particles, this effect needs to be corrected. Fig. 6.9 shows an example of the active and dead SPD modules in the inner and outer layers of the SPD during one run of 2016 data taking. The empty blocks represents the dead modules during the data taking. For this analysis we considered the runs which have similar SPD map (Fig. 6.9) to have an uniform SPD status for the whole sample. By selecting one SPD map, we removed some runs, resulting

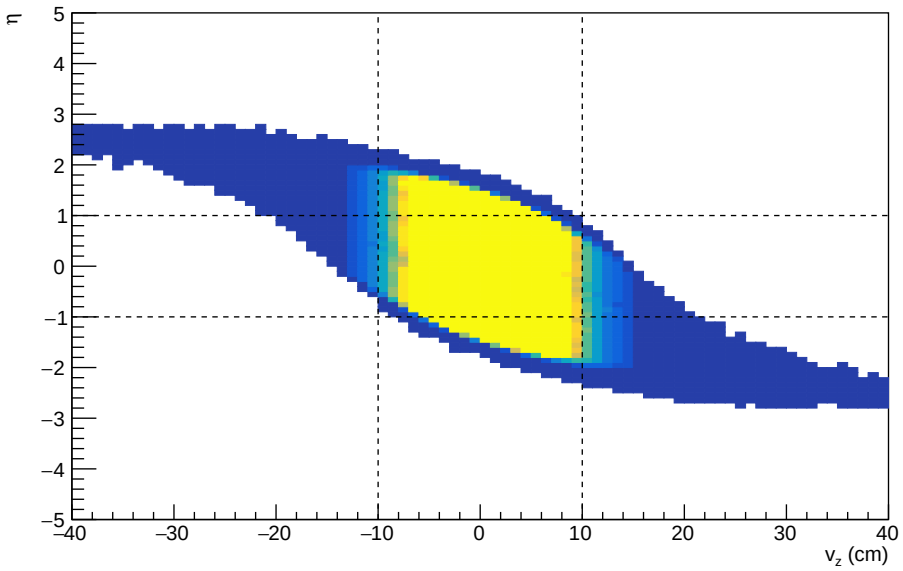

Figure 6.8: SPD tracklets in η-v_z plane.

in a reduction of the statistics by less than $\sim 1\%$. The number of events shown in Table. 6.1 is counted after this selection.

Fig. 6.10 shows the average reconstructed number of tracklets as a function of z_v within the z_v, η ranges for the whole 2016 sample. The average number of tracklets is low along the edges of the z-coordinate reflecting the drop of SPD efficiency for the corresponding modules.

To convert the SPD tracklets into charged particles, the SPD tracklets should be corrected from inefficiency. In the following section we will explain the correction procedure.

6.3.2 Data-driven correction method

The data-driven correction method [126] is based on the use of average number of SPD reconstructed tracklets ($N_{\rm trk}^{\rm raw}$) as a function of the z-vertex. The principle of this correction is to equalize the SPD efficiency along the z-vertex direction. The correction relies on the average tracklet distribution as a function of z-vertex (Fig. 6.10) where the tracklets were counted within the detector acceptance. The physical properties of the events do not change depending on the position of reconstruction within the same detector acceptance region. So we should see a flat distribution of average tracklet versus z-vertex if the detector efficiency was homogeneous. But we observe a non-flat trend because of the SPD dead modules resulting in the inefficiencies and losses of acceptance.

The data-driven correction is a 1D $A \times \epsilon$ correction based on data. According to this correction method we used Eq. 6.2 where $N_{\rm trk}^{\rm cor}$ is obtained by adding or subtracting missing tracklets randomized by a poisson generator. The number of missing tracklets (ΔN) is computed using Eq. 6.3 with $\langle N_{\rm trk}^{\rm raw} \rangle (v_z^0)$, a chosen reference[4] at a specific z-vertex position (v_z^0).

[4]The chosen reference is either at the maximum or minimum value of the $\langle N_{\rm trk}^{\rm raw} \rangle$ distribution (Fig. 6.11).

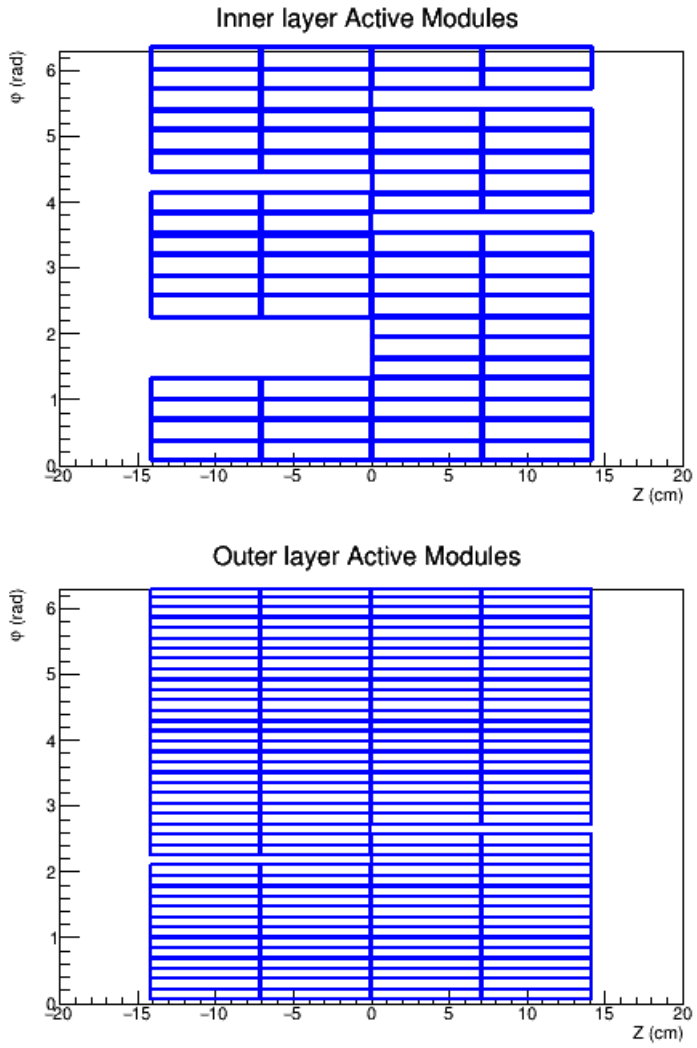

Figure 6.9: Active and inactive SPD modules during the run number 254419 of 2016 data taking

$$N_{\rm trk}^{\rm cor} = N_{\rm trk}^{\rm raw}(v_{\rm z}) \pm \Delta N_{\rm rand} \tag{6.2}$$

$$\Delta N = N_{\rm trk}^{\rm raw}(v_z)\frac{\langle N_{\rm trk}^{\rm raw}\rangle(v_z^0) - \langle N_{\rm trk}^{\rm raw}\rangle(v_z)}{\langle N_{\rm trk}^{\rm raw}\rangle(v_z)} \tag{6.3}$$

Correcting low multiplicity events with respect to the minimum of $\langle N_{\rm trk}^{\rm raw}\rangle$ with Eq.6.2 can result in creation of corrected events with non-physical properties. According to this method, the ΔN value will always be less than zero which can give us negative $N_{\rm trk}^{\rm cor}$ depending on the $N_{\rm trk}^{\rm raw}$ in the event, while correcting with minimum a reference. As we can not have negative tracklets, another correction was proposed using a binomial random generator. Here, the binomial distribution ranges between 0 and $N_{\rm trk}^{\rm raw}$ which prevents to obtain any negative value of corrected tracklets, $N_{\rm trk}^{\rm cor}$.

$$N_{\rm trk}^{\rm cor} = gRandom \longrightarrow Binomial(N_{\rm trk}^{\rm raw}(v_{\rm z}), \frac{\langle N_{\rm trk}^{\rm raw}\rangle(v_z^0)}{\langle N_{\rm trk}^{\rm raw}\rangle(v_z)}) \tag{6.4}$$

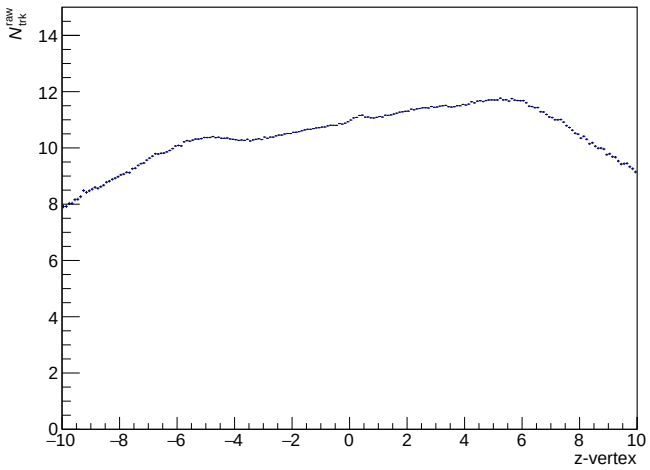

Figure 6.10: Event averaged number of tracklets $\langle N_{\rm trk} \rangle$ as a function of z-coordinate of the SPD vertex.

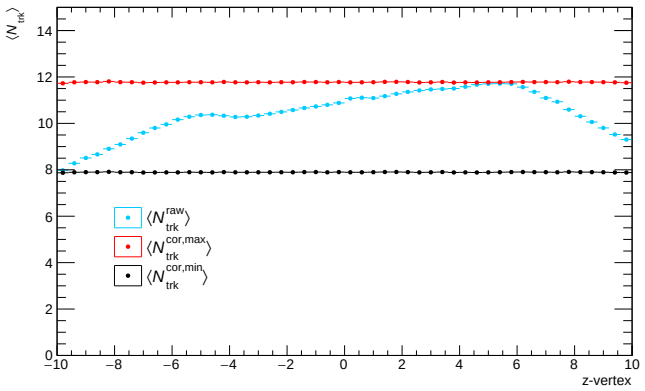

Figure 6.11: $\langle N_{\rm trk}^{\rm raw} \rangle$, $\langle N_{\rm trk}^{\rm cor,max/min} \rangle$ as a function of z-vertex.

Fig. 6.11 represents an example plot showing the average raw and corrected (to maximum/minimum) traklets as a function of z-vertex. The light blue distribution is the raw distribution. The red (or black) distribution is corrected using maximum (or minimum) value from raw distribution as an input of the data driven correction. After the correction the distribution becomes flat.

Fig. 6.12 shows the effect of data driven correction in the tracklet distribution. We observe a widening of the tracklet distribution when correcting with maximum and the opposite for the correction with minimum. The data-driven correction can be done using both references (maximum and minimum).

We chose to use the maximum as our reference and verified that normalizing to the minimum does not lead to any significant difference.

6.3.2.1 Choice of the reference distribution

The SPD inefficiency can be different for different triggers fired in the same event. In our case we studied the average $N_{\rm trk}^{\rm raw}$ versus z-vertex distribution for CMUL7 and CINT7

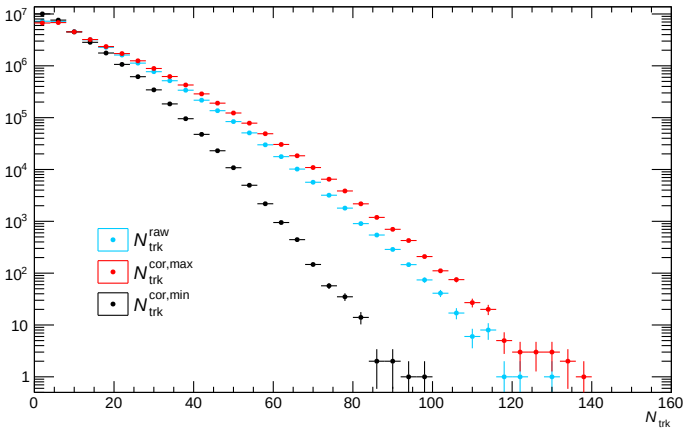

Figure 6.12: The tracklet distribution before and after applying the data-driven correction. The blue is the raw distribution, the red one is the corrected distribution with respect to maximum and the black one represents the corrected distribution with respect to minimum.

triggers. Fig. 6.13 shows the ratio of CMUL7 profiles over CINT7 profile with full 2016 statistics before correction. The ratio is not completely flat and the difference is due to bias of the di-muon trigger. This is possibly due to the decay probability of pions and kaons into muons before the absorber of the muon spectrometer which affects the di-muon trigger events.

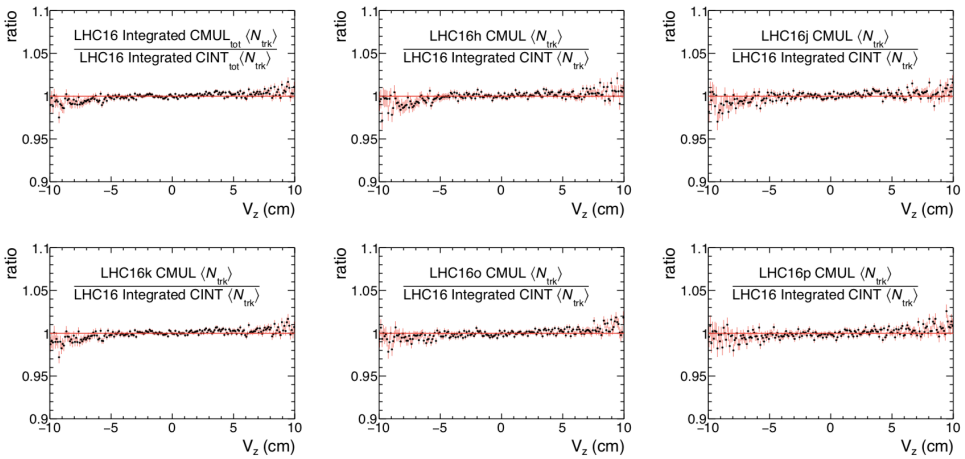

Figure 6.13: TProfile ratio of CMUL7 per period to CINT7 integrated

On the other hand, Fig. 6.14 presents the ratio of CINT7 per analyzed periods over CINT7 integrated profile before correction. It shows a flat distribution for all the periods with some statistical fluctuations.

As our multiplicity estimation is dependent on the CINT7 (or MB) trigger, we chose the MB distribution as an input for the data-driven correction. In order to optimize our choice of the reference distribution for data driven correction, we used the integrated sample from CINT7 trigger for the whole data sample. This allows us to use same multiplicity slicing for the whole sample.

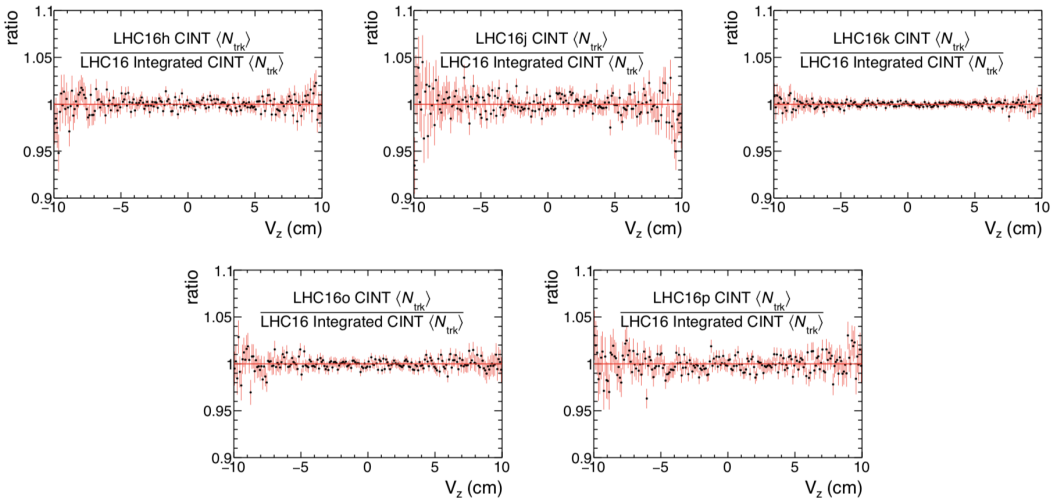

Figure 6.14: TProfile ratio of CINT7 per period to CINT7 integrated

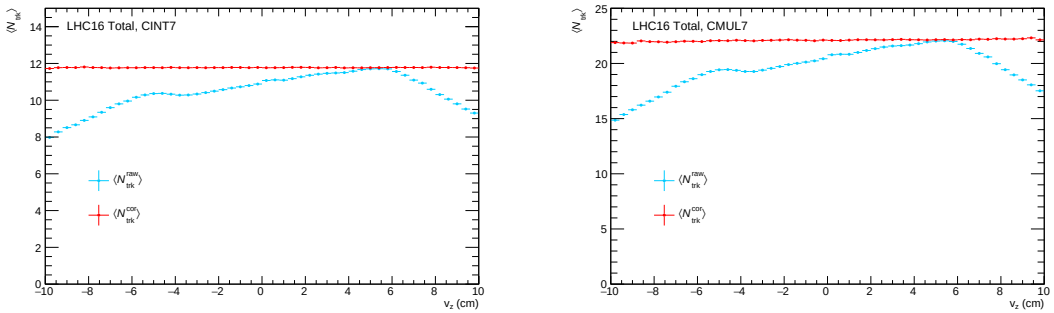

Figure 6.15: CINT7 and CMUL7 $\langle N_{\mathrm{trk}} \rangle$ as a function of (z-vertex) in the integrated sample.

The equalization procedure flattens the distribution to the maximum average tracklet shown in Fig. 6.15. Fig. 6.15 presents $\langle N_{\mathrm{trk}} \rangle$ as a function of z-vertex for CMUL7 and CINT7, the raw distribution in light blue and the corrected distribution in red (with maximum reference) for all the 2016 integrated sample. The correction is performed for all the periods separately using the same profile as well as the reference value.

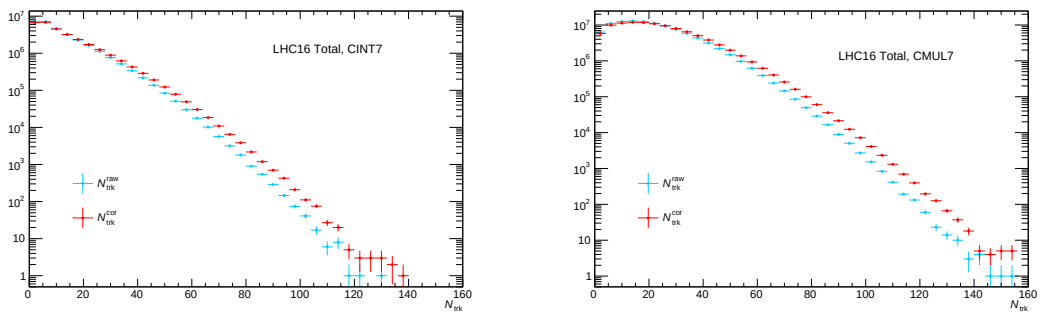

Figure 6.16: CINT7 and CMUL7 $N_{\mathrm{trk}}^{\mathrm{raw}}$ and $N_{\mathrm{trk}}^{\mathrm{cor}}$ distribution in the integrated sample

In our further analysis the combined (LHC 16h + 16j + 16k + 16o +16p) sample is used. Fig. 6.16 presents the $N_{\rm trk}$ distribution before (blue) and after (red) correction for CMUL7 and CINT7. After correction, the tracklet distribution is shifted to higher multiplicities. We can see that the events with small number of tracklets is lower after correction and the events having large number of tracklets are higher after correction than in the raw tracklet distribution. This is due to the data driven correction which re-distributes the events from lower to higher multiplicity events.

6.3.2.2 Comparison between data and MC

To study the correlation between the corrected tracklets and charged-particle multiplicity we rely on the MC simulations. In ALICE two sets of MC simulation are produced for pp 13 TeV 2016 data sample. One is produced using PYTHIA MC event generator [77] and the other one is produced using EPOS MC event generator [127]. Table. 6.2 shows the MC event generators for corresponding data periods used in this analysis.

MC periods	MC generator	Anchored to
LHC17f5	PYTHIA8	LHC16h
LHC17e5	PYTHIA8	LHC16j
LHC17d20a1	PYTHIA8	LHC16k
LHC17d16	PYTHIA8	LHC16o
LHC17d18	PYTHIA8	LHC16p
LHC17d20a2	EPOS-LHC	LHC16k

Table 6.2: MC production used for this analysis

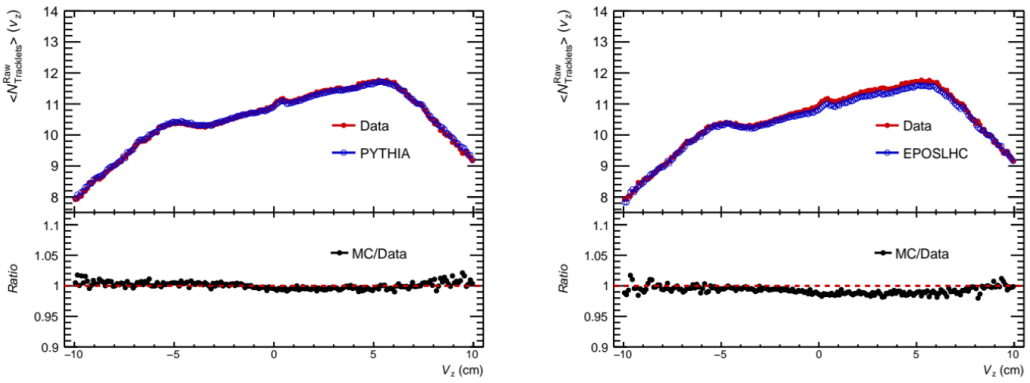

Figure 6.17: The comparison of average raw tracklets as a function of z-vertex distributions between data and MC (PYTHIA, EPOS).

The average reconstructed raw tracklets as a function of v_z (in Fig. 6.17) shows similar trend in data and MC simulations from PYTHIA and EPOS. There are small differences between the tracklets and z-vertex distributions. To consider these differences, the data-driven correction is applied to MC using the data profile and reference value. It allows us to have the same multiplicity bins both in data and MC. We have also used MC profile as an input for the data-driven correction on MC sample to estimate the systematic uncertainty.

6.3.2.3 Data-driven correction in MC

We used the same procedure to apply the inefficiency correction in MC as described in section 6.3.2. We have used data profile and it's reference value to obtain the $\langle N_{\rm trk}^{\rm cor}\rangle$ in MC. Only after that we are able to compare the multiplicity distribution in data and MC. Fig. 6.18 shows two example plots with the $\langle N_{\rm trk}^{\rm raw}\rangle$, $\langle N_{\rm trk}^{\rm cor}\rangle$ and $\langle N_{\rm ch}\rangle$ as a function of z-vertex for PYTHIA (left) and EPOS (right) MC sample.

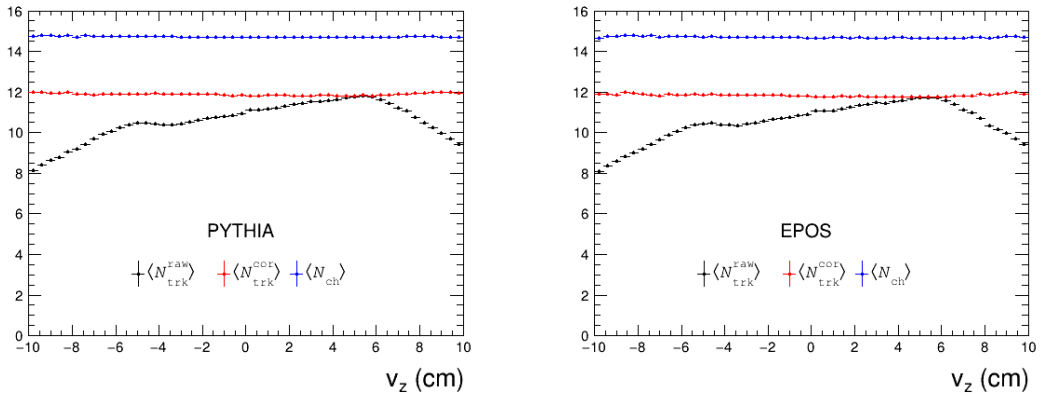

Figure 6.18: The average number of raw tracklets $\langle N_{\rm trk}^{\rm raw}\rangle$, corrected tracklets $\langle N_{\rm trk}^{\rm cor}\rangle$ and charged particles $\langle N_{\rm ch}\rangle$ versus z-vertex distributions.

Fig. 6.19 shows the comparison of raw, corrected tracklet distributions and the charged particle distribution from PYTHIA (left) and EPOS (right) event generations. Note that in low multiplicity events, $N_{\rm ch}$ is lower than $N_{\rm trk}{}^{raw/cor}$ because the probability to produce events with small number of charged particles is lower than the probability to produce events with small number of tracklets.

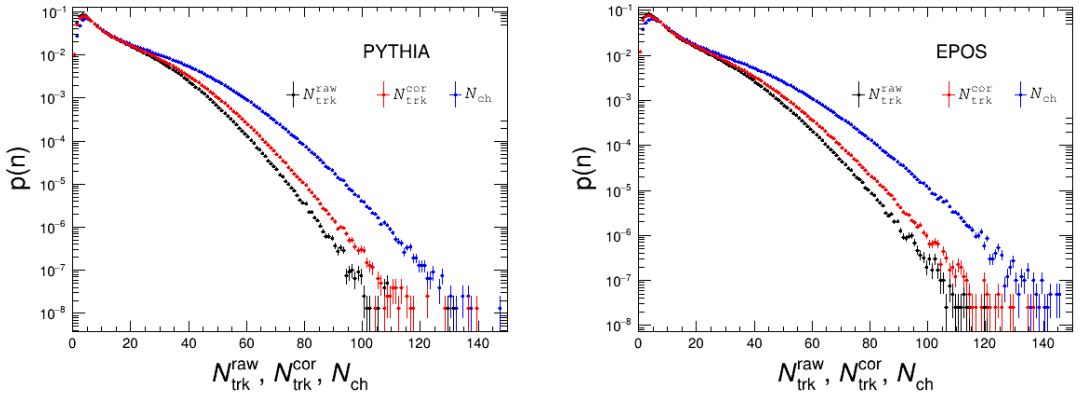

Figure 6.19: Probability distributions of $N_{\rm trk}^{\rm raw}$,$N_{\rm trk}^{\rm cor}$ and $N_{\rm ch}$

Using the same distribution and reference to correct both data and MC allows to compare the multiplicity bins in data and MC directly. Fig. 6.20 is our $N_{\rm ch}$-$N_{\rm trk}^{\rm cor}$ correlation plot which will be used for the estimation of $\mathrm{d}N_{\rm ch}/\mathrm{d}\eta_{|\eta|<1}$.

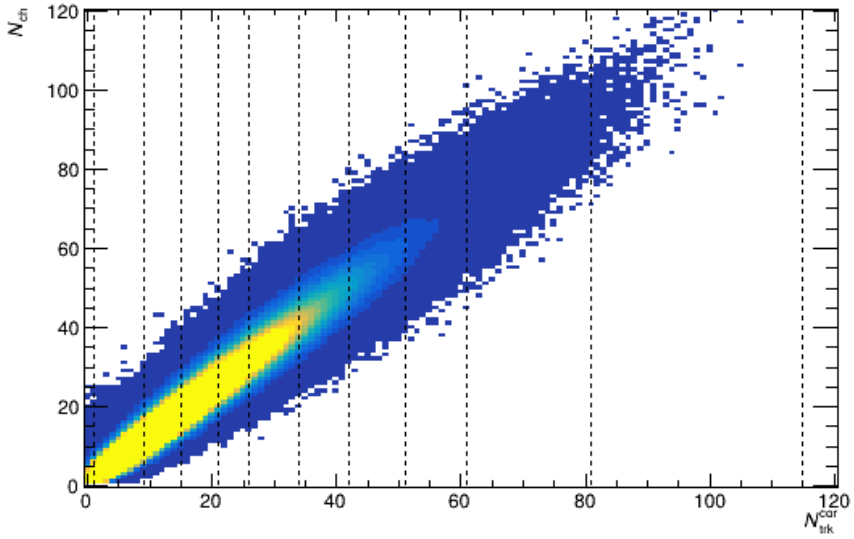

Figure 6.20: N_{ch}-$N_{\mathrm{trk}}^{\mathrm{cor}}$ correlation plot

6.3.3 Tracklet to charged particle conversion

The average number of primary charged particles is approximately proportional to the average number of corrected tracklets, $\langle N_{\mathrm{trk}}^{\mathrm{cor}} \rangle$, within the same acceptance of the detector. Thus we get Eq. 6.5.

$$\mathrm{d}N_{\mathrm{ch}}/\mathrm{d}\eta_{|\eta|<1} = \alpha \times \langle \mathrm{N}_{\mathrm{trk}}^{\mathrm{cor}} \rangle_{|\eta|<1} \tag{6.5}$$

First we define our multiplicity bins i by selecting some $N_{\mathrm{trk}}^{\mathrm{cor}}$ ranges in the corrected tracklet distribution in data as shown in Fig.6.21. The size of each multiplicity bins is adopted to have reasonable statistics for Υ signal extraction. This leads to having a broader range for high number of $N_{\mathrm{trk}}^{\mathrm{cor}}$ events. These $N_{\mathrm{trk}}^{\mathrm{cor}}$ ranges are used in MC distributions as well.

The correlation between charged particles and corrected tracklets is extracted from the profile of the two dimensional N_{ch}-$N_{\mathrm{trk}}^{\mathrm{cor}}$ correlation (shown in Fig.6.20).
Two methods are used to fit the 2D N_{ch}-$N_{\mathrm{trk}}^{\mathrm{cor}}$ correlation to obtain the N_{ch} values. The two methods are described in following:

- A polynomial fit
- A linear fit

6.3.3.1 Polynomial fit

With this approach an ad-hoc polynomial fitting function f is applied to the integrated range starting from $N_{\mathrm{trk}}^{\mathrm{cor}} \geq 1$ in Fig. 6.22. In the two dimensional correlation plot there is no entry for zero tracklets as the $N_{\mathrm{trk}}^{\mathrm{cor}} = 0$ events are rejected by the event cut $N_{contributor} > 0$. The fitting function f has two different forms (shown in Eq. 6.6) depending the value of x_0. x_0 is basically the $N_{\mathrm{trk}}^{\mathrm{cor}}$ value when the $N_{\mathrm{trk}}^{\mathrm{cor}} - N_{\mathrm{ch}}$ correlation is deviating from the linearity.

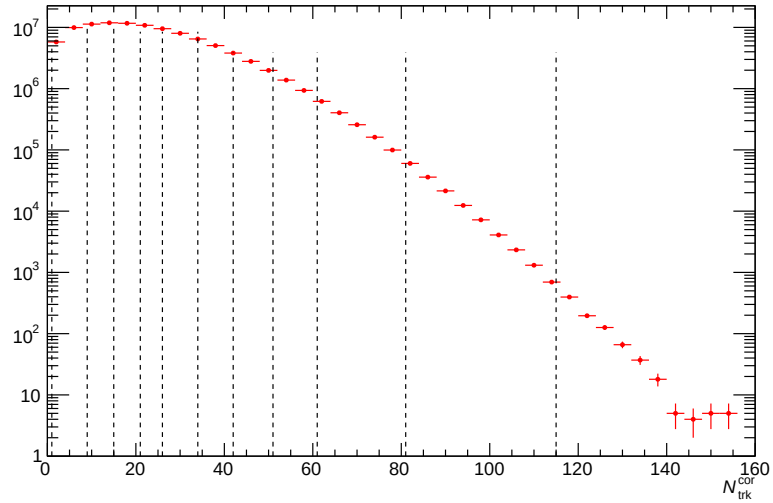

Figure 6.21: $N_{\rm trk}^{\rm cor}$ distribution from data. Here the vertical black lines represent the boundary of each multiplicity bin.

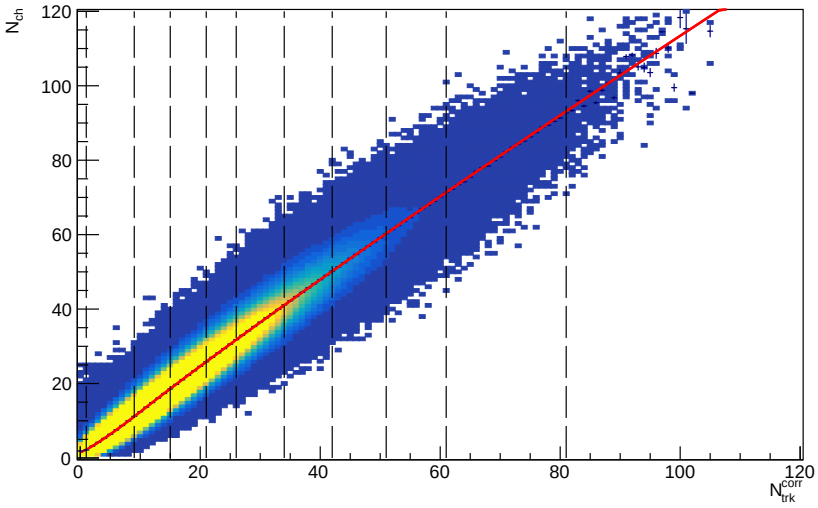

Figure 6.22: $N_{\rm ch}$-$N_{\rm trk}^{\rm cor}$ correlation plot fitted by an ad-hoc polynomial function.

$$\begin{aligned} f(x) &= ax^c + b \text{ for } x < x_0 \\ f(x) &= a2x^{c2} + b2 \text{ for } x \geq x_0 \end{aligned} \tag{6.6}$$

where,

$$\begin{aligned} a2 &= (\tfrac{ac}{c2})x_0^{c-c2} \\ b2 &= (\tfrac{a-ac}{c2})x_0^c + b \end{aligned}$$

Then the $\langle N_{\rm ch}\rangle$ was evaluated by using Eq. 6.7. With this procedure the average charged particles, $\langle N_{\rm ch}\rangle$ is estimated weighted by the number of MB events from data in each multiplicity bin which reduces the biases between the data and MC distributions.

$$\langle N_{ch}^i\rangle = \frac{\sum N_j \times f \rightarrow Eval(N_{trk}^{cor,j})}{\sum N_j} \tag{6.7}$$

Here $\langle N_{ch}^{i} \rangle$ is the average number of charged particles, N_j is the number of events in each N_{trk}^{cor} bin taken from data. This method shows a good agreement with N_{ch}-N_{trk}^{cor} correlation. We used the values using the add-hoc polynomial fit as the central values.

6.3.3.2 Linear fit

This approach uses a simple linear fit using $N_{\rm ch} = \alpha \times N_{\rm trk}^{\rm cor}$ where α is a correlation factor. α can be extracted in the integrated case (α_{global}) and also in multiplicity bins (α_i) in Fig. 6.23. Then α_i values are used to compute the average charged particles in each multiplicity bins using Eq. 6.8. In order to avoid the bias due to events in zero tracklets region, the fit function is forced to pass through (0,0). Uncertainty is taken from the uncertainty on the fit. We can also use our global alpha value (α_{global}) in Eq. 6.8 instead of α_i to have an extreme estimation of the average number of charged particles. Fig. 6.24 shows the ratio between the α_{global} and α_i in each multiplicity bins. A maximum $\sim 6\%$ deviation in the α_i values with respect to α_{global} is observed in the very low and high multiplicity bins. As MC simulations can not reproduce the data fully, we used this deviation as a source of the systematic uncertainty in order to be conservative.

$$\langle N_{\rm ch} \rangle_i = \alpha_i \times \langle N_{\rm trk}^{\rm cor} \rangle_i \tag{6.8}$$

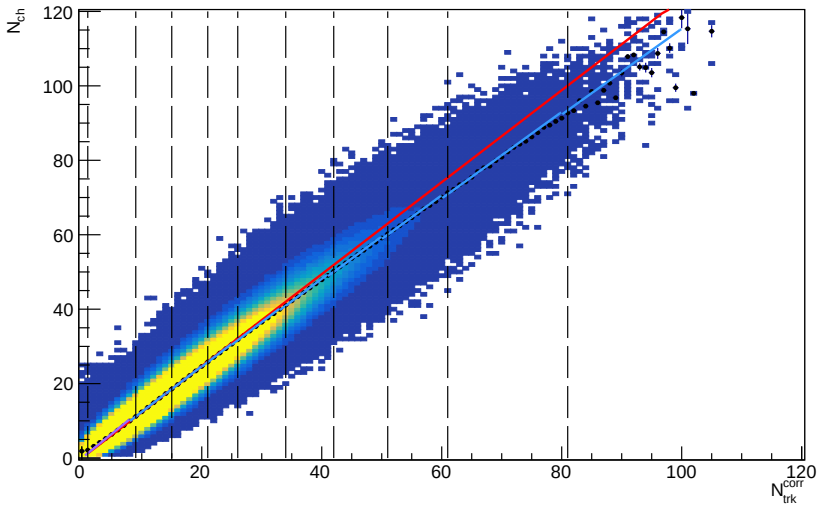

Figure 6.23: $N_{\rm ch}$-$N_{\rm trk}^{\rm cor}$ correlation plot fitted by a simple linear function

Finally, the α_i values can be used in Eq. 6.9 to get the average charged particle pseudo-rapidity density, $\langle {\rm d}N_{\rm ch}/{\rm d}\eta \rangle_i$ values in multiplicity bins i.

$$\langle {\rm d}N_{\rm ch}/{\rm d}\eta \rangle_i = \frac{\alpha_i \langle N_{\rm trk}^{\rm cor} \rangle_i}{\Delta\eta} \tag{6.9}$$

Here, $\langle N_{\rm trk}^{\rm cor} \rangle_i$ is taken from data, $\Delta\eta$ is the pseudo-rapidity range (in this case $\Delta\eta = 2$) and α_i is taken from MC simulations as explained earlier.

If the $N_{\rm ch}$-$N_{\rm trk}^{\rm cor}$ correlation would have been perfectly linear, the α_{global} could be used directly to obtain the charged particle pseudo-rapidity density. In reality, the correlation is not perfectly linear because of the detector resolution. So, this method can not provide a good $N_{\rm ch}$ estimation. This linear fit method has been used only as a source of uncertainty

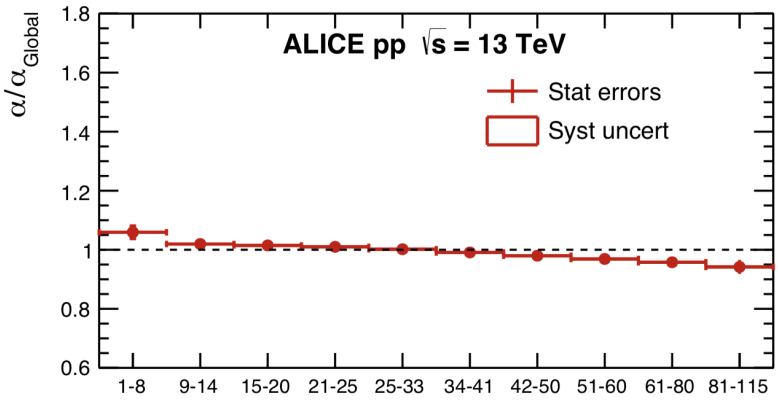

Figure 6.24: Comparison between global alpha and alpha in bins

estimation and will be explained in the next section.

6.3.4 Systematic uncertainty on the multiplicity estimation

In this section, we will present the sources of uncertainties that we considered for this work.

- Residual z-vertex dependence
- Different MC simulations
- Data-driven correction input
- Different fitting functions

6.3.4.1 Uncertainty on residual z-vertex dependence

To estimate the uncertainty on z-vertex dependence, we choose five sets of sample depending on N_{trk}^{cor} in different z-vertex ranges. We consider the following ranges:

1. $-10 < v_z < 10$
2. $-10 < v_z < -5$
3. $-5 < v_z < 0$
4. $0 < v_z < 5$
5. $5 < v_z < 10$

We extracted our α_i and $\langle N_{ch} \rangle_i$ for each of this ranges.

6.3.4.2 Uncertainty on different MC event generators

There is a small effect depending on the MC event generators we are using to obtain our pseudo-rapidity charged-particle density. For this work we used the centralized ALICE simulation using two MC event generators (PYTHIA and EPOS LHC).

6.3.4.3 Uncertainty on the input of the data-driven correction

We investigated one more source of uncertainty which is the dependence of the profiles coming from the difference between the MC and the data. To control the difference coming from this source we also use the MC profiles as an input of the data-driven correction.

6.3.4.4 Uncertainty on non-linearity

We rely on the fitting function to calculate the pseudo-rapidity charged-particle density. In our previous section, we explained the two fitting functions that we are using. The deviation from the linearity has been obtained bin-by-bin as an additional systematic after combining the past three uncertainties.

6.3.4.5 Computation of uncertainties for polynomial and linear fit

We combined the tests on z-vertex (5), different MC samples (2), different data driven inputs (2) in total 20 tests, by using Eq.6.10 and 6.11 for the calculation of statistical and systematic uncertainties respectively. Here, n represents the number of the tests, e_{x_i} is the statistical error and x_i is the obtained value for each test, $\bar{x}$ is the mean value of all the tests.

$$e_{\bar{x}}^{stat} = \frac{1}{n}\sum_{i=1}^{n}\sigma_{x_i} \tag{6.10}$$

$$\sigma_{\bar{x}}^{syst} = \sqrt{\frac{\sum_{i=1}^{n}(x_i - \bar{x})^2}{n}} \tag{6.11}$$

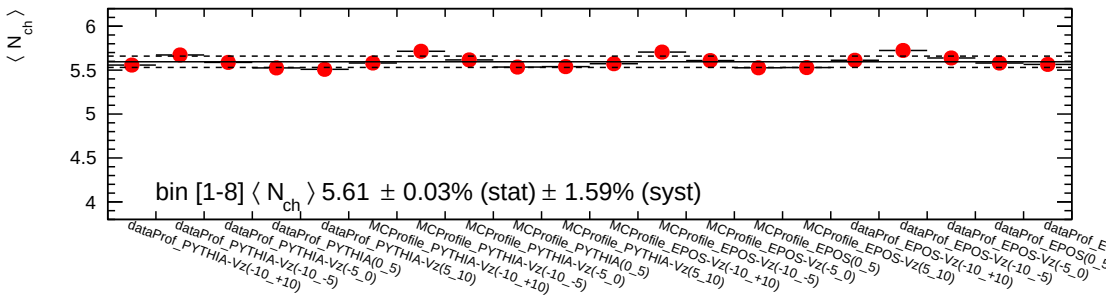

Figure 6.25: $\langle N_{ch} \rangle$ systematic uncertainty in the first multiplicity bins from ad-hoc polynomial fit.

Fig. 6.25 shows the computation of mean number of charged particle in first multiplicity bin using method explained earlier for add-hoc polynomial fit. The values for each multiplicity bins are listed in table. 6.3.

$N_{trk}^{cor} bin$	$\langle N_{ch} \rangle \pm stat \pm syst$
$Integrated$	14.66 ± 0.03% ± 0.31%
$[1-8]$	05.61 ± 0.03% ± 1.59%
$[9-14]$	13.94 ± 0.01% ± 0.29%
$[15-20]$	21.35 ± 0.01% ± 0.32%
$[21-25]$	28.08 ± 0.01% ± 0.39%
$[26-33]$	35.41 ± 0.01% ± 0.62%
$[34-41]$	44.62 ± 0.01% ± 0.88%
$[42-50]$	54.06 ± 0.02% ± 1.14%
$[51-60]$	64.41 ± 0.03% ± 1.39%
$[61-80]$	77.67 ± 0.05% ± 1.71%

Table 6.3: $\langle N_{ch} \rangle$ with statistical and systematic uncertainties (weighted by data)

The uncertainty due to the non linearity has been assigned from the linear fit method. The final α in each bin and in integrated case have been calculate combining 20 tests (similar to the polynomial method). Then the difference between the α factors in bins and the integrated case has been used as an additional systematic for non linearity. We denote this systematic as δ. The associated α and δ values are listed in table. 6.4.

$N_{trk}^{cor} bin$	$\alpha \pm stat \pm syst$	δ
Integrated	1.22 ± 0.02% ± 0.65%	
$[1-8]$	1.29 ± 2.02% ± 1.10%	5.4%
$[9-14]$	1.24 ± 1.36% ± 0.29%	1.6%
$[15-20]$	1.24 ± 1.03% ± 0.35%	1.6%
$[21-25]$	1.23 ± 0.91% ± 0.44%	0.8%
$[26-33]$	1.22 ± 0.63% ± 0.62%	0.0%
$[34-41]$	1.21 ± 0.54% ± 0.88%	0.8%
$[42-50]$	1.19 ± 0.46% ± 1.15%	2.5%
$[51-60]$	1.18 ± 0.41% ± 1.42%	3.3%
$[61-80]$	1.17 ± 0.29% ± 1.76%	4.3%

Table 6.4: Computation of the systematic uncertainty on $\langle N_{ch} \rangle$

6.3.5 Minimum Bias trigger efficiency for INEL>0

We have calculated the MB trigger efficiency ($\epsilon^{i}_{INEL>0}$) for each multiplicity bins using eq.6.12. This efficiency factor is basically the ratio of the charged-particle distribution with and without MB trigger selection (kINT7) excluding all the event cuts.

$$\epsilon^{i}_{INEL>0} = \frac{N_{events} \text{ with kINT7 (PS+ No Event Cut)}}{N_{events} \text{ without kINT7 (PS + No Event Cut)}} \tag{6.12}$$

Here, INEL>0 corresponds the inelastic events where at least one charged particle was produced.

Fig.6.26 shows that the efficiency is very close to unity except for the integrated and first multiplicity bin. The number of events before and after the trigger selection is tabulated in 6.5. The efficiency factor for the integrated case is used to normalize the relative Υ

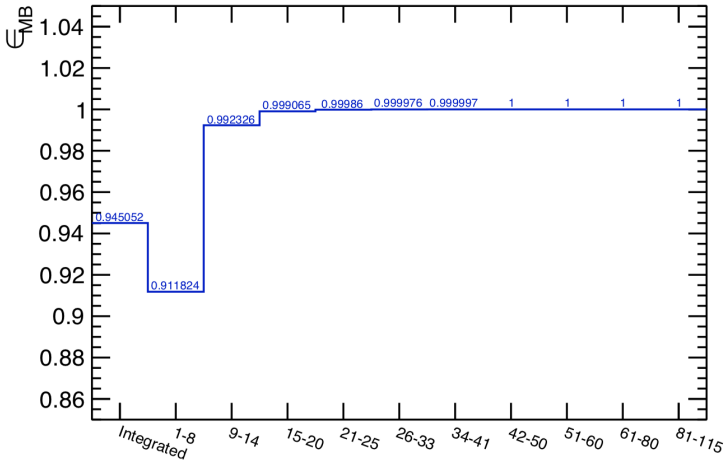

Figure 6.26: ϵ_{MB} in integrated sample and multiplicity bins.

yields (see section 6.5).

N_{trk}^{cor} Bin	with kINT7	without kINT7	$\epsilon^{i}_{INEL>0}$
Integrated	135766927	143660759	0.94
$[1-8]$	72128196	79103227	0.91
$[9-14]$	25405646	25602114	0.99
$[15-20]$	15018655	15032717	0.99
$[21-25]$	8156032	8157170	0.99
$[26-33]$	7638624	7638811	0.99
$[34-41]$	3399163	3399172	0.99
$[42-50]$	1342173	1342173	1.00
$[51-60]$	376670	376670	1.00
$[61-80]$	81574	81574	1.00
$[81-115]$	1710	1710	1.00

Table 6.5: $\epsilon^{i}_{INEL>0}$ in multiplicity bins.

6.3.5.1 Correction factor in the first bin for relative charged-particles

The MB trigger efficiency is negligible for most of the multiplicity bins except for the first bin where the efficiency is 91%. Moreover the first bin is affected by the vertex QA cuts as these cuts mostly remove the very low multiplicity events. A correction must be applied to account for this by comparing the mean number of charged particles with these event cuts before and after the trigger selection. The correction factor is formulated in eq. 6.13.

$$\epsilon^{1}_{INEL>0,\langle N_{ch}\rangle} = \frac{\langle N_{ch}\rangle[N_{ch} \geq 1 + kINT7 + vtxQA]}{\langle N_{ch}\rangle[N_{ch} \geq 1 + vtxQA]} \tag{6.13}$$

MC	$\langle N_{ch}\rangle[N_{ch} \geq 1 + KINT + vtxQA]$	$\langle N_{ch}\rangle[N_{ch} \geq 1 + vtxQA]$	$\epsilon^{1}_{INEL>0,\langle N_{ch}\rangle}$
PYTHIA8	5.708	5.512	1.035
EPOS	5.683	5.457	1.0414

Table 6.6: $\epsilon^{1}_{INEL>0,\langle N_{ch}\rangle}$ in first multiplicity bins.

Therefore, we have computed the correction factor for the first bin, $\epsilon^{1}_{INEL>0,\langle N_{ch}\rangle} = 1.038 \pm 0.0032$ (0.32% Syst.). The relative multiplicity should be divided by this correction factor.

6.3.6 Self-normalised charged-particle multiplicity computation

Finally the self-normalised multiplicity $(\mathrm{d}N_{\mathrm{ch}}/\mathrm{d}\eta/\langle \mathrm{d}N_{\mathrm{ch}}/\mathrm{d}\eta\rangle)_i$, in each bin is computed by using eq. 6.14

$$\left(\frac{\mathrm{d}N_{\mathrm{ch}}/\mathrm{d}\eta}{\langle \mathrm{d}N_{\mathrm{ch}}/\mathrm{d}\eta\rangle}\right)_i = \frac{\langle N_{ch}\rangle_i}{\langle \mathrm{d}N_{\mathrm{ch}}/\mathrm{d}\eta\rangle \times \Delta\eta \times \epsilon^{i}_{INEL>0,\langle N_{ch}\rangle}} \tag{6.14}$$

Here, $\langle N_{ch}\rangle_i$ is the average number of charged particles (taken from table. 6.3), $\langle \mathrm{d}N_{\mathrm{ch}}/\mathrm{d}\eta\rangle$ is the average charged particle density in the full 2016 data sample, $\Delta\eta$ is the pseudo-rapidity range (in this case $\Delta\eta = 2$) and $\epsilon^{i}_{INEL>0,\langle N_{ch}\rangle}$ is the correction factor for INEL>0 selection in each multiplicity bin. As explained before, this term is negligible for all the multiplicity bins except for the first bin. The value of $\langle \mathrm{d}N_{\mathrm{ch}}/\mathrm{d}\eta\rangle$ is 7.02 ± .11 (syst) has been taken from an independent analysis [128]. This value is compatible with our computed value within the uncertainties.

Finally, the statistical uncertainty is calculated by a squared sum of all the terms (considering them uncorrelated) in Eq. 6.14. The systematic uncertainty in each multiplicity bin is computed by a squared sum of all the contributions in Eq. 6.14 and the δ values from table. 6.4. The final computed values are presented in table 6.7.

$N^{cor}_{trk} bin$	$(\mathrm{d}N_{\mathrm{ch}}/\mathrm{d}\eta/\langle \mathrm{d}N_{\mathrm{ch}}/\mathrm{d}\eta\rangle)_i$ ± stat ± syst
$[1-8]$	0.38 ± 0.03% ± 5.85%
$[9-14]$	0.99 ± 0.01% ± 2.26%
$[15-20]$	1.52 ± 0.01% ± 2.26%
$[21-25]$	2.00 ± 0.01% ± 1.80%
$[26-33]$	2.52 ± 0.01% ± 1.69%
$[34-41]$	3.18 ± 0.01% ± 1.97%
$[42-50]$	3.85 ± 0.02% ± 3.16%
$[51-60]$	4.59 ± 0.03% ± 3.91%
$[61-80]$	5.53 ± 0.05% ± 4.89%

Table 6.7: $(\mathrm{d}N_{\mathrm{ch}}/\mathrm{d}\eta/\langle \mathrm{d}N_{\mathrm{ch}}/\mathrm{d}\eta\rangle)_i$ with final systematic uncertainties.

6.4 Υ yield measurement

The Υ states are studied via their decay into di-muon measured with the muon spectrometer. In this section we will focus on Υ yield measurement. The main goal is to obtain the self-normalised Υ yield $\frac{\mathrm{d}N_\Upsilon/\mathrm{dy}}{\langle \mathrm{d}N_\Upsilon/\mathrm{dy}\rangle}$ for each multiplicity bin which has been defined earlier. For this analysis Υ are measured in the di-muon decay channel at forward rapidity ($-4 < \eta < -2.5$). The Υ yield can be obtained as

$$\Upsilon = \frac{N_\Upsilon}{A \times \varepsilon . BR_{\Upsilon \longrightarrow \mu^+\mu^-} . N_{MB}^{eq}} \tag{6.15}$$

Here, N_Υ is the number of Υ in the analyzed sample. $A \times \varepsilon$ is the acceptance-efficiency of the detector, $BR_{\Upsilon \longrightarrow \mu^+\mu^-}$ is the branching ratio of Υ decaying into two muons ($2.48 \pm 0.05\%$) and N_{MB}^{eq} is the number of MB events which is equivalent to the number of di-muon events which is triggered for the analysis.

Finally we are interested in the number of self-normalised Υ yields in each multiplicity bin i which is the ratio of the yield in an bin and the total sample.

$$\Upsilon_i^{rel} = \frac{N_\Upsilon^i}{N_\Upsilon^{tot}} \tag{6.16}$$

Since the detector effects do not change in different tracklet bins, the $A \times \varepsilon$ factor will cancel out, $BR_{\Upsilon \longrightarrow \mu^+\mu^-}$ factor also cancel out as it is constant. While these factors are needed to calculate the absolute yield, we can calculate the relative yield without these factors.

However, we also need to normalize the Υ yields to the number of minimum bias events and for this we used the ratio of equivalent number of MB events in integrated and in multiplicity bin ($\frac{N_{MB}^{equiv}}{N_{MB}^{equiv,i}}$), normalization factor (see section 6.4.4). In addition we need to apply efficiency (ϵ) correction due to the event selections. The computation of ϵ factors will be described in section 6.4.5. Therefore, the calculation of self-normalized Υ yields can be re-written from Eq.6.1 as:

$$\Upsilon_i^{rel} = \frac{\Upsilon_i}{\Upsilon_{tot}} = \frac{dN_\Upsilon/dy}{\langle dN_\Upsilon/dy\rangle} = \frac{N_i^\Upsilon}{N_{tot}^\Upsilon} \times \frac{N_{MB}^{equiv}}{N_{MB}^{equiv,i}} \times \epsilon \tag{6.17}$$

6.4.1 Muon Tracks selection

We select di-muon unlike sign trigger events (CMUL7) with physics selection.

Muon candidates are selected with the corresponding selection criteria:

- Moun tracks reconstructed in the tracking chambers are required to match a track reconstructed in the trigger system. This cut removes the background associated to the hadrons which are misidentified as muons.

- A low-p_T (Lpt) trigger threshold of 1GeV/c is applied to suppress the amount of low p_T tracks that can contribute to the combinatorial background of di-muon invariant mass spectrum.

- The selected muons are required to lie within the limit $17.5 < R_{\rm abs} < 89$ cm, where $R_{\rm abs}$ is the radial transverse position of the muon tracks at the end of the front absorber. This cut is used to avoid the multi-scattering effects of reconstructed tracks due to the interaction with different absorber materials.

- The momentum times the distance to the closest approach (pDCA) is within 6 σ of the distribution, this cut removes fake tracks not pointing to the vertex.

- The muon are required to be in the acceptance of the muon spectrometer, $-4.0 < \eta < -2.5$.

Di-muon pairs are formed with individual muons satisfying the above criteria. They are selected with two additional criteria :

- The total charge of the di-muon pair is 0.

- The pair is required to be within the acceptance of the spectrometer $(-4.0 < y < -2.5)$.

6.4.2 Υ signal extraction

In this section we will describe the Υ signal extraction procedure in the multiplicity bins that we defined in the previous section. The track selection criteria has been discussed in section 6.4.1. First, the invariant mass $M_{\mu\mu}$ for each of the selected di-muon pair is computed as

$$M_{\mu\mu} = \sqrt{(E_1 + E_2)^2 - [(p_{1,x} + p_{2,x})^2 + (p_{1,y} + p_{2,y})^2 + (p_{1,z} + p_{2,z})^2]} \tag{6.18}$$

Here, $M_{\mu\mu}$ is the mass of di-muon, E_1 and E_2 are the energy of the two muons, ($p_{1,x}$, $p_{1,y}$, $p_{1,z}$) and ($p_{2,x}$, $p_{2,y}$, $p_{2,z}$) represent the momentum components of μ_1 and μ_2 respectively. The energy of each muon track is calculated using Eq.6.19.

$$E_i^2 = p_i^2 + m_\mu^2 \tag{6.19}$$

Fig. 6.27 shows the reconstructed di-muon mass spectra.
The number of Υ are obtained by performing signal extraction on the invariant mass-spectra for the defined multiplicity bins. The signal extraction procedure are a sum of functions that models both signal and background.

- **Signal:** The Υ states are described by a sum of three extended Crystal Ball functions. The CB2 function (A.1) consists of a Gaussian core extended with two tails, one on each side. The tails are simple power law of exponent "n". α corresponds to the number of sigmas at which the tail starts.

- **Background:** The background is included in fit of the signal extraction using one of the three functions which are the product of two exponential functions, the product of an exponential and a power law function and a variable width Gaussian.

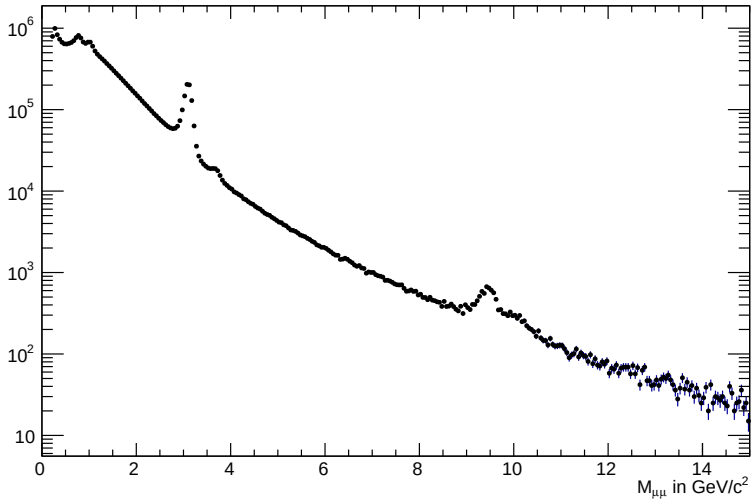

Figure 6.27: Di-muon invariant mass spectra

6.4.2.1 Fit strategy

The fit of the di-muon invariant mass distribution is fitted with four iterative steps described below. At the N+1 step free parameters are initialized with values obtained at N step. Fits are performed within the considered fit range. Only fits satisfying convergence conditions are kept. Different steps of the procedure are illustrated on Fig. 6.28.

- STEP 1: the di-muon invariant mass is fitted outside the signal range ($M_{\mu^+\mu^+}$ = [8.2-10.7] GeV/c^2), background parameters are free.
- STEP 2: fit the 1S with background + Gaussian with the exclusion of the 2S+3S range ($M_{\mu^+\mu^+}$ = [9.9-10.8] GeV/c^2), all are parameters free.
- STEP 3: fit the 1S with background + 1 CB2 with the exclusion of the 2S+3S range ($M_{\mu^+\mu^+}$ = [9.9-10.8] GeV/c^2), CB2 tail parameters are fixed, other parameters are free.
- STEP 4: fit the complete di-muon invariant mass distribution with background + 3 CB2 with fixed tail parameters (MC or data-driven tails) for Υ(1S). The mass and the sigma are free for Υ(1S). For Υ(2S) and Υ(3S), the mass and sigma are fixed to the 1S with the PDG ratio, other parameters are free.

The χ^2 is used to evaluate the fit quality. The sum of the squares of the difference between the observed y-value, y_i and the fitting function evaluated at x_i is calculated as $\chi^2 = \sum_{i=1}^{N} \frac{(y_i - f(x_i))^2}{\sigma_i^2}$. Here, σ_i is the uncertainty at point i.

The ndf is the degrees of freedom of the fit and is defined as $ndf = N - N_{\text{fit}}$. Here N is the data points and N_{fit} refers to the number of fit parameters in the fitting function. For a good fit, $\chi^2/ndf \approx 1$.

The fit were considered good fit when the **significance** of the signal was $(S/\sqrt{S+B}) \geq 3$. Here, S and B corresponds to signal and background respectively.

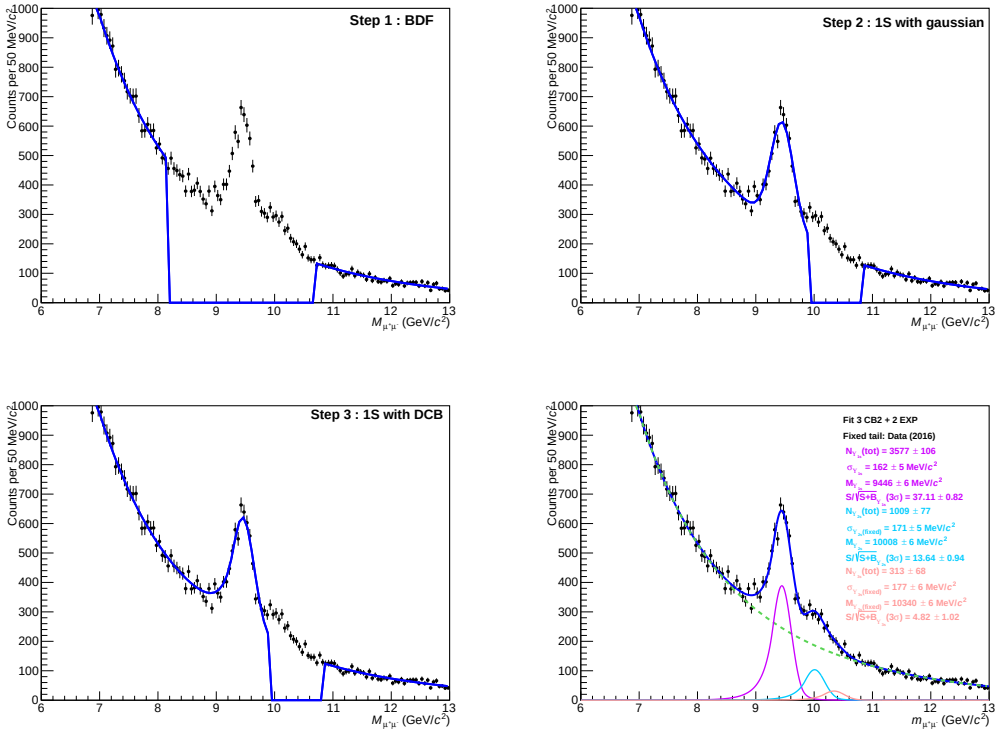

Figure 6.28: Example fit of the di-muon invariant mass with 3 CB2 for the signal. The four plots presents the four step of the fit.

	MC tails at 13 TeV	Data driven tails at 13 TeV
α_1	0.9360	0.9862
n_1	2.3156	7.5389
α_2	2.0873	2.1242
n_2	2.2530	4.3541

Table 6.8: Tail parameters used in the analysis: fixed to the simulations at 13 TeV or estimated with a data-driven method.

We also considered the fits to be counted when covariance matrix status was three which means the uncertainties are accurate.

6.4.2.2 Tail parameters

Muon multiple scattering and energy loss fluctuations in the front absorber as well as residual misalignment of the tracking chambers lead to a tail at low and high invariant mass. Due to the complexity of the signal, made of the addition of 3 CB2, the large number of parameters, and the limited statistics, the tail parameters can not be let free in the fit. It leads to a systematic overestimation of the tail component and a non physical shape of the extended tails. For this analysis the tail parameters are fixed either with MC simulations (section B.0.1) or with a data-driven estimation (section B.0.2). The tail parameters we have used for this analysis are summarized in Table.6.8. Here α_1, n_1 parameters describe the right tail and the α_2, n_2 parameters describe the tail on the left side.

6.4.2.3 Fit range

Three fitting ranges are tested to fit the invariant mass distribution.

- 6-13 GeV/c^2
- 5-14 GeV/c^2
- 7-12 GeV/c^2

6.4.2.4 Υ(nS)-to-Υ(1S) resolution ratio

In the integrated case mass and width of Υ(1S) are left free. To take into account for the possible the Υ(2S) and Υ(3S) mass shift, masses are fixed to the Υ(1S) with PDG ratio using Eq.6.20 and Eq.6.21 respectively. The mass of Υ(1S, 2S and 3S) are denoted as $m_{\Upsilon(1S)}$, $m_{\Upsilon(2S)}$ and $m_{\Upsilon(3S)}$.

$$m_{\Upsilon(2S)} = m_{\Upsilon(1S)} \times \frac{m^{PDG}_{\Upsilon(2S)}}{m^{PDG}_{\Upsilon(1S)}} \tag{6.20}$$

$$m_{\Upsilon(3S)} = m_{\Upsilon(1S)} \times \frac{m^{PDG}_{\Upsilon(3S)}}{m^{PDG}_{\Upsilon(1S)}} \tag{6.21}$$

Similarly, the width of Υ(2S) [$\sigma_{\Upsilon(2S)}$] and Υ(3S) [$\sigma_{\Upsilon(3S)}$] are fixed to Υ(1S) using Eq.6.22 and Eq.6.23 respectively.

$$\sigma_{\Upsilon(2S)} = \sigma_{\Upsilon(1S)} \times \frac{m^{PDG}_{\Upsilon(2S)}}{m^{PDG}_{\Upsilon(1S)}} \tag{6.22}$$

$$\sigma_{\Upsilon(3S)} = \sigma_{\Upsilon(1S)} \times \frac{m^{PDG}_{\Upsilon(3S)}}{m^{PDG}_{\Upsilon(1S)}} \tag{6.23}$$

The mass and width of Υ(1S) were free while performing fit in the integrated samples. But in the case of fitting in multiplicity bins they were fixed to the integrated case and 1σ variation is considered in the systematic.

Fig. 6.29 shows an example of signal extraction in the integrated sample where the violet, light blue and light red curves represents the 3 CB2 fit functions representing Υ(1S), Υ(2S) and Υ(3S). The black points represent the data, the green dotted line describes the background and the blue curve presents the signal.

Fig. 6.30 shows some example plots of the Υ signal extraction in different multiplicity bins.

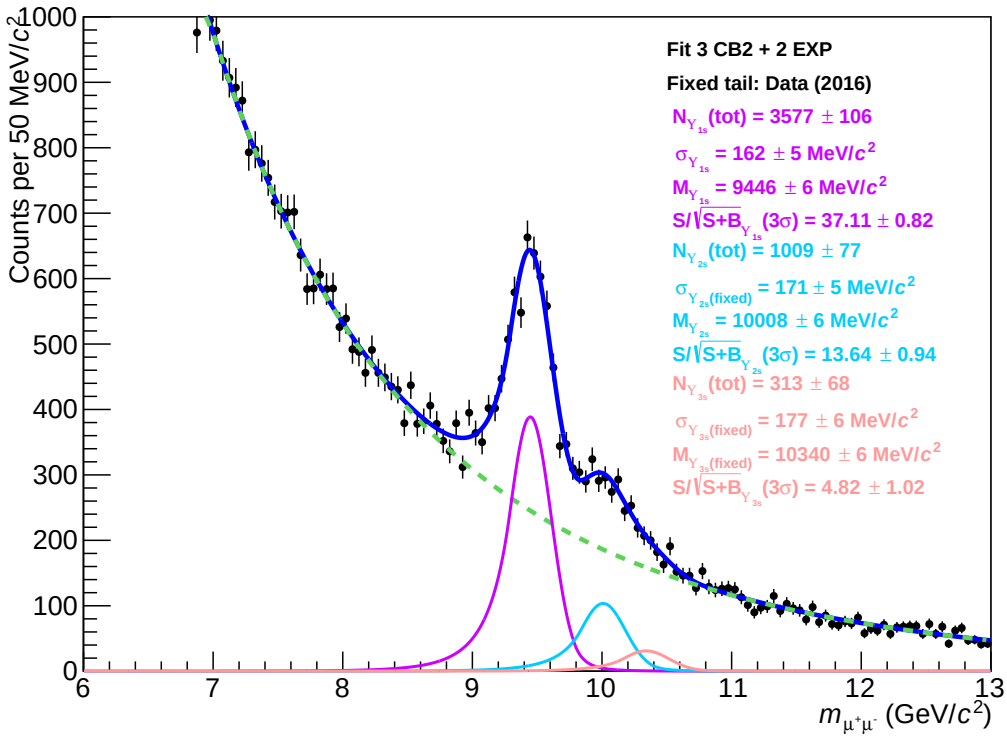

Figure 6.29: Signal extraction in the integrated sample

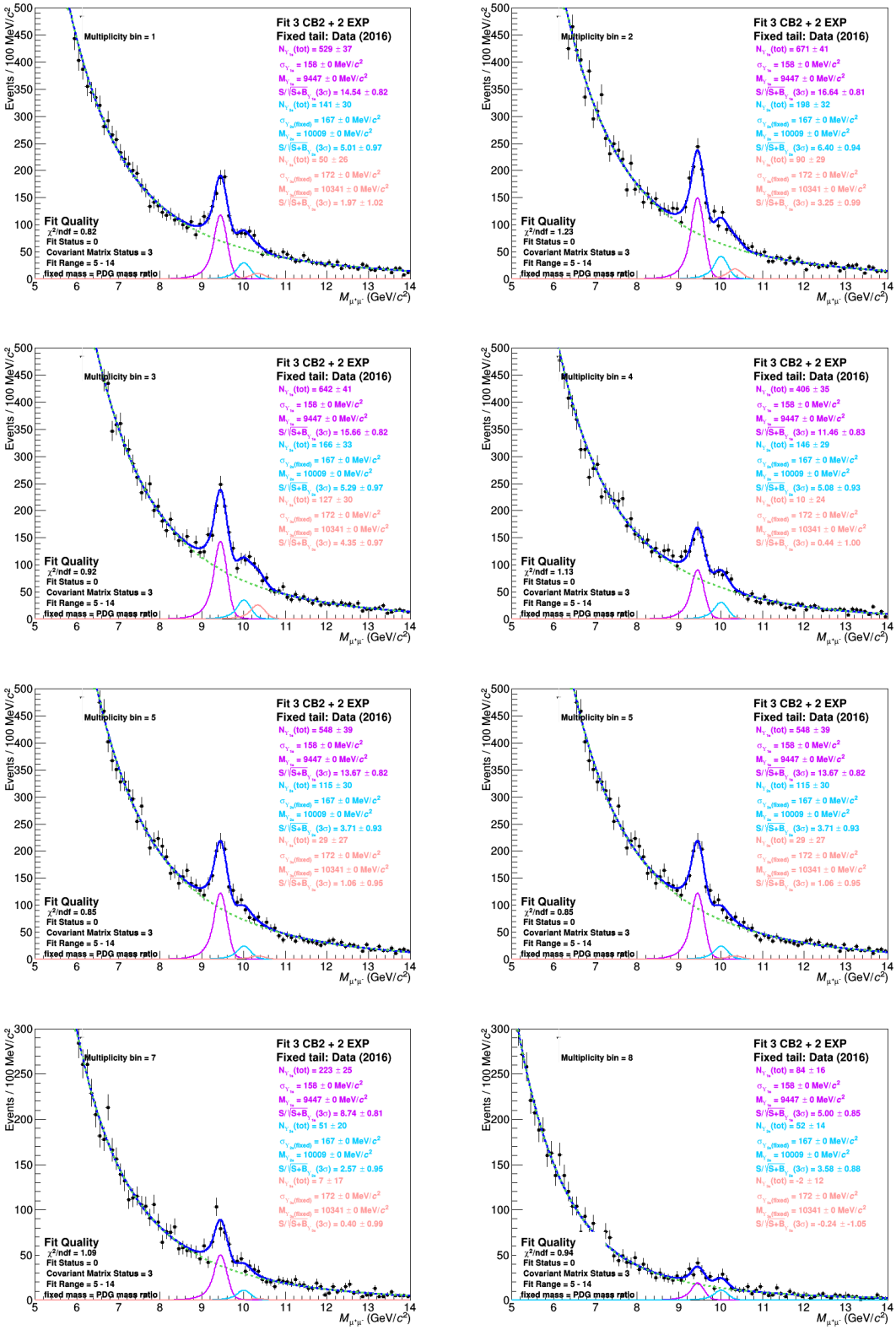

Figure 6.30: Signal extraction in different multiplicity bins.

6.4.3 Υ yields

The raw number of Υ yields are obtained by following the procedure explained in section 6.4.2. For the integrated case there are in total 18 tests. These 18 tests are selected over all possible combination of 1 DCB, 3 background functions, 2 tails and 3 fitting ranges. The central values are taken from the mean of all the tests. The statistical uncertainty is given by the mean over all uncertainties. The systematic uncertainty is taken as the standard deviation. Fig. 6.31 and Fig. 6.32 show the number of Υ(1S) (top) and Υ(2S) (bottom) in the integrated 2016 data sample respectively.

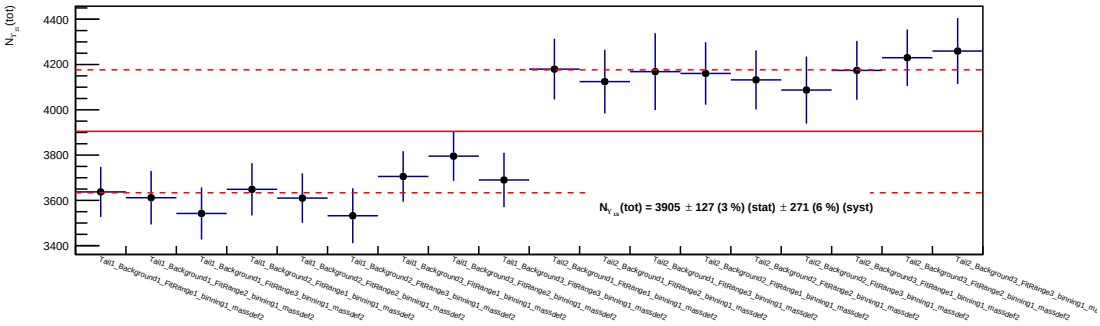

Figure 6.31: The raw number of Υ(1S) in the integrated 2016 data sample.

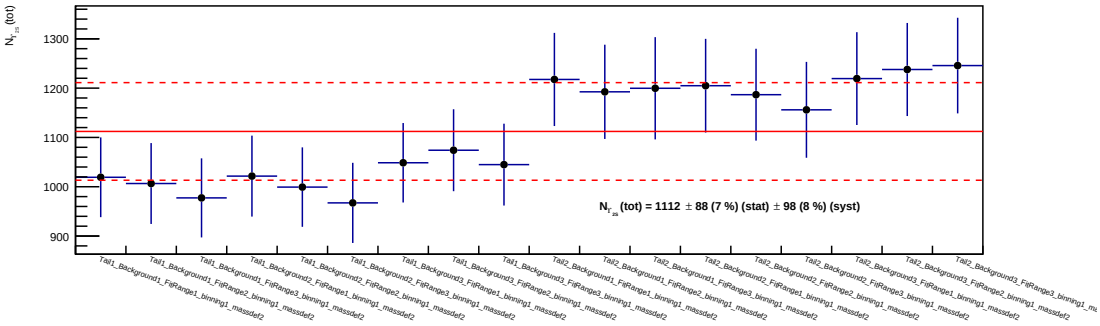

Figure 6.32: The raw number of Υ(2S) in the integrated 2016 data sample.

The raw yields extracted in each multiplicity bins are obtained similar to the integrated case. In addition to the 18 tests considered in the integrated case, 1σ variation of $\sigma_{\Upsilon_{1S}}$ and $m_{\Upsilon_{1S}}$ has been taken into account which makes the total number of tests in each multiplicity bin to be 162. Fig. 6.33 shows an example plot of Υ(1S) yields in the multiplicity bin concerning the N_{trk}^{cor} range 9-14. To compute the Υ yields in multiplicity bin we considered all the fits which converged (162 - x tests, assuming the number of test failed is x; the empty bins in Fig. 6.33 represents the failed tests). We took the mean value of all successful tests as our central value. The statistical uncertainty was given by the mean over all uncertainties. The systematic uncertainty was taken to be the standard deviation. The Υ(1S) and Υ(2S) yields are presented in Table 6.9.

The relative Υ yield in a multiplicity bin i can be computed as $N_{\Upsilon}^{i}/N_{\Upsilon}^{tot}$. To compute relative Υ(1S) and Υ(2S) in each multiplicity bin, all variations of the background and fitting ranges are combined for the same set of tail, σ and mass.This makes in total 1458 possible combinations. Fig. 6.34 shows an example of relative Υ(2S) yields in the multiplicity bin where N_{trk}^{cor} range is 42-50.

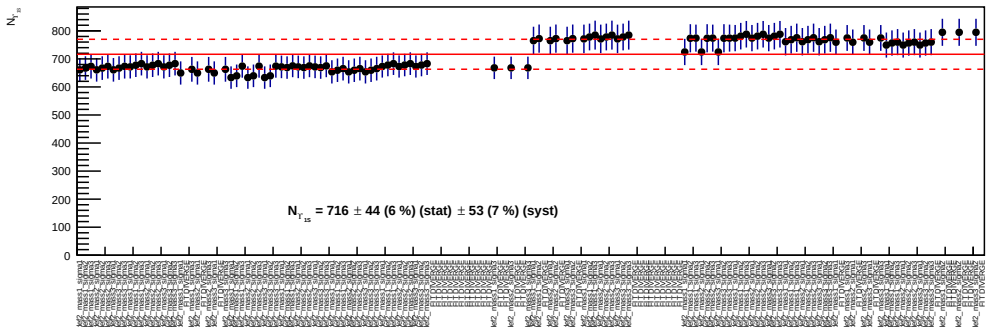

Figure 6.33: Raw number of Υ(1S) yields in the N_{trk}^{cor} bin 9-14.

N_{trk}^{cor} Bin	$N_{\Upsilon_{1S}}$ ± stat ± syst	$N_{\Upsilon_{2S}}$ ± stat ± syst
Integrated	3905 ± 127 ± 271	1112 ± 88 ± 99
[1 – 8]	581 ± 40 ± 42	156 ± 33 ± 15
[9 – 14]	716 ± 44 ± 53	213 ± 36 ± 20
[15 – 20]	701 ± 45 ± 48	190 ± 37 ± 16
[21 – 25]	437 ± 38 ± 41	152 ± 32 ± 17
[26 – 33]	608 ± 43 ± 47	130 ± 34 ± 14
[34 – 41]	413 ± 35 ± 31	120 ± 28 ± 13
[42 – 50]	248 ± 27 ± 17	62 ± 21 ± 5
[51 – 60]	91 ± 19 ± 5	
[61 – 80]	50 ± 13 ± 4	

Table 6.9: Raw Υ(1S), Υ(2S) yields in integrated case and in different multiplicity bins.

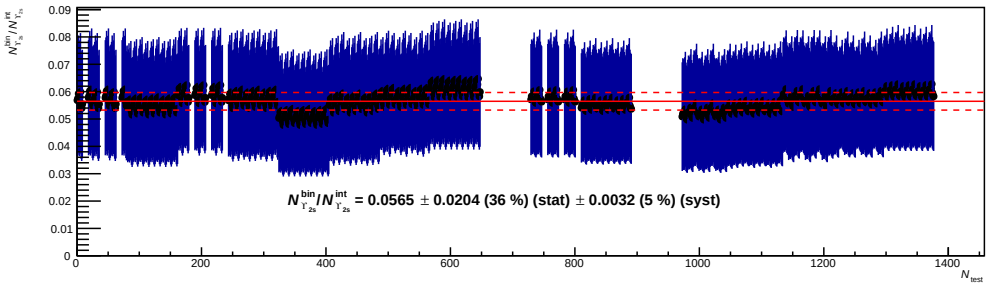

Figure 6.34: Relative Υ(2S) in multiplicity bin ($42 \geq N_{trk}^{cor} \geq 50$)

The results are presented in Table 6.10 for relative Υ(1S) and Υ(2S) yields in all considered multiplicity bins.

N_{trk}^{cor} Bin	$\Upsilon_{1S,i}^{rel}$ ± stat ± syst	$\Upsilon_{2S,i}^{rel}$ ± stat ± syst
$[1-8]$	$0.1476 \pm 7\% \pm 2\%$	$0.1394 \pm 22\% \pm 4\%$
$[9-14]$	$0.1838 \pm 7\% \pm 2\%$	$0.1923 \pm 18\% \pm 4\%$
$[15-20]$	$0.1790 \pm 7\% \pm 2\%$	$0.1711 \pm 21\% \pm 4\%$
$[21-25]$	$0.1117 \pm 9\% \pm 5\%$	$0.1365 \pm 22\% \pm 6\%$
$[26-33]$	$0.1548 \pm 7\% \pm 3\%$	$0.1161 \pm 27\% \pm 7\%$
$[34-41]$	$0.1058 \pm 9\% \pm 3\%$	$0.1084 \pm 24\% \pm 6\%$
$[42-50]$	$0.0638 \pm 11\% \pm 2\%$	$0.0565 \pm 36\% \pm 5\%$
$[51-60]$	$0.0235 \pm 21\% \pm 2\%$	
$[61-80]$	$0.0130 \pm 26\% \pm 4\%$	

Table 6.10: Relative Υ(1S), Υ(2S) in different multiplicity bins.

6.4.4 Event Normalization

The Υ yields are extracted using di-muon trigger. To calculate the corresponding Υ yields in MB trigger, we need to introduce a normalization factor. The factor is based on the ratio of MB events and CMUL events and can be written as:

$$N_{MB}^{equiv} = F_{norm} \times N_{CMUL} \tag{6.24}$$

F_{norm} is a global normalization factor and can be calculated by using following equation.

$$F_{norm} = \frac{N_{MSL}}{N_{MSL\&0MUL}} \times \frac{N_{MB}}{N_{MB\&0MSL}} \tag{6.25}$$

where N_{MSL} is the number of physics selected MSL events, N_{MB0MSL} is the sub-sample of MB events containing also the 0MSL trigger input, $N_{MSL0MUL}$ is the sub-sample of MSL events containing also the 0MUL trigger input. Eq.6.25 can also be calculated in a run-by-run basis. If j presents the number of runs we get:

$$N_{MB}^{equiv} = \sum_{j} F_{norm}^{j} \times N_{MUL}^{j} \tag{6.26}$$

Fig.6.35 shows the calculated run-by-run with normalization factor using in Eq.6.26. F_{norm}^{j} does not vary much from run to run.

The normalization factor in multiplicity bin i can be calculated either directly by using eq.6.25 as:

$$N_{MB}^{equiv,i} = F_{norm}^{i} \times N_{MUL}^{i} \tag{6.27}$$

Or, in a run-by-run basis as written in eq.6.28

$$N_{MB}^{equiv,i} = \sum_{j} F_{norm}^{i,j} \times N_{MUL}^{i,j} \tag{6.28}$$

F_{norm}^{j} is a normalization factor originating from a global normalisation factor, Therefore, eq.6.17 can be rewritten by using eq.6.24 and eq. 6.27 as following:

$$\Upsilon_{i}^{rel} = \frac{\Upsilon_{i}}{\Upsilon_{tot}} = \frac{dN_{\Upsilon}/dy}{\langle dN_{\Upsilon}/dy \rangle} = \frac{N_{i}^{\Upsilon}}{N_{tot}^{\Upsilon}} \times \frac{F_{norm} \times N_{MUL}}{F_{norm}^{i} \times N_{MUL}^{i}} \times \epsilon \tag{6.29}$$

Here,

$$F_{norm} = \frac{1}{N_{MUL}} \sum_{j} F_{norm}^{j} N_{MUL}^{j} \tag{6.30}$$

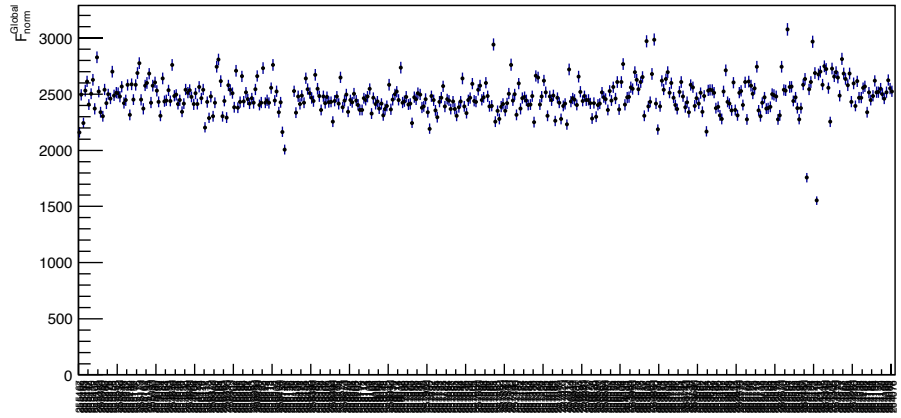

Figure 6.35: F_{norm}^{global} run-by-run for total 2016 data sample (431 runs)

$$F_{norm}^{i} = \frac{1}{N_{MUL}^{i}} \sum_{j} F_{norm}^{j} N_{MUL}^{j} \frac{N_{MB}^{i,j}}{N_{MB}^{j}} \tag{6.31}$$

The calculated values of F_{norm}^{i} in multiplicity bins are shown in table.section 6.4.4

Multiplicity bin (i)	$N_{\rm trk}^{\rm cor}$ range	F_{norm}^{i}
1	$[1-8]$	6809.4 ± 0.0170
2	$[9-14]$	2835.7 ± 0.0074
3	$[15-20]$	1758.9 ± 0.0048
4	$[21-25]$	1280.8 ± 0.0039
5	$[26-33]$	974.4 ± 0.0039
6	$[34-41]$	741.4 ± 0.0027
7	$[42-50]$	590.4 ± 0.0031
8	$[51-60]$	481.1 ± 0.0046
9	$[61-80]$	385.1 ± 0.0085

Finally eq.6.29 can be described in a run-by-run basis as:

$$\Upsilon_{i}^{rel} = \frac{\Upsilon_{i}}{\Upsilon_{tot}} = \frac{dN_{\Upsilon}/dy}{\langle dN_{\Upsilon}/dy \rangle} = \frac{N_{i}^{\Upsilon}}{N_{tot}^{\Upsilon}} \times \frac{\sum_{j} F_{norm}^{j} N_{MUL}^{j}}{\sum_{j} F_{norm}^{j} N_{MUL}^{j} \frac{N_{MB}^{i,j}}{N_{MB}^{j}}} \times \epsilon \tag{6.32}$$

We calculated the normalisation factor for each multiplicity bin by following Eq.6.17 and Eq.6.32. Fig.6.36 shows the comparison of the normalisation factors ($\frac{N_{MB}^{equiv}}{N_{MB}^{equiv,i}}$ and $\frac{\sum_{j} F_{norm}^{j} N_{MUL}^{j}}{\sum_{j} F_{norm}^{j} N_{MUL}^{j} \frac{N_{MB}^{i,j}}{N_{MB}^{j}}}$). The difference between the two methods shows similar result. Table 6.11 shows the equivalent number of MB events for integrated and multiplicity bins. The final normalization factors are calculated using Eq.6.17 from the values listed in the Table 6.11.

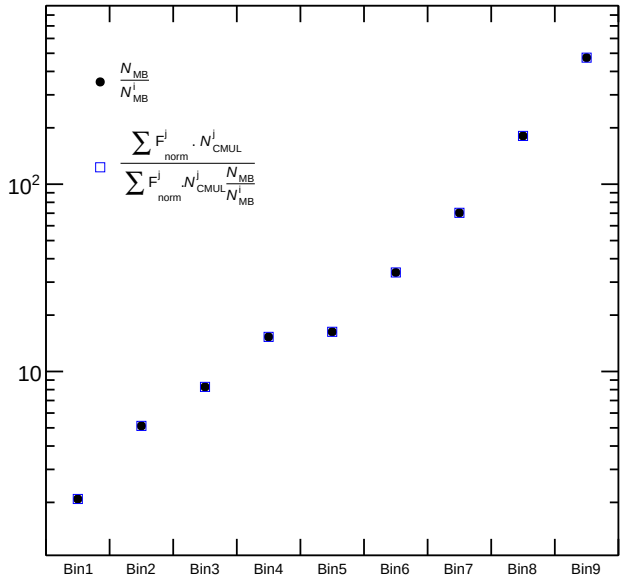

Figure 6.36: Comparison of two methods normalization factor calculation in 2016 data sample

Multiplicity bin (i)	N_{trk}^{cor} range	N_{MB}	$\frac{N_{MB}^{equiv}}{N_{MB}^{equiv,i}}$
Integrated		29392133	
1	1-8	14199098	2.07
2	9-14	5843366	5.03
3	15-20	3584406	8.20
4	21-25	1934966	15.19
5	26-33	1817695	16.17
6	34-41	875026	33.59
7	42-50	419768	70.02
8	51-60	163544	179.72
9	61-80	62410	470.95

Table 6.11: The normalisation factors in multiplicity bins.

6.4.5 Efficiency and corrections factors for relative Υ

We recall Eq.6.17:

$$\Upsilon_i^{rel} = \frac{\Upsilon_i}{\Upsilon_{tot}} = \frac{dN_\Upsilon/dy}{\langle dN_\Upsilon/dy \rangle} = \frac{N_i^\Upsilon}{N_{tot}^\Upsilon} \times \frac{N_{MB}^{equiv}}{N_{MB}^{equiv,i}} \times \epsilon$$

Here, ϵ corresponds to a set of efficiency factors which can be written as Eq. 6.33.

$$\epsilon = \frac{\epsilon_{INEL>0,i}}{\epsilon_{INEL>0}} \times \epsilon_{vtx,QA} \times \frac{1}{\epsilon_{INEL=0}} \times \epsilon_{pu} \tag{6.33}$$

Here, $\epsilon_{INEL>0}$ corresponds to the correction factor due to the INEL>0 selection in multiplicity bins and in integrated case which are shown in Tab. 6.5. $\epsilon_{vtx,QA}$ is the efficiency factor due to the vertex QA cuts for MB and Υ events. $\epsilon_{INEL=0}$ is the correction factor for the contamination of INEL=0 events and ϵ_{pu} is the correction factor due to the pile-up rejection.

6.4.5.1 Vertex QA efficiency

As we applied vertex QA cuts (section 6.2.2.2) to select our events, we computed the efficiency for these associated cuts. We have compared the number of MB events and the number of raw Υ yields using vertex QA cuts and without vertex QA cuts to calculate vertex QA efficiency using Eq. 6.34. The efficiency for the MB events is calculated using Eq. 6.35 and is used to correct the relation charged-particle multiplicity. The number of MB events and raw Υ yields counted with or without using the vertex QA cuts are listed in Table. 6.12.

$$\epsilon_{vtx,QA} = \frac{[\text{Integrated } N_{\Upsilon}/N_{MB}] \text{ (with vertex QA)}}{[\text{Integrated } N_{\Upsilon}/N_{MB}] \text{ (without vertex QA)}} \tag{6.34}$$

$$\epsilon^{\text{MB}}_{\text{vtx,QA}} = \frac{N_{\text{MB}}(\text{with vertex QA cuts})}{N_{\text{MB}}(\text{without vertex QA cuts})} \tag{6.35}$$

	With vertex QA cuts	Without vertex QA cuts
N_{MB}	29392133	31368338
$N_{\Upsilon(1S)}$	3990±125	4120±127

Table 6.12: Integrated number of MB events and raw Υ(1S) yields.

$$\epsilon_{vtx,QA} = 1.03 \pm 0.04$$
$$\epsilon^{MB}_{vtx,QA} = 0.94 \pm 0.00$$

6.4.5.2 INEL>0 efficiency correction for relative Υ yield in the first bin

As we showed is section 6.3.5 the efficiency is close to unity for all the multiplicity bins excepts for the first bin, the relative Υ yield must be corrected accordingly. The correction factor for the first bin has been calculated as follow:

$$\epsilon^{1}_{INEL>0,yield} = \frac{N_{events}[N_{ch} \geq 1 + kINT7 + vtxQA]}{N_{events}[N_{ch} \geq 1 + vtxQA]} \tag{6.36}$$

MC	$N_{events}[N_{ch} \geq 1 + kINT7 + vtxQA]$	$N_{events}[N_{ch} \geq 1 + vtxQA]$	$\epsilon_{INEL>0,yield}$
Pythia8	6821059	7499789	0.91
Epos	9770456	10588405	0.92

Table 6.13: Efficiency for INEL>0 selection

$$\boxed{\epsilon^{1}_{INEL>0,yield} = 0.916 \pm 0.006 \text{ (0.6\% syst)}}$$

6.4.5.3 Correction for INEL=0 contamination

A strict INEL> 0 condition is applied only on MC sample. The data sample includes a contamination of INEL = 0 events. This factor should be evaluated and corrected to the yield. The combination of vtxQA and INE=0 contamination corrections of MB events can be done in two ways:

- To Correct for vtxQA from data then correct for the contamination w/o vtxQA:

$$f1 = \frac{N_{events}(N_{ch} = 0 \text{ and w/o vtxQA + PS})}{N_{events}(N_{ch} \geq 0 \text{ and w/o vtxQA + PS})} = 0.02 \tag{6.37}$$

  Correction factor = $\frac{1.0-f1}{\epsilon^{MB}_{vtx,QA}} = 1.04$

- To Correct for the contamination with vtxQA then correct for vtxQA from MC:

$$\epsilon^{MB}_{vtx,QA}(MC, INEL > 0) = \frac{N_{events}(N_{ch} \geq 0 \text{ and with } vtxQA + PS)}{N_{events}(N_{ch} \geq 0 \text{ and w/o } vtxQA + PS)} = 0.962 \tag{6.38}$$

$$f2 = \frac{N_{events}(N_{ch} = 0 \text{ and with } vtxQA + PS)}{N_{events}(N_{ch} \geq 0 \text{ and with } vtxQA + PS)} = 0.008 \tag{6.39}$$

  Correction factor = $\frac{1.0-f2}{\epsilon^{MB}_{vtx,QA}(MC,INEL>0)} = 1.03$

Therefore, we have found 1% difference between two methods and 0.5% difference between two MC generators. Thus, we used 1.5% systematic uncertainty on the $\epsilon_{INEL=0}$ factor to take into account these differences. We have used the first method to calculate the $\epsilon_{INEL=0}$ factor. The computed final value is, $\epsilon_{INEL=0} = \frac{1}{1-f1}$ =1.02 ± 0.015 (1.5% Syst.) This correction factor will divide to yield.

$$\boxed{\epsilon_{INEL=0} = 1.02 \pm .015}$$

6.4.5.4 Efficiency for pile-up rejection

The pileup efficiency factor can be calculated by comparing MB events with and without pileup cuts using Eq. 6.40 in MC and data. We found the efficiency for pile-up in each multiplicity bin to be close to unity.

$$\epsilon_{pu} = \frac{N^{i}_{PS}/N^{total}_{PS\ w/o\ pile-up}}{N^{i}_{PS}/N^{total}_{PS\ with\ pile-up}} \tag{6.40}$$

6.4.6 Systematic uncertainties on relative Υ

We consider the following systematic uncertainty sources:

- Signal extraction: The uncertainty on signal extraction was estimated by varying fit conditions. We found around 2-4% uncertainty on relative Υ(1S) and 4-7% on relative Υ(2S) per multiplicity bin (section 6.4.2).

- Normalization: We have tested two different normalization methods for the di-muon to MB normalization. We found that the contribution from this source is negligible see (section 6.4.4).
- Pile-up: The uncertainty due to pile-up removal was also tested by removing the pile-up cuts. In this case we found the difference to be less than 1%

In addition to the uncertainty described above we have also applied an additional uncertainty due to our INEL>0 event selection. The computed INEL>0 efficiency is 0.94

6.5 Relative Υ yields in multiplicity bins

Finally the relative Υ(1S) and Υ(2S) yields are calculated using Eq. 6.41. Note that in Eq. 6.41, the efficiency factor, $\epsilon_{INEL>0,i} = 1$ for all bins except for the first bin. The contribution from ϵ_{pu} is considered to be 1 for all multiplicity bins.

$$\Upsilon_i^{rel} = \frac{\Upsilon_i}{\Upsilon_{tot}} = \frac{dN_\Upsilon/dy}{\langle dN_\Upsilon/dy \rangle} = \frac{N_i^\Upsilon}{N_{tot}^\Upsilon} \times \frac{N_{MB}^{equiv}}{N_{MB}^{equiv,i}} \times \frac{\epsilon_{INEL>0,i}}{\epsilon_{INEL>0}} \times \epsilon_{vtx,QA} \times \frac{1}{\epsilon_{INEL=0}} \times \epsilon_{pu} \quad (6.41)$$

The calculated final values for relative Υ(1S) and Υ(2S) for each multiplicity bin is listed in Tab. 6.5

N_{trk}^{cor}	$N_{\Upsilon(1S)_i^{rel}}$ ± stat ± syst	$N_{\Upsilon(2S)_i^{rel}}$ ± stat ± syst
$[1-8]$	0.30 ± 8.06% ± 2.57%	0.28 ± 22.36% ± 4.31%
$[9-14]$	1.00 ± 8.06% ± 2.50%	1.04 ± 18.44% ± 4.27%
$[15-20]$	1.58 ± 8.06% ± 2.50%	1.51 ± 21.38% ± 4.27%
$[21-25]$	1.83 ± 9.85% ± 5.22%	2.23 ± 22.36% ± 6.18%
$[26-33]$	2.70 ± 8.06% ± 3.35%	2.02 ± 27.29% ± 7.16%
$[34-41]$	3.83 ± 9.85% ± 3.35%	3.92 ± 24.33% ± 6.18%
$[42-50]$	4.81 ± 11.70% ± 2.50%	4.26 ±36.22% ± 5.22%
$[51-60]$	4.55 ± 21.38% ± 2.50%	
$[61-80]$	6.60 ± 26.31% ± 4.27%	

6.6 Results

In this section we present the relative Υ(1S), Υ(2S) and their ratio as a function of charged-particle multiplicity at forward rapidity in Fig. 6.37, 6.38 and 6.39 respectively. In the figures, the solid circles represent the data points, vertical black lines represent the statistical errors and the boxes show the systematic uncertainty.

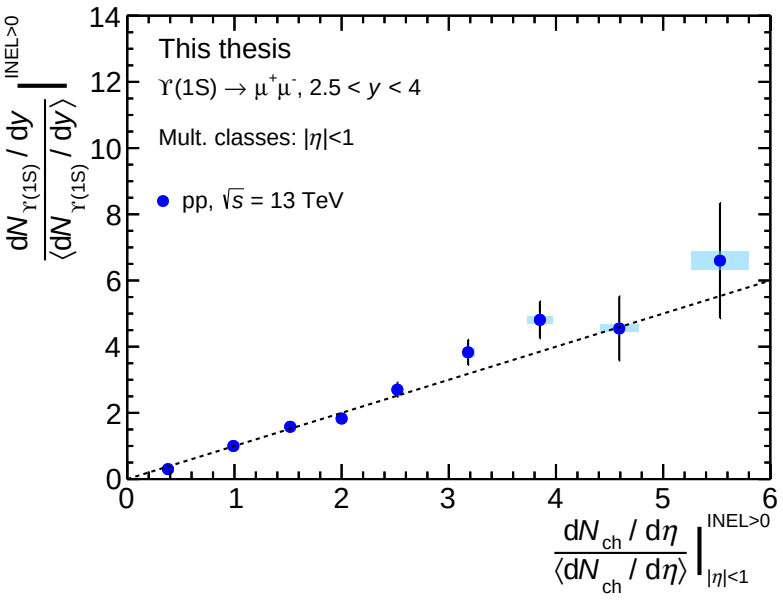

Figure 6.37: Relative Υ(1S) yield as a function of charge-particle multiplicity, the black dashed line is drawn to x=y correlation.

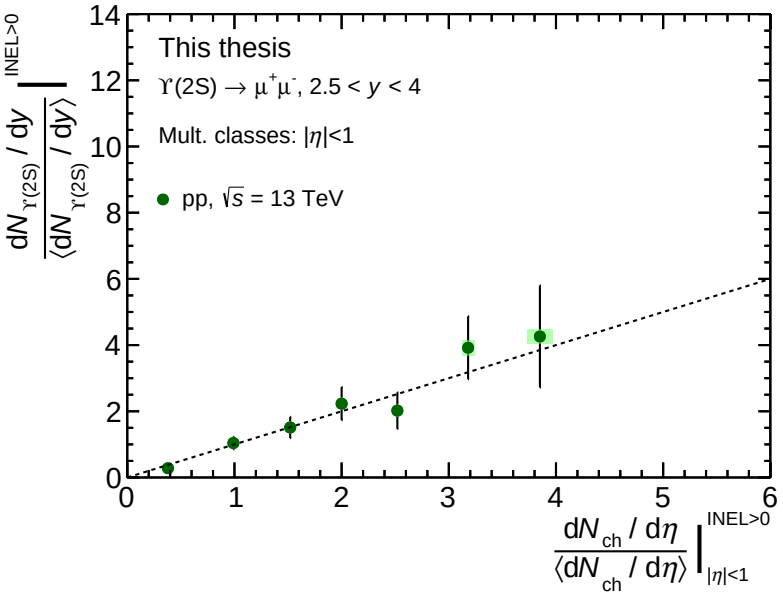

Figure 6.38: Relative Υ(2S) yield as a function of charge-particle multiplicity, the black dashed line is drawn to x=y correlation.

By analyzing 2016 data sample in pp collision at $\sqrt{s} = 13$ TeV, we are able to reach up to ~ 6 times the relative charged particle multiplicity for Υ(1S) and $\sim$4 times for Υ(2S). For Υ(3S) the statistics was not enough to perform this analysis. Reproducing these results with more statistics (full RUN 2 ALICE data sample) will give more precision.

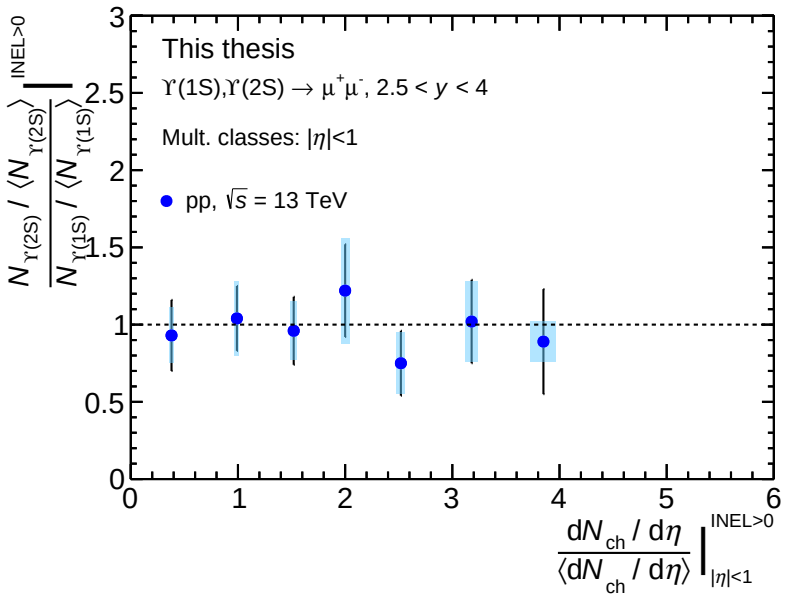

Figure 6.39: Relative ϒ(1S) yield as a function of charge-particle multiplicity, the black dashed line is drawn to x=y correlation.

Summary

In this chapter we presented the first measurement of the ϒ production rate as a function of charge-particle multiplicity using the ALICE framework. The charged particle multiplicity was measured at mid-rapidity using the SPD tracklets as a multiplicity estimator. The Upsilons are measured at forward rapidity from their decay to di-muon using the muon spectrometer. Finally we presented the ϒ(1S), ϒ(2S) and their ratio as a function of multiplicity. Due to lack of statistics the study of ϒ(3S) is not possible. In the next chapter we will present the interpretation of these results.

Chapter 7

Interpretation and discussions

In this chapter we will present the comparison of the self-normalized Υ production as a function of the charged-particle multiplicity with other existing self-normalized quarkonium and open heavy flavor results, introduced in section 3.3.

In section 6.6 we presented the first measurement of self-normalized $\Upsilon(1S)$ and $\Upsilon(2S)$ as a function of multiplicity (Fig. 6.37 and 6.38) in pp collisions at $\sqrt{s} = 13$ TeV. In Fig.7.1 the top panels show the self-normalized $\Upsilon(1S)$ and $\Upsilon(2S)$ versus self-normalized multiplicity and the bottom panel shows the ratio between self-normalized Υ states and self-normalized multiplicity. For both panels, the error bars indicate the statistical uncertainties, the boxes represent the systematic uncertainties. The black dashed line represents a straight line drawn for x=y correlation (top panel) and for y=1 correlation (bottom panel).

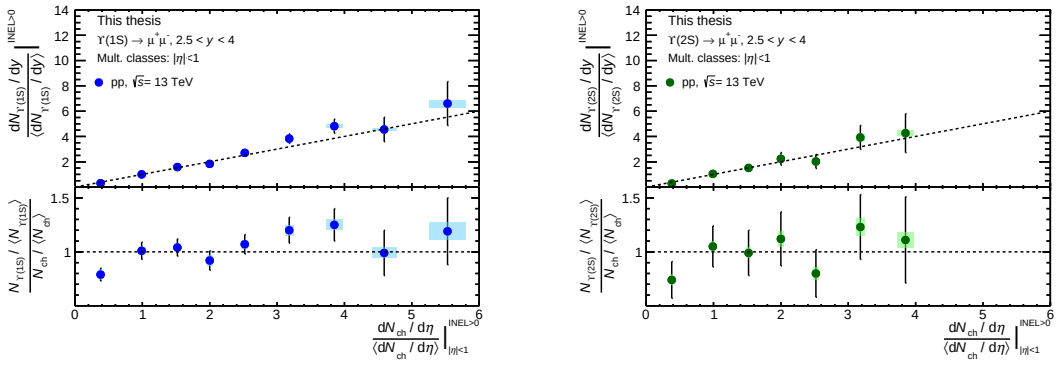

Figure 7.1: Self-normalized $\Upsilon(1S)$ and $\Upsilon(2S)$ in the top panels and their ratio with multiplicity in the bottom panels as a function of the self-normalized charged-particle multiplicity

A small deviation from x=y correlation is observed for both $\Upsilon(1S)$ and $\Upsilon(2S)$ in the first bin where the mean multiplicity is below 1. At least 1 times the mean multiplicity is required to have a Υ production that scales with the standard scaling expectation of MPI scenario as described in section 3.3. The rest of the points show a linear correlation which is compatible with the simple MPI expectation (x=y) within the current uncertainties for both Υ_{1S} and $\Upsilon(2S)$ (Fig. 7.1 bottom panels).

In order to quantify the approximate linear evolution of this correlation we fitted the results with a linear and a 2nd order polynomial function for the $\Upsilon(1S)$ (Fig. 7.2(left)) and $\Upsilon(2S)$ (Fig. 7.2(right)). The experimental data of $\Upsilon(1S)$ is better described by the 2nd

order polynomial fit with a $\chi^2/ndf = 1.04$ than the linear fit. Also for Υ(2S) the 2nd order polynomial fit gives better description with a $\chi^2/ndf = 0.68$. The small deviation of Υ(1S) at high multiplicity is still compatible with linearity within the current uncertainties.

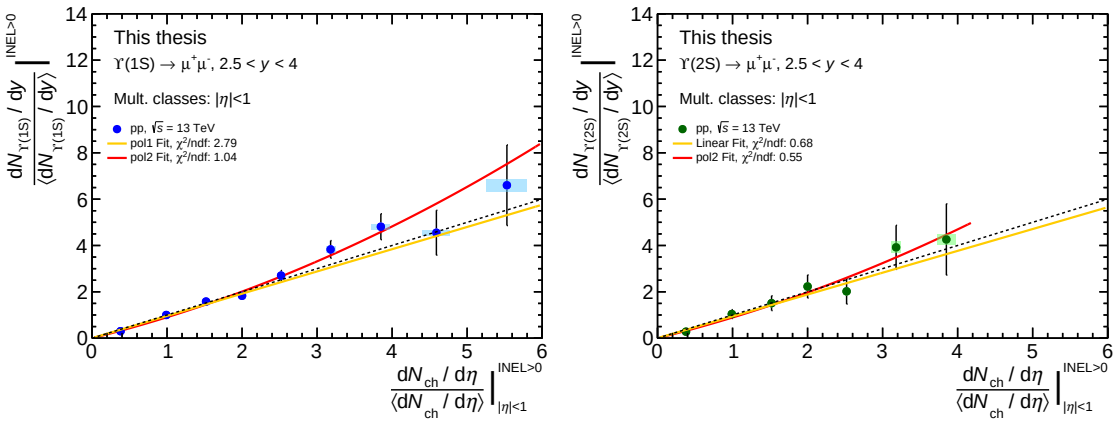

Figure 7.2: Relative Υ_{1S} and Υ_{2S} yield as a function of multiplicity fitted with linear (orange line) and polynomial functions (red line).

The ratio between self-normalized Υ(1S) and Υ(2S) as a function of multiplicity is shown in Fig.7.3. The blue points are the ratios, the black vertical lines represents the combined statistical and systematic uncertainties. The dashed black line is drawn at y=1. The ratio shows a flat trend. When the Υ is measured at forward rapidity and multiplicity is measured at mid-rapidity, the probability to produce a Υ(2S) with respect to its mean is similar to the probability to produce a Υ(1S) with respect to its mean, independent of the multiplicity. The red line refers to a linear fit which describes the data.

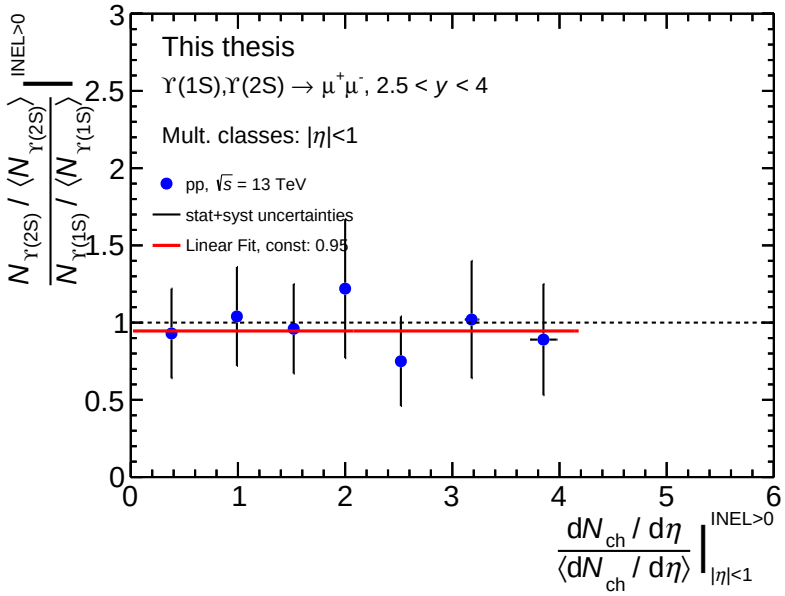

Figure 7.3: Ratio of relative Υ_{2S} and Υ_{1S} as a function of charged-particle multiplicity.

The CMS results in pp collisions at $\sqrt{s} = 2.76$ TeV showed a stronger than linear increase when the Υ and multiplicity (charged tracks) are measured at mid-rapidity [6]. The article

also presents the results for mid-rapidity Υ production as a function of mean transverse energy measured at forward rapidity. It shows a linear increase. We have computed the ratio of $N_{\Upsilon(2S)}/\langle N_{\Upsilon(2S)}\rangle$ over $N_{\Upsilon(1S)}/\langle N_{\Upsilon(1S)}\rangle$ as a function of mean transverse energy $E_T/\langle E_T\rangle$ presented in Fig.7.4 (top panel). The values are taken from [6]. This measurement was performed with a rapidity-gap which is opposite to the rapidity-gap configuration used for the Υ measurements presented in this thesis. Even though the charged-particle multiplicity and transverse energy are not similar observable, their self-normalized quantities can be compared quantitatively. We observe a flat trend, fitted with a constant at one. This shows similar flat trend as presented in 7.3.

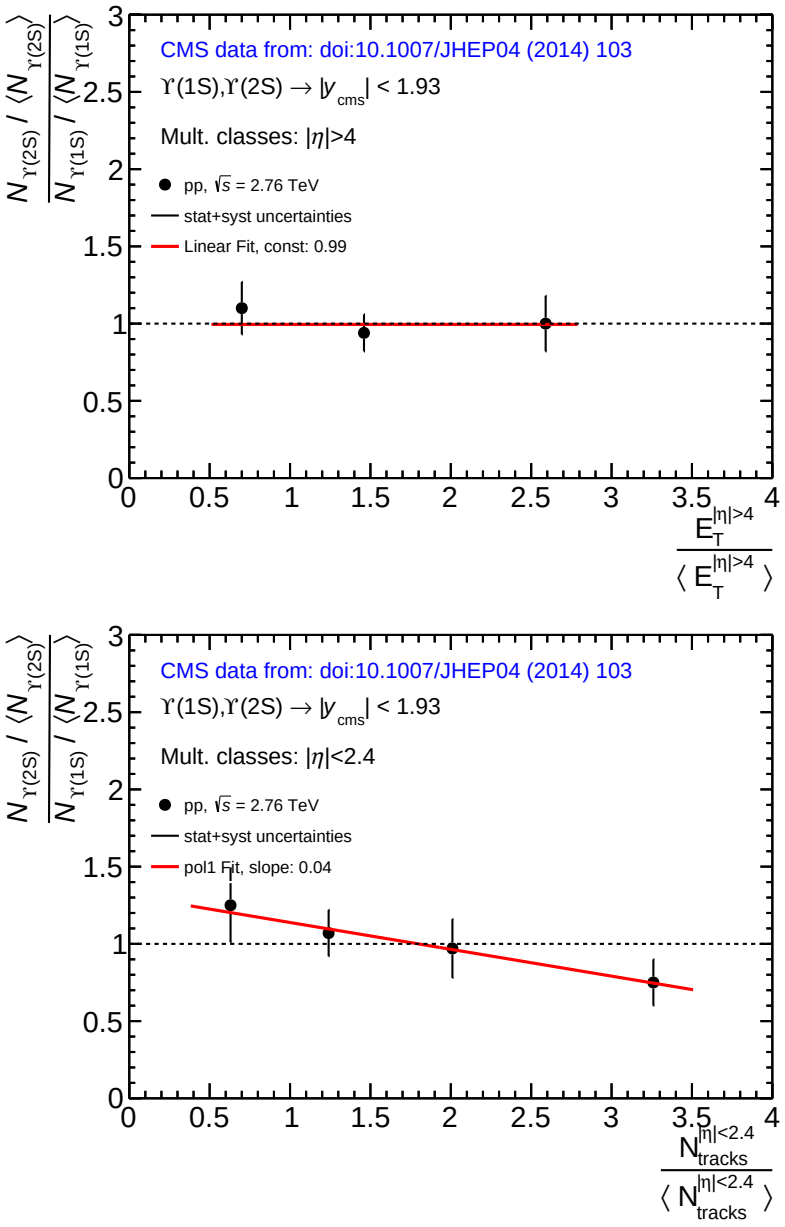

Figure 7.4: Ratio of relative Υ_{2S} and Υ_{1S} as a function of transverse energy (left) and charged tracks (right), the black dashed lines are drawn at y=1

We have also computed the ratio of $N_{\Upsilon(2S)}/\langle N_{\Upsilon(2S)}\rangle$ over $N_{\Upsilon(1S)}/\langle N_{\Upsilon(1S)}\rangle$ as a function of the mean number of tracks $N_{tracks}/\langle N_{tracks}\rangle$ in the mid-rapidity regions shown in Fig.7.4 (bottom panel). The values are taken from [6]. This measurement was performed with-

out a rapidity-gap. It shows a completely different behavior than the measurement with rapidity gap. The right figure shows around 40% decrease. The first three points are still compatible with unity within the uncertainties. It is the last point which triggers the hint of a decreasing slope. It is surprising that at low multiplicity the ratio is greater than one. Indicating that the probability to produce Υ(2S) with respect to its mean is higher than Υ(1S) at low multiplicity. In the article [6], a direct ratio of Υ(2S) over Υ(1S) was shown. The ratio showed a decreasing trend towards higher N_{tracks}. One of the hypothesis to account for this decrease is the dissociation of Υ(2S) in the final state with comover-like effect. It would be difficult to understand the increase at low multiplicity for the self-normalized ratio, under this hypothesis.

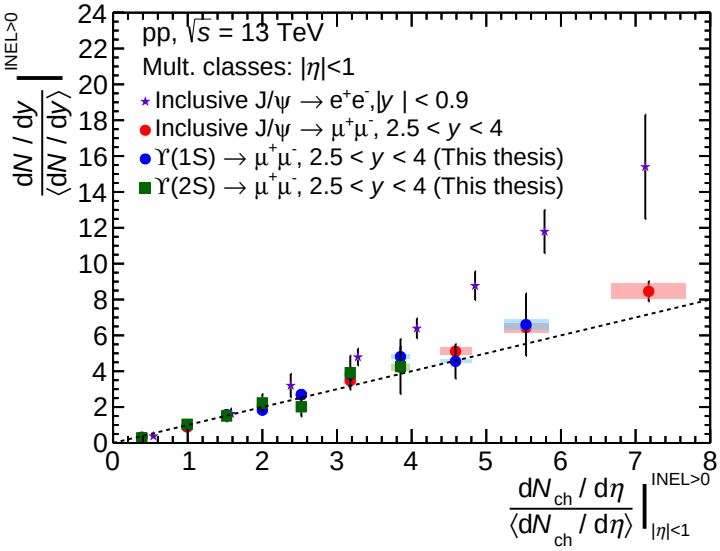

Figure 7.5: Quarkonium production as function of multiplicity

The quarkonia measurements as a function of multiplicity performed in 2016 using ALICE data recorded in pp collision at $\sqrt{s}$ =13 TeV are shown in Fig. 7.5. This figure shows the measured quarkonia in different rapidity ranges (forward and mid-rapidity) with multiplicity always measured at mid-rapidity.

In Fig. 7.5, the blue points represents the self-normalized J/ψ measured at mid-rapidity, the red points shows the self-normalized J/ψ measured at forward rapidity, the violet and green points represents the self-normalized Υ(1S) and Υ(2S) measured at forward rapidity, respectively. For all the cases, multiplicity is always measured at mid-rapidity. The error bars indicate the statistical uncertainty of the extracted yield, the boxes represent the systematic uncertainty on the yield and the multiplicity.

It is clearly visible that Υ(1S) and Υ(2S) show similar trend with J/ψ when the self-normalized yields are measured at forward rapidity. All the self-normalized quarkonia yields measured at forward rapidity increases approximately linearly with the increasing multiplicity. But the self-normalized J/ψ yields measured at mid-rapidity increases stronger than linearly with the increasing multiplicity. This indicates that the correlation is different while measuring the quarkonium and multiplicity in the same rapidity region than introducing a rapidity gap between quarkonium and multiplicity.

We also compare the multiplicity dependence of Υ(1S) with J/ψ (in Fig. 7.6) in pp colli-

sions at $\sqrt{s} = 13$ TeV. The black points are the ratios, the black vertical lines represents the combined statistical and systematic uncertainties. The dashed black line is drawn at y=1. The red line refers to a linear fit which describes the data. We observe a flat trend which is similar to the trend observed for the ratio of Υ(2S) over Υ(1S) (Fig. 7.3). This indicates that the correlation between the self-normalized yields in forward rapidity and multiplicity at mid-rapidity is independent of mass and quark content within the current uncertainties.

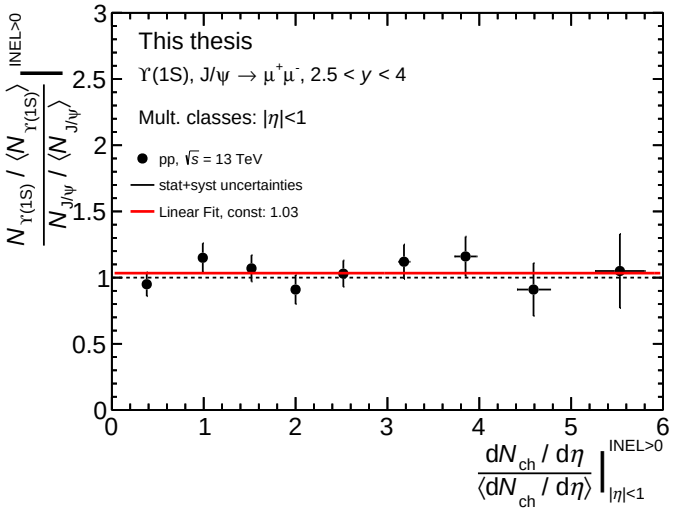

Figure 7.6: Ratio of relative Υ_{1S} and J/ψ as a function of charged-particle multiplicity.

The bottomonium sector can be investigated further in pp collisions as proposed in following:

- Study of Υ production as function of multiplicity when Υ and multiplicity are both measured at forward rapidity. This measurement can be performed in ALICE by measuring Υ in muonic channel and charged-particle multiplicity in the V0C detector which is located at forward rapidity with RUN 2 combined statistics.
- Study of Υ production as function of multiplicity when Υ is measured at mid-rapidity and multiplicity is measured at forward rapidity. The first measurement of Υ production as a function of transverse energy by CMS which qualitatively shows linear correlation. This will be interesting to verify the measurement at higher energy with charged-particle multiplicity. It is not possible to perform this measurement in ALICE with RUN2 data because of low statistics. Hopefully in RUN 3, this measurement can be performed in ALICE by measuring Υ in electron channel and charged-particle multiplicity in the V0C detector.

As the rapidity gap has a considerable affect on this correlation, the above studies can give us more precise idea about the evolution of this correlation in pp collisions. In addition to quarkonium, the correlation for D-mesons are interesting as well. The correlation measured for D-mesons without any rapidity gap shows stronger than linear increase as seen for quarkonium. The stronger increase still remains when the correlation is measured with a rapidity gap [72]. The D-mesons are measured at mid-rapidity and multiplicity is measured in forward rapidity. The observed trend raises the question either the rapidity gap has a larger impact when the hard probes are measured at forward rapidity or the correlation is different for open heavy-flavor and quarkonium when applying the rapidity gap.

Chapter 8

Conclusion

In the first chapter of this manuscript, we discussed the theoretical background of particle physics for this thesis. We introduced elementary particles of the standard model and their interactions. The strong interaction forces the quarks and gluons to be confined into hadrons. The quark-gluon plasma is a deconfined state of quark and gluons at high energy. The evolution of QGP can be studied in heavy-ion collision for which different parts of hadronic collision need to be understood properly. The observable, charge-particle multiplicity allows us to study the soft particle production in hadronic collisions. The LHC is the most powerful and complex experimental facility at present where different collisions systems are being investigated at different energies. In this context, the studies of hadronic collisions are becoming more challenging. At high energy, the high multiplicity pp collisions is showing very intriguing signs which were believed to be observed in Pb-Pb collisions due to the formation of QGP. This challenges our current understanding of pp collisions and motivates the study of different correlations in the system such as particle production as a function of multiplicity. In the second chapter, we discussed the quarkonia production as a hard process. The quarkonium is an important probe to study QGP as it is formed in the early stage of a collision and can be affected by the presence of QGP. The production of quarkonium is a very complicated process which needs both pQCD and non-pQCD approach. This makes the understanding of quarkonium production and it's correlation with the charged particles produced in the same collision very interesting. The correlation between quarkonium or any hard probe and multiplicity can be studied in different configurations of kinematic regions, collision energies and systems. Among all of these, the most interesting one is the rapidity dependence of this correlation. We presented a summary on the study of this correlation based on the available experimental results and theoretical predictions. In the third chapter we presented a short description about the LHC and it's major experiments. We described different parts of the ALICE detector in detail which were used for this thesis (e.g SPD, muon spectrometer). Finally, one of the future upgrade project concerning muon trigger system was discussed. The fourth chapter was dedicated to test bench performance study for FEERIC cards which will be fully operational after LS2. The methodology and work procedure of this thesis has been presented in detail in the fifth chapter. The charged-particle was estimated from SPD tracklets and the upsilon signals measured in the muon spectrometer. We presented different systematic sources and their contributions to the final uncertainty calculation. The results showed in this chapter are discussed and interpreted in the sixth chapter.

The Υ production at forward rapidity as a function of the charged-particle multiplicity at mid-rapidity shows a linear increase with increasing multiplicity. The relative Υ(1S) and Υ(2S) yields are reached about 6 times and 4 times mean multiplicity respectively which is higher than the measurements from CMS [6]. Furthermore, the rapidity dependence on the measured correlations is confirmed by different probes (J/ψ, Υ and D-meson).

No clear energy dependence is found within the current uncertainties. The study of this correlation can be extended to other self-normalized observables like mean transverse momentum ($\langle p_{\mathrm{T}} \rangle$) and mean transverse energy ($\langle E_T \rangle$) which will give additional information to compare the correlation in different systems (pPb, PbPb).

Bibliography

[1] S. L. Glashow, J. Iliopoulos and L. Maiani, *Weak interactions with lepton-hadron symmetry*, *Physics Review D* **2** (1970) 1285.

[2] S. Weinberg, *A model of leptons*, *Physical Review Letters* **19** (1967) 1264.

[3] F. Halzen and A. D. Martin, *Quarks and leptons: An introductory course in modern particle physics*, *New York, Usa: Wiley (1984) 396p* .

[4] M. Gell-Mann, *Symmetries of baryons and mesons*, *Physics Review* **125** (1962) 1067.

[5] O. W. Greenberg, *Spin and unitary-spin independence in a paraquark model of baryons and mesons*, *Physical Review Letters* **13** (1964) 598.

[6] CMS collaboration, V. K. S. Chatrchyan, G. Hmayakyan, *Event activity dependence of Υ(nS) production in $\sqrt{s_{NN}} = 5.02$ TeV pPb and $\sqrt{s} = 2.76$ TeV pp collisions*, *Journal of High Energy Physics* **04** (2014) 103 [1312.6300].

[7] Particle Data Group collaboration, M. Tanabashi, K. Hagiwara, K. Hikasa, K. Nakamura, Y. Sumino, F. Takahashi *et al.Physics Review D* **98** (2018) 030001.

[8] A. Salam and J. C. Ward, *Weak and electromagnetic interactions*, *Il Nuovo Cimento (1955-1965)* **11** (1959) 568.

[9] F. Englert and R. Brout, *Broken symmetry and the mass of gauge vector mesons*, *Physical Review Letters* **13** (1964) 321.

[10] G. Aad, T. Abajyan, B. Abbott, J. Abdallah, S. A. Khalek, A. Abdelalim *et al.*, *Observation of a new particle in the search for the Standard Model Higgs boson with the ATLAS detector at the LHC*, *Physics Letters B* **716** (2012) 1 .

[11] S. Chatrchyan, V. Khachatryan, A. Sirunyan, A. Tumasyan, W. Adam, E. Aguilo *et al.*, *Observation of a new boson at a mass of 125 GeV with the CMS experiment at the LHC*, *Physics Letters B* **716** (2012) 30 .

[12] R. P. Feynman, *The behavior of hadron collisions at extreme energies*, *Conference Proceedings.* **C690905** (1969) 237.

[13] D. J. Gross and F. Wilczek, *Asymptotically free gauge theories. i*, *Physics Review D* **8** (1973) 3633.

[14] H. D. Politzer, *Asymptotic freedom: An approach to strong interactions*, *Physics Reports* **14** (1974) 129 .

[15] J. C. Collins and M. J. Perry, *Superdense matter: Neutrons or asymptotically free quarks*, *Physical Review Letters* **34** (1975) 1353.

[16] E. V. Shuryak, *Quantum chromodynamics and the theory of superdense matter*, *Physics Reports* **61** (1980) 71 .

[17] P. Rosnet, *Quark-Gluon Plasma: from accelerator experiments to early Universe*, in *11th Rencontres du Vietnam: Cosmology: 50 years after CMB discovery Quy Nhon, Vietnam, August 16-22, 2015*, 2015, 1510.04200.

[18] S. B. Rüster, V. Werth, M. Buballa, I. A. Shovkovy and D. H. Rischke, *Phase diagram of neutral quark matter: Self-consistent treatment of quark masses*, *Physics Review D* **72** (2005) 034004.

[19] Z. Fodor and S. Katz, *Critical point of QCD at finite T and μ, lattice results for physical quark masses*, *Journal of High Energy Physics* **2004** (2004) 050.

[20] A. Bazavov, H.-T. Ding, P. Hegde, O. Kaczmarek, F. Karsch, N. Karthik *et al.*, *Chiral crossover in QCD at zero and non-zero chemical potentials*, *Physics Letters B* (2019) .

[21] M. A. C. Lamont, *Neutral Strange Particle Production in Ultra-Relativistic Heavy Ion collisions $\sqrt{s_{NN}} = 130$ GeV*, Ph.D. thesis, Birmingham University, 2002.

[22] T. Matsui and H. Satz, *J/ψ Suppression by Quark-Gluon Plasma Formation*, *Physics Letters* **B178** (1986) 416.

[23] J. D. Bjorken, *Energy Loss of Energetic Partons in Quark-Gluon Plasma: Possible Extinction of High p_{T} Jets in Hadron-Hadron Collisions*, *FERMILAB-PUB-82-059-THY, FERMILAB-PUB-82-059-T* (1982) .

[24] L. Ramello, *Quarkonium production and suppression in Pb+Pb and p+A collisions at SPS energies*, *Nuclear Physics A* **774** (2006) 59 .

[25] A. Buckley, J. Butterworth, S. Gieseke, D. Grellscheid, S. Höche, H. Hoeth *et al.*, *General-purpose event generators for LHC physics*, *Physics Reports* **504** (2011) 145.

[26] T. Sjöstrand, S. Mrenna and P. Skands, *PYTHIA 6.4 physics and manual*, *Journal of High Energy Physics* **2006** (2006) 026.

[27] H. Drescher, M. Hladik, S. Ostapchenko, T. Pierog and K. Werner, *Parton-based Gribov-Regge theory*, *Physics Reports* **350** (2001) 93 .

[28] S. Höche, *Introduction to parton-shower event generators*, in *Proceedings, Theoretical Advanced Study Institute in Elementary Particle Physics: Journeys Through the Precision Frontier: Amplitudes for Colliders (TASI 2014): Boulder, Colorado, June 2-27, 2014*, pp. 235–295, 2015, 1411.4085, DOI.

[29] H. Lai, J. Huston, S. Kuhlmann, J. Morfin, F. Olness, J. Owens *et al.*, *Global QCD analysis of parton structure of the nucleon: CTEQ5 parton distributions*, *The European Physical Journal C - Particles and Fields* **12** (2000) 375.

[30] R. P. Feynman, *Very high-energy collisions of hadrons*, *Physical Review Letters* **23** (1969) 1415.

[31] Z. Koba, H. Nielsen and P. Olesen, *Scaling of multiplicity distributions in high energy hadron collisions*, *Nuclear Physics B* **40** (1972) 317 .

[32] UA5 collaboration, G. J. Alner *et al.*, *Multiplicity distributions in different pseudorapidity intervals at a CMS energy of 540 GeV*, *Physics Letters* **160B** (1985) 193.

[33] Ames-Bologna-CERN-Dortmund-Heidelberg-Warsaw Collaboration collaboration, A. Breakstone, R. Campanini, H. B. Crawley, G. M. Dallavalle, M. M. Deninno, K. Doroba *et al.*, *Charged multiplicity distribution in* pp *interactions at CERN ISR energies*, *Physics Review D* **30** (1984) 528.

[34] A. Giovannini and R. Ugoccioni, *Clan structure analysis and QCD parton showers in multiparticle dynamics. an intriguing dialog between theory and experiment*, *International Journal of Modern Physics A* **20** (2005) 3897 [hep-ph/0405251].

[35] J. F. Grosse-Oetringhaus and K. Reygers, *Charged-particle multiplicity in proton–proton collisions*, *Journal of Physics G: Nuclear and Particle Physics* **37** (2010) 083001.

[36] UA5 collaboration, G. J. Alner *et al.*, *Scaling violations in multiplicity distributions at 200 GeV and 900 GeV*, *Physics Letters* **167B** (1986) 476.

[37] T. Alexopoulos *et al.*, *The role of double parton collisions in soft hadron interactions*, *Physics Letters* **B435** (1998) 453.

[38] G. Alner, K. Alpgard, P. Anderer, R. Ansorge, B. Asman, S. Berglund *et al.*, *UA5: A general study of proton-antiproton physics at* $\sqrt{s} = 546$ *GeV*, *Physics Reports* **154** (1987) 247 .

[39] ALICE collaboration, *Charged-particle multiplicity measurement with Reconstructed Tracks in pp Collisions at* $\sqrt{s} = 0.9$ *and 7 TeV with ALICE at the LHC*, *ALICE-PUBLIC-2013-001* (2013) 27.

[40] The CMS collaboration, V. Khachatryan, A. M. Sirunyan, A. Tumasyan, W. Adam and T. Bergauer, *Observation of long-range, near-side angular correlations in proton-proton collisions at the LHC*, *Journal of High Energy Physics* **2010** (2010) 91.

[41] B. Alver, B. B. Back, M. D. Baker, M. Ballintijn, D. S. Barton, R. R. Betts *et al.*, *System size dependence of cluster properties from two-particle angular correlations in* $\mathrm{Cu} + \mathrm{Cu}$ *and* $\mathrm{Au} + \mathrm{Au}$ *collisions at* $\sqrt{s_{NN}} = 200$ *gev*, *Physics Review C* **81** (2010) 024904.

[42] R. Hagedorn and J. Rafelski, *From hadron gas to quark matter, 1*, no. CERN-TH-2947. Sep, 1980.

[43] A. Capella, *Strangeness enhancement in heavy ion collisions*, *Physics Letters B* **364** (1995) 175 .

[44] K. Safarík, *Strangeness production at CERN SPS*, *Journal of Physics G: Nuclear and Particle Physics* **27** (2001) 579.

[45] NA49 collaboration, A. M. for the NA49 Collaboration:, S. V. Afanasiev, T. Anticic, D. Barna, J. Bartke, R. A. Barton *et al.*, *Lambda production in central Pb+Pb collisions at CERN-SPS energies*, *Journal of Physics* **G28** (2002) 1761.

[46] STAR Collaboration collaboration, B. I. Abelev, M. M. Aggarwal, Z. Ahammed, B. D. Anderson, D. Arkhipkin, G. S. Averichev *et al.*, *Enhanced strange baryon production in Au+Au collisions compared to* $p + p$ *at* $\sqrt{s_{NN}} = 200$ *GeV*, *Physics Review C* **77** (2008) 044908.

[47] ALICE collaboration, J. Adam *et al.*, *Enhanced production of multi-strange hadrons in high-multiplicity proton-proton collisions*, *Nature Physics* **13** (2017) 535 [1606.07424].

[48] J. J. Aubert, U. Becker, P. J. Biggs, J. Burger, M. Chen, G. Everhart *et al.*, *Experimental observation of a heavy particle J*, *Physical Review Letters* **33** (1974) 1404.

[49] J. E. Augustin, A. M. Boyarski, M. Breidenbach, F. Bulos, J. T. Dakin, G. J. Feldman *et al.*, *Discovery of a narrow resonance in e^+e^- annihilation*, *Physical Review Letters* **33** (1974) 1406.

[50] S. W. Herb, D. C. Hom, L. M. Lederman, J. C. Sens, H. D. Snyder, J. K. Yoh *et al.*, *Observation of a Dimuon Resonance at 9.5 GeV in 400 GeV Proton-Nucleus Collisions*, *Physical Review Letters* **39** (1977) 252.

[51] W. R. Innes *et al.*, *Observation of Structure in the Υ Region*, *Physical Review Letters* **39** (1977) 1240.

[52] K. Ueno, B. C. Brown, C. N. Brown, W. R. Innes, R. D. Kephart, T. Yamanouchi *et al.*, *Evidence for the υ(2s) and a search for new narrow resonances*, *Physical Review Letters* **42** (1979) 486.

[53] CDF Collaboration collaboration, T. Affolder, H. Akimoto, A. Akopian, M. G. Albrow, P. Amaral, S. R. Amendolia *et al.*, *Production of $\Upsilon(1S)$ mesons from χ_b decays in $p\overline{p}$ collisions at $\sqrt{s} = 1.8$TeV*, *Physical Review Letters* **84** (2000) 2094.

[54] C. Quigg and J. L. Rosner, *Quantum mechanics with applications to quarkonium*, *Physics Reports* **56** (1979) 167 .

[55] A. Andronic, F. Arleo, R. Arnaldi, A. Beraudo, E. Bruna, D. Caffarri *et al.*, *Heavy-flavour and quarkonium production in the LHC era: from proton-proton to heavy-ion collisions*, *The European Physical Journal C* **76** (2016) 107.

[56] H. Fritzsch, *Producing heavy quark flavors in hadronic collisions–' a test of Quantum Chromodynamics*, *Physics Letters B* **67** (1977) 217 .

[57] E. C. Poggio, H. R. Quinn and S. Weinberg, *Smearing method in the quark model*, *Physics Review D* **13** (1976) 1958.

[58] J. Amundson, O. boli, E. Gregores and F. Halzen, *Colorless states in perturbative QCD: Charmonium and rapidity gaps*, *Physics Letters B* **372** (1996) 127 .

[59] J. P. Lansberg, *Total J/Psi and Υ production cross section at the LHC: theory vs. experiment*, *International Conference of High Energy Physics* **ICHEP2010** (2010) 206 [1012.2815].

[60] G. T. Bodwin, E. Braaten and G. P. Lepage, *Erratum: Rigorous QCD analysis of inclusive annihilation and production of heavy quarkonium*, *Physics Review D* **55** (1997) 5853.

[61] M. Butenschoen and B. A. Kniehl, *J/ψ Polarization at the Tevatron and the LHC: Nonrelativistic-QCD Factorization at the Crossroads*, *Physical Review Letters* **108** (2012) 172002.

[62] B. Gong, L.-P. Wan, J.-X. Wang and H.-F. Zhang, *Polarization for Prompt J/ψ and ψ(2s) Production at the Tevatron and LHC*, *Physical Review Letters* **110** (2013) 042002.

[63] K.-T. Chao, Y.-Q. Ma, H.-S. Shao, K. Wang and Y.-J. Zhang, *J/ψ Polarization at Hadron Colliders in Nonrelativistic QCD*, *Physical Review Letters* **108** (2012) 242004.

[64] S. Porteboeuf and R. G. de Cassagnac, *J/ψ yield vs. multiplicity in proton-proton collisions at the LHC*, *Nuclear Physics B - Proceedings Supplements* **214** (2011) 181 .

[65] B. Trzeciak, *Measurements of Quarkonium Polarization and Production versus Charged-Particle Multiplicity in p+p Collisions at $\sqrt{s} = 500 GeV$ in the STAR Experiment: The XXVth International Conference on Ultrarelativistic Nucleus-Nucleus Collisions*, *Nuclear Physics A* **956** (2016) 721.

[66] ALICE collaboration, B. Abelev *et al.*, *J/ψ Production as a Function of Charged Particle Multiplicity in pp Collisions at $\sqrt{s} = 7$ TeV*, *Physics Letters* **B712** (2012) 165 [1202.2816].

[67] ALICE collaboration, S. G. Weber, *Measurement of J/ψ production as a function of event multiplicity in pp collisions at $\sqrt{s} = 13, TeV$ with ALICE*, *Nuclear Physics* **A967** (2017) 333 [1704.04735].

[68] ALICE collaboration, J. Adam *et al.*, *Measurement of charm and beauty production at central rapidity versus charged-particle multiplicity in proton-proton collisions at $\sqrt{s} = 7$ TeV*, *Journal of High Energy Physics* **09** (2015) 148 [1505.00664].

[69] ALICE collaboration, D. Thakur, *Quarkonium production as a function of charged-particle multiplicity in pp and pPb collisions measured by ALICE at the LHC*, *Proceedings of Science* **HardProbes2018** (2019) 164 [1901.02627].

[70] ALICE collaboration, D. Adamov *et al.*, *J/ψ production as a function of charged-particle pseudorapidity density in p-Pb collisions at $\sqrt{s_{\rm NN}} = 5.02$ TeV*, *Physics Letters* **B776** (2018) 91 [1704.00274].

[71] J. Crkovská, B. Espagnon and Z. Conesa del Valle, *Study of the J/ψ production in pp collisions at $\sqrt{s}$ =5.02 TeV and of the J/ψ production multiplicity dependence in p-Pb collisions at $\sqrt{s_{\rm NN} = 8.16}$ TeV with ALICE at the LHC*, Ph.D. thesis, 2018.

[72] ALICE collaboration, J. Adam *et al.*, *Measurement of D-meson production versus multiplicity in p-Pb collisions at $\sqrt{\rm s_{NN}} = 5.02$ TeV*, *Journal of High Energy Physics* **08** (2016) 078 [1602.07240].

[73] L. Kosarzewski, *Measurements of Upsilon production in pp collisions at $\sqrt{s} = 500$ GeV with the STAR experiment*, Ph.D. thesis, 2018.

[74] CMS collaboration, *Dependence of the $\Upsilon(nS)$ production ratios on charged particle multiplicity in pp collisions at $\sqrt{s} = 7$* TeV, 2016.

[75] STAR collaboration, B. Trzeciak, *J/ψ and $\psi(2S)$ measurement in p+p collisions $\sqrt{s}$ = 200 and 500 GeV with the STAR experiment*, *Journal of Physics: Conference Series* **668** (2016) 012093 [1512.07398].

[76] ALICE collaboration, J. Adam *et al.*, *Centrality dependence of inclusive J/ψ production in p-Pb collisions at $\sqrt{s_{\rm NN}} = 5.02$ TeV*, *Journal of High Energy Physics* **11** (2015) 127 [1506.08808].

[77] T. Sjöstrand, S. Mrenna and P. Skands, *A brief introduction to PYTHIA 8.1*, *Computer Physics Communications* **178** (2008) 852.

[78] S. G. Weber, A. Dubla, A. Andronic and A. Morsch, *Elucidating the multiplicity dependence of J/ψ production in proton-proton collisions with PYTHIA8*, *The European Physical Journal C* **79** (2019) 36.

[79] K. Werner, B. Guiot, I. Karpenko and T. Pierog, *Analyzing radial flow features in p-Pb and p-p collisions at several TeV by studying identified-particle production with the event generator EPOS3*, *Physics Review C* **89** (2014) 064903.

[80] E. G. Ferreiro and C. Pajares, *High multiplicity pp events and J/ψ production at energies available at the CERN Large Hadron Collider*, *Physics Review C* **86** (2012) 034903.

[81] B. Z. Kopeliovich, H. J. Pirner, I. K. Potashnikova, K. Reygers and I. Schmidt, *J/ψ in high-multiplicity pp collisions: Lessons from pa collisions*, *Physics Review D* **88** (2013) 116002.

[82] L. Evans and P. Bryant, *LHC Machine*, *Journal of Instrumentation* **3** (2008) S08001.

[83] E. Mobs, *The CERN accelerator complex*, *General Photo, OPEN-PHO-ACCEL-2016-009* (2016) 1.

[84] ATLAS collaboration, G. Aad, E. Abat, J. Abdallah, A. A. Abdelalim, A. Abdesselam, O. Abdinov *et al.*, *The ATLAS Experiment at the CERN Large Hadron Collider*, *Journal of Instrumentation* **3** (2008) S08003.

[85] CMS collaboration, S. Chatrchyan, G. Hmayakyan, V. Khachatryan, A. M. Sirunyan, W. Adam, T. Bauer *et al.*, *The CMS experiment at the CERN LHC*, *Journal of Instrumentation* **3** (2008) S08004.

[86] LHCb collaboration, A. F. Barbosa, I. Bediaga, G. Cernicchiaro, G. Guerrer, H. P. L. Jr, A. A. Machado *et al.*, *The LHCb detector at the LHC*, *Journal of Instrumentation* **3** (2008) S08005.

[87] ALICE collaboration, K. Aamodt, A. A. Quintana, R. Achenbach, S. Acounis, D. Adamov, C. Adler *et al.*, *The ALICE experiment at the CERN LHC*, *Journal of Instrumentation* **3** (2008) S08002.

[88] ALICE collaboration, B. Abelev *et al.*, *Technical design report for the upgrade of the ALICE Inner Tracking System*, *Journal of Physics G: Nuclear and Particle Physics* **41** (2014) 087002.

[89] ALICE collaboration, G. Dellacasa *et al.*, *ALICE: Technical design report of the Time Projection Chamber TPC*, Tech. Rep. CERN-OPEN-2000-183, CERN-LHCC-2000-001, 2000.

[90] ALICE collaboration, G. Dellacasa *et al.*, *ALICE: Technical design report of the Time of Flight system (TOF)*, 2000.

[91] ALICE collaboration, P. Cortese *et al.*, *ALICE: Addendum to the technical design report of the Time of Flight system (TOF)*, Tech. Rep. CERN-LHCC-2002-016, 2002.

[92] ALICE collaboration, S. Acharya *et al.*, *The ALICE Transition Radiation Detector: construction, operation and performance*, *Nucl. Instrum. Meth.* **A881** (2018) 88 [1709.02743].

[93] ALICE collaboration, F. Piuz, W. Klempt, L. Leistam and D. Groot, *ALICE high-momentum particle identification: Technical Design Report*, Tech. Rep. CERN-LHCC-98-019, Geneva, 1998.

[94] ALICE collaboration, P. Cortese, G. Dellacasa, R. Gemme, L. Sitta, R. M, A. Ahmad *et al.*, *ALICE Electromagnetic Calorimeter Technical Design Report*, Tech. Rep. CERN-LHCC-2008-014. ALICE-TDR-14, Aug, 2008.

[95] J. Allen, C. Bernard, O. Bourrion, M. Chala, M. Del Franio, O. Driga *et al.*, *ALICE DCal: An Addendum to the EMCal Technical Design Report Di-Jet and Hadron-Jet correlation measurements in ALICE*, Tech. Rep. CERN-LHCC-2010-011. ALICE-TDR-14-add-1, Jun, 2010.

[96] ALICE collaboration, G. Dellacasa *et al.*, *ALICE Technical Design Report of the photon spectrometer (PHOS)*, Tech. Rep. CERN-LHCC-99-04, 1999.

[97] ALICE collaboration, J. Adam, D. Adamová *et al.*, *ALICE: Addendum to the Technical Design Report of the Photon Multiplicity Detector (PMD)*, Tech. Rep. CERN-LHCC-2003-038, 2003.

[98] ALICE collaboration, P. Cortese *et al.*, *ALICE Technical Design Report on forward detectors: FMD, T0 and V0*, Tech. Rep. CERN-LHCC-2004-025, Geneva, 2004.

[99] ALICE collaboration, J. Adam, D. Adamová *et al.*, *Performance of the ALICE VZERO system*, *Journal of Instrumentation* **8** (2013) P10016.

[100] ALICE collaboration, G. Dellacasa *et al.*, *ALICE Technical Design Report of the Zero Degree Calorimeter (ZDC)*, Tech. Rep. CERN-LHCC-99-05, Geneva, 1999.

[101] ALICE collaboration, A. Villatoro Tello, *AD, the ALICE diffractive detector*, *American Institute of Physics Proceedings* **1819** (2017) 040020.

[102] ALICE collaboration, J. Adam, D. Adamová *et al.*, *The ALICE Forward Multiplicity Detector*, *International Journal of Modern Physics* **E16** (2007) 2432.

[103] ALICE collaboration, A. Fernández *et al.*, *ACORDE, a Cosmic Ray Detector for ALICE*, *Nucl. Instrum. Meth.* **A572** (2007) 102 [physics/0606051].

[104] A. collaboration, *Alignment of the ALICE Inner Tracking System with cosmic-ray tracks*, *Journal of Instrumentation* **5** (2010) P03003.

[105] D. Elia, J. Grosse-Oetringhaus, M. Nicassio and T. Virgili, *The pixel detector based tracklet reconstruction algorithm in ALICE*, Tech. Rep. ARDA-Note-2009-005, CERN, Geneva, Nov, 2009.

[106] J. Alme, Y. Andres, S. Bablok, N. Bialas, R. Bolgen, U. Bonnes *et al.*, *The ALICE TPC, a large 3-dimensional tracking device with fast readout for ultra-high multiplicity events*, *Nuclear Instruments and Methods in Physics Research Section A: Accelerators, Spectrometers, Detectors and Associated Equipment* **622** (2010) 316.

[107] W. Blum, W. Riegler and L. Rolandi, *Particle detection with drift chambers; 2nd ed.* Springer, Berlin, 2008, 10.1007/978-3-540-76684-1.

[108] S. van der Meer, *Calibration of the effective beam height in the ISR*, Tech. Rep. CERN-ISR-PO-68-31. ISR-PO-68-31, Geneva, 1968.

[109] ALICE collaboration, G. Dellacasa *et al.*, *ALICE technical design report of the dimuon forward spectrometer*, Tech. Rep. CERN-LHCC-99-22, Geneva, 1999.

[110] L. S. Azhgirey, I. S. Baishev, K. M. Potter and V. V. Talanov, *Machine Induced Background in the Low Luminosity Insertions of the LHC*, .

[111] ALICE collaboration, D. Nouais *et al.*, *The ALICE silicon drift detector system*, *Nucl. Instrum. Meth.* **A501** (2001) 119.

[112] ALICE collaboration, B. Abelev *et al.*, *Upgrade of the ALICE Experiment: Letter Of Intent*, *Journal of Physics* **G41** (2014) 087001.

[113] ALICE Collaboration collaboration, C. W. Fabjan, L. Jirdn, V. Lindestruth, L. Riccati, D. Rorich, P. Van de Vyvre *et al.*, *ALICE trigger data-acquisition high-level trigger and control system: Technical Design Report*, Technical Design Report ALICE. CERN, Geneva, 2004.

[114] ALICE collaboration, *Performance of the ALICE experiment at the CERN LHC*, *International Journal of Modern Physics A* **29** (2014) 1430044.

[115] H. Engel, T. Alt, T. Breitner, A. G. Ramirez, T. Kollegger, M. Krzewicki *et al.*, *The ALICE high-level trigger read-out upgrade for LHC Run 2*, *Journal of Instrumentation* **11** (2016) C01041.

[116] ALICE collaboration, B. Abelev *et al.*, *Upgrade of the ALICE Experiment: Letter of Intent*, *Journal of Physics G: Nuclear and Particle Physics* **41** (2014) 087001.

[117] ALICE collaboration, Abelev *et al.*, *Technical design report for the upgrade of the alice inner tracking system*, *Journal of Physics* **G41** (2014) 087002.

[118] R. Arnaldi, A. Baldit, V. Barret, N. Bastid, G. Blanchard, E. Chiavassa *et al.*, *Beam and ageing tests with a highlysaturated avalanche gas mixture for the ALICE pp data taking*, *Nuclear Physics B - Proceedings Supplements* **158** (2006) 149 .

[119] R. Arnaldi, A. Baldit, V. Barret, N. Bastid, G. Blanchard, E. Chiavassa *et al.*, *Front-end electronics for the RPCs of the ALICE dimuon trigger*, *IEEE Transactions on Nuclear Science* **52** (2005) 1176.

[120] ALICE Collaboration collaboration, P. Antonioli, A. Kluge and W. Riegler, *Upgrade of the ALICE Readout and Trigger System*, Tech. Rep. CERN-LHCC-2013-019. ALICE-TDR-015, Sep, 2013.

[121] B. Joly, P. Dupieux, S. Manen, F. Jouve and R. Vandaele, *Upgrade of the ALICE muon trigger electronics*, vol. 9, 02, 2014, DOI.

[122] T. A. Collaboration, G. Aad, E. Abat, J. Abdallah, A. A. Abdelalim, A. Abdesselam *et al.*, *The ATLAS experiment at the CERN Large Hadron Collider*, *Journal of Instrumentation* **3** (2008) S08003.

[123] T. C. Collaboration, S. Chatrchyan, G. Hmayakyan, V. Khachatryan, A. M. Sirunyan, W. Adam *et al.*, *The CMS experiment at the CERN LHC*, *Journal of Instrumentation* **3** (2008) S08004.

[124] ALICE collaboration, *FEERIC: Front-End Electronics for the Resistive Plate Chambers of the ALICE Muon Identifier*, 2016.

[125] "Tdc-gpx from acam datasheet."

[126] D. Adamová, M. Aggarwal, G. A. Rinella, M. Agnello, N. Agrawal, Z. Ahammed *et al.*, *J/ψ production as a function of charged-particle pseudorapidity density in p-pb collisions at $\sqrt{s_{\rm NN}} = 5.02$ tev*, *Physics Letters B* **776** (2018) 91.

[127] T. Pierog, I. Karpenko, J. M. Katzy, E. Yatsenko and K. Werner, *EPOS LHC: Test of collective hadronization with data measured at the CERN Large Hadron Collider*, *Physics Review C* **92** (2015) 034906.

[128] J. Adam, D. Adamová, M. Aggarwal, G. A. Rinella, M. Agnello, N. Agrawal *et al.*, *Pseudorapidity and transverse-momentum distributions of charged particles in proton-proton collisions at $\sqrt{s} = 13$ TeV*, *Physics Letters B* **753** (2016) 319 .

Appendices

Appendix A

Fit functions

A.0.1 Extended Crystal Ball

The extended crystal ball (CB2) function is used for fitting the signal region and defined as:

$$f_{\text{signal}}(x;\mu,\sigma,\alpha,n) = N \cdot \begin{cases} \exp\left[\frac{(x-\mu)^2}{2\sigma^2}\right] & \text{for} \quad \alpha_L > \frac{(x-\mu)}{\sigma} > -\alpha_R \\ A \cdot \left[B - \frac{(x-\mu)}{\sigma}\right]^{-n_L} & \text{for} \quad \frac{(x-\mu)}{\sigma} \leq \alpha_L \\ C \cdot \left[D - \frac{(x-\mu)}{\sigma}\right]^{-n_R} & \text{for} \quad \frac{(x-\mu)}{\sigma} \geq \alpha_R \end{cases} \tag{A.1}$$

where

$$\begin{aligned} A &= \left(\tfrac{n_L}{|\alpha_L|}\right)^{n_L} \exp\left(-\tfrac{|\alpha_L|^2}{2}\right) & C &= \left(\tfrac{n_R}{|\alpha_R|}\right)^{n_R} \exp\left(-\tfrac{|\alpha_R|^2}{2}\right) \\ B &= \tfrac{n_L}{|\alpha_L|} - |\alpha_L| & D &= \tfrac{n_R}{|\alpha_R|} - |\alpha_R| \end{aligned} \tag{A.2}$$

A.0.2 Variable Width Gaussian

The function has the following four parameters: normalisation factor N and three parameters ($\bar{x}$, α,β). The function is defined as:

$$f(x) = N \times exp\Big(\frac{-(x-\bar{x})^2}{2\sigma^2}\Big) \tag{A.3}$$

Here,

$$\sigma = \alpha + \beta\Big(\frac{x-\bar{x}}{\bar{x}}\Big)$$

A.0.3 Double exponential

The double exponential function has four parameters and is defined as:

$$f(x) = exp(a + b * x) + exp(c + d * x) \tag{A.4}$$

Appendix B

Tail parameters

B.0.1 MC tails

The tails from Monte Carlo simulation are extracted by fitting the reconstructed di-muon invariant mass spectrum from MC with a CB2 functions. Fig. B.1 shows the MC tails which are used for this analysis.

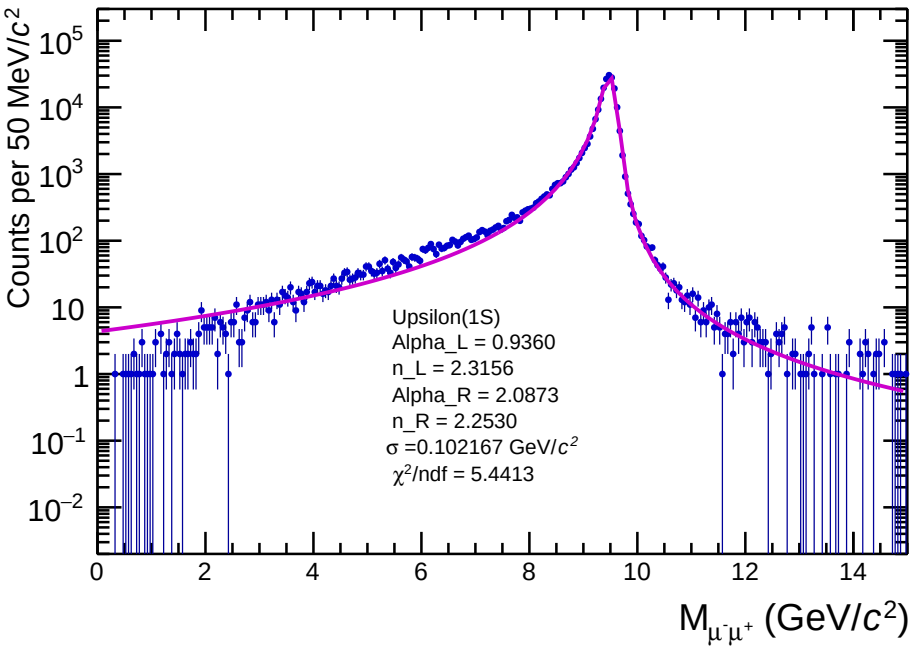

Figure B.1: Tail parameter extracted from pp 13 MC simulation using extended Crystal Ball function.

B.0.2 Data driven tails

The tails from data are extracted by fitting the di-muon invariant mass spectrum as described in 6.4.2.1. The tail parameters are bounds to 100 to ensure convergence of the fit. This procedure is tested under various fitting conditions, the same as for the fits in the integrated case (except that the background is fixed while tails are free) with the addition of two fitting ranges and three signal exclusion ranges. The various fitting conditions can be summarized as follow:

- 2 seeds for the MC tails from Monte Carlo simulations with the 2016 data sample and 2016 data sample

- 3 background functions: product of 2 exponential, product of an exponential and a power law, variable width gaussian
- 5 fitting ranges: [6-13], [5-14], [7-12], [5-12], [7-14] GeV/c^2
- 3 signal exclusion ranges [8.3-10.8], [8.5-11.315], [8.66-11.155] GeV/c^2. The first range is the historical one used for this procedure, the two next are estimated requiring to be 6 or 5 σ away from the 1S state on the left and 3S state mass position on the right. The σ is taken as 160 MeV/c^2 from the fit on the integrated data sample with free background

All values are then computed as the mean of all variations, the statistical error as the mean of all statistical errors and the systematic as 1σ deviation to the mean. Only fit with good quality are considered as valid (Fit status =0 + Covariant matrix status =3). If the condition is not required, values are arbitrary set to 0 in the plot and rejected in the computation. Values of tail parameters ending at the boundary (> 90) are plotted but not taken into account in the computation. The extracted value is taken as the mean of the distribution.

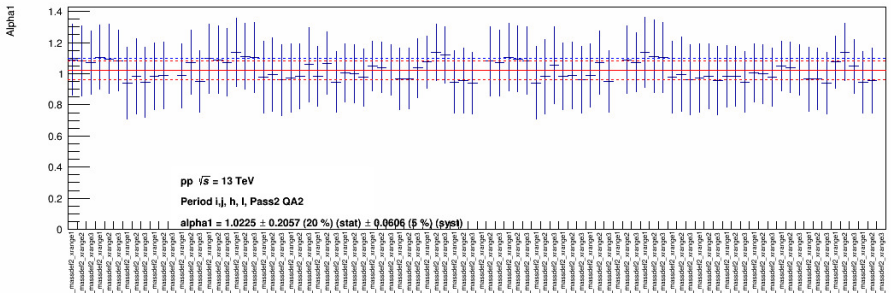

Figure B.2: Extraction of the α_1 parameter of the left tail under various fit conditions, with the data-driven fit procedure.

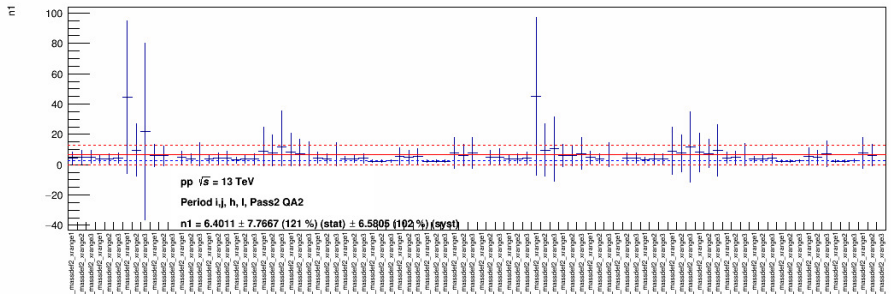

Figure B.3: Extraction of the n_1 parameter of the left tail under various fit conditions, with the data-driven fit procedure.

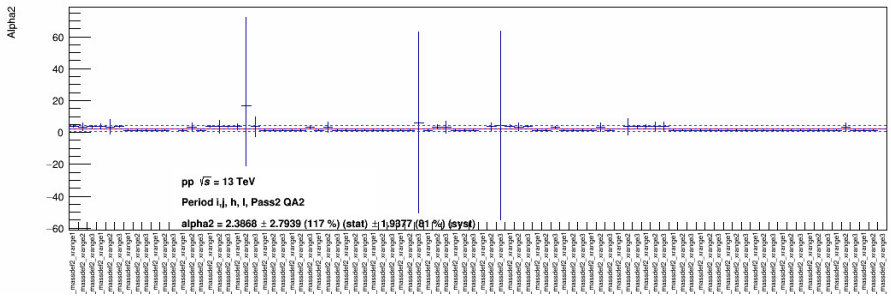

Figure B.4: Extraction of the α_2 parameter of the left tail under various fit conditions, with the data-driven fit procedure.

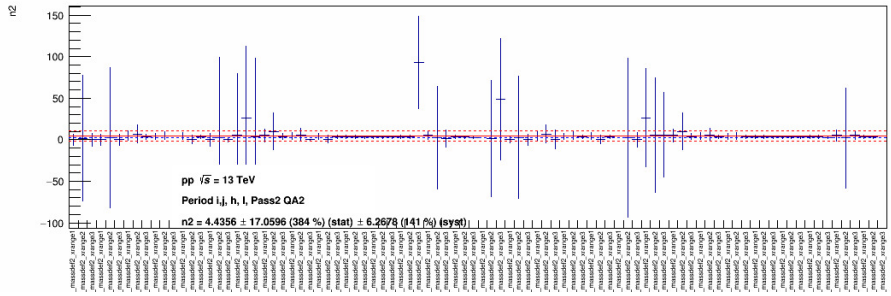

Figure B.5: Extraction of the n_2 parameter of the left tail under various fit conditions, with the data-driven fit procedure.

Appendix C

Additional figures

C.0.1 Charged-particle multiplicity

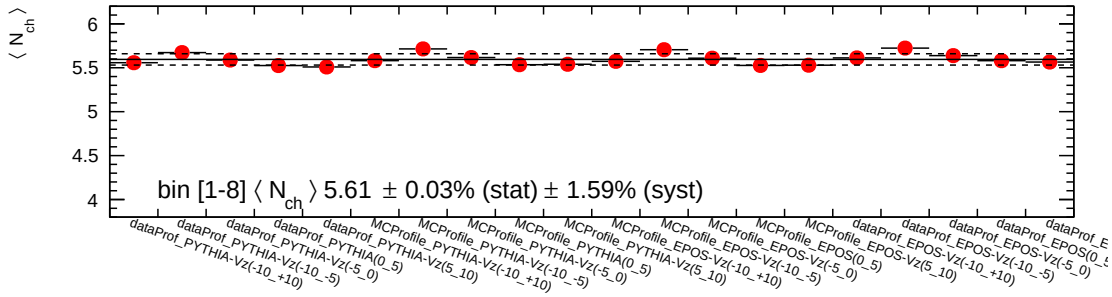

Figure C.1: Bin 1

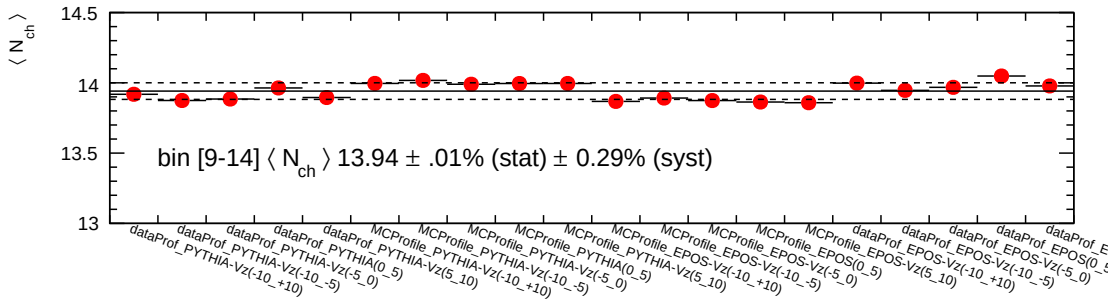

Figure C.2: Bin 2

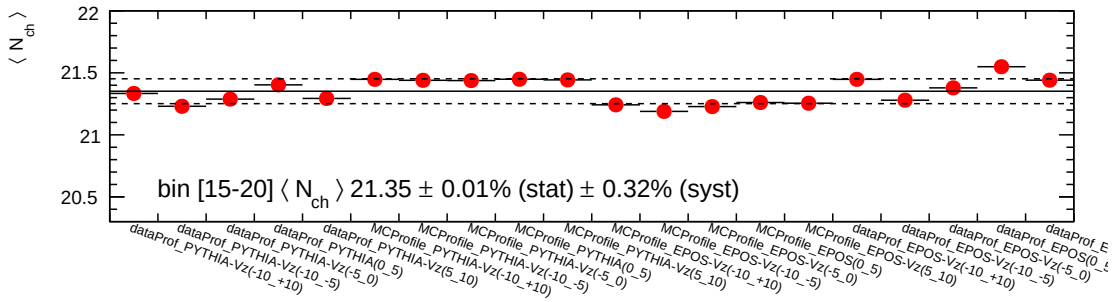

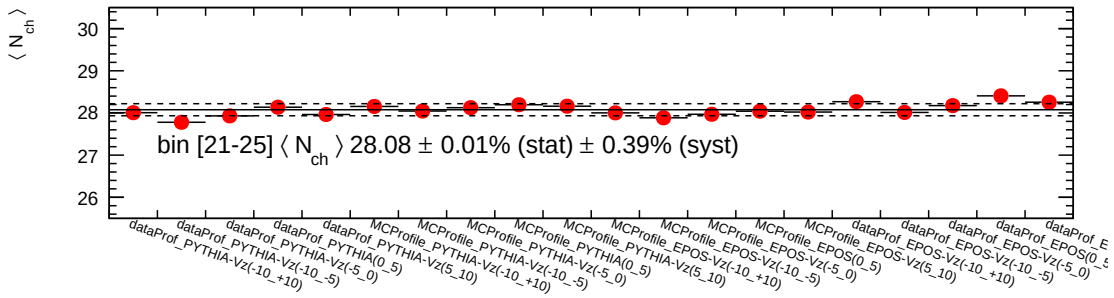

Figure C.3: Bin 3

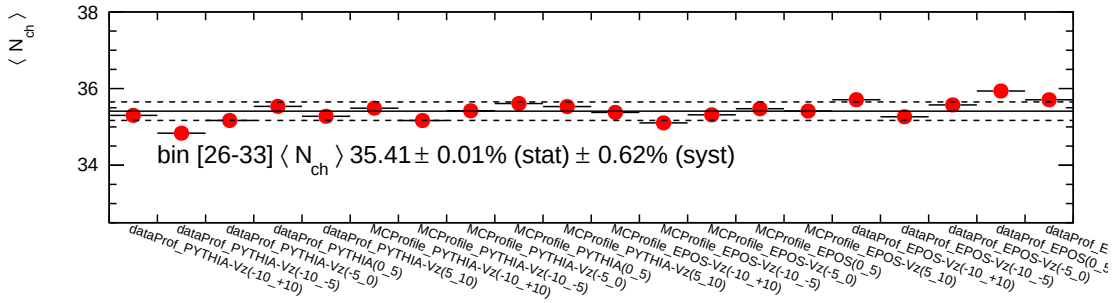

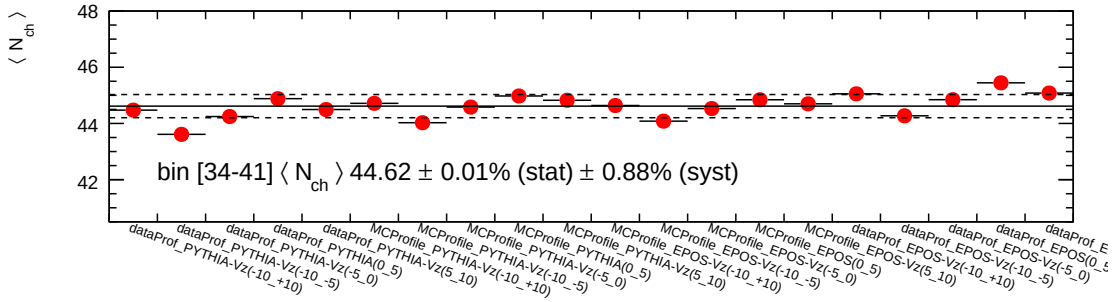

Figure C.4: Bin 4

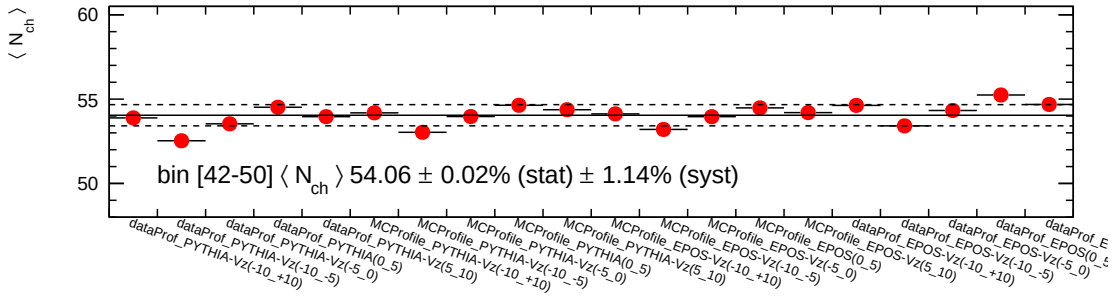

Figure C.5: Bin 5

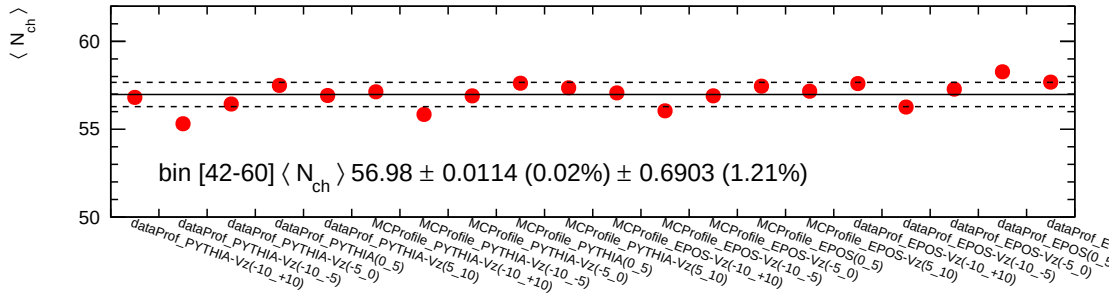

Figure C.6: Bin 6

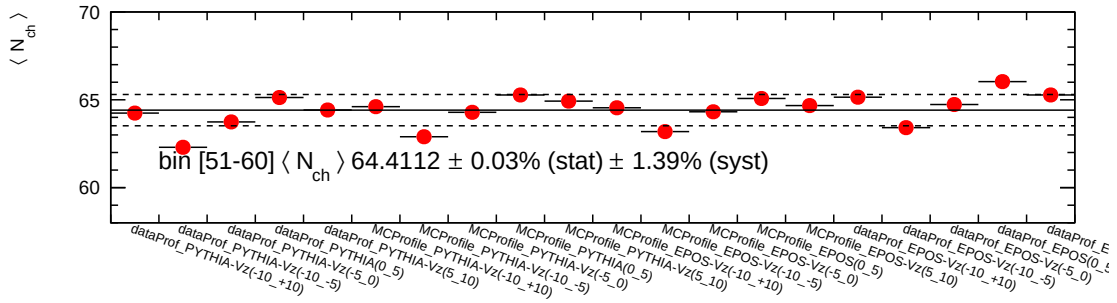

Figure C.7: Bin 7

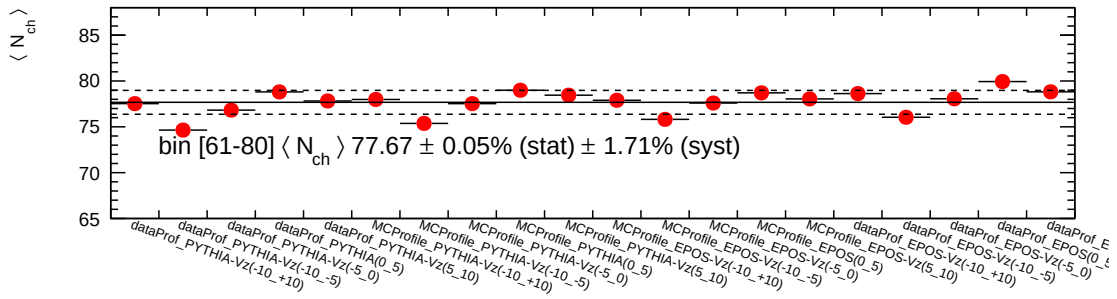

Figure C.8: Bin 8

C.0.2 Signal extraction

The following figures shows: χ^2/ndf of the fit for the integrated case in Fig. C.9, sigma of Υ(1S) in Fig. C.10, mass of Υ(1S) in Fig. C.11, mass of Υ(1S) in Fig. C.11, significance of Υ(1S) in Fig. C.12 and significance of Υ(2S) in Fig. C.13.

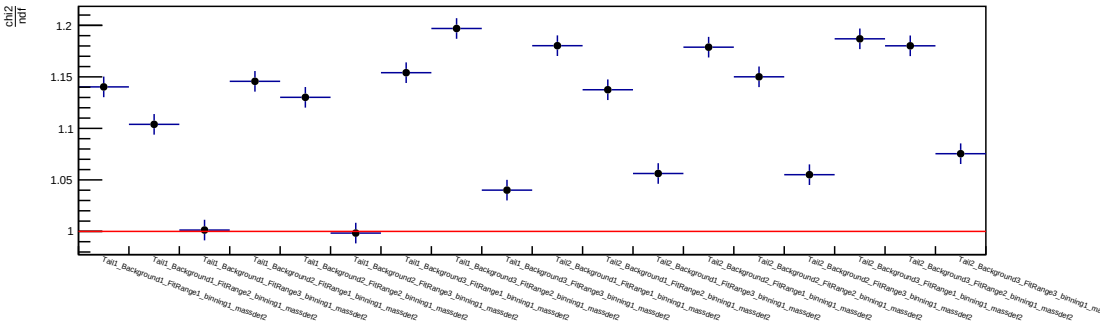

Figure C.9: χ^2/ndf of the fit for integrated case.

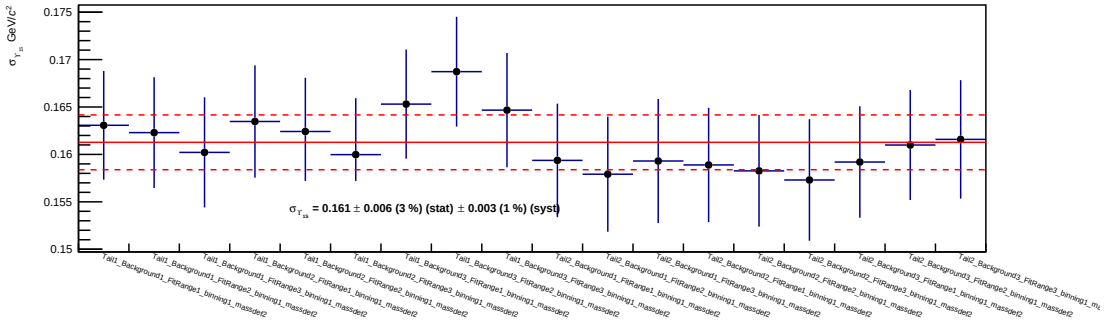

Figure C.10: $\sigma_{\Upsilon_{1S}}$ in the integrated case.

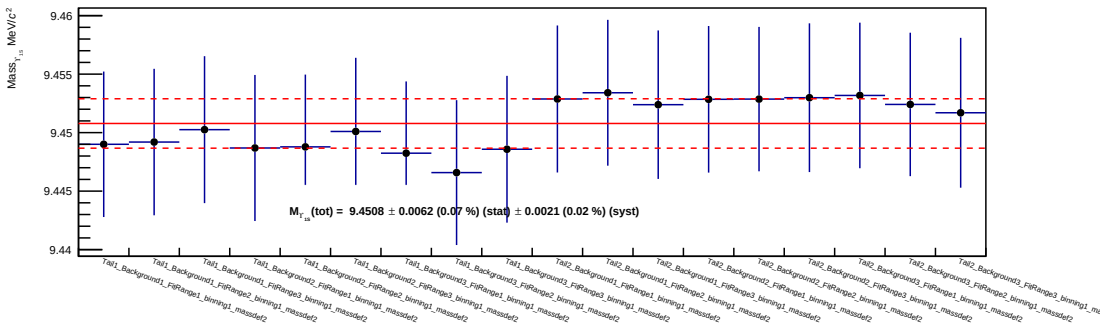

Figure C.11: Mass of Υ(1S), $M_{\Upsilon_{1S}}$ in the integrated case.

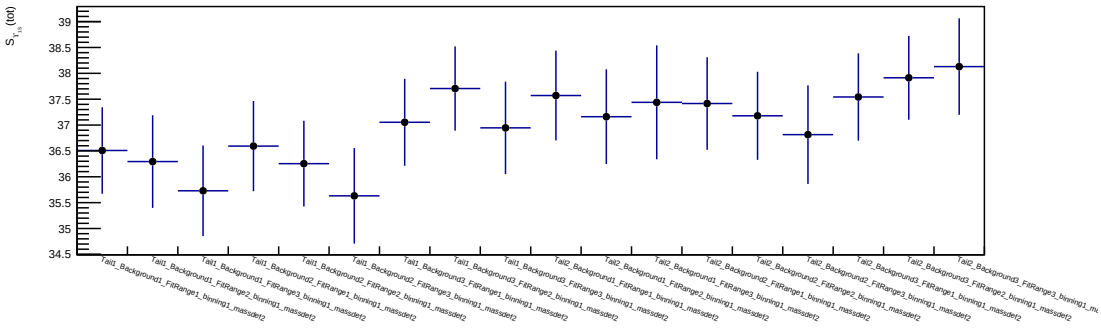

Figure C.12: Significance of Υ(1S) in the integrated case.

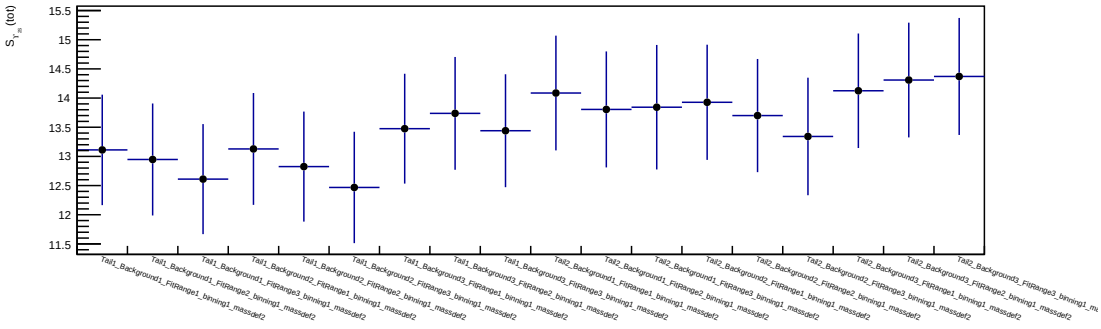

Figure C.13: Significance of Υ(2S) in the integrated case.

Appendix D

Efficiency pile-up in multiplicity bins

The pile-up effects have been studied in two groups: low and high pile-up runs. The run has been flagged as low or high pile-up based on the average number of inelastic (INEL) collisions per bunch crossing(μ). Fig. D.1 shows the μ values as a function of run numbers. The run numbers having high μ values are discarded by the Data Processing Group(DPG) in ALICE. For example, the run numbers in 2016 j period which have $\mu > 0.05$, have been discarded by PDG.

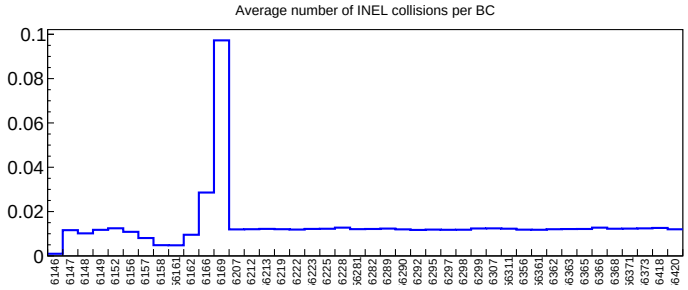

Figure D.1: The μ-values as a function of run numbers for LHC 16j period.

In this analysis, the run numbers which have $\mu \leq 0.006$ are grouped as low pile-up and the rest are grouped as high pile-up runs. The effects of APS (section 6.2.2.1) pile-up rejection has been studied in these two groups. Table D.1 shows the ϵ^i_{pu} in low pile-up runs (second column) and in high pile-up runs (third column). ϵ^i_{pu} has been calculated using Eq.6.40 for each multiplicity bins. The pile-up efficiency factors in multiplicity bins are close to unity.

N^{cor}_{trk} Bin	$\epsilon^i_{pu,low}$	$\epsilon^i_{pu,high}$
1-8	0.999	0.999
9-14	0.998	0.999
15-20	1.000	0.999
21-25	1.000	1.000
26-33	0.998	0.998
34-41	0.997	1.000
42-50	1.000	0.999
51-60	0.999	0.998
61-80	0.998	0.997

Table D.1: ϵ^i_{pu} in multiplicity bins.

Appendix E

Data-MC comparison

The comparison between average number of tracklets in data and MC as a function of v_z has been presented in section 6.3.2.2. The ratios show negligible difference between data and MC (Fig.6.17). We have compared the tracklet and v_z distributions different MC generators (PYTHIA and EPOS) to the data.

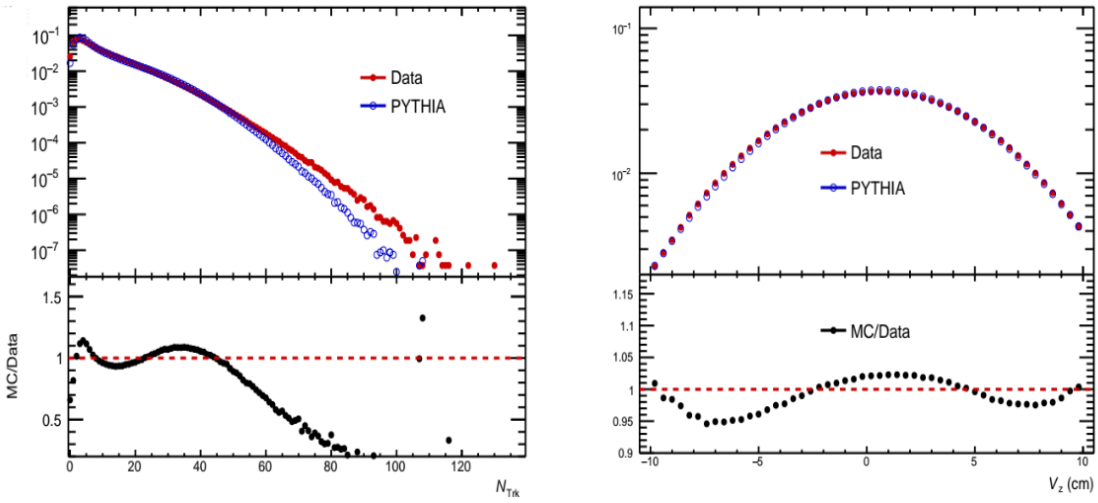

Figure E.1: $N_{\text{trk}}^{\text{raw}}$, v_z distributions from data and PYTHIA event generator (top panels) and data-MC ratios are shown (bottom panels).

The comparison plots between data and PYTHIA8 distributions are shown in Fig E.1. The tracklet distributions show differences in the region where the number of raw tracklets is below 5 and above 55. The MC vertex distributions along the z coordinate show a maximum 5% deviation to data distributions.

Similarly the comparison plots between data and EPOS distributions are shown in Fig. E.2. The tracklet distributions show differences in the region where the number of raw tracklets is below 5 and above 60. The vertex distributions along the z coordinate showa maximum of 7%.

These differences have been taken into account into systematic uncertainties by applying the data-driven correction section 6.3.2 using the average tracklets versus v_z as an input from each of the MC generators. To correct these effects in the corrected tracklet distributions, an additional weight from data events are applied while evaluating the average charged particles.

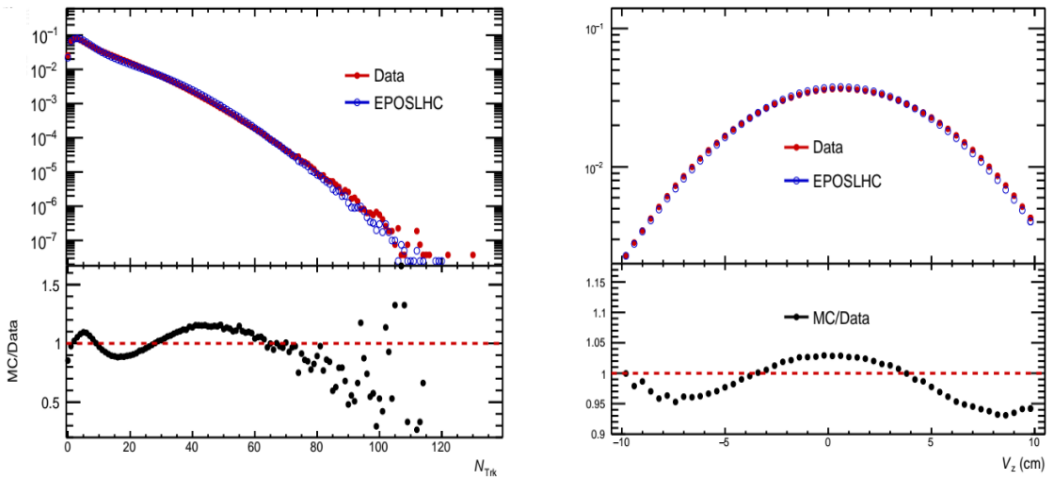

Figure E.2: $N_{\mathrm{trk}}^{\mathrm{raw}}$, v_z distributions from data and EPOS event generator (top panels) and data-MC ratios are shown (bottom panels).

Appendix F

Run II data sample

The analysis presented in this thesis is performed on the 2016 data sample which is a fraction of whole Run II data. The analysis performed on 2016 data sample is not enough to extract Υ(3S) in multiplicity bins. The full RUN2 data[1] that can be used for this analysis has almost 3 times more statistics which will help to have more precision on the results. Table F.1 shows the approximate MB and MUL events in whole RUN2 data. The analysis on additional statistics is ongoing.

Data sample (periods)	N_{MB}	N_{MUL}
2016 (h+j+k+o+p)	29.4 M	103.3 M
2017 (i+m+r)	26.3 M	70 M
2018 (f+m+l+p)	46.6 M	136.8 M
Total	102.3 M	310.1 M

Table F.1: Approximate statistics on RUN2 data sample.

[1] 2015 cannot be used because of high pile-up effects.

List of Figures

List of Tables

Abstract

Study of Υ production as a function of multiplicity in pp collisions at $\sqrt{s}$ = 13 TeV with ALICE at LHC.

The study of quarkonium (J/ψ or Υ) in proton-proton (pp) collisions is interesting as both perturbative and non perturbative aspects of Quantum ChromoDynamics (QCD) are involved in the production mechanism. The quarkonium production as a function of charged-particle multiplicity has been measured in pp collisions with the ALICE detector at the Large Hadron Collider (LHC). They exhibit a non-trivial correlation that can lead to a better understanding of the multi-parton interaction mechanism in the initial state of the collision as well as possible collective effects in small systems. The study of the latest data sample recorded at the LHC in pp collisions at the highest collision energies ever reached in the laboratory ($\sqrt{s}$ = 13 TeV) will allow to investigate high multiplicity events. In ALICE, quarkonia are measured down to zero transverse momentum. Charmonia (J/ψ, $c\bar{c}$) are detected via their decay into di-electrons at mid-rapidity ($|y|< 0.9$) and dimuons at forward rapidity ($2.5 < y < 4$). Bottomonia (Υ, $b\bar{b}$) are detected via their decay into dimuons at forward rapidity. Charged-particle multiplicity is measured using track segments in the silicon pixel detector in $|\eta|< 1$. In this thesis, we will present the first ALICE measurements of relative Υ(1S) and Υ(2S) production as a function of multiplicity in pp collisions at $\sqrt{s}$ =13 TeV. We will discuss the ratio of the relative Υ(2S) over Υ(1S) as a function of charged-particle multiplicity. The comparison between the relative J/ψ and Υ(1S) yields measured at forward rapidity as a function of multiplicity will also be discussed. This will provide insight of possible dependence of the measured correlation with different mass and quark contents as well as the evolution with rapidity range and the collision energy.

Keywords
Quarkonium, Υ, Large Hadron Collider (LHC), A Large Ion Collider Experiment (ALICE), proton-proton collisions, charged-particle multiplicity, Multi-Parton Interactions (MPI).

Étude du taux de production des Upsilons en fonction de la multiplicité des particules chargées dans les collisions proton-proton à $\sqrt{s} = 13$ TeV avec ALICE au LHC.

L'étude des mécanismes de production des quarkonia (J/ψ au Υ) dans les collisions proton-proton (pp) est intéressante car elle nécessiten de prendre en compte les aspects perturbatifs et non perturbatifs de la ChromoDynamique Quantique (QCD). La production de quarkonia en fonction de la multiplicité des particules chargées a été mesurée pour la première fois dans les collisions pp avec le détecteur ALICE au Grand collisionneur de Hadrons (LHC). Ces mesures présentent une corrélation non triviale qui peut conduire à une meilleure compréhension du mécanisme d'interaction partonique multiple dans l'état initial de la collision ainsi que des effets collectifs possibles dans les petits systèmes. L'étude du dernier échantillon de données enregistré au LHC en collision pp aux énergies les plus élevées jamais atteintes en laboratoire ($\sqrt{s}$=13 TeV) permettra d'étudier des événements à forte multiplicité. Avec ALICE, les quarkonia sont mesurés jusqu'à des impulsions transverses nulles. Les charmonia (J/ψ, $c\bar{c}$) sont détectés par leur désintégration en diélectrons à mi-rapidité ($|y|< 0.9$) et en dimuons en rapidité à l'avant ($2.5 < y < 4$). Les bottomonia (Υ, $b\bar{b}$) sont détectées par leur décroissance en dimuons en rapidité à l'avant. La multiplicité des particules chargées est mesurée à l'aide de segments de traces avec le détecteur à pixels de silicium en $|\eta|< 1$. Dans cette thèse, nous présenterons les premières mesures réalisées avec ALICE des productions relatives d'Υ(1S) et Υ(2S) en fonction de la multiplicité des collisions pp à $\sqrt{s}$ =13 TeV. Nous discuterons du rapport relatif des Υ(2S) par rapport au Υ(1S) en fonction de la multiplicité des particules chargées. La comparaison entre les J/ψ et Υ(1S) mesurés en rapidité avant en fonction de la multiplicité sera également examinée. Ces études permettront d'examiner la dépendance possible de la corrélation mesurée avec les différentes masses des quarkonia considérs et les différents types de contenus en quark. La dépendance en fonction du domaine en rapidité et de l'énergie de la collision sera également considérée.

Mot clés
Quarkonium, Upsilon, Grand Collisionneur de Hadrons (LHC), A Large Ion Collider Experiment (ALICE), collisions proton-proton, multiplicité en particules chargées, Interactions Partoniques Multiples (MPI).